



HAL
open science

Multi-scale study of the degradation of railway ballast

Ivan Deiros Quintanilla

► **To cite this version:**

Ivan Deiros Quintanilla. Multi-scale study of the degradation of railway ballast. Mechanical engineering [physics.class-ph]. Université Grenoble Alpes, 2018. English. NNT: 2018GREAI025 . tel-01858650

HAL Id: tel-01858650

<https://theses.hal.science/tel-01858650>

Submitted on 21 Aug 2018

HAL is a multi-disciplinary open access archive for the deposit and dissemination of scientific research documents, whether they are published or not. The documents may come from teaching and research institutions in France or abroad, or from public or private research centers.

L'archive ouverte pluridisciplinaire **HAL**, est destinée au dépôt et à la diffusion de documents scientifiques de niveau recherche, publiés ou non, émanant des établissements d'enseignement et de recherche français ou étrangers, des laboratoires publics ou privés.

THÈSE

Pour obtenir le grade de

DOCTEUR DE LA COMMUNAUTE UNIVERSITE GRENOBLE ALPES

Spécialité :

Matériaux, Mécanique, Génie Civile, Electrochimie

Arrêté ministériel : 25 mai 2016

Présentée par

Ivan DEIROS QUINTANILLA

Thèse dirigée par **Gaël COMBE**
Codirigée par **Fabrice EMERIAULT**
Encadrée par **Charles VOIVRET**
Co-encadrée par **Jean-François FERELLEC**

Préparée au sein du **Laboratoire 3SR : Sols, Solides, Structures et Risques**
dans l'**École Doctorale I-MEP²**
et du **groupe SNCF (CIFRE)**

Multi-scale study of the degradation of railway ballast

Thèse soutenue publiquement le **2 mai 2018**,
devant le jury composé de :

M. William POWRIE

Professeur, University of Southampton, Rapporteur et Président du jury

M. Mathieu RENOUF

Chargé de Recherche, Université de Montpellier, Rapporteur

M. Juan Carlos QUEZADA

Maître de Conférences, INSA Strasbourg, Examineur

M. Gaël COMBE

Professeur, Université Grenoble Alpes, Directeur de thèse

M. Fabrice EMERIAULT

Professeur, Université Grenoble Alpes, Codirecteur

M. Charles VOIVRET

Ingénieur, SNCF Réseau, Encadrant

M. Jean-François FERELLEC

Ingénieur, SNCF Réseau, Co-encadrant



*He was determined to discover the underlying logic behind the universe.
Which was going to be hard, because there wasn't one.*

Terry Pratchett in *Mort*

ACKNOWLEDGEMENTS

And who would have thought, almost five years after we started this adventure abroad, Grenoble has become a very important part of me, a second hometown, from where I am not at all in a hurry to leave. People who know me, even if just a little bit, know how attached I am to those mountains!

A PhD thesis is a long journey, no need to say, and like in all long journeys, many people become directly or indirectly involved, people who do their bit to help it become possible.

I would like to start with my supervisors, the conceivers of the idea, the guides on the execution. This project is as much theirs as it is mine. From that first interview with Gaël during the master, I knew this topic was for me (although I never expected working on railways in a geomechanics laboratory!). Thanks for trusting and choosing me for such an exciting challenge. From the experience and guidance of Gaël and the advices and super-detailed reviews of Fabrice, to the enriching debates and knowledge of Charles (you are very guilty that I speak something similar to French now...) and the support and availability of Jean François: having four supervisors is not always easy, but I actually believe you all have complemented each other perfectly. I hope you have enjoyed as much as I have!

I would also like to thank the jury members for having done the effort of reading the manuscript and coming to my thesis defence. I specially very much appreciated that the questions time evolved, not that much like in a strict examination, but rather in a discussion atmosphere between scientists interested on the topic. I feel the debate engaged was enriching for all of us.

Thanks to the SNCF for still believing in research. It is always nice to see big companies investing in projects that not always provide straight-forward revenue, but also looking for the long-term benefits. It was a great experience to have had the opportunity to spend a full year working in the I&R department. Thanks to all the people I worked with during my stay in Paris, especially to Viet Hung for being an inestimable support with LMGC90 and a great workmate with whom discuss; and a special mention to Olivier and Noura, because being officemates isn't incompatible with becoming good friends.

And thanks to the 3SR Laboratory and the great team of people working there, working in such an international, multicultural but, especially, friendly environment is really rewarding. Thanks to Jean Benoît for his priceless help with the BCR3D and the laser, to Pascal and Eddy with the tomograph, and to Rémi and Jérôme for doing the dirty job of solving the computer messes we do every day. And thanks to Francesca for letting me be part of your master internship, being able to share my little knowledge and experience was one of the best experiences of the PhD, I learnt a lot of it.

In fact, all of this wouldn't have been possible without Albert telling me about the master he was doing in this small town in the Alps, and without Cino allowing me to take part of this

amazing experience that it is the Master GCER. That year was amazing and I keep very good friendships from it, and it has been essential to share this long journey with many of my classmates, it made things much easier.

And friends... it is not possible to carry out such a great endeavour without them: friends from the master, friends from the lab, friends from Grenoble and Paris, and all of those friends I left in Barcelona that, despite the distance, we managed to keep contact with. I won't say names because I highly risk to unfairly forget people. You have all been a key part of this. However, I would regret if I don't give a special shout-out to Carlos: a humble classmate, a hardworking officemate, but overall a trustworthy person who has inevitably become a very good friend.

Last but not least, I don't forget my parents. Their support has always been tireless and essential for keeping on, whatever the decision I have taken in my life. And, of course, I have nothing but words of gratitude for Aina, my inseparable partner: this has been and still is our story. I will never be grateful enough for all the sacrifices you have done to make this possible. This thesis is for you, because without you it simply wouldn't have had any sense at all.

ABSTRACT

After some years of high-speed lines in France (HSL), ballast has proven not to be resistant enough. The performance of ballast, as a thin layer of coarse grains, strongly depends on the shape, size and mineralogical nature of the grains composing it. However, in HSL, grains wear faster than expected due to the traffic of trains at high speeds and the accumulation of maintenance operations (tamping). Ballast replacement has therefore been required much before than its originally expected lifespan.

Under the dynamic stresses imposed by the circulation of trains and tamping operations, ballast is gradually worn by fragmentation of grains and attrition at the contacts. The direct consequence of this degradation is the evolution of grain size and shape: the grading curve is shifted towards small and fine particles and the grains progressively lose their angularity. Eventually, the cumulated wear will no longer allow ballast to perform properly: the shear resistance of the layer is reduced limiting both the anchorage of sleepers and the distribution of loads to the platform. In addition, the presence in excess of fine particles renders tamping ineffective (fast evolution of track defaults) and reduces the permeability of the track. Thus, in order to search for optimized solutions for prolonging ballast lifespan, it is crucial to first understand the origins and mechanisms leading to ballast degradation when it is subjected to complex loading, for building a predictive model of ballast wear.

The degradation of contact interfaces generates fine particles. The associated mass flux, which depends on the loading conditions, has been classically predicted by Archard equation. The model assumes that the generated volume of wear is proportional to the normal force and the relative displacement between the surfaces. Therefore, it is crucial to quantify the forces at the contact scale and the relative displacements between ballast grains in sliding contact. Discrete elements simulations by NSCD are used as a tool for performing a change in scale from the track scale to the contact scale, giving information of ballast as a granular layer, from its global behaviour down to the contact forces and relative displacements between grains. Contacts with a higher potential of generating fine particles (according to Archard model) are then identified and reproduced experimentally by two-grain shearing tests. In parallel, the Micro-Deval standard attrition test is used as a link between numerical and experimental results to validate Archard model, and to study the evolution of grain morphology by scanning a sample of grains using X-ray tomography at different stages of the test. Both experimental campaigns show the weakness of sharp asperities, especially on edges and vertexes.

A model in two phases is proposed, accounting for a first phase of fast and aggressive degradation due to the high stress at the contact interface and a more stable second phase with a lower wear rate. A critical stress is identified as a threshold between phases. This model is then applied at each individual contact on the numerical simulations, resulting in a first approach of the production curve of fine particles within the track.

RÉSUMÉ

Pour voies ferrées à grandes vitesses (LGV, Lignes à Grande Vitesse), la durabilité des performances du ballast de chemin de fer n'est pas aussi importante qu'attendu. Le comportement mécanique de cette couche granulaire mince dépend fortement de la forme, la taille et la minéralogie des grains. Sur les LGV, les grains s'usent plus vite qu'attendu, essentiellement à cause de l'accumulation des opérations de maintenance appelées bourrage. Une conséquence à cela est un renouvellement complet du ballast avec une fréquence largement supérieure à ce qui était initialement prévu à la création de ces lignes.

Soumis à des contraintes dynamiques combinées (trafic ferroviaire et des opérations de bourrage), les grains de ballast se dégradent par fragmentation et par attrition aux contacts. Les conséquences directes de cette dégradation progressive sont l'évolution de la taille et de la forme des grains. La courbe granulométrique est alors translatée vers les petits éléments, avec une présence notable de particules très fines résultant de l'usure des grains. De plus, l'angularité des grains est progressivement diminuée. Au-delà d'un certain temps, le cumul de dégradation se traduit par une chute des performances mécaniques du ballast. Le ballast ne remplit plus efficacement ses fonctions. La résistance latérale de la voie est réduite, limitant ainsi la répartition des contraintes sur la plateforme et l'ancrage des traverses. La présence excessive de fines rend le bourrage inefficace et diminue la perméabilité de la voie. Par conséquent, pour trouver des solutions optimales pour prolonger la durée de vie du ballast, il est nécessaire d'abord de bien comprendre les origines et mécanismes menant à l'usure des grains, pour finalement construire un modèle prédictif de dégradation.

La dégradation des interfaces au contact génère de particules fines. La quantité de fines produite, laquelle dépend des conditions de chargement, est classiquement prédite par l'équation d'Archard. Ce modèle part du principe que le volume d'usure généré est proportionnel à la force normale et au déplacement relatif entre les surfaces en contact. La simulation numérique par éléments discrets (NSCD) d'une portion de voie de chemin de fer soumis à un chargement cyclique est un outil nécessaire pour réaliser la transition entre l'échelle de la voie et l'échelle du contact, fournissant les informations sur le ballast en tant que couche granulaire, depuis son comportement global jusqu'aux forces de contact et les déplacements relatifs entre les grains. Les contacts montrant un grand potentiel de génération de fines (selon le modèle d'Archard) sont identifiés et reproduits expérimentalement avec des essais de cisaillement entre deux grains. Parallèlement, l'essai d'attrition Micro-Deval est utilisé pour relier les résultats numériques et expérimentaux, et ainsi valider le modèle d'Archard, et pour suivre l'évolution de la forme des grains avec l'aide des scans d'un échantillon de grains par tomographie RX à différents états d'usure. Les deux campagnes d'essais montrent la faiblesse des aspérités les plus aiguisées, dont spécialement celles sur les arêtes et sommets.

Un modèle prédictif d'usure en deux phases est donc proposé. La première phase décrit une usure rapide due aux fortes contraintes normales à l'interface de contact, et la deuxième phase

décrit un taux d'usure plus modéré. Une contrainte seuil permet d'identifier clairement le passage d'une phase à une autre. Sur la base des déplacements relatifs intergranulaires observés dans la simulation numérique discrète, ce modèle est appliqué pour chaque contact dont l'histoire de chargement est variable. Une estimation de la courbe de génération de fines dans la voie est ainsi proposée.

TABLE OF CONTENTS

INTRODUCTION	13
I. BALLAST WEAR: A MULTI-SCALE PROBLEM	17
1.1 Introduction.....	18
1.1 The track.....	19
1.1.1 Track section	19
1.1.2 Train loads	21
1.1.3 Maintenance cycle of the track	24
1.2 Ballast: granular layer	27
1.2.1 Ballast characteristics	27
1.2.2 Ballast life cycle	29
1.2.3 Previous works on ballast degradation	30
1.3 Contact scale: tribology.....	32
1.3.1 Friction	32
1.3.2 Contact wear	35
1.3.3 Archard equation to wear	36
1.4 From the track to the grain: NSCD	37
1.4.1 Non-Smooth Contact Dynamics	40
1.4.2 Contact detection and particle shape	41
1.4.3 Previous works on numerical particle degradation	42
1.5 Conclusions.....	44
II. MICRO-DEVAL TEST	45
2.1 Introduction.....	46
2.2 Micro-Deval standard test	46
2.3 Numerical simulation of the Micro-Deval	47
2.3.1 Description of the system	48
2.3.2 Dynamics of the system	49
2.3.3 Contact forces	50
2.3.4 Friction work	51
2.4 Experimental Micro-Deval test	53
2.4.1 Test procedure	53
2.4.2 Evolution of the mass of the sample	53
2.5 Estimation of Archard coefficient for Micro-Deval test.....	58
2.6 Adequacy of Micro-Deval test	59
2.7 Conclusions.....	60

III. EVOLUTION OF MORPHOLOGY	63
3.1 Introduction.....	64
3.2 Morphology indicators.....	64
3.2.1 General shape parameters	65
3.2.2 Spherical harmonics series (SHS)	66
3.2.3 Curvature	68
3.3 X-ray tomography	68
3.3.1 Generalities	68
3.3.2 Test procedure	69
3.3.3 Samples	71
3.4 Evolution of scalar parameters	73
3.4.1 Grain descriptors	74
3.4.2 Shape parameters	77
3.4.3 SHS analysis	78
3.4.4 Summary	80
3.5 Curvature analysis.....	81
3.5.1 Curvature filter scale	82
3.5.2 Evolution of the asperity radii	83
3.5.3 Link between asperity radii and wear	89
3.6 Morphology evolution on the track	91
3.7 Conclusions.....	93
IV. THE TRACK AT THE CONTACT SCALE	95
4.1 Introduction.....	96
4.2 Numerical simulation of a TGV track.....	96
4.2.1 Description of the system	97
4.2.2 Type of contacts	99
4.2.3 Contact forces	99
4.2.4 Relative displacement at the contact scale	102
4.2.5 Friction work	104
4.3 Shearing experiments	107
4.3.1 Samples	107
4.3.2 Known problems and calibration tests for F_z	108
4.3.3 Test summary	110
4.4 Friction coefficient	112
4.4.1 Geometry correction	113
4.4.2 Friction coefficient ballast – concrete	115
4.4.3 Friction coefficient ballast – ballast	116
4.5 Morphology of the contact area	119
4.5.1 Evolution of the distance between samples (decrease of Z)	119

4. 5. 2	Estimation of the contact area	120
4. 5. 3	Evolution of the contact area	125
4. 5. 4	Volume loss	129
4. 6	Influence of water	131
4. 7	USP tests	133
4. 8	Conclusions	137
V.	BALLAST WEAR MODEL	139
5. 1	Introduction	140
5. 2	Basic simplifications	140
5. 3	Archard in two phases	141
5. 3. 1	Estimation of Archard coefficient for each phase	142
5. 3. 2	Length of Phase 1	143
5. 4	Algorithm	146
5. 5	Results	148
5. 5. 1	Wear evolution	148
5. 5. 2	Influence of parameter φ	150
5. 5. 3	Influence of tamping	151
5. 6	Perspectives of improvement	152
	CONCLUSIONS & PERSPECTIVES	155
	REFERENCES	159
	ANNEX A. DEVICES AND SAMPLES	167
A. 1.	BCR3D device	168
A. 1. 1.	Sample description and preparation	168
A. 1. 2.	Positioning the sample in the machine	172
A. 2.	Laser profilometre	174

INTRODUCTION

In 2013, more than 60% of the French railway budget was earmarked for track maintenance and renovation of tracks. A big effort has been done since in order to increase the amount of kilometres of revamped tracks. However, these operations are costly, especially for a saturated network, very sensitive to any kind of perturbation in the system. It is thus desired to optimize the maintenance of the track in order to maximise the time between full renovations. Ballast, as the layer of coarse grains located immediately below the sleepers, plays a key role in the degradation of the railway track. After some years of high-speed railway lines (HSL) in France, ballast grains proved not to be resistant enough, suffering a much faster degradation than expected. This ultimately encouraged a higher exigence for the materials of the aggregates, which lead to an improvement of the situation. However, in order to develop more efficient solutions for ballasted tracks in a technic-economic context, a proper knowledge of the sources and mechanisms of ballast degradation is required.

Under the combination of both the dynamic stress imposed by traffic and maintenance operations, ballast is gradually worn by fragmentation of grains and attrition at the contacts. The direct consequence of this degradation is the evolution of grain size and shape: the grading curve is shifted toward smaller particles, steadily producing very small particles called “fines” in the process, and grain shape tends toward rounded grains that progressively lose the characteristic sharpness and angularity of new ballast. Eventually, the accumulation of degradation makes ballast unable to fulfil its functions. The loss of angularity reduces the capacity of the layer to keep the sleepers in place, while the excessive presence of fines reduces the permeability of the track and the efficacy of the maintenance operations. The consequences of ballast degradation are therefore relatively well-known, but a deeper study on its origins is still necessary.

Objectives and methodology

It is therefore of industrial interest to build a predictive model of ballast wear along its lifespan in the track. The current empirical models used by railway industry do not give any information about the origins of wear. This knowledge and a proper prediction would allow for conceiving optimized solutions for maintenance on ballasted tracks in a technic-economical context.

From a scientific point of view, unlike grain breakages, granular wear due to the friction between particles has been relatively little investigated so far. A better understanding of these mechanisms, especially at a micro-scale level, has then a particular interest. The application of analytical models coming from tribology, although mostly conceived for controlled manufacturing and wear of metals, can offer a new perspective of this phenomenon at the interface scale.

In order to develop a model of railway ballast degradation, we propose a multi-scale approach combining numerical simulations and experimental tests.

The difficulty of performing reliable experimental tests at the track scale for assessing micro-scale phenomena within the ballast layer, such as contact forces or the amount of generated fines, makes it necessary to turn to numerical simulation by discrete elements. These simulations allow a change in scale from the track scale to the contact scale, giving us information on ballast as a granular layer, zooming in from its global behaviour down to the contact forces and relative displacements between grains. The goal of this project is then not to predict wear by simulating it numerically, but to extract from simulations the involved quantities in wear mechanisms and then to apply an analytical predictive model.

Wear, as a surface interacting phenomenon, is studied by tribology, so a first literature research on this field is required in order to obtain a proper model to apply to the case of irregular grains in contact. Experimental tests are then proposed for studying wear at the contact scale and for assessing the analytical model, modifying or calibrating it to the specific case of ballast. The standard attrition test of Micro-Deval is proposed as a reproducible economical test, located at an intermediate scale, which serves as a link between simulations and experimental tests. Parallel to the quantification of fines, a morphological study using X-ray tomography is proposed in order to better understand the evolution of grain shape and angularity along the degradation process.

Organisation of the thesis

This thesis consists of five main chapters, followed by conclusions and annexes. Chapter I serves as a context introduction of the problem and as a bibliographic summary of the different works performed so far on the different mechanisms and tools that will be of interest along the project. We approach this study in the same order that motivates this thesis, performing a multi-scale transition from the track scale to the contact scale: starting from the global description of the track, then describing the ballast layer, and ending with a brief introduction to tribology, contact friction and wear, and the predictive model of Archard for abrasive wear. Finally we present Non-Smooth Contact Dynamics as the numerical tool that will allow us to

perform this change in scale along the thesis.

Chapter II presents the standard attrition test of Micro-Deval. This test is performed both numerically and experimentally, so it serves as a link between both kinds of results. Using the simulations, we analyse the internal mechanisms in the system and we apply Archard model in order to assess the friction work generated within the cylinder. The test is then performed experimentally stopping the device at different intervals in order to build the curve of mass loss. Both results are then linked and a first wear coefficient is computed for the case of the Micro-Deval test.

Chapter III presents a morphological tracking and analysis of a sample of seven ballast grains. Taking advantage of possibility of stopping the Micro-Deval device, we identify the grains and we scan them using X-ray tomography at different states of wear. Shape parameters are then computed and their evolution curve is presented. Finally, a deep analysis of the evolution of asperity radii is performed.

In Chapter IV, we perform the change in scale from the track to the contact scale. First, we present and analyse the numerical simulation of the passage of a High-Speed train over a section of the track. We apply Archard to the simulations and we identify the characteristic contacts showing a higher potential of generating fine particles. These contacts between two grains are then reproduced experimentally by using the shearing device BCR3D. The contact interface is scanned using a laser profilometre in order to assess the evolution of the contact area and the volume lost during the tests. Archard model is then evaluated for the case of two ballast grains in quasi-static contact.

Following the previous results, Chapter V presents a first proposition of wear model for ballast. The algorithm and all the input parameters are carefully detailed, and some results and analysis are given using the model. Finally, the current limitations of the model, along with the corresponding lines of development and improvement, are described.

In the last section, the partial conclusions of the different chapters are summarized and discussed from a general perspective of the project, proposing future lines of research and some perspectives and improvements about the model.

I. BALLAST WEAR: A MULTI-SCALE PROBLEM

1. 1	Introduction.....	18
1. 2	The track.....	19
	1. 2. 1 Track section	19
	1. 2. 2 Train loads	21
	1. 2. 3 Maintenance cycle of the track	24
1. 3	Ballast: granular layer	27
	1. 3. 1 Ballast characteristics	27
	1. 3. 2 Ballast life cycle	29
	1. 3. 3 Previous works on ballast degradation	30
1. 4	Contact scale: tribology.....	32
	1. 4. 1 Friction	32
	1. 4. 2 Contact wear	35
	1. 4. 3 Archard equation to wear	36
1. 5	From the track to the grain: NSCD	37
	1. 5. 1 Non-Smooth Contact Dynamics	40
	1. 5. 2 Contact detection and particle shape	41
	1. 5. 3 Previous works on numerical particle degradation	42
1. 6	Conclusions.....	44

1.1 INTRODUCTION

This first chapter after the introduction serves as a bibliographic summary to frame the industrial context, some relevant previous works and the different tools that will be useful during the thesis. With this goal in mind, along the different section we will perform a transition in scale from the general context to the specific problem, i.e. starting from a general overview of the track and progressively zooming into the ballast layer and finishing at the contact scale between grains.

Hence, first of all, we need to understand what we are studying and why, and that means to place ballast in its particular context: the railway track. We will start giving a brief description of the ballasted railway track and we will introduce the different components and layers by following the diagram of the typical transversal section. Afterwards, and in order to understand the life cycle of the track and the reasons leading to the necessity of maintenance, we will identify and quantify the different external loadings intrinsic to the passage of trains. After several cycles of loading, these efforts eventually induce defaults in the track geometry that need to be corrected for a proper operation of the track. Tamping will be then introduced as the maintenance operation that allows for this geometry correction.



Figure 1.1 Railway track next to Gare d'Austerlitz in Paris.

Once presented general context and the maintenance cycle of the track, we will focus on the component of the track that is the aim of this project: ballast as the granular layer below the rails. We will start describing the general functions this layer needs to fit. As a granular layer, these functions will only be possible if a proper selection of the grains is performed. Thus we will describe which mechanical and morphological characteristics we search on the grains and why, explaining the selection methods and filters. However, along the lifespan of ballast and mainly due to the passage of trains and tamping, grains gradually lose some of these characteristics. Understanding the lifecycle of the aggregates, we will arrive to the main focus of this project: the degradation of the grains.

First of all, we will present some previous works and studies on this problem that have attempted to assess the amount of fines generated within the track and the influence of these particles on the track behaviour. However, these studies generally face the problem from an

engineering point of view, i.e. quantifying wear for a particular case without going deeper searching for the reasons of this phenomenon. This project approaches the problem from a different point of view, trying to give an answer to the causes of the degradation, so that it would be possible to predict it, not only for a specific case, but whatever the conditions of the track.

Therefore, we will perform a literature review of wear itself at the micro-scale, which is a field studied by tribology. Henceforth we will present some basic tribology concepts such as friction and some examples of kinds of wear. Then we will focus on the equation proposed by Archard in 1953 for predicting wear, which is still widely used and will serve as a reference model for wear prediction throughout this project. Some previous works that have used this specific model in different contexts will be presented.

Ballast degradation is a multi-scale phenomenon, which is produced at the contact scale but depends on the conditions and loading of the track and the ballast layer. In order to perform this transition, numerical simulations based on the Non-Smooth Contact Dynamics method will be used. Therefore, we will give a brief introduction to this tool that will be used all along the thesis, as well as some previous works that applied this method to the specific case of ballast.

1. 1 THE TRACK

We understand the track as all the components and structure allowing the circulation of trains (Figure 1.1). This structure supports and transfers to the platform the external loading intrinsic to the passage of railway vehicles. It also has a damping effect in mechanical and acoustical vibrations, drains rainfall water and keeps vegetation away from the rails. The geometric and mechanical requirements of the track are given by standard norms [1, 2, 3] that assure a homogenous quality all along the line. These standards are even stricter when dealing with High-Speed Lines (HSL) in order to favour commercial speeds of over 300 km/h.

1. 1. 1 Track section

In order to have an accurate overview of the track, we need to first describe the different parts, from the ground up to the rails, their function and their location within the system. Figure 1.2 shows the typical cross section of a ballasted track and the differences in the sub-layers between new and conventional lines. We can distinguish between two big groups of components:

- Track superstructure or track panel: formed by rails and switches, sleepers, occasional pads and the fastening system.
- Track foundation or track bed: formed by the ballast layer and all the sub-layers below it, where the track panel lies.

The first element and the only one in contact with the vehicles are rails, which are made of

structural steel bars and are in charge of driving trains and transmitting loads to the sleepers. The different segments are aluminothermically welded in-situ and attached to the sleeper blocks by the fastening system [1, 2]. Below the rails, rubber elastic pads are placed to ensure the contact between the lower surface of the pad and the sleeper [4, 5].

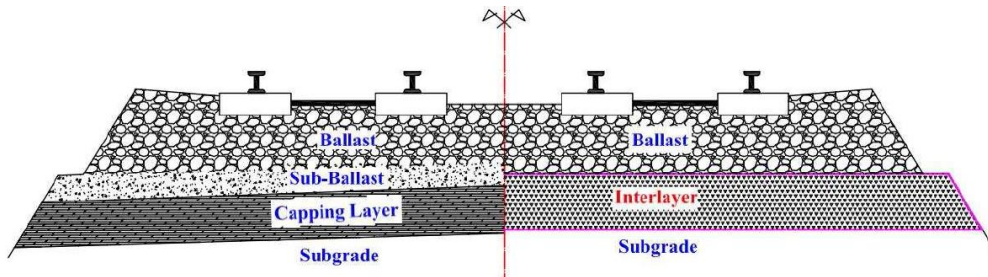


Figure 1.2 Comparison between new (left) and conventional (right) ballasted tracks [6].

The next element are sleepers, which are embedded inside the ballast layer (Figure 1.3) and serve to transfer dynamic and static loads to ballast, to keep the track gauge and to give a certain inclination to the rails when required. These sleepers can be made of wood, concrete or even steel, the concrete ones being the sleepers used in French HSL. Modern sleepers are usually formed, either by two concrete blocks linked by a steel bar called twin-block sleepers, or, more commonly, by a single concrete block called mono-block sleepers. Occasional pads are placed under the concrete blocks of the sleepers, called Under-Sleeper Pads (USP), in order to reduce vibrations in urban areas or to soften the contact with ballast reducing wear of the aggregates [7, 8, 9, 10].

Below the super-structure we find the track bed, formed by different layers. The upper layer of the track bed is always ballast, which is formed by 25/50 mm gravel with a minimum thickness of 30 cm. It anchors the sleepers in position and receives loading from the track panel and redistributes it to the sub-layers. Since this layer is the main focus of this project, it will be explained in detail in section 1. 2. Below the ballast layer we find the sub-layers, which represent the transition from the ballast to the subsoil. The setup of these layers varies depending on the type of line.



Figure 1.3 Ballast surrounding the sleepers below the rail.

In conventional lines, we find the Interlayer or ITL, which is formed of ballast grains mixed with fines up to the scale of clay. This layer is not constant in composition, but it performs a transition from clean ballast at the top to a larger amount of fines at the bottom, where it usually presents a high-density and very low permeability [11].

In new lines, a 20 cm layer of sub-ballast is placed under ballast, formed by compacted clean gravel within the range 0/31.5 mm of grain-size (smaller than ballast). This layer allows a better redistribution of the loadings, hence improving the load-bearing capacity of the soil, and protects the platform against erosion and frost. Below the sub-ballast layer we find the capping layer, composed of sandy gravel 0/31.5 mm, which provides a stable foundation for the upper layers [4].

Finally, on both cases, below all the sub-layers we find the subgrade, formed either directly by the natural soil or by added soil. This soil can be stabilized if the properties are not good enough.

From the rail, as the only component in contact with the trains, down to the subsoil, one of the main functions of the track system is to transmit and spread the loadings coming from the circulation of trains, so that the geometry of the track is kept while the degradation of the different layers is minimized.

1. 1. 2 Train loads

In order to understand the maintenance cycle of the track, we need to first know the loads it needs to resist. Loads transmitted to the track can have different natures, but train traffic is the most important source. We classify the different efforts taking into account their direction with respect to the rails: vertical, lateral and longitudinal (Figure 1.4).

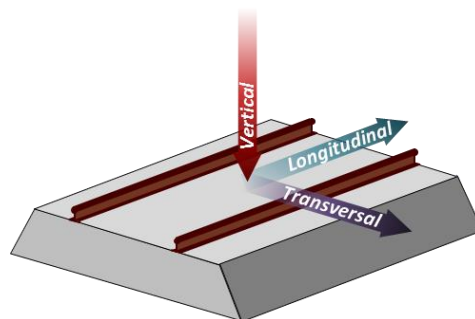


Figure 1.4 Directions of the loading on the track.

Vertical forces are the main ones and correspond to a combination of static and dynamic efforts. They mainly come from the weight of both the train, usually expressed on mass per axle, and the track itself for the lower layers. According to the International Union of Railways (UIC) [12], tracks can be divided into five categories depending on its permissible mass per axle:

- Class A for 16 tons / axle.
- Class B for 18 tons / axle.
- Class C for 20 tons / axle.
- Class D for 22.5 tons / axle.
- Class E for 25 tons / axle.

As a reference, most of TGV's used on French HSL have an axle load of 17 tons [13].

Lateral efforts, i.e. horizontal but perpendicular to the rails, are exerted by the wheels especially in curves. Ballast layer has crucial role locking the sleepers in position when these efforts become important. Finally, longitudinal efforts, i.e. parallel to rails, are mainly due to acceleration and braking of the trains. However, these efforts are usually not important compared to the vertical ones.

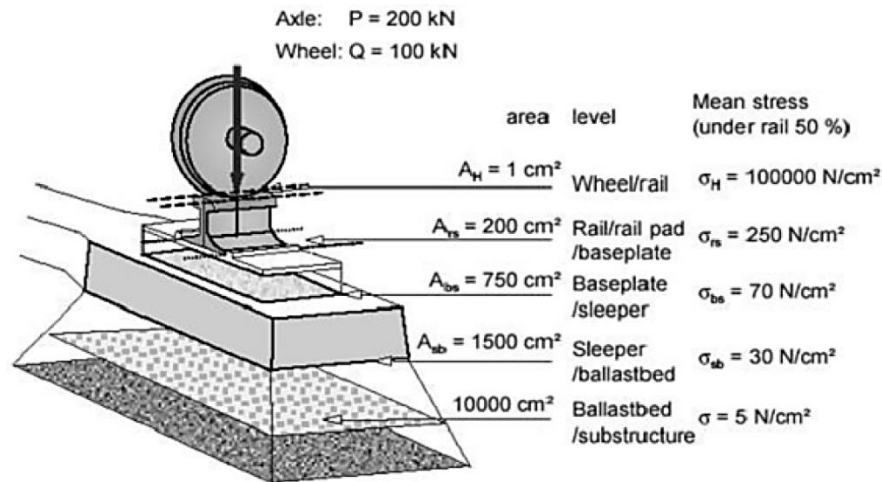


Figure 1.5 Example of load transmission from the wheel to the ballast layer [14].

The irregularities and geometric defaults of the track and the rails, and all kinds of discontinuities breaking the homogeneity of the track, such as not welded joints or the passage over track switches, can make these efforts become more important and contribute even more to the degradation of the track.

As we have explained, these loads are transmitted downwards, being gradually damped from layer to layer (Figure 1.5). As an example and because it will be later useful during the numerical simulations of the track, we will present below the computation of the vertical force transmitted by the rails to the sleeper.

Computation of the vertical force signal

Even knowing the axle load of the train, there are many factors influencing the actual vertical force that is transmitted to the sleeper. As a continuous system where all elements are linked by the rail and the sleepers, the vertical load is not only influencing the direct layers below it but it is spread over the neighbour sleepers. Measuring the force transmitted by the trains is usually performed via indirect measurements, such as the deformation of the rail measured by strain gauges [4]. This measurement, though, overestimates the actual load received by the sleeper, since it does not take into account the energy dissipation of under-rail pads and the redistribution of the load among the neighbour sleepers. This redistribution depends on the deflection of the rail and the softness of the sublayers, which makes it not straight forward to compute experimentally the actual load transmitted from the rail to the sleeper.

In order to estimate the vertical loading exerted to the sleeper by a bogie passage, the analytic formula given by Sauvage [15, 13, 16] is commonly used. Sauvage observed that the area of

influence and the level of spreading of the load will be mainly determined by the rigidity of the soil underneath, so he used the linear theory of Boussinesq, considering the track as a multi-layer system, to consequently compute the spreading of the load. According to his calculations, the force signal at each instant t is given by the following expression:

$$F(t) = \frac{Q \cdot Y}{2} \cdot \left[X \left(\frac{v \cdot t - a}{d} \right)^2 + X \left(\frac{v \cdot t - a - L}{d} \right)^2 \right] \quad (1.1)$$

Where:

- Q is the axle load [N].
- Y is a coefficient ranging between 0 and 1, which takes into account the redistribution of the load with the neighbour sleepers depending on the rigidity of the soil.
- X is also a coefficient ranging between 0 and 1 depending on the rigidity of the soil. Both coefficients X and Y are given by tables.
- v is the speed of the train [m/s].
- t is the time [s].
- a is the critical distance corresponding to the initial position where the load is zero [m], usually taken as $5 \cdot d$.
- d is the distance between two consecutive sleepers [m].
- L is the distance between both axles of a bogie [m].

As an example of application, let us take the conditions of the numerical simulation of the passage of a HSL train over a section of a track that will be presented in section 4. 2. In the simulation, we will consider only one sleeper block from a twin-block sleeper, i.e. only half of the track. We will assume that each of the blocks takes half of the load. For computing the force signal that we need to apply on the sleeper block, we take the typical values for a HSL:

- $Q = 20$ tons/axle. Since only half sleeper is simulated, we will assume that both halves take the same load, so 10 tons/axle (100 000 N) are considered.
- $X = 0.61$ and $Y = 0.46$ (considering a rigid soil with $E_s = 100$ MPa).
- $v = 300$ km/h (83.3 m/s).
- $a = 3.0$ m, $d = 0.6$ m and $L = 3.0$ m.

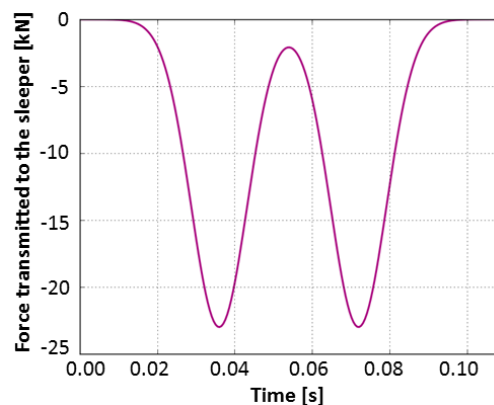


Figure 1.6 Force signal transmitted to one sleeper block of a twin-block sleeper by the rail during the passage of a HSL bogie.

These values applied to the expression of Sauvage results on a double peak signal with a total length of 0.1 seconds and a maximum value of about 23 kN (Figure 1.6). Finally, the distance between bogies (19 m) is considered along with the speed of the train in order to establish the repetition of the loading cycles over time (see Figure 4.2).

1. 1. 3 Maintenance cycle of the track

Even if the ballast layer is relatively flexible, the cyclic efforts eventually produce a rearrangement of the ballast grains, either due to wear or to a relocating of the particles, producing permanent deformations. These deformations are usually produced under the sleeper [17, 18], moving the track from the theoretical position. The consequence is the creation of what it is known as geometric track defaults, which are the main cause of track maintenance. These defaults result in a reduction of the passenger comfort in a first level and in security issues when these defaults become more important. They are identified thanks to sensors located in specific trains that circulate along the line comparing in real time the actual geometry of the track with the theoretical geometry. When these defaults overpass a certain threshold, maintenance operations are required in order to correct them before they become more serious.

Geometric track defaults

We can distinguish between defaults in the vertical plane and in the horizontal plane [19, 17]. On the vertical plane we can define three different kinds of defaults:

- Longitudinal level default: gap between the longitudinal track level and the theoretical level. It mainly depends on the settlement of the track.
- Warp or torsion default: vertical transversal difference between both rails.
- Crosslevel or cant default: difference between the theoretical cant, i.e. the transversal inclination of the track in curves, and the measurement.

On the horizontal plane we can distinguish two kinds of defaults:

- Rail gauge default: difference in the distance between both rails, breaking the parallelism either by making the track gauge too wide or too narrow.
- Alignment error: transversal variation of the centre of the track with respect to the theoretical trajectory line.

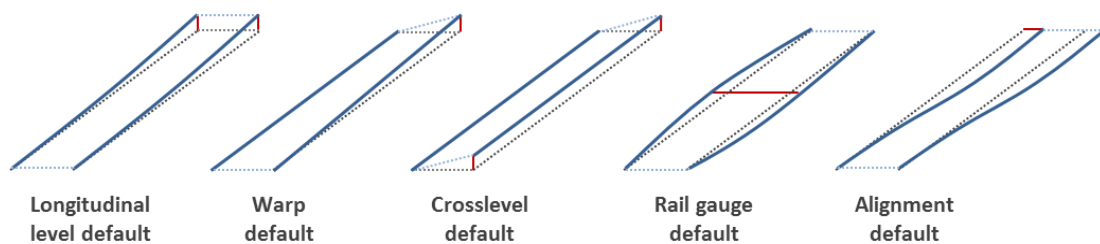


Figure 1.7 Geometric errors of the track.

Figure 1.7 shows a summary of all the different geometric errors. Depending on the kind of trains circulating on the line and their commercial speeds, thresholds for geometry error will be more or less strict and they will result in a speed reduction or in an urgent maintenance. In fact, according to what we have seen so far, HSL do not present a significant difference with conventional lines in terms of loads. The main difference in terms of maintenance cycles comes from the geometry thresholds that are required in order to ensure comfort and security when circulating at high speeds. These limits are necessarily stricter, but this also implies that they will be overpassed faster after every maintenance operation. In consequence, the frequency of tamping will be inevitably higher in HSL.

Since the sleepers are attached to the rail, their settlement is limited by the deformation of the rail. Sometimes the differential settlement between neighbour sleepers is large enough not to be followed by the rail deformation, creating gaps or voids between the sleeper and the aggregates, phenomenon that is known as voided or loose sleepers [1, 2]. This default is not strictly considered as a geometric default, but it has similar security consequences, as well as leading to significant wear on the ballast layer and the sleeper blocks due to the continuous impacts.



Figure 1.8 Compacted grains below the sleeper after a vibration test.

Geometric defaults are directly related to the settlement and movements of the trackbed layers, especially the ballast layer. Horizontal defaults are mainly produced when the ballast fails at locking the sleeper at place against the lateral efforts. On the other hand, vertical defaults appear due to the progressive settlement of the ballast layer and the sub-layers, but mainly when the grains located immediately below the sleepers are compacted and flattened (Figure 1.8) [3, 17, 13].

All these defaults are therefore inevitable due to the granular nature of ballast, but this same nature allows also for a relatively easy correction of the defaults by vibrating and mixing the grains, so that the new rearrangement recovers the initial geometry. This maintenance operation is known as tamping.

Tamping: maintenance operation

Once the admitted thresholds are reached or overpassed, tamping is required to recover the optimal geometry of the track. During this operation, the tamping machine lifts rails and sleepers and aligns them to the correct horizontal and vertical position. Meanwhile vibrating tines are introduced into the ballast layer on both sides of the sleeper and they are pushed together packing the ballast under the lifted sleeper, so that the sleeper will stay in position

after it is released. Then the tamping machine proceeds to the next sleeper. Actually, for a better time optimization of the procedure [20], up to three sleepers are usually tamped simultaneously. Figure 1.9 shows the vibrating tines of a tamping machine that can pack up to three sleepers at the same time.



Figure 1.9 Tamping machine.

This operation is hence very effective and crucial for the security of the track. However, it has a major drawback concerning the ballast layer. It is intuitive and it has been proven that the introduction of the vibrating tines inside the ballast layer is indeed very aggressive for the ballast layer, leading to important wear and even to grain crushing. Perales [21, 22] performed a grain-size analysis by collecting ballast samples on a testing track. The grain-size curves of ballast samples before maintenance and after 45 cycles of tamping show a clear reduction of the ballast grain-size on the larger particles (> 50 mm) and the appearance of small and fine particles (Figure 1.10). Paderno [18] also observed a reduction of the overall grain size and a reduction of the angularity of the grains due to tamping on the Swiss railway network. She observed that the grains located below the sleeper were especially affected, since they are the ones that are more impacted by the penetration of the tines.

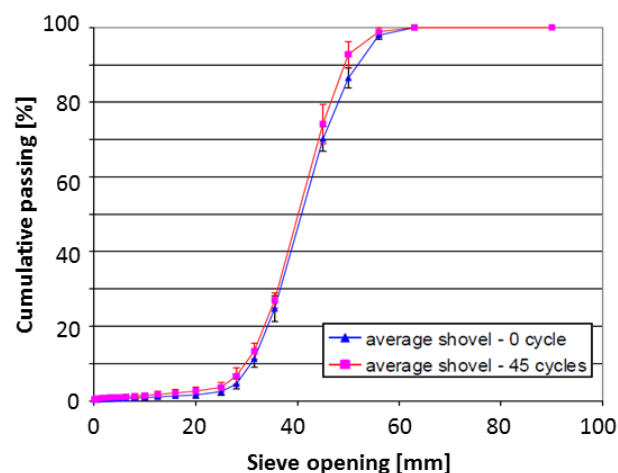


Figure 1.10 Effect of 45 tamping cycles on the grain-size distribution [21].

We have seen how ballast, as the upper layer of the trackbed, plays a key role on the maintenance cycle of the track. However, so far we have observed its behaviour in the general context of the track. In order to better understand the importance of ballast, it is necessary to now zoom into the layer.

1. 2 BALLAST: GRANULAR LAYER

Recalling the description of the transversal section of the track (Figure 1.2), the ballast layer is the upper layer of the track bed, immediately below the track panel. Thus it is the granular layer that is in direct contact with the sleepers and, as we have seen, its main functions are to fix the position of the track panel to avoid geometric defaults and to transfer and redistribute the loading coming from the trains towards the sub-layers.

For HSL and concrete sleepers, the ballast layer is recommended to be around 0.35 m thick, measured below the sleeper [23], and it is formed by centimetric-sized sharp aggregates with a very homogeneous grain size distribution. The size of the particles, ranging from 25 to 50 mm, leaves large enough voids in-between to quickly drain rainfall water. As a relatively flexible layer, it also absorbs part of the mechanical and acoustic vibrations of the track and, as we explained in the previous section, its malleability helps the correction of track geometry during tamping operation. Finally, it also helps to keep down undesired vegetation from the rails.

1. 2. 1 Ballast characteristics

In order to be suitable to perform all these functions, ballast needs to follow some quality criteria:

- A specific grain-size distribution and low presence of small particles for ensuring good mechanical properties and a proper drainage of the track.
- High angularity and sharpness at edges and vertexes to ensure a good shearing resistance of the layer.
- High mechanical resistance to wear to keep angularity and reduce the production of fine particles.
- Insensibility to water and ice.
- Homogeneity of grain morphology, avoiding too elongated or too flat shapes.

The mineralogy of the grains will usually depend on the available materials in the country and in the closer quarries. However, the previous restrictions will narrow down the possible candidates. Due to its high performance and availability, granite is the first option for most French railway lines, especially for HSL.

Morphology requirements

SNCF uses ballast 31.5/50 for their new lines, which means that at least 50% of the sample in mass needs to stay within the range from 31.5 mm to 50.0 mm when sieved following the standard procedure [24]. Figure 1.11 shows the grain-size curves that delimit the acceptable ballast distribution [25, 26]. All ballast samples for new lines are required to fall into the green area.

On the lower part of the curves, there is a specific limitation concerning the amount of fine

particles that can be present in the sample when ballast is still new. We understand as fine particles all elements passing through the 1.6 mm sieve. These fines will be measured by wet sieving and they cannot represent more than 0.5% of the total mass of the sample.

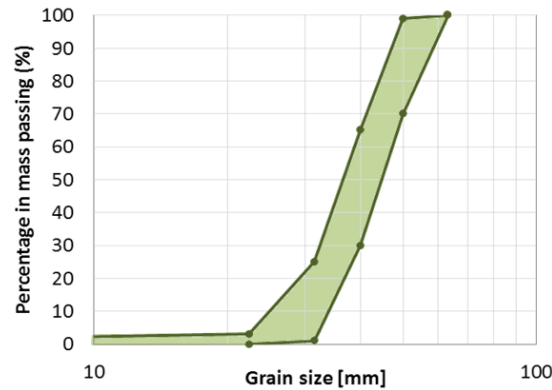


Figure 1.11 SNCF accepted ballast grain-size distribution (green area).

A SNCF study [27] on the ageing of ballast proposed a classification of the layer depending on the percentage of grains passing the 25 mm sieve, considering that ballast is new if less than 5% pass through this sieve, while on the opposite side ballast would be considered very polluted if more than 30% of the sample is smaller than 25 mm.

Concerning the morphology of the grains, some tests included in the corresponding European Norms [28] define shape coefficients that serve as a filter for avoiding extreme shapes. For instance, only up to 6% in mass of the ballast sample can present a length over 100 mm (note that the length is not necessarily equal to the sieve size).

Mechanical requirements

Ballast samples need to pass the tests of Micro-Deval and Los Angeles in the quarry in order to classify the sample according to its resistance to attrition and to fragmentation, respectively [29, 30]. In both cases, the test consists of a rotating cylinder where ballast grains are put inside. These tests are quick and repeatable, allowing for an inexpensive way of classifying aggregates before delivering it to the railway track.

Micro-Deval consists of a 20 cm in diameter and 40 cm long cylinder where 10 kg of grains turn producing fines due to the constant friction between grains. This test will be explained and analysed in detail in this project in section 2. 2. On the other hand, the cylinder of Los Angeles test is bigger and it adds steel balls and a steel plate inside the cylinder. Ballast and balls are pushed up by the plate and let them fall from a certain height. This way, fines are mainly produced due to impacts against the bottom part of the cylinder. In both cases, the percentage of particles smaller than 1.6 mm at the end of the test will give the test coefficient.

As shown by Bach et al. [31], impact forces in the Los Angeles test are indeed twice as big as impact forces in the Deval machine. And this is also seen on the production of fines on each test, where the same material will produce between twice and three times more fines in the Los Angeles device than in the Micro-Deval. This is not surprising, since the Micro-Deval

machine was conceived to wear grains by abrasion and not by impacts, which is a much slower process.

Table 1.1 shows the different kinds of ballast accepted by SNCF according to their Micro-Deval and Los Angeles coefficients [26]:

	Los Angeles	Micro-Deval
C2	14	5
C4	16	7
C5	20	11

Table 1.1 SNCF classification of ballast according to its Los Angeles and Micro-Deval coefficients. The coefficients are calculated in both cases as the percentage of fines ($D < 1.6\text{mm}$) generated during the test.

C2 ballast is used for HSL ($v > 220\text{ km/h}$), while C4 is left for conventional lines ($v \leq 220\text{ km/h}$). C5 can only be used for the ballast renovation and refilling of certain types of lines [23].

1. 2. 2 Ballast life cycle

Thus, the ideal ballast has a homogeneous size and it is clean from fine particles, it presents a high angularity and a high resistance to wear. However, even with the strictest of the selection methods, the efforts suffered due to the constant passages of trains eventually produce erosion on the grains.

This erosion is characterized by a reduction of the angularity, smoothing sharp edges and vertexes and flattening surface texture, the overall shape of the grains become more rounded (Figure 1.12), and in the process, fine particles are inevitably produced. In extreme cases, grains even crush in smaller particles changing the grain-size distribution of the sample.



Figure 1.12 New grain (left) compared to a grain after a Micro-Deval test (right).

In addition, the progressive settlement of the layer produce geometry defaults in the track and eventually requiring maintenance operations. As we have seen, tamping is very aggressive for the ballast layer, increasing the amount of cumulated wear every time it is performed. In HSL, tamping is performed more frequently, so this extra addition of wear becomes an especially serious issue. As the grains become more and more rounded they lose angularity, reducing the interlocking forces and the anisotropy of the contact network, which results in a gradual decrease of the shear strength of the layer [32]. This decrease in the track performance consequently reduces the time before track defaults appear again. Henceforth, every cycle the

frequency of tamping becomes higher, aggravating the situation. Meanwhile, the fine particles generated due to wear accumulate inside the voids of the ballast layer, reducing the permeability of the track.

Eventually, the performance of the track becomes so low and maintenance is thus required so often that ballast layer needs to be renewed. This operation consists in extracting all the ballast from the track, sieving it to keep the biggest grains, and refill the track with new ballast along with the grains that have passed the filter. Figure 1.13 shows the machine that performs this operation. Ballast is removed from the front (left of the image) and pushed backwards to a system of sieves located in the following carriages. A gap where the track remains in air is left (middle of the image). Finally, filtered ballast along with new ballast stocked in the following carriages is used to refill the track (right side of the image).

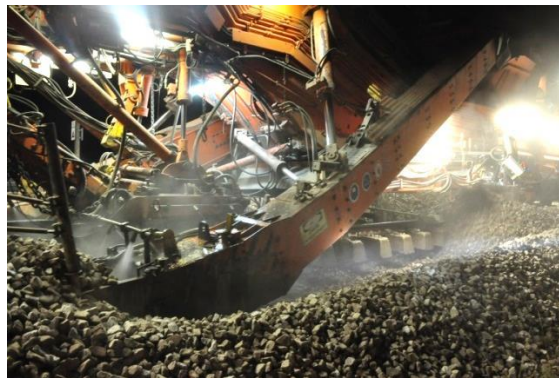


Figure 1.13 Ballast renewal machine.

This operation is performed when tamping is not effective anymore. However, it represents the very last resort due to its high economic cost, as well as the corresponding perturbation of the normal service of the affected segment of track. Therefore, it is clear that we would like to extend the lifespan of ballast as much as possible and the only way to do that is by finding ways to reduce ballast degradation.

This is a well-known problem of all countries that have traditionally invested in ballasted tracks. Several works have been performed trying to understand and quantify this phenomenon and some of them will be presented in the next section.

1. 2. 3 Previous works on ballast degradation

First of all, searching for the sources of fine particles within the ballast layer, Selig and Waters [3] confirmed that ballast wear is indeed the main source of fines, quantifying at 76% the amount of them coming from ballast itself. The other sources may be particles coming from the lower trackbed layers and the subsoil, from external contaminants (e.g. atmospheric particles or train fouling), or from the degradation of the sleeper.

In one of the first studies about this problem in 1985, Lecocq [33] proposed a combined index of ballast resistance including the Deval, in dry and wet conditions, and Los Angeles coefficients. As expected, he showed that the lifespan of ballast in terms of production of fines

is indeed related to the resistance of the granular material. He also established at 12.5% the maximum amount of fines before the ballast layer becomes completely plugged. In the same line of investigation, trying to link the standard coefficients with the lifespan of ballast, McDowell et al. [34] confirmed a correlation between the Micro-Deval and Los Angeles coefficients with the change in the grain-size distribution during a box-test, i.e. an experimental simulation of track conditions on a 700x300x450 mm box.

Another line of investigation focuses more, not on the source of the fine particles but on their influence on the mechanical behaviour of the ballast layer. Indraratna et al. [35] confirmed that fouling reduces the shearing resistance of the layer, first by reducing the surface roughness and thus acting as an apparent lubrication, and for high-levels of contaminants by not-allowing grains to repack by forming a compacted layer between grains (Figure 1.14). At the grain-scale, Lim [36] observed a size-effect on ballast crushing, following a Weibull distribution, where small particles showed statistically larger strength than bigger ones. He also concluded that the conditions of standard abrasion tests are very far from real conditions in the track. He proposed then to find new methods for assessing ballast quality reflecting actual performance of the material.

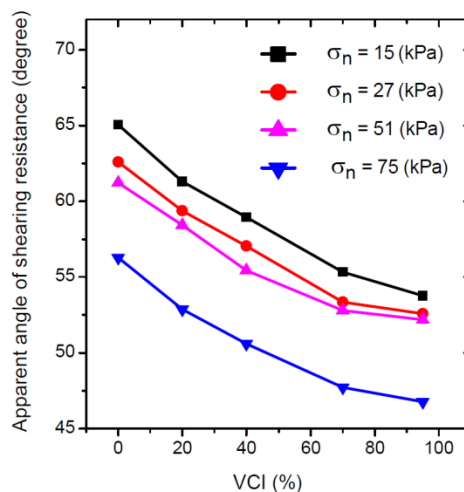


Figure 1.14 Effect of Void Contaminant Index (VCI), which measures the degree of ballast fouling, on the apparent angle of shearing resistance of ballast [35].

However, there are not too many works actually predicting the amount of fines that the track generates. Due to traffic restrictions and to the intrinsic difficulty of extracting ballast samples from the track, it becomes very complicated to obtain in-situ measurements of the track. Reduced models become therefore necessary, like the box-test or the SNCF device Vibrogir [37], a vibrating machine that simulates the passage of trains over a sleeper. Perales [22] performed experimental tests on Vibrogir recuperating ballast samples at regular intervals. That way he could quantify the amount of relatively small particles ($D < 25$ mm) generated by the passage of trains under one sleeper. He estimated that 170 g of these particles were generated per million tons of train traffic (Figure 1.15). He also observed that the production of fines and grain fragmentation is higher during the first cycles of loading and tends to stabilise afterwards.

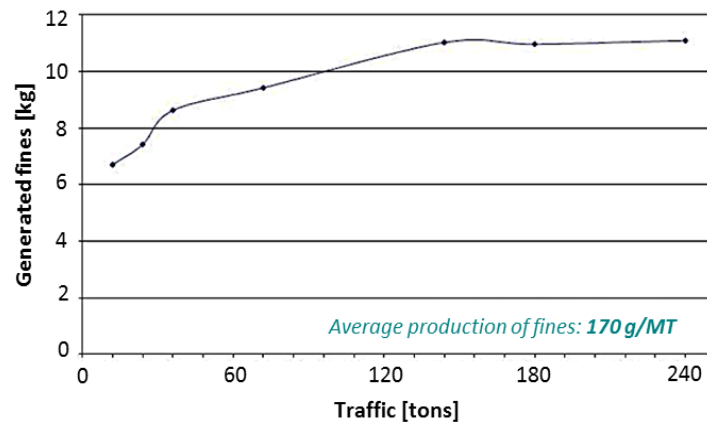


Figure 1.15 Evolution of the production of small particles ($D < 25 \text{ mm}$) on the Vibrogir [22].

However, the lower part of the grain-size curve corresponding to actual fines, is still not evident to recuperate and quantify experimentally, even in these reduced tests. Approaching the problem from a different point of view becomes then necessary. And this is precisely the main motivation of this project. Wear is essentially a contact scale phenomenon. Thus we will not try to quantify fines experimentally at the track scale. Instead, we will perform a change in scale from the track to the grain scale, and then we will estimate wear using the analytical models given by the science field that studies this phenomenon at the micro-scale: tribology.

1. 3 CONTACT SCALE: TRIBOLOGY

So far in this chapter we have introduced the problem that ballast degradation represents for the track performance and maintenance. We have seen that, in order to understand the mechanisms leading to wear we need to look at the contact scale. Thus, in order to understand the mechanisms and predict wear, it is necessary to turn to tribology, i.e. the science in charge of studying the interaction between surfaces in relative motion.

When two surfaces are in contact, forces of action and reaction are brought into play. During this interaction, surface structure may change and matter may transfer from one surface to the other or break away and fall out of the contact region [38]. This interaction is represented by friction, wear and lubrication, the first two being the most representatives of the interaction between ballast grains.

1. 3. 1 Friction

Friction is defined as the resistance exerted by the surfaces against relative motion. It depends on the materials of both bodies involved as well as on the environmental conditions surrounding the interface. In dry conditions, friction force has long been observed to be often linearly proportional to the contact normal force. This phenomenon was first observed already by Da Vinci but he did not publish his discoveries, it was rediscovered by Amontons [39] and

further developed by Coulomb [40], so this proportionality, usually expressed by the friction coefficient μ , is generally known as the Coulomb friction:

$$\mu = \frac{F_T}{F_N} \quad (1.2)$$

Where F_T is the tangential force required to start the relative motion between both surfaces, and F_N is the normal force at the contact interface. In some cases, the friction coefficient is also expressed as the maximum angle θ one surface could stay over the other, without any other forces than weight and friction force interfering, without sliding due to gravity. In this case, the friction coefficient would be expressed as the tangent of the angle: $\mu = \tan(\theta)$. For most common materials, μ ranges between 0.1 and 1.0.

Influence of surface roughness

In nature, or even in controlled manufacturing, perfectly flat surfaces do not exist. At a larger or smaller scale, asperities are always present and they interfere at the contact interface. When two surfaces become in contact, only the tops of these asperities are actually touching. We call this touching the real contact area, which is commonly only a small fraction of the measurable apparent contact area [38]. The real contact area will then depend on the elastic or plastic deformation of the asperities due to the applied load. In fact, it has been found that, for both elastic and plastic contacts, the real contact area is almost proportional to the normal load [41, 42].

This last observation has two main consequences. The first one is that the apparent contact area does not affect friction force [43], which is considered one of the fundamental laws of friction. This means that a bigger contact surface (e.g. bigger sample) but with the same properties and roughness will not increase nor decrease the friction coefficient. In other words, if the load is the same, for a bigger apparent contact area, the asperities will deform less resulting in a similar real contact area. It is then the increase of the real contact area, due to the load, that increases friction [44].

The second one is that, at the micro-scale, friction appears to be independent of the surface roughness. We may understand the resistance to relative motion as the force required to “climb” or deform a certain asperity that blocks the tangential movement [45]. We would then expect a higher friction for rough materials. However, micro-asperities usually deform or break under shearing, so they pose a certain resistance but there is not an interface dilation effect. On the other hand, for very smooth surfaces the real contact area grows fast when the load increases, resulting as well in a high friction coefficient. Therefore, when dealing with roughness at the micro and nano-scales, the increase of real contact area in smooth surfaces compensates the presence of micro-asperities. For these particular cases, friction is almost independent of roughness [46].

However, when the surfaces are rougher and larger asperities come into play, measuring the friction coefficient can indeed depend on the surface texture, since blockage between asperities may occur, resulting in an irregular sliding path with “uphills” and “downhills”. If the

computation of the friction coefficient is not geometrically corrected in consequence, it will lead to irregular measurements of this parameter along the slide. This is the case, for example, of friction between aggregates or rocks joints, which usually present large asperities over the faces. This kind of measurements at the grain-scale is system dependant, with several factors interfering, such as the level of roughness, the hardness of the material and the orientation or distribution of the asperities. It is thus difficult to directly correlate friction with specific roughness parameters [47].

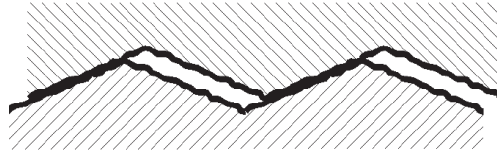


Figure 1.16 Interface with two levels of roughness [48]. The primary level will force the interface to climb the asperity (dilation) or to break or deform it. The secondary level (micro-asperities) will mainly deform either plastically or elastically.

If the normal loading is high enough, it may happen that these asperities break apart or progressively wear along the loading cycles. This leads to an adaptation of one surface over the other, tending to a flat trajectory over the cyclic segment (see section 4.5.2). At the macro-scale, blockages tend to disappear, so friction coefficient will tend to be more regular over the segment, and more similar to the corrected coefficient. At the asperity-scale, the smoothing resulting from wear will lead to an adaptation of one surface to the other, flattening the sliding path and thus increasing the real contact area, which can lead to a slight increment of the friction coefficient [49]. Finally, these broken asperities will occasionally stay within the contact interface, in what is known as the third-body (Figure 1.17), influencing the sliding motion.

Influence of third-body

When wear is produced at the contact interface, small particles can be trapped between the asperities, affecting the dynamics of the interfacial problem [50, 51]. These small particles, commonly called third-body in tribology, can interfere in the relative movement between both bodies increasing the friction coefficient measured at a larger scale [38]. On the other hand, some particles can roll and ease the motion, consequently reducing the measured friction coefficient. However, in most of the cases, the rolling particles represent only around 10% of the third-body [38], leading to an overall increase of μ due to the presence of third-body.

During a cyclic shear test, such as the ones we will be performing in this project, it is expected to encounter both, the smoothing or adaptation of both surfaces in contact and the appearance of the third-body. As we have seen, both mechanisms induce an overall increase of the friction force. Henceforth, we can expect an increase of the friction coefficient along the test, especially during the first cycles of shearing.

However, friction evolution is not enough to describe the wear process, since it does not give any information about the amount of matter that is lost on the process. For that it is necessary to study the different known wear mechanisms that have been identified and classified by tribology.



Figure 1.17 Wear produced by shearing two ballast grains in the BCR3D device along 200 cycles at 1.2 mm of amplitude. Fines can be expelled out of the interface or remain trapped within.

1. 3. 2 Contact wear

Wear is defined as the gradual loss of matter resulting from the contact of surfaces in relative motion [52]. Due to its inevitable presence in our daily life, especially in the duration and maintenance of tools, wear of materials has always worried human beings. Since the industrial revolution, at the beginning of the 19th century, and the proliferation of machinery, several investigations have been carried out in order to reduce maintenance costs [53, 54]. For this reason, most of wear mechanism described in the literature are related to phenomena affecting mostly metals, such as corrosion or delamination. Therefore, in this section we will not describe all the possible mechanisms, since most of them do not concern aggregates, but we will focus our attention on the mechanism that fits better the interaction between rocks: abrasive wear.

Abrasive wear happens when an asperity of a solid surface slides along a softer asperity under load, breaking apart the last one [52, 38]. Abrasion can happen either by gradual cutting of one surface over the other removing tiny particles or debris, or by a fragmentation of an asperity through a localized fracture, which will often result in a larger removal of matter. Third-body may also interfere in this process, due to the small trapped particles causing additional abrasion to one or both surfaces.

Thus by definition this mechanism always involves a harder and a softer material. However, this does not mean that both materials need to be different for abrasion wear to happen. On friction between heterogeneous materials, such as granite, this difference in hardness can happen at a local scale. For instance, in granite rocks, quartz is harder than the other components of the grain [55], so asperities involving a quartz crystal will likely wear softer asperities by abrasion. Thus friction will produce abrasion wear on one surface or on the other depending on the local hardness of the asperity in contact.

However, understanding why wear happens is not enough to be able to quantify it. In the following section, we will present the most common model for predicting abrasion wear introduced by Archard in 1953 [56].

1.3.3 Archard equation to wear

The earliest contributions to predicting wear through equations were made by Holm in 1946 [57]. Holm related the volume lost by wear to the sliding distance and the real contact area. Seven years later, Archard simplified Holm's model and proposed an expression based also on the normal force, which is easier to measure than the real contact area. Archard defined the volume produced due to wear (V_w) as proportional to the normal force (F_N) and the tangential relative displacement ($Disp$) between the surfaces in contact (sliding motion), and inversely proportional to the hardness of the softest material (H):

$$V_w = K \cdot \frac{F_N \cdot Disp}{H} \quad (1.3)$$

Where K is a dimensionless coefficient often called wear or Archard coefficient.

The product $F_N \cdot Disp$ is directly related to the friction energy or friction work produced due to the relative displacement between both surfaces. During this project we will be referring to this product as the friction work.

This expression was initially conceived for predicting adhesive wear, but it was later found useful also for representing abrasive wear, just by taking a different coefficient K . Wear coefficient determines the aggressiveness of wear and depends on the contact morphology and conditions [58]. For abrasive wear, this coefficient typically ranges between 10^{-6} for soft wear to 10^{-1} for severe wear [38]. On the other hand, computing the hardness of the materials is not always evident. Hardness is sensitive to the way it is measured and the indenting tool used. Several tests and grading scales can be found in the industry and the literature that not always give the same values. However, in this project we will be studying contacts between ballast grains, so at the macro-scale, both materials will be the same. For this reason and for practical uses, H will be assumed to be constant and included into the wear coefficient, giving a coefficient k with units Pa^{-1} :

$$k = \frac{K}{H} \quad (1.4)$$

More modern and complex models have been proposed after Archard. Bahadur [59] first and Meng and Ludema [60] later on presented compilations of dozens of wear equations and models published between 1937 and 1995. In most of the cases, rather than general models, these equations attempted to give an answer to a specific case of wear. However, in the end and due to its simplicity and efficiency, Archard model is still widely used in tribology and most of modern models are actually extensions of Archard equation [46, 61, 62].

Archard model, although simple in construction, has been found to be useful not only for metals but for a wide variety of materials. Concerning rocks, several experiments [63, 64, 65] have been conducted shearing different rock surfaces, which showed a good correlation with Archard model for low slip velocity (0.15 mm/s). However, recent studies [66] have revealed that when high-velocities and large displacements are considered (up to 270 mm/s and 220 m,

respectively) wear rates of granite showed power relations to normal stress instead of the linear relation predicted by Archard. The case of ballast is, though, closer to the first cases, so we consider Archard model as a good candidate for our first approach to a degradation model of ballast.

If we know the wear coefficient, e.g. by calibrating the model experimentally, Archard equation is relatively easy to be applied on numerical simulations in order to predict wear. This is the case, for instance, of Rycroft et al. [67], who applied Archard to the case of granular flows in pebble-bed nuclear reactors in order to quantify the dust generated due to the sliding of the pebbles against the reactor walls. Involving geomaterials, Rojek et al. [68] used the model to predict wear on roadheader picks in underground excavations. Both examples applied Archard to discrete elements simulations in order to avoid simulating actual wear in the particles. And this is also our proposed approach to the case of ballast.

Numerical simulations allow us to understand the granular behaviour and to assess some internal parameters, such as contact forces or relative displacements, which would be very complex to identify experimentally. The idea is then to use these simulations in order to extract the important quantities involved in wear according to Archard model (relative displacements and contact forces). Then we will perform experimental tests at the contact scale, where fines are more easily quantified, in order to calibrate the model and, if required, propose some modifications for the specific case of ballast. Finally, we will apply the calibrated model again to the numerical simulations in order to estimate the amount of fines generated within the track. It is therefore a multi-scale process, going from the track to the contact-scale and back. And the main tool that will allow us to perform this scale transition is numerical simulations by discrete elements, and more specifically the Non-Smooth Contact Dynamics method (NSCD), which will be presented in the next section.

1. 4 FROM THE TRACK TO THE GRAIN: NSCD

As we have seen, studying the different elements of the track experimentally is not always evident, especially when trying to assess internal parameters of the layers such as propagation of forces and waves, internal displacements or wear.

The exponential increase of the performance of numerical modelling has allowed for the introduction of every time more complex and precise models that can simulate the track with relative accuracy. However, since the beginnings of numerical simulations, ballast layer along with the other sub-layers has been traditionally considered as a continuous deformable medium using finite elements (Figure 1.18a). This simplification allows for studying the behaviour of the track as a whole, for a relatively low computational cost. Studies of wave propagation, vibrations or even track deformation [69, 70, 71] can be performed with satisfactory results using a continuous model. This approximation though fails to reproduce the complexity of granular layers, simplifying the complex phenomena by observable and measurable parameters that not always fit the reality. And this issue becomes a critical obstacle when we zoom into the grain scale.

The heterogeneity of granular layers, such as ballast, entails the necessity of modelling the particles as individual entities. This is numerically solved by using what it is known as discrete elements (Figure 1.18b). This method makes it possible to simulate and analyse the ballast layer and the interactions between grains, taking into account the heterogeneous morphological characteristics of the aggregates. However, the computational cost is still very important and even using optimized methods, such as parallelized calculations [72], the simulation time for a small section of the track has an order of magnitude of weeks or months. In railways, this method is then limited for studying contact-scale mechanics, particle-related phenomena or when it is indispensable to take into account the heterogeneity of ballast. It is thus the tool to perform the desired transition in scale from the track to the contact.

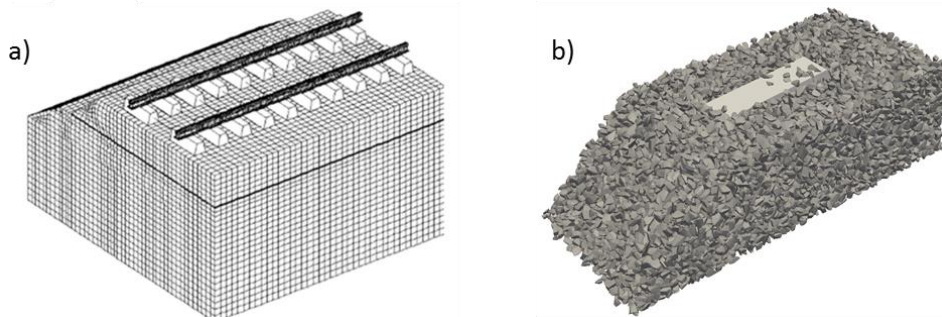


Figure 1.18 a) Track simulated by finite elements [69]. b) Track simulated by discrete elements.

There are traditionally two approaches when using discrete elements:

- “Smooth” methods, based on the Molecular Dynamics approach, they accept local deformation of grains at the contact, including interpenetration to the laws describing contacts. Traditionally used for the study of fluids and atomic-scale systems, Cundall [73] extended this approach to the case of solids by adding contact and friction laws.
- “Non-smooth” methods, based on the hypothesis of rigidity of the contacts, i.e. the contact does not deform, while the body may deform or not, not allowing for interpenetration between particles. Among the approaches using this methods, in the case of dense granular media where several interactions occur simultaneously, Non-Smooth Contact Dynamics (NSCD) is the best adapted [74, 75, 76].

The degree of deformation at the contact point will determine which kind of approach suits better for each case. By definition, ballast layer is formed by rigid aggregates, which do not allow for large deformations. In this case, Molecular Dynamics method would need a too small time step in order to properly deal with such a large rigidity at the contact point [19]. Contact Dynamics, however, works better with rigid bodies and allows for larger time steps.

In addition, “smooth” methods allow for interpenetration, using this overlapped volume to compute the contact force. It is a suitable method for sphere-shape particles, where it is easy to calculate the overlap and the barycentre of this overlap. However, when dealing with irregular polyhedral particles like the case of ballast, this computation is not straight forward and would represent a problem. The choice of non-interpenetration given by Contact Dynamics facilitates this computation for irregular particles, where the shape only plays a role at the step of contact detection [77, 78].

NSCD seems then the best option for ballast simulations. The main drawback of this choice is the lack of elasticity at the contact, which even if small for granite aggregates, it does exist in reality. This assumption is valid for dynamic systems but it can lead to the accumulation of small errors along the cycles in quasi-static systems, especially when analysing long-term phenomena such as the settlement of the track. Nevertheless, we consider that, for the case of this project, this limitation is not affecting significantly the results and we can assume the simplification. This is so because the goal is not to study long-term parameters but to identify the characteristic contacts happening at the loading. Due to the high rigidity of ballast, we consider that contact forces and relative displacements will be similar whether considering slight elasticity or completely rigid contacts.

This method has been traditionally used by the SNCF since 2003, when Combe [79] performed a first validation of 2D NSCD simulations by comparing them to experimental tests with Schneebeli rod samples. A further development of the method towards the 3D case was made by Saussine in 2004 [2], generalising the algorithm for contact detection and adding a database of one thousand polyhedral ballast grains. NSCD is since then used to perform analysis of different phenomena involving the heterogeneity of the ballast layer and it has provided some interesting results concerning the maintenance cycle of the track.

In 2012, Quezada [17] proposed a predictive model of track settlement based on the mechanical characterization of ballast using Panda penetrometer and the typical loading of the track. For this purpose, he used NSCD to analyse the ballast layer at the grain-scale and to assess the pertinence of using the Panda penetrometer to characterize the granular layer.

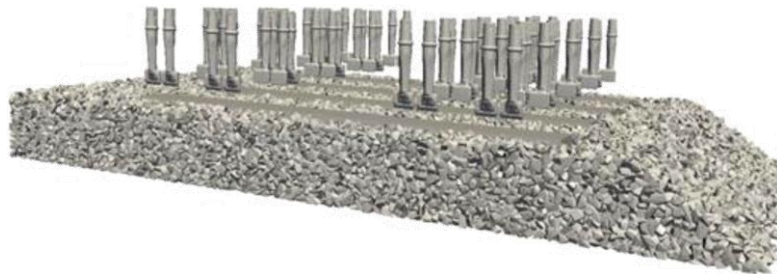


Figure 1.19 Simulation of a multi-unit tamping on four mono-block sleepers simultaneously [20, 80].

Tamping has also been a recurrent object of study. In 2007, Azema [19] analysed the different phases of the maintenance operation simulating them using NSCD. He proposed, in order to improve the compaction of the ballast layer, to increase the frequency of the ties during the sinking and the extraction phases and to reduce it during the compaction phase. In 2011, Hoang et al. [81] simulated 7 sleeper blocks to analyse the influence of tamping one sleeper on the compaction of the neighbour blocks. The study showed a favourable effect on the already tamped sleepers but a negative effect on the not-tamped sleepers. Furthermore a larger simulation was performed in 2014 by Voivret et al. [20], simulating 9 sleeper blocks and using 115 000 polyhedral grains (Figure 1.19), in order to show the efficiency of multi-unit tamping. Following the maintenance study and simulations of Voivret, in 2017 Ferrellec et al. [80] numerically compared the efficiency of two different stabilisation methods used after tamping:

dynamic stabilisation and crib compaction. They concluded that the innovative crib compaction, although being slightly less performant, represents a potential alternative to dynamic stabilisation.

Other phenomena have also been studied using NSCD by SNCF, such as the ballast flight phenomena, analysed by Saussine and Néel in 2014 [82], or the efficiency of USP on transmitting load by decreasing the contact force and redistributing the efforts, analysed by Voivret and Nhu in 2016 [10].

NSCD has been proven to be an effective method to numerically model and simulate the behaviour of the ballast layer. Thus we consider that it is a good candidate to perform the required simulations for this project. For this purpose, we will use the open-source software called LMG90 developed by the CNRS and the University of Montpellier [83]. In the following section, we will present in more detail the NSCD method.

1. 4. 1 Non-Smooth Contact Dynamics

The NSCD algorithm works with the following ordered steps:

1. Contacts are detected.
2. Contact forces and particle velocities are determined, based on the contact laws and the fundamental dynamic equation.
3. Particle positions are updated in accordance.

As we have explained, NSCD is based on the hypotheses that interpenetrations between particles are not allowed and contacts are considered as completely rigid. This means that, in the first step, if a contact between two particles is detected, only two situations are possible:

- The two particles exert a force against each other. In this case, the relative normal velocity must be zero so they cannot get closer, which would lead to interpenetration.
- Both particles are about to separate, so the contact force is zero, but the normal velocity between them is positive (understanding as positive the separation direction).

These conditions are known as the Signorini conditions and can be summarized with the diagram in Figure 1.20a [74, 75].

The other law considered in the algorithm is the Coulomb friction, which defines the tangential force required to have tangential velocity as a fraction of the normal force given by the friction coefficient μ (see section 1. 3. 1). This implies two things: the tangential force will never be higher than $|\mu \cdot F_N|$, and tangential relative velocity will be zero if the tangential force is below that value. This condition can be summarized with the diagram in Figure 1.20b [74, 75].

This is the simplest model for NSCD and the one that will be used for ballast, but this method can be complemented with other interactions, such as particle cohesion by introducing modifications to the Signorini condition. Finally, collisions are treated using the restitution law of Newton, where we can damp the normal relative velocity by applying a restitution coefficient ranging from 0, on perfectly inelastic collisions, to 1, on elastic shocks. For dense

collections of rigid grains and slow collisions, such as the case of ballast, a restitution coefficient of 0 has been proven to be convenient [77, 78].

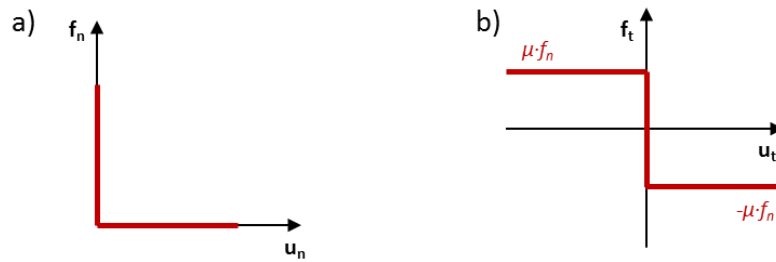


Figure 1.20 a) Signorini contact conditions. b) Coulomb friction conditions. Where f_n and f_t are the normal and tangential contact forces and u_n and u_t are the normal and tangential relative velocities, respectively, and considering $u_n > 0$ when both particles separate from each other.

1. 4. 2 Contact detection and particle shape

As we have seen, in NSCD the shape of the particles only takes part in the detection of the contacts. At the beginning of each iteration, an algorithm searches and identifies the different contacts within the system. The goal of this algorithm is then to understand, for each couple of particles in potential contact, if the two bodies are actually in contact and, in that case, determine the coordinates of the contact. The easiest case is that of spherical particles, where it is only needed a radii verification to detect contacts, and the contact coordinates will also be easily determined as it will lay on the line joining both centres of the spheres. However, for complex shapes this operation is not so evident, especially in 3D, and it can represent a serious constraint on the computational time required for the simulation.

By definition and nature, ballast presents sharp edges and irregular shapes, so it is not well represented by simple spheres [84]. Some studies have approached the problem by creating clusters of spheres of different sizes (Figure 1.21a), so that they approximate the shape of a real grain while keeping the advantages of spheres [35, 85, 86, 87]. However, these methods usually use a limited number of spheres, resulting in too smooth edges and vertexes. When trying to better approximate the sharpness of ballast, the number of spheres per cluster increases fast [88], up to a point that it is not worthy anymore to use spheres instead of polyhedral particles.

In order to keep the angularity of the grains, polyhedral particles are traditionally used by the SNCF (Figure 1.21b). A database of polyhedral ballast grains was created from the 3D scan of real grains [2]. These scanned grains were simplified in order to reduce the number of faces and vertexes per particle, always trying to keep the overall shape, grain-size distribution and angularity. This procedure resulted in a library of one thousand polyhedral particles containing from 12 to 70 faces and from 8 to 37 vertexes [19]. The contact detection for polyhedra is solved in a two-step algorithm, performing a first rough detection acting as a filter and discarding couples of particles that are not close enough to be in potential contact, and a finer detection to actually identify contacts among the possible candidates. The fine detection can be solved either by the method of Common Plane introduced by Cundall [73], or by the 3D generalization of the Shadow Overlap method introduced by Saussine [2].

This database, although satisfactory, is still a simplification of the complexity and heterogeneity of ballast grains. The SNCF is investing in creating a more realistic database that could give accurate answers to problems requiring a finer description of the grains, such as the influence of grains shape and ballast degradation on the behaviour of the track. A recent work made by Ouhbi [89, 90] proposes a method of generating realistic grains mathematically, using Proper Orthogonal Decomposition, optimizing the number of required faces and vertexes required (Figure 1.21c). This way it is possible, not only to artificially generate new particles, but to introduce the degree of degradation we desire for them. This last method is still very new and the complexity of the particles (despite the optimization), makes it suitable for the moment only for very specific problems.

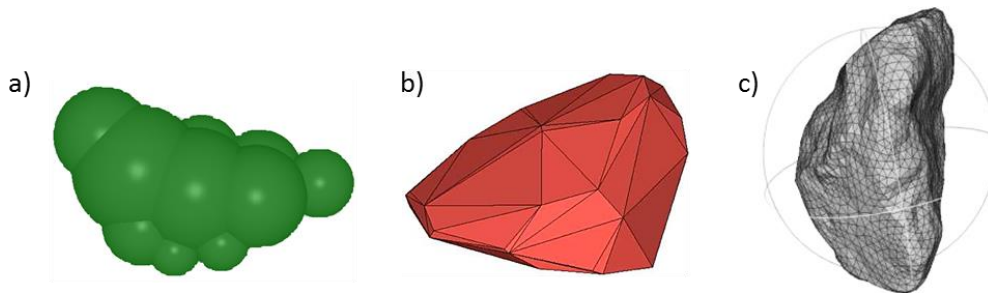


Figure 1.21 Different examples of ballast modelling: a) clusters of spheres [35], b) polyhedral particles [19] and c) realistic grains by POD generation [89].

For this project we will be using the polyhedra database, which we consider precise enough to assess the contact forces and the relative displacements at the contact scale. In any case, none of these particles are breakable or wearable, i.e. they stay the same along the full simulation. And this is so because simulating breakage or wear in an accurate enough way is not evident at all and, in the best of cases, it results in a high computational cost. In the next section we will present some attempts and proposals to introduce degradation on ballast simulations.

1. 4. 3 Previous works on numerical particle degradation

Simulating particle breakage and degradation in discrete elements would be a step further on the simulation of railway ballast. However, as we have seen, discrete elements are already very costly in terms of computational time, even when dealing with simplified models of the track. Introducing breakage means, in the simplest case, dividing the particles into pieces so that they can be split in several parts. Only with this operation, we are already increasing the number of grains and thus the number of interactions, increasing the computation time. Despite this, there have been some attempts to perform approximations to the problem in granular simulations.

Most of these works have focus on particle breakage, at larger or smaller scale, and they usually consist in adding detachable particles to the main grain. This is commonly used along with clusters of spheres [35, 91, 92], where some spheres of the cluster can detach from the main cluster if a certain stress level is reached (Figure 1.22a). This method allows for representing breakage of small asperities, represented by small detachable spheres. Moreover,

these detached particles will remain in the system as they would do in reality. However, this approximation delimits the crack to pre-built paths and pre-defined chunks of matter, giving a very limited perspective of actual particle breakage. Again, if we desire to improve the results, we should model particles with a large number of spheres, penalizing the suitability for large simulations.

Another approach, proposed by Lobo-Guerrero [93] for 2D disk-shaped ballast grains, replaces the damaged particle by two or more smaller disks (Figure 1.22b). Still, this approach is far from reproducing breakage in a realistic way.

Some other methods, such as the Von Mises approach of Eliáš [94], try to give not so predefined breaking path by actually dividing the particle into fragments (Figure 1.22c), obtaining a better representation of particle breakage. These methods, however, are usually very costly in computational time, so they are limited to simulation with a relatively low number of particles.

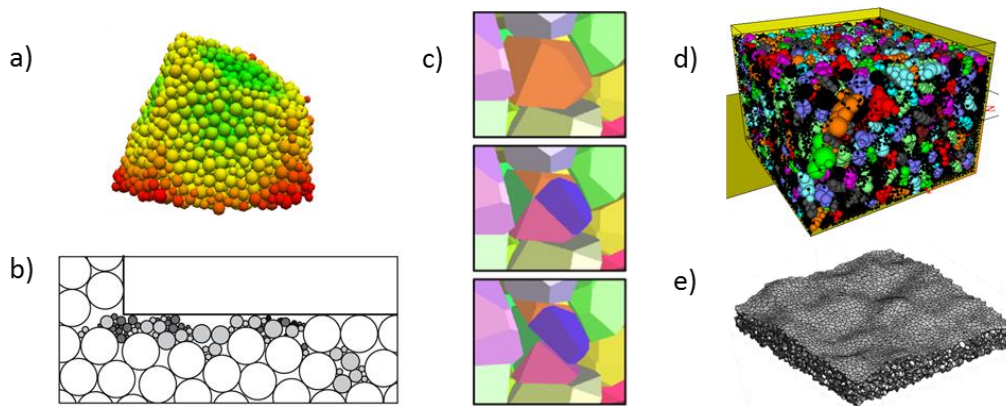


Figure 1.22 a) Ballast particle modelled by a large cluster of detachable spheres [91]. b) Breakage represented by replacing the original particle by smaller ones [93]. c) Particle breakage into parts by stress criterion [94]. d) Study of ballast fouling by adding small detachable spheres to the clusters [35]. e) Wearable surface generated by Voronoi tessellation [95].

The representation of wear is even more complicated due to the small size of the resulting particles. The works of Indraratna and Ngo [35] concerning the influence of ballast fouling, or McDowell and Li [96] analysing the breakage of asperities, used the previous approach of adding small particles (spheres) to the grains (Figure 1.22d). Even if small, these particles are still several orders of magnitude larger than what we understand as fines. Mollon proposed a Voronoi approach [95] for reproducing actual surface degradation by dividing the wearable surface into very small Voronoi volumes (Figure 1.22e). Again, this kind of methods can give a more representative view of the problem but they are limited to a single surface. It would not be computationally applicable to a macro-scale simulation of the track, where thousands of particles are involved.

In conclusion, wear is a very complex phenomenon, which is not easy to reproduce numerically. The different attempts in the literature are either too costly in computational time or they fail to reproduce the phenomenon accurately enough. It is then needed a different approach to the problem. In this project we propose to use the numerical simulations only as a tool to perform the change in scale from the track to the contact. We will then not simulate

actual wear, instead we will extract from the simulations the quantities involved in the wear processes and we will apply these quantities to the predictive model of wear proposed by Archard.

1.5 CONCLUSIONS

In this chapter we have presented the maintenance cycles of the track and the ballast layer in particular and we have explained the problem that ballast degradation represents to the railway industry. A proper and precise understanding of the problem would allow us to predict the critical accumulation of fine particles in the track. Therefore, a model of ballast wear is required in order to propose optimal solutions.

For studying ballast degradation, it is necessary to study the interaction between surfaces. Thus we have briefly presented friction and wear in tribological terms and we have introduced a simple but widely used model given by Archard equation to predict wear. We have introduced some works using this model and we have concluded that it is a good candidate for helping us to create our degradation model.

Wear is therefore a contact-scale phenomenon that is influenced by the general behaviour of the granular package. This change of scale from the track response to the consequences at the contact level, in terms of forces and relative displacements, will be performed using numerical simulations by discrete elements, more specifically using NSCD. We have thus briefly presented this method, its advantages and limitations, and some works previously performed by the SNCF.

However, we have also seen that the attempts of simulations wear numerically are either too costly in terms of computational time or they are not accurate enough. We have then proposed not to simulate actual wear, but to extract the values involved in wear mechanisms and to apply them to an analytical model given by tribology, such as Archard equation. In order to calibrate the model, we will perform experimental tests at the contact-scale using the values extracted from the numerical simulations.

In the following chapters, we will perform different experiments and simulations, always taking this multi-scale methodology as a reference, with the final goal of proposing a degradation model for ballast. We have considered the standard abrasion Micro-Deval test as a good starting point, since it is widely used in the railway industry and it can be easily performed, both numerically and experimentally.

II. MICRO-DEVAL TEST

2. 1	Introduction.....	46
2. 2	Micro-Deval standard test	46
2. 3	Numerical simulation of the Micro-Deval	47
	2. 3. 1 Description of the system	48
	2. 3. 2 Dynamics of the system	49
	2. 3. 3 Contact forces	50
	2. 3. 4 Friction work	51
2. 4	Experimental Micro-Deval test	53
	2. 4. 1 Test procedure	53
	2. 4. 2 Evolution of the mass of the sample	53
2. 5	Estimation of Archard coefficient for Micro-Deval test.....	58
2. 6	Adequacy of Micro-Deval test	59
2. 7	Conclusions.....	60

2.1 INTRODUCTION

After some years of service of the first high-speed service in France, ballast has proven not to be resistant enough. Ballast grains show a faster degradation than expected and tamping operations are required more often than desired. In order to fight against this issue, railway industry has focused its efforts on improving the resistance of the grains by searching for the best quality of the material of the aggregates. A strict selection of the samples is performed just after the extraction of the mineral in the quarry, classifying the aggregates depending on their resistance to attrition and to impacts. Tests like Micro-Deval (attrition) or Los Angeles (impact) have become very handy and widely used due to their repeatability and relatively low price.

For the same reason, these tests can be easily reproduced at the laboratory. Since this project is focused on wear due to attrition, Micro-Deval has been chosen as the test of study. At the same time, due to its simplicity, this test is also easy to reproduce numerically, providing a first link between experimental and numerical results.

Henceforth, in this chapter we will present and analyse a numerical simulation of the Micro-Deval test, which will allow us to understand the dynamics of the grains within the drum and to analyse the contact forces, relative displacements and consequently the friction work part of Archard equation. On the other hand, we will also perform the test experimentally, stopping the machine at different intervals to quantify the generated fines, with the objective of building the curve of mass loss. Both results will then be linked in order to give an estimation of the Archard wear coefficient for this standard test. Finally, some discussion about the adequacy of the test, comparing the drum system with the track conditions, will be presented.

2.2 MICRO-DEVAL STANDARD TEST

Attrition resistance of ballast grains is experimentally assessed in a Micro-Deval device, following the corresponding European railway standards. Specifically, the characteristics of the device and the test procedure are described in the European Norm EN 1097-1 "Tests for mechanical and physical properties of aggregates" [29]. However, this test was originally conceived to be used on smaller aggregates (e.g. for roads) and it was later adapted to railway ballast. Annex E of the norm EN 13450 "Aggregates for railway ballast" [25] describes the modifications of the machine and procedure in order to perform the test with these grains.

During this test a sample of grains is turned inside a metallic cylinder. The numerous contacts within the device, both between grains and with the steel drum, produce an accelerated wear process in the aggregates which causes changes in the morphology of ballast grains similar to those produced in the track.



Figure 2.1 Micro-Deval device in the 3SR Laboratory, with larger cylinders adapted to ballast grains.

The cylinders used for the adapted test for ballast are bigger than the original, presenting an internal length of 400 mm and an inner diameter of 200 mm (Figure 2.1). The device makes the cylinders turn at 100 RPM during 2h 20' for a total of 14 000 revolutions. Nevertheless, even if it is not needed for the norm, the machine allows for interrupting and resuming the test at any moment. The sample consists of 10 kg of ballast grains ranging from 31.5 mm to 50 mm, half of it within the range 31.5 -40 mm and the other half within 40-50 mm. The steel balls added in the original test are not used with ballast samples. Finally, 2 litres of water are added inside the drum.

Once the test is finished, it is sieved in order to separate the fine particles from the grains. Everything passing through a 1.6 mm sieve is considered as fines. The adapted Micro-Deval coefficient (MDA) is then calculated as:

$$MDA = \frac{10000 - m}{100} \quad (2.5)$$

Where m is the mass in grams of the oversized fraction retained on the 1.6 mm sieved.

This was a brief summary of the standard procedure that needs to be followed in quarries before providing ballast to the railway industry. However, the goal of this project is not to assess the Micro-Deval coefficient, but to understand the wear procedure and to understand how the amount of generated fines changes depending on the conditions. For this reason, we did not stick to the exact procedure but some slight changes have been introduced instead. The detailed experimental test will be explained in section 2. 4.

2. 3 NUMERICAL SIMULATION OF THE MICRO-DEVAL

In order to understand the dynamics within the sealed drum, a discrete element simulation of the test has been performed. This simulation will show the trajectory of the grains as well as the interactions, i.e. contact forces and relative displacements, between grains and between the drum and the grains. The software chosen for these simulations is LMGC90, an open-source code developed by the University of Montpellier, using a Non-Smooth Contact Dynamics approach (NSCD) (see section 1. 4. 1).

2.3.1 Description of the system

The drum has been numerically built following the specifications of the European Norm described before, i.e. 40 cm long with a 20 cm inner diameter and set to turn at 100 RPM. The cylinder is closed on each side. On the other hand, ballast grains have been randomly chosen from the SNCF database of ballast, which contains 1000 different modelled grains. This database was built following the correct ballast grain-size distribution, using polyhedral shapes containing from 12 to 70 faces and from 8 to 37 vertices. In order to cover the required 10 kg of ballast, we compute the volume of each chosen grain and the corresponding mass using the average granite density of 2700 kg/m^3 . Finally, 109 grains are required for the simulation, which is a similar number of grains to the experimental tests performed. Figure 2.2 shows a 3D perspective of the simulation, the colours only representing the identification number of each grain, so that it is possible to observe the mixing inside the drum.

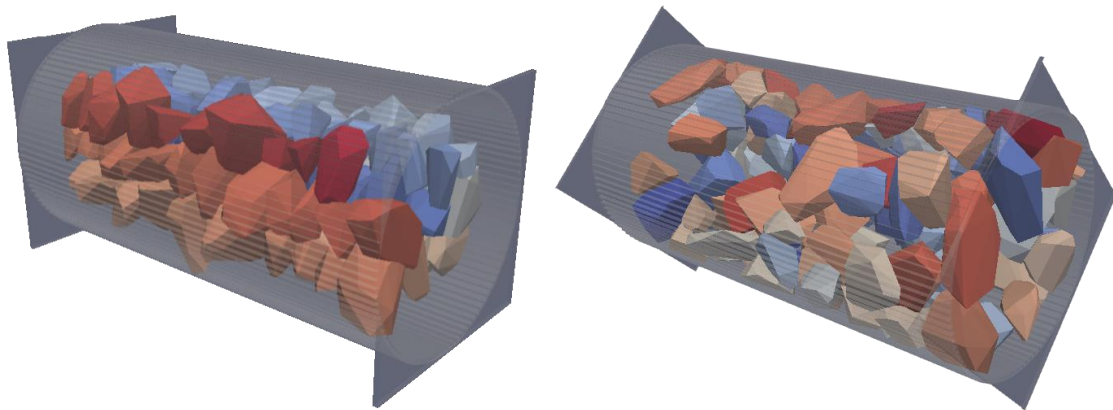


Figure 2.2 Simulation of the Micro-Deval test. Left: initial state, grains start in a dense grid with some overlap allowed. Right: the test running, initial overlaps quickly disappear and do not affect the simulation. Colours have only an identification purpose.

It is important to remark that the grain-size range of the database fits the thresholds of the track but not necessarily the 31.5 – 50 mm range of the Micro-Deval test. Choosing the grains randomly does not ensure the exact required distribution for the standard test. As we will see in the experimental tests, grain-size might have a slight influence on the Micro-Deval coefficient, but the differences between samples are not significant enough for the purpose of this project.

Collisions are considered perfectly inelastic (restitution coefficient equal to zero) and grains are modelled as rigid bodies. Wear is not modelled during the simulation, so grains do not change at all over time. Thus, only 35 seconds of test have been simulated since system conditions remain the same along time. The time step considered is 10^{-4} seconds but data is saved every 50 time steps (i.e. every $5 \cdot 10^{-3}$ seconds). The model is built by settling the ballast grains in a tight grid inside the cylinder, allowing for an initial overlap between grains (see Figure 2.2 left). As the test starts, grains fall by gravity to the bottom of the cylinder and the dynamics of the system quickly deletes the overlaps. Due to the dynamics of the system and the looseness of the package, this transition phase is very short and does not affect the results.

Friction coefficient between ballast grains has been established as 0.8, which is the classic value used by SNCF in their DEM simulations [17]. This value has been confirmed in this project (section 4. 4. 3) to be a good value for both new grains and eroded grains. Between ballast and the metallic drum, friction coefficient has been arbitrarily set at 0.4. In order to simplify the simulation and to reduce computational cost, water is not considered. This restriction will mean that, for a proper comparison, most of experimental tests will also be performed without water.

2. 3. 2 Dynamics of the system

Ballast wears inside the cylinder due to the numerous contacts between grains and against the cylinder, those contacts provoking friction and eventually breaking the micro-asperities of the grains. However, we do not know the order of magnitude of the forces involved in these contacts. In fact, we do not even know how the grains move inside the cylinder. Are they turning with the drum? Is the centrifugal force large enough to keep grains stuck to the cylinder? Or is the full sample instead staying in the bottom swinging from one side to the other? Thus, the first thing we can study is the trajectory of the grains during the test. Figure 2.3a shows the trajectory during 5 seconds of a random grain inside the cylinder. This is just a short example with the idea to have a clean visualisation, but this kind of trajectories are repeated and followed by all grains.

The first thing we can notice is that in those 5 seconds, the grain turns around the cylinder about 8.6 times. In 5 seconds, the cylinder makes 8.3 turns. Therefore, the assembly of grains not only turns with the drum rotation, but also it does approximately at the same rate of the cylinder.

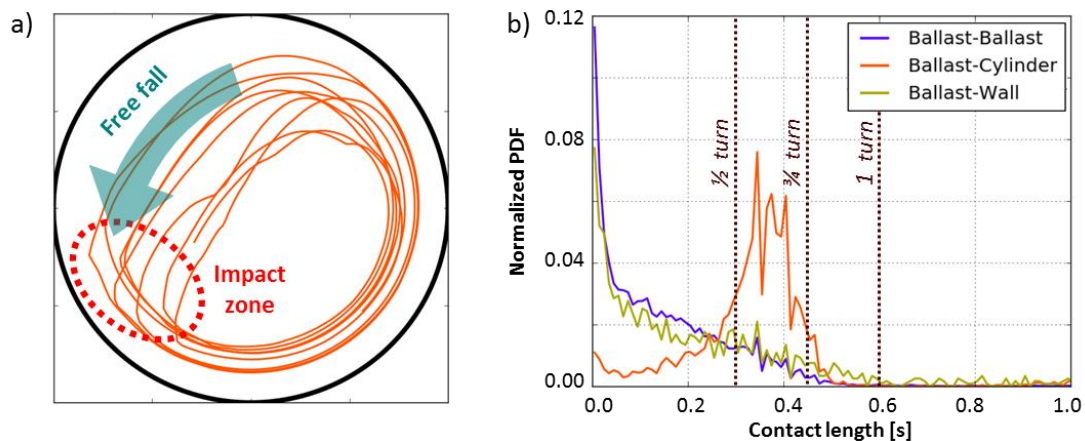


Figure 2.3 a) Trajectory of a random grain during 5 seconds of simulation. b) Normalized PDF of the contact duration.

However, grains do not get stuck to the cylinder during the full turn. First, they go upwards with the cylinder pushed by friction and the centrifugal force. Once they reach almost the top, they start a free fall towards the other side of the drum impacting the metallic wall or other grains. During the upwards phase, the trajectory of the grains alternates between smaller and

larger radius, i.e. the grain being closer or further from the centre of the cylinder, depending on its location inside the assembly of grains.

Figure 2.3b shows the normalized probability density function (PDF) of the contact duration between ballast grains and between grains and the cylinder, distinguishing between the side walls and the cylinder itself. Taking a look at the grain-cylinder contacts, we can observe that most of them last for between half and three quarters of a turn. This means that the free fall takes between one quarter and half turn. Finally, we can observe how, due to the dynamics of the system, ballast-ballast contacts are generally brief lasting for less than a quarter of a turn.

2.3.3 Contact forces

Now that we know that ballast grains follow several phases during every turn, we can expect a large variability of the forces between the upwards movement and the impacts after the free fall.

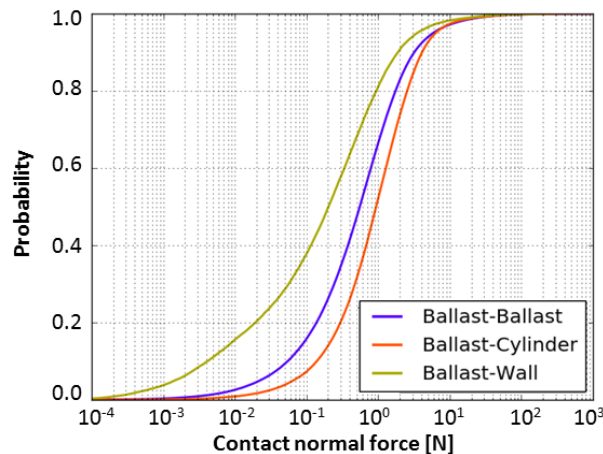


Figure 2.4 Distribution of the contact normal forces.

<i>Normal forces [N]</i>	Mean	Percentile 99	Percentile 99.9	Max
Ballast – Ballast	2	26	144	1 712
Ballast – Cylinder	3	24	185	1 747
Ballast – Wall	1	19	103	282

Table 2.1 Some numerical values of the curves shown in Figure 2.4.

Figure 2.4 shows the cumulated density function of the contact normal forces during the 35 seconds of simulation (see Table 2.1 for some numerical values). As we can observe, ballast-ballast contacts are in average softer than ballast-cylinder contacts. This is coherent since, during the upwards phase, grains trapped on the bottom of the assembly and touching the cylinder are affected by the mass of the grains over them. However, this is only true for low-intensity contacts. When dealing with impacts, this difference disappears, i.e. after the free fall, impacts can happen against the cylinder, but also against other grains.

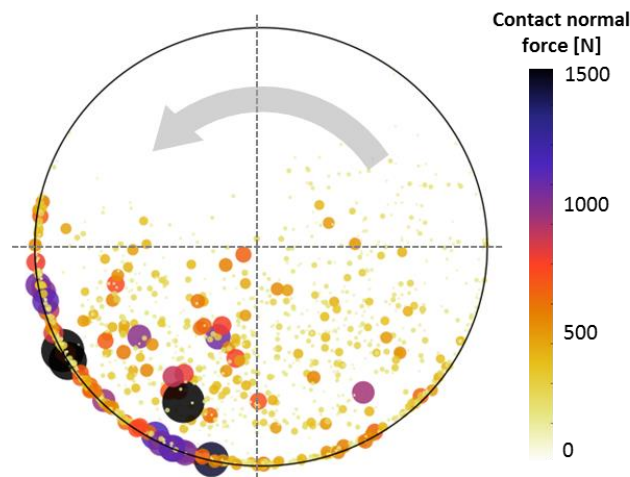


Figure 2.5 Normal forces during the 35 seconds of Micro-Deval simulation.

During the upwards phase, contact forces present a very low intensity, in most of the cases below 5 N. Figure 2.5 shows how most of the strong contact forces are located in the low-left quadrant, i.e. where impacts take place. Despite being less frequent, these impacts are much stronger and can reach forces over 1 kN, so they are probably the main responsible for the eventual major breakages empirically observed in some grains.

2.3.4 Friction work

Archard model (see section 1.3.3) predicts that wear is proportional to the product of normal force and tangential relative displacement at the contact ($F_N \cdot Disp$), which we called friction work. The relative displacement is approximated as the product of the time step and the tangential velocity at the contact point. This may lead to an overestimation of the relative displacement on impacts and short contacts since they often do not last more than one timestep. And as we have seen in the previous section, impacts often present as well larger normal forces, so the combination of both may result in an overestimation of the friction work. In any case, this will serve to get an order of magnitude of the contribution of this kind of contacts in comparison to the friction contacts.

Let us divide the section of the cylinder in a uniform grid (cell size of 2 x 2 mm) and then sum the friction work of each contact happening inside each of the cells of this grid. As we can see in Figure 2.6a, during the upwards movement, grains are more compacted and the number of contacts is much higher than inside the impact quadrant, where contacts are more randomly located. Using the same grid, we can analyse where within the drum friction work is higher. Figure 2.6b shows the distribution of the average friction per Micro-Deval turn around the cylinder. We can observe that the order of magnitude of the friction work is similar in both the impact and the upwards zone. This means that the intensity of the impacts is enough to compensate the reduced number of contacts. Or, in other words, during the upwards movement there are so many contacts that despite not being very intense, they cumulate a high amount of friction work, i.e. potential wear. The high importance of the friction mechanism during the upwards phase and the relatively low-intensity impacts in comparison

of other tests like Los Angeles, confirms the proper name of attrition test for the Micro-Deval test, although attrition is not the only mechanism acting.

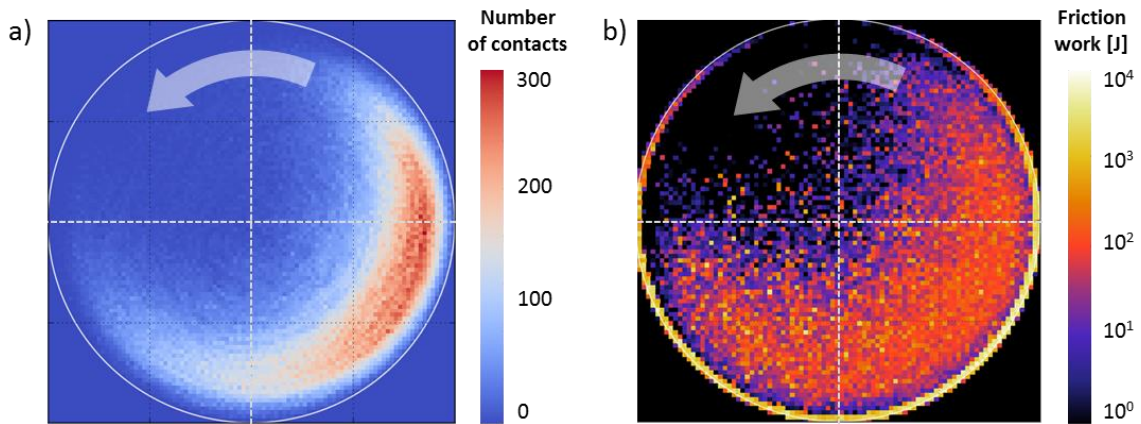


Figure 2.6 a) Distribution of ballast – ballast contacts. b) Distribution of the friction work per turn.

However, this is the amount of work produced by the contact and absorbed by both bodies. In order to estimate the amount of ballast wear produced in that contact, it is necessary to establish which fraction of the contact energy is absorbed by the grains. Since the main goal is to obtain a global approximation of the wear, in the case of ballast – ballast contacts it is acceptable to consider that each grain absorbs half of the energy. When the ballast is in contact with the drum, contact forces are similar but relative displacements are higher due to the lower friction coefficient, leading to a higher friction work. However, it can be observed empirically on the experimental test that the cylinder (or the water, if present) is significantly heated due to the friction, losing part of the energy. Following empirical observations in other MDA tests involving only one grain and metal balls [97, 98], the amount of energy in ballast-drum contacts causing grain degradation can be estimated between 10% and 15% of the friction energy of the contact. For this calculation, the least favourable case of 15% is considered.

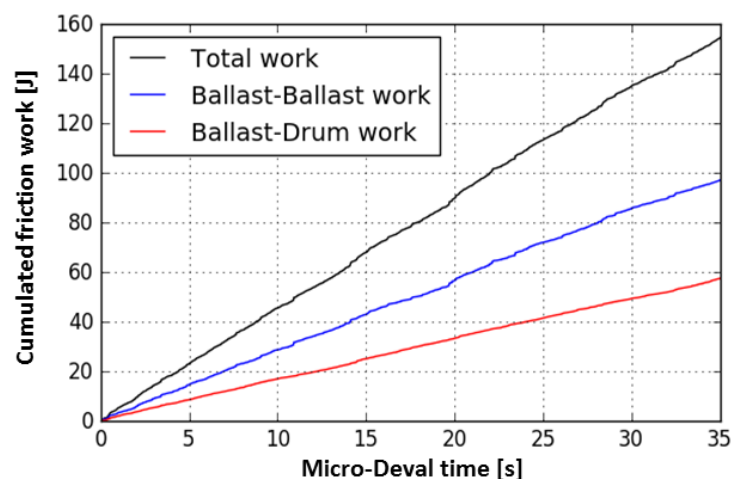


Figure 2.7 Cumulative evolution of the friction work along the simulation time.

Figure 2.7 shows the cumulated friction work absorbed by the sample of grains along the simulation time, for each kind of contact. As expected, due to the homogeneity of the test

throughout time, i.e. conditions not changing and grains not evolving in shape, the evolution of the friction work is linear. We can also observe that the transition regime at the beginning of the simulation is not affecting the results. Thus the total friction work rate inside the system is constant and equal to 4.4 J/s, absorbed by all ballast grains.

In fact, not only the work rate is constant, but also the amount of work absorbed by each individual grain is also relatively homogeneous, which is not surprising because all grains have a similar size, so a similar average number of contacts (coordination number) per rotation of the drum.

2. 4 EXPERIMENTAL MICRO-DEVAL TEST

2. 4. 1 Test procedure

In order to understand how grains lose matter in the Micro-Deval device and to compare it to the results obtained numerically, the test was performed experimentally in the 3SR Laboratory. However, some modifications to the standard test were introduced. The main difference is that water was not initially added to the cylinder. The reason is that we neither added water to the simulation so this measure was necessary in order to keep the same conditions to be able to compare results. Finally, in order to study the influence of the water, we performed some other tests following the same procedure but adding the 2 litres of water.

Apart from that, for the sake of simplicity, we chose the grains randomly from a big bag of ballast, with the only restriction of trying to take grains that were arbitrarily big enough. Therefore, the grain-size distribution of the samples resulting from this random selection may not follow exactly the strict requirements of the standards.

The second difference is that we wanted to keep track of the loss of mass along the test, so we stopped the machine at different intervals in order to weight the sample. In most of the tests, the sample was weighted every 20 minutes, but we also performed one stopping the sample every 5 minutes and also some full tests without stops. In order to weight the sample, we had to clean the grains after each stop from the fines surrounding them. We initially used a brush in order to avoid the drying process, but afterwards we thought that a hairdryer would dry the grains fast enough, so we started cleaning the grains directly with water. After the cleaning, we opted to remove the fines from the sample every time, or to change the water on the wet tests.

2. 4. 2 Evolution of the mass of the sample

During the wear process inside the device, ballast grains lose mass. Figure 2.8 shows the grains before and after the test. We can observe how sharp edges are smoothed and grains present a much rounder shape. All this mass lost is the responsible for the powder surrounding the

grains after the test. However, not only fine particles are created. Eventually small fragments were broken from the grains. Thus a threshold between fragments and fines is required.

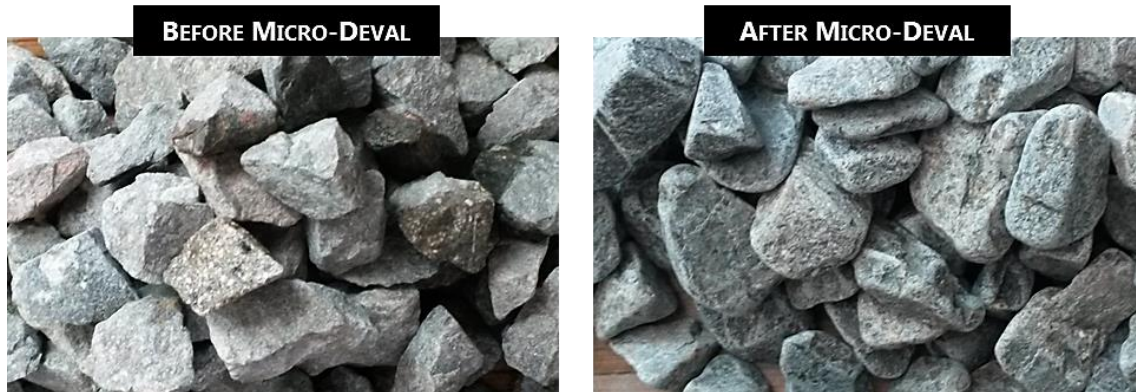


Figure 2.8 Ballast grains before and after a full Micro-Deval test.

After each stop, fragments approximately between 2 and 20 mm were separated from the sample. These fragments were big enough not to be considered fine particles (the norm fixes the threshold at 1.6 mm), but small enough not to be considered ballast grains. For this reason, these fragments were not added to the total amount of fines, but neither were they added again to the sample for the next Micro-Deval cycle.

The following table summarizes the different tests and gives the final amount of fine particles generated from each sample:

		Type of ballast	Stops interval	Generated fines	Observations
DRY conditions	1	Mix	Every 5 minutes	287.8 g	
	2	Conventional	Every 20 minutes	269.6 g	
	3	HSL	Every 20 minutes	228.5 g	
	4	HSL	Every 20 minutes	286.0 g	
	5	HSL	Every 20 minutes	255.7 g	Sample in water for 10 min before the test
	6	HSL	10 – 30 – 70 – 140 min	221.2 g	
	7	HSL	Full test - no stops	182.8 g	
	8	HSL	Full test - no stops	182.4 g	
	9	HSL	Half test – no stops	132.0 g	70 minutes test
	10	HSL	Half test – no stops	153.8 g	70 minutes test
WET conditions	11	HSL	Every 20 minutes	453.9 g	
	12	HSL	Every 20 minutes	394.5 g	
	13	HSL	Every 20 minutes	413.1 g	
	14	HSL	Full test - no stops	425.3 g	
	15	HSL	Full test - no stops	447.9 g	
	16	HSL	Full test - no stops	444.0 g	Sample in water for 24h before the test
	17	HSL	Full test - no stops	496.7 g	Sample in water for 10 days before the test

Table 2.2 Summary of the Micro-Deval tests.

Note that the Micro-Deval coefficient would be just the amount of fines in grams divided by 100. We can already observe the significant difference between the tests in dry and wet conditions, but let us study in detail the evolution of the mass during the test for each kind of conditions.

Dry conditions

As we have described, initially the tests were performed in dry conditions, i.e. without adding the 2 litres of water required in the standard test, in order to be as close as possible to the conditions of the numerical simulations. This procedure was followed on 10 different tests with different intervals between stops. During the tests, granite ballast for High-Speed Lines (HSL) was used (C2). However, on the first two tests, ballast for conventional lines (C4) was also used. This last ballast comes from the same quarry as the HSL ballast and its mineralogy is also granite, but the sample did not pass the standard thresholds on the Micro-Deval and Los Angeles test (see section 1. 2. 1).

Figure 2.9a shows the evolution of all samples tested in dry conditions, along with the final point of the tests without stops. The first thing we can notice is that there is an important variability in the results, that comes from the fact that samples are formed by a relatively small number of grains (around 100), so the result will be sensitive to the chosen rocks and their morphological features. In the standard test this variability is reduced limiting the grain-size distribution of the samples and always performing the test over two samples and averaging the result. In any case, for the goal of this project, our procedure is sufficient to observe wear tendencies.

The orange line corresponds to the test performed with conventional ballast, and the purple one to a sample formed with mixed ballast. These tests where ballast for conventional lines was involved are located on the upper half of fines production, as expected. Nevertheless, as we have explained, both kinds of ballast present basically the same mineralogy, so the differences are not significant, and there is one of the HSL samples that produced more fines.

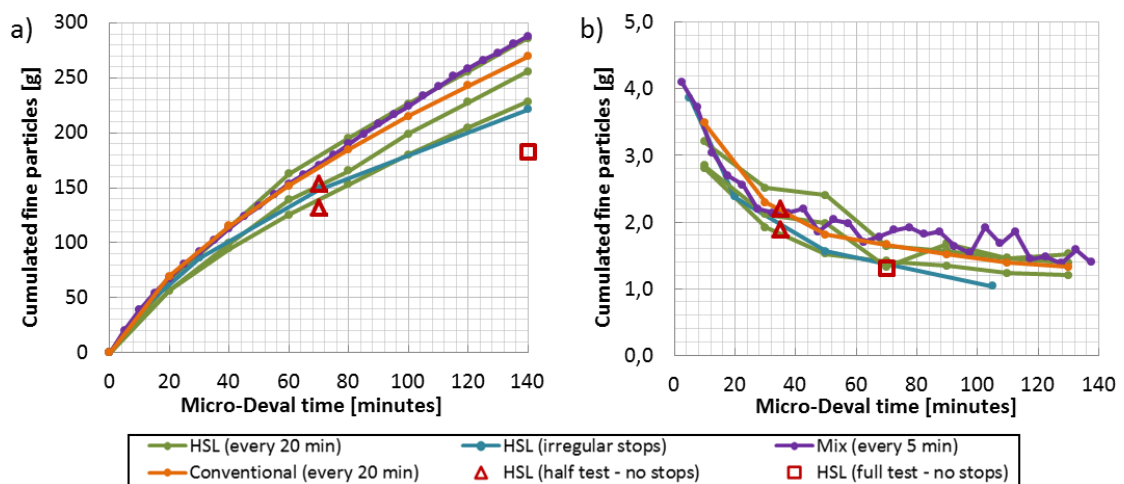


Figure 2.9 a) Cumulated production of fine particles along the Micro-Deval test. b) Wear rate, i.e. slope of plot a), along the Micro-Deval test. The data points have been added in the middle of each interval.

On the other hand, the amount of stops seems to have a perceptible role on the wear of the grains. The test stopping every 5 minutes is the one producing the largest amount of fines, while both tests without stops are significantly below the rest. This behaviour could happen because in every interruption, grains are cleaned and fines are removed from the sample. These fines cover the grains creating a protecting layer for small asperities and therefore reducing wear. Thus every time grains are cleaned asperities become exposed to contacts and impacts and wear is again produced more easily.

In any case, all the tests follow the same trend: they have an aggressive start and, after the first half of the test, the production of fines is stabilised and almost linear. This trend can be seen even clearer on Figure 2.9b which shows the derivative of the other plot, i.e. the evolution of the wear rate. Therefore two well-distinguished phases are identified: at the beginning of the test, the wear rate is higher, but it decreases rapidly following approximately a power law. After the first hour of test, the production of fines tends to stabilise to a fixed wear rate of 1.2 – 1.3 g / minute.

This behaviour is not surprising, new grains present weak asperities and sharp edges and vertexes that are easily removed during the first minutes of the test. Once these features disappear, wear is still produced but at a lower rate. A deep analysis of the evolution of the asperities and the morphology of the grains will be presented in Chapter III.

Wet conditions

The study of the influence of water has been performed as part of the Master Thesis of Stocco [99]. The goal of these tests was to compare the results in dry conditions with the standard test, i.e. adding the 2 litres of water in the cylinder. Again, the sample was weighted at different intervals, drying the grains with a hairdryer at each stop. Each time, muddy water was removed, the cylinder was cleaned and 2 new litres of clear water were added. Seven tests have been performed in wet conditions, three stopping every 20 minutes and four full tests without stops, all of them using HSL ballast.

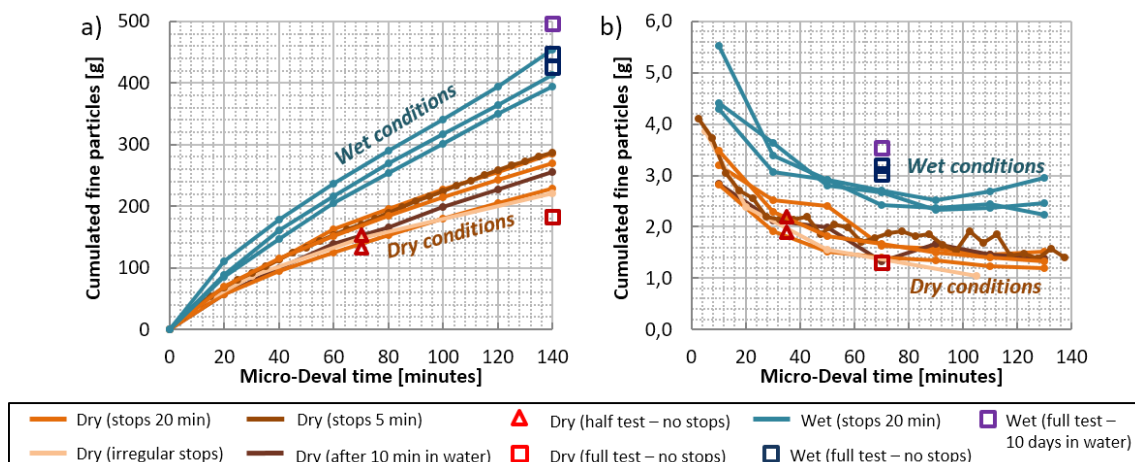


Figure 2.10 Cumulated production of fine particles (a) and evolution of the wear rate (b) in wet and dry conditions. Again, for the wear rate the data points have been added in the midpoint of each interval.

Figure 2.10 shows the cumulated production of fines (a) and the evolution of the wear rate (b) of these tests in wet conditions (in blue), compared to the results obtained in the previous section in dry conditions (in orange and red). We can clearly see how the production of fines with the presence of water is significantly higher than in dry conditions. By the end of the test, the total amount of wear is almost doubled.

On the other hand, we can recognise the same two phases described in the previous section. In fact, the evolution of the wear rate is very similar for wet and dry conditions, only that it is shifted up. That means that in wet conditions wear rate is higher in both the aggressive and the linear phase. In this last linear phase, the wear rate in wet conditions tends to about 2.5 g / minute, basically doubling the wear rate in dry conditions.

One explanation for this behaviour could be a chemical (mineral components sensitive to water agents) or micro-mechanical (presence of water inside eventual micro-cracks of the rock) influence of water, eventually modifying the mechanical properties of the grains. Some studies [100, 101] show a reduction in granite strength when moisture is present. However, ballast is already crushed material that rarely presents cracks large enough to allow water to penetrate in the relatively short duration of the test. In any case and in order to check this assumption, two of the four tests in wet conditions without stops have been performed leaving the samples in saturated conditions before the test: one of them leaving the sample for 24h inside water and one leaving the sample for 10 days. We also performed one of the tests in dry conditions after leaving the sample for 10 minutes in water before drying it with the hairdryer and starting the test. The test presenting the higher production of fines in Figure 2.10a, producing almost 500 g, is indeed the test performed after leaving the sample in water for 10 days. However, the difference with the other tests is not that significant and neither the 24h-test nor the 10 minute-test shows any difference with the rest. In any case, thanks to the permeability of the ballast layer grains should dry fast after rainfall and they should never stay in saturated conditions, at least not for so long time. Therefore, the chemical or micro-mechanical effect of water is not actually representative for us and for the purpose of ballast we can consider the material as inert.

A more plausible explanation might be related to the number of stops and the cleaning effect. As we saw in the tests in dry conditions, after certain Micro-Deval time, grains are surrounded by a thin layer of fines, protecting the small asperities against wear. In wet conditions, water continuously cleans the grains not allowing fine particles to stay stuck to the particles. The protection layer is then not formed and asperities are exposed to impacts and contacts. In addition, the relatively small amount of water, along with the centrifugal force pushing it to the upwards zone of the cylinder, is probably not enough to serve as a damping layer on the impact zone. One last observation that goes along the same lines is the fact that, in wet conditions, there is not such a clear difference between tests stopping and not stopping the machine, i.e. between cleaning or not the sample in the middle of the test. This is so because in this case, grains are cleaned all along the test and the protection layer is continuously removed. Even if water is slightly muddy after mixing with fines, the dynamics of the system does not allow those fines to get stuck again on the grains.

2.5 ESTIMATION OF ARCHARD COEFFICIENT FOR MICRO-DEVAL TEST

After having analysed the numerical and the experimental results, it is now time to combine them using Archard model in order to build a first predictive equation of wear for the Micro-Deval test. Note that, for such a dynamic system, this will be just a rough estimation, since impacts, which we have seen that play an important role, are not properly dealt by Archard model and should likely be treated with a different model. All in all, this will allow us to obtain the order of magnitude of the wear coefficient for the attrition test for comparing it with the track system in the following chapters.

Let us first recall the equation of Archard:

$$V_w = k \cdot F_N \cdot Disp = k \cdot W_{fr} \quad (2.6)$$

Where V_w is the volume of fine particles generated in m^3 , F_N the normal force at the contact in Newtons and $Disp$ the tangential relative displacement between grains in meters.

The product $F_N \cdot Disp$, which we have called friction work (W_{fr}), has been estimated thanks to the numerical simulations. On the other hand, the wear volume V_w , and more specifically the wear rate, can be obtained from the curves of mass loss extracted from the experimental tests. It is then possible to link both results using Archard's model to get a first estimation of the wear coefficient k .

As we have seen, wear in the Micro-Deval achieves a stable regime where fines are produced at a constant rate. And this quasi-linear production of fines observed after the initial stages of the test is coherent with the constant rate of friction work extracted from the numerical simulations. Thus, from a macro-scale point of view, i.e. averaging all the contacts within the test, the proportionality between the friction work and wear, given by the wear coefficient k in Archard equation, can be considered as reasonable once is the linear phase of the test reached after the aggressive start.

In dry conditions, and once the stable regime is achieved, an average constant wear rate of 1.3 g/minute can be assumed. For wet conditions, the wear rate is almost double and equal to 2.5 g / minute. On the other hand, the work rate extracted from the simulations is 4.4 J/s. Taking the granite density as 2700 kg/m³ and using Archard equation in its rate form, we can estimate the wear coefficient after the corresponding adjustments to the units:

$$\dot{V}_w = k \cdot \dot{W}_{fr} \quad (2.7)$$

$$\dot{V}_{w \text{ dry}} = 1.3 \frac{g}{min} \cdot \frac{1 \text{ kg}}{1000 \text{ g}} \cdot \frac{1 \text{ m}^3}{2700 \text{ kg}} \cdot \frac{1 \text{ min}}{60 \text{ s}} = 8.02 \cdot 10^{-9} \frac{m^3}{s} \quad (2.8)$$

$$\dot{V}_{w \text{ wet}} = 2.5 \frac{g}{min} = 1.54 \cdot 10^{-8} \frac{m^3}{s} \quad (2.9)$$

The Archard coefficient for the linear phase will then be:

- $k_{\text{dry}} = 1.8 \cdot 10^{-9} \text{ Pa}^{-1}$
- $k_{\text{wet}} = 3.5 \cdot 10^{-9} \text{ Pa}^{-1}$

This coefficient k has units because it is the simplification $k = K/H$, where K is the original wear coefficient and H the hardness of the softest material measured in Pa, as we explained in section 1.3.3. Hardness is a difficult value to assess because it depends on the chosen test so it was simplified for this project taking profit of the fact that, in ballast – ballast contacts, both materials are the same so hardness will be a constant in the equation. However, using some tables of Vickers and Knoop tests [102], we can approximate granite hardness to about 8 – 10 GPa. This would mean that the dimensionless Archard coefficient would be around 15 for dry conditions and around 30 for wet conditions. Knowing that 10^{-1} is already considered severe wear in Archard's model, this value is then extremely high even for an irregular surface texture as that of ballast grains. But the reason has already been explained: in the Micro-Deval test not only friction wear is produced, but impacts are also involved and do represent a significant source of fines. This part of wear is extremely aggressive, eventually provoking major breakages that are not accurately predicted by Archard equation.

In any case, this was a macro-scale overview of the test. In order to better understand what happens at the grain scale, it is necessary to follow how grain morphology evolves during the process. This will be explored in the Chapter III.

2.6 ADEQUACY OF MICRO-DEVAL TEST

Micro-Deval is a widely used test for assessing attrition resistance. The relatively small diameter of the cylinder and the tight density of grains within favour the continuous friction between particles. This is well distinguished from other similar tests like Los Angeles where the cylinder is larger, reducing the density of grains, and includes a plate that rises the ballast to let it fall from a higher height, searching mostly for strong impacts between the grains and the drum. Moreover, the fast rotation of the cylinder helps to accelerate the ageing, even for high-resistance aggregates, and the final shape of the grains is not so different from the grains in the track after years in service. However, as we have seen, this dynamics leads to impacts becoming also a wear mechanism of the grains.

In any case, these dynamics or aggressiveness is almost a need. Attrition wear in certain materials such as granite is a very slow process that would need much longer tests, which would probably lack the convenience that represents having a quick, easy and economical filter of aggregates, such as Micro-Deval.

On the other hand, it is clear that loads and conditions within the test are considerably different from those in the railway track. We need to be aware that we are not testing grains in anything similar to the conditions that they will need to suffer during their lifespan. Grains in

the Micro-Deval wear all around their surface while in the track they find themselves blocked by the neighbour grains, only having contacts at specific areas. Intuitively, Micro-Deval is more similar to the tamping operation, where ballast is mixed dynamically with relative freedom to move. During tamping, not only the fast penetration of the tines produces wear, but also friction and impacts between grains happen during the vibration. In addition, tamping rearranges grains changing the contact points, so that wear will be produced over other areas of the grain surface.

In conclusion, Micro-Deval represents an appropriate control test for testing the resistance material thanks to its repeatability, its economic cost and because it can be quickly performed in the quarry before delivering the ballast. It is true, impacts are involved but attrition is still a relevant mechanism involved. This is an understandable and coherent compromise to be able to wear high-resistance materials in a relatively short time. However, we should keep in mind that we are not only testing attrition resistance.

Finally, we cannot expect to directly link the Micro-Deval coefficient with the future behaviour of the sample in the track. It serves as a filter or as a classification method, but conditions in the track are so different that a more complex model needs to be applied in order to accurately predict wear and so lifespan of ballast.

2.7 CONCLUSIONS

In this chapter we have studied in detail the most used test in the railway industry when assessing the resistance of aggregates to friction wear. The main two goals of this chapter were to discuss the suitability of this test as an attrition test for railway ballast and to take profit of the simplicity of the system to use it as a tool to link experimental and numerical results.

The deep analysis of the test helped to better understand the mechanisms involved within the drum, which is already an innovative study in the literature. Attrition happens to be one of the main generators of wear but not the only one. The fast rotation of the drum leads to grains impacting the opposite wall after a free fall phase. These impacts result in the strongest contact forces of the system, presumably being the main responsible of the eventual major breakages of the grains.

Due to the homogeneity of the system, all grains are subjected to approximately the same contact forces and friction work. This leads to a global linear evolution of friction energy in the system.

Experimental tests stopping the machine at different intervals helped us to track the mass of the sample all along the test. This showed a clear behaviour in two phases on all the samples. First, grains show a faster and more aggressive degradation due to probably the presence of weak features, such as small vertexes or very sharp edges, which break or erode fast. After the first half of the test, degradation becomes a more stable process, following an almost linear production of fines. The processes explaining these phases at the scale of the grain will be studied in the next chapter.

The presence of water in the drum appeared to be critical for the accelerated degradation. Samples in which water was added produced almost double amount of fines than samples tested in dry conditions. This could be due to the washing effect of water, removing the protection layer that fine particles create around the grains when they get stuck to them. In the track, rain water can wash grains in the same way, especially the area surrounding a contact and pushing the fines towards the lower-part of the layer. However, contacts between grains in the track are tighter and remain for a longer time, preserving the contact interface from accumulating enough fines to create a protection layer, but also from water to remove the fines that may get trapped inside. Thus, the washing effect of water in the track will be presumably less important than in the Micro-Deval. The effect of water in cyclic shearing between two grains will be studied in section 4. 6.

On the other hand, the chemical effect of water was discarded, at least for a relatively short-term exposition of the grains to water like in the Micro-Deval, since no significant differences in the results of the tests were observed when the samples were left in water for hours or days. This is also the normal case of railway tracks: rainfall water is quickly filtered to the ground and grains generally dry fast after rain episodes. However, when fines accumulate, the track lose its draining capacity, letting water to stay longer in the ballast layer and, along with low temperatures, can result in a problem for ballast especially due to freeze-thaw cycles.

Finally, we used Archard model to link experimental and numerical results. The linear phase of the degradation process observed experimentally is coherent with the linear evolution of the friction work observed in the simulations. Both results have been put together in order to estimate the Archard wear coefficient for the specific case of the Micro-Deval test. The calculation showed a combined coefficient K (being $K = k / H$) of $1.8 \cdot 10^{-9} \text{ Pa}^{-1}$, which is a significantly high value. This was not actually a surprise, since impacts play indeed an important role inside the cylinder and major breakages can also occur. These two related mechanisms are very aggressive, much more than attrition wear. However, the results of Archard coefficient in Micro-Deval test need to be taken cautiously, since this model was not conceived to predict wear due to impacts and could not be accurate enough.

III. EVOLUTION OF MORPHOLOGY

3. 1	Introduction.....	64
3. 2	Morphology indicators	64
	3. 2. 1 General shape parameters	65
	3. 2. 2 Spherical harmonics series (SHS)	66
	3. 2. 3 Curvature	68
3. 3	X-ray tomography	68
	3. 3. 1 Generalities	68
	3. 3. 2 Test procedure	69
	3. 3. 3 Samples	71
3. 4	Evolution of scalar parameters	73
	3. 4. 1 Grain descriptors	74
	3. 4. 2 Shape parameters	77
	3. 4. 3 SHS analysis	78
	3. 4. 4 Summary	80
3. 5	Curvature analysis.....	81
	3. 5. 1 Curvature filter scale	82
	3. 5. 2 Evolution of the asperity radii	83
	3. 5. 3 Link between asperity radii and wear	89
3. 6	Morphology evolution on the track	91
3. 7	Conclusions.....	93

3.1 INTRODUCTION

As we have seen in the previous chapter, Micro-Deval test is not only a way to assess the resistance of the material to abrasion, but also an accelerated way to obtain worn ballast grains, which morphological characteristics do not differ in excess from those grains at the end of their lifespan in the railway track.

During the stops performed along the test, one could notice in a qualitative way, both visually and feeling the roughness of the grains, that ballast aggregates lose their texture considerably fast during the first minutes of the test. Edges and vertexes are progressively being smoothed along the full test, while the general shape is not substantially changed.

Due to the characteristics of the Micro-Deval device, it is possible to identify and recover from the sample an arbitrary amount of grains. This way, using a 3D imaging device such as X-ray tomography, it is possible to track the evolution of the morphology and to understand how the matter is lost all around the grains.

This knowledge complements the general result of production of fines given by the attrition test, giving a closer look to wear at the grain scale and making it possible to identify the different mechanisms involved in this loss of matter.

3.2 MORPHOLOGY INDICATORS

In order to describe the morphology of a particle, there is a large number of quantities, parameters and definitions used in the literature. Implicitly or explicitly, most of these parameters characterizing the morphology are classified or ordered using different levels or scales, depending on how general or how in detail the parameter describes the grain. For example, some authors [103] divide this classification into three different levels: shape (macro-scale), angularity (meso-scale) and texture (micro-scale).

At large scales, sphericity, elongation and flatness are usually used to provide a general idea of the grain shape. The intermediate scale is focused on describing the roundness of the grain, i.e. how sharp are the angles and borders, and it is usually described using the opposite parameter: angularity. Finally, in order to describe the micro-scale features on aggregates, the main parameter to define the surface texture is roughness, usually given by different scalar parameters.

In the section below, we will briefly define the parameters that have been considered and calculated for this project. They correspond to an arbitrary selection, following a previous work summarized in the Master thesis [98, 97]. In the end, the choice of the parameters is not that important for us, as far as they allow us to have an idea of the evolution of the morphology at all the scales.

3.2.1 General shape parameters

The typical way of describing the general shape of a grain is by defining its three characteristic lengths, which are given by inscribing the grain into a rectangular prism (Figure 3.1). The lengths correspond then to the sides of that cuboid: S (shortest), I (intermediate) and L (longest). There are multiple ways of choosing the circumscribing prism that will give slightly different results. The method we have applied in this project defines the three sides of the prism as the longest distances following the three principal directions of inertia of the grain.

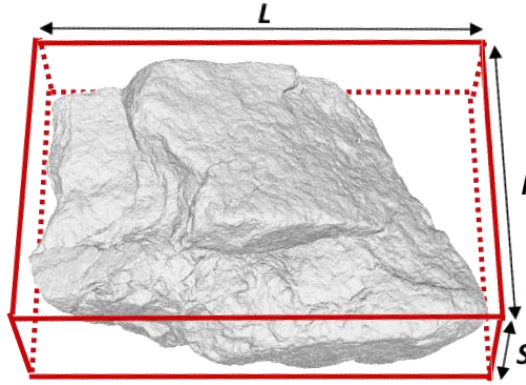


Figure 3.1 Definition of the characteristic lengths using a circumscribed prism.

Using these three characteristic lengths, several parameters can be defined as different aspect ratios, so that they define different features of the general shape [104, 105]:

$$\text{Sphericity } (\Psi) = \sqrt[3]{\frac{S \cdot I}{L^2}} \quad (3.10)$$

$$\text{Elongation ratio } (ER) = \frac{I}{L} \quad (3.11)$$

$$\text{Flatness ratio } (FR) = \frac{S}{I} \quad (3.12)$$

$$\text{Flatness - elongation } (FE) = \frac{L}{S} \quad (3.13)$$

$$\text{Shape factor } (SF) = \frac{FR}{ER} \quad (3.14)$$

$$\text{Shape factor Barksdale } (SF_{Bark}) = \frac{S}{\sqrt{L \cdot I}} \quad (3.15)$$

According to the presented definitions, the first three parameters, along with the proposed definition of the Shape Factor by Barksdale, range from 0 to 1, the latter value corresponding to the case of either a sphere or a cube. The other two parameters also have a value of 1 in the case of cubes or spheres, but while the SF is always equal or higher than one by definition, FE can take either values higher or smaller than 1.

Using the parameters ER and FR , Zingg [106] proposed a basic classification of aggregates establishing four different categories depending on a fixed threshold: blades, rods, disks and spheroids. This classification and definition of the different categories is usually presented in the form of a diagram (Zingg's diagram) that is shown in Figure 3.2 and for our grains in the corresponding section of results.

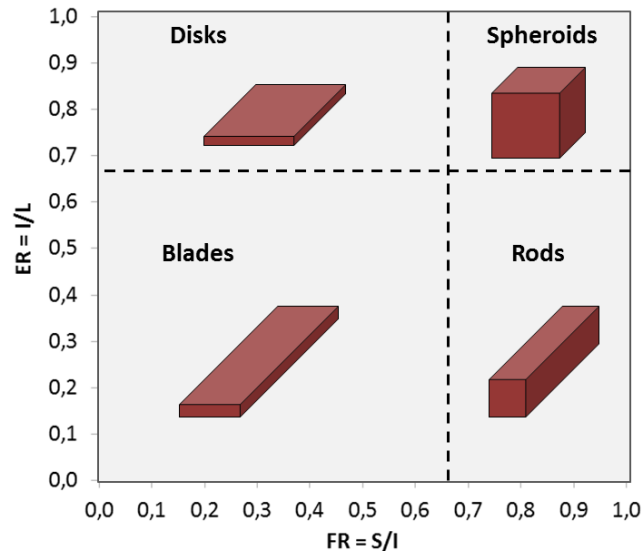


Figure 3.2 Zingg's diagram.

3. 2. 2 Spherical harmonics series (SHS)

All the previous scalar parameters can only describe the general shape of the grain and do not offer any information about the smaller scales such as angularity or texture.

When a multi-scale description of the morphology is needed, other methods that can deal with all three levels of description are commonly used. Fourier analysis of the contour can be used when dealing with 2D particles [107], obtaining different signatures for different scales depending on the frequency. If a 3D description is needed there are two methods that can be used to analyse image data: wavelet method [108] and spherical harmonic analysis [109]. The second method has been chosen for this project since it was also used to deal with 3D X-ray tomography data in the original paper.

The data given by an imaging device such as X-ray tomography, once it has been filtered and the grain has been isolated, can be expressed as a discrete cloud of points. It is then possible to express the coordinates of all points forming the contour surface of the grain using spherical coordinates on the form $R(\theta, \phi)$, where R is the radial distance from the centre of mass to a surface point, $\theta \in [0, \pi]$ is the polar coordinate and $\phi \in [0, 2\pi)$. The idea of this method is to describe the morphology of the grain using spherical harmonic series, where as we consider more and more coefficients (longer series), the detail of the description gets higher, identifying different signatures for the different scales: shape, angularity and texture.

The series are expressed as:

$$R(\theta, \phi) = \sum_{n=0}^{\infty} \sum_{m=-n}^n a_{nm} \cdot Y_n^m(\theta, \phi) \quad (3.16)$$

Where Y_n^m are the spherical harmonic functions:

$$Y_n^m(\theta, \phi) = \sqrt{\frac{(2n+1) \cdot (n-m)!}{4\pi \cdot (n+m)!}} \cdot P_n^m(\cos(\theta)) \cdot e^{im\phi} \quad (3.17)$$

Where P_n^m are the associated Legendre polynomials. The system can then be solved using a matrix notation of the form $R_{(N \times L)} = Y_{(N \times L)} \times a_{(L \times 1)}$ [110], where $L = (n_{\max} + 1)^2$ and N the number of voxels of the surface. The quantification of form (or general shape), angularity and surface texture is based on the signatures given by the coefficients a_{nm} , and using the thresholds proposed by Masad et al. [111]:

$$Form = \sum_{n=1}^4 \sum_{m=-n}^n |a_{nm}| \quad (3.18)$$

$$Angularity = \sum_{n=5}^{25} \sum_{m=-n}^n |a_{nm}| \quad (3.19)$$

$$Texture = \sum_{n=26}^{n_{\max}} \sum_{m=-n}^n |a_{nm}| \quad (3.20)$$

As a benchmark, some reference values for regular shapes, along with the average value for the studied ballast grains (before erosion) are presented below:

	Sphere	Cube	Tetrahedron	Dodecahedron	New ballast grain (average)
Form	0.000	0.194	0.004	0.000	0.697
Angularity	0.000	0.278	0.307	0.287	0.742
Texture	0.000	0.031	0.042	0.030	0.075

Table 3.1 Benchmark for SHS analysis.

Except for ballast grains, all presented polyhedrons are regular, not elongated nor flat, so their general shapes do not differ too much from that of a sphere. More irregular shapes like ballast grains will present values closer or even higher than 1 for the form signature. On the other hand, in these examples angularity is not so similar to that of a sphere, but still, due to their perfectly flat faces, they do not show high values. Again, ballast grains obtain larger values around 0.7. Finally, texture has always lower values than the other two signatures, but we can still see a difference between regular polyhedrons and ballast grains. It is important to remark that the angles of the regular shapes also affect the texture value. This is so because, in the

end, the threshold between signatures is just an arbitrary coefficient of the harmonic series, i.e. an artificial border in a continuously decreasing scale, so it is not surprising that all signatures are, in a higher or lower level, affected by all changes in the morphology.

In conclusion, even if it is not always very obvious in this benchmark, higher values indicate how far the studied morphology is from that of a sphere. It has also been seen in the examples that these parameters are hard to interpret when trying to compare very different shapes. However, it is indeed a very useful method when comparing a shape with a slight variation of itself, like comparing the same ballast grain between different states of erosion.

3. 2. 3 Curvature

The last parameter that we will discuss during this morphology analysis will be curvature. Curvature can be defined as the inverse of the radius of the best-fitting sphere at each point of the surface. By definition, this parameter is not inherent to the full grain but it is locally calculated all around the surface. It is then a micro-scale parameter, not related to the general shape, but to angularity and to roughness. It will be used in order to have a more detailed analysis of the evolution of the asperities of the grain and their contribution to the general wear.

There are several methods to calculate the curvature in a mesh. Since we have used MeshLab as the software to manage the different meshes, we have chosen for this project an already implemented method in the program called Algebraic Point Set Surfaces or APSS [112]. This algorithm shows robustness and a good fit to the actual shape. It has the additional advantage to add a filter scale that will allow us to take into account the neighbour areas when computing the curvature. The introduced scale will thus affect the radius of surrounding area that will be considered, depending on the detail we would like to acquire from the analysis. More information and some examples will be shown at section 3. 5. 1.

Finally, even if the value given by the program is curvature, in most of the cases we will be talking about the inverse: asperity radius. The reason is just because we consider it more intuitive to understand and to visualize.

3. 3 X-RAY TOMOGRAPHY

3. 3. 1 Generalities

Due to its availability in the laboratory, the imaging device chosen to obtain a 3D model of the ballast grains has been X-ray Computed Tomography (CT). The idea of these scans is to track the evolution of the shape of a sample of grains that will be progressively worn using the Micro-Deval device.

This X-ray CT technology is used in several domains of science such as medicine, properties of

materials, soil behaviour, etc. During a CT slice, an X-ray source emits rays towards the sample having a detector screen on the opposite side. The density of the material through which the X-rays have to pass will determine the grey scale on the output image [113, 114].

If we take several slices of the sample at different angles, an algorithm makes it possible to combine them to create a 3D image. In the tomography device of the laboratory, the source and the detector remain static during the imaging, while it is the sample that turns to complete a full 360° rotation (Figure 3.3).

The resolution of the image will depend on several factors such as the size of the sample, the desired level of zoom or the amount of slices to take (which will of course increase the time of the test). The resolution chosen for this project is 50 μm / voxel, which is high enough to describe all the features of the surface of ballast grains and low enough to be able to scan up to seven grains in a single day. The reconstruction of each grain is then performed using 1 440 projections per full tomography.

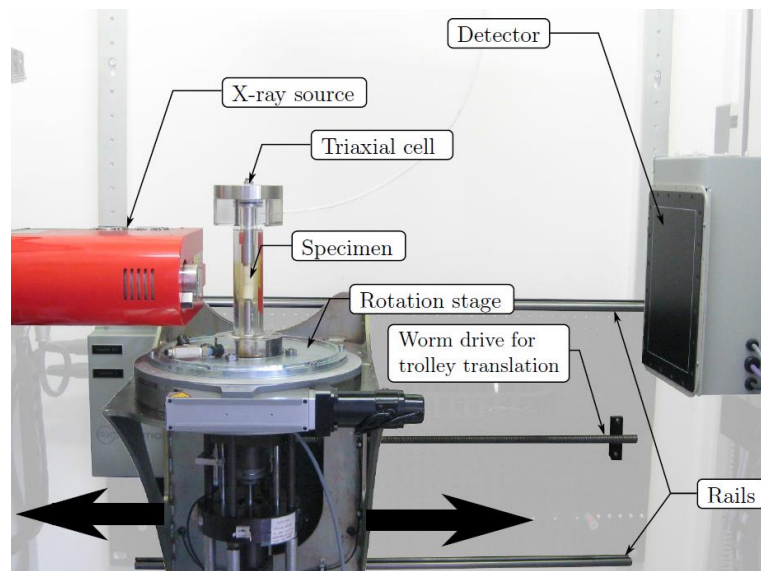


Figure 3.3 Operational diagram of the X-ray tomography device [113]. The source along with the detector film on the opposite side takes sectional images of the sample placed on a rotating stage allowing a complete 360° turn.

The main potential of tomography is to study the inner part of the materials. Thanks to X-rays, it is possible to see cracks, pores and heterogeneities of the grain. However, this information, although interesting, is not directly relevant for this project, so a post-processing step will be necessary in order to extract only the surface voxels of the grain.

3.3.2 Test procedure

In this analysis we will take profit of the possibility to stop the Micro-Deval device at different stages to recover a sample, consisting always of the same grains, in order to follow the evolution of the morphology due to the wear process occurring within the attrition test.

A total of seven different HSL ballast grains with different shapes and apparent colours were

chosen to define the sample of study (more details of the particular grains in the next section). These grains were numbered with a marker on one of their faces to be able to identify them among the full test sample.

Micro-Deval

The Micro-Deval test was performed using the same specifications as in Chapter II, in dry conditions and removing the fines after each stop. Thus following the European standards [29, 25], along with the seven grains for the analysis, more grains were randomly selected to complete a 10 kg sample. This sample, initially formed by 92 grains (94 after the first cycle because of two major breakages), was also weighted at every stage to complement the analysis and to compare with the other tests previously performed.

We have already observed how wear in the Micro-Deval is not constant along time. It is faster at the beginning and it tends to a constant regime by half the test. Hence the stops were not programmed at constant intervals as last time, but at incremental intervals corresponding to a cumulated time of test of 10, 30, 70 and 140 minutes. If we add a tomography scan of the grains before any erosion, a total of 5 scans per grain have been performed.

After each cycle, the grains were cleaned using water and dried. The full sample was then weighted and the selected grains were separated to be scanned. Since the matter lost on the faces is significantly lower than on the edges and vertexes, the marked numbers were never completely erased from the surface, so it was always possible to identify the seven grains.

Imaging and post-processing

During the scanning time, the ballast grain needs to stand in a fixed position in front of the X-ray source. The sample will be located on a rotating disc, so it needs to be fixed somehow to a support so that this rotation does not change the position of the grain within the system support – sample. In addition and as we have seen, the density of X-rays reaching the detector on the other side of the sample will depend mostly on the density of the material they need to pass through. Thus, in order to obtain a clean image of the grain, it is necessary to choose low-density materials for that basis, in opposition to the high density of granite, in order to have enough contrast to isolate the grain from the support in the post-processing.

With these constraints, two solutions have been used, the 2nd one being more effective and thus used from then on. The 1st idea was to directly fix the grain to an EPS foam basis with play dough and tape (Figure 3.4a). It was a simple method that allowed for positioning the grain in the desired position. We performed some of the first scans with this method but we realized that the contrast between the play dough and the granite, even if different, was not high enough and sometimes the isolation was not easy. For this reason, some of the first scans have some surface noise at the face where the grain was standing on. The 2nd solution was to put the grain in a plastic vase locking its movement with EPS pieces, trying that the grain did not touch the vase (Figure 3.4b). This solution was more restrictive in the positioning of the grain, but in the end it became much better than the first one in order to isolate the grain afterwards.

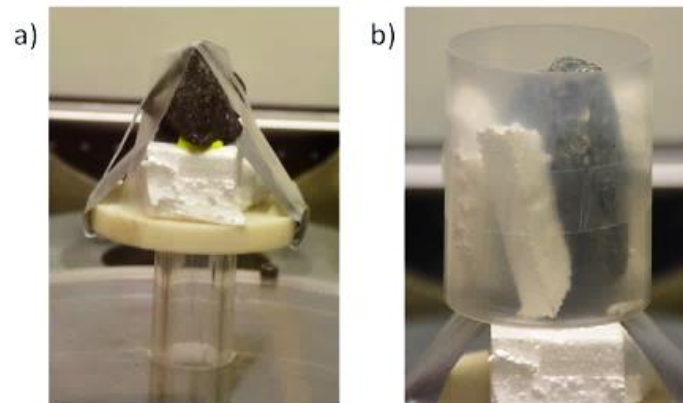


Figure 3.4 Solutions to fix the ballast grain to the rotating disk of the tomography device.

Once the settings of the device are introduced, the tomography can start, taking a bit less than one hour per grain with this set up.



After the scan, the software XAct takes all the slices and makes a first reconstruction of the sample. From this first approach, we can correct some geometry issues, either external (e.g. the sample slightly moving during the scan can be corrected using some reference images) or inherent to the apparatus (e.g. tilt, offsets, etc.). Afterwards, it is necessary to select the correct range of grey values from the image histogram, so that we only select the grey scale within the grain is located. This way we delete all the support elements and, of course, the surrounding air. Finally, we crop the image from useless information in order to reduce its final size and we proceed to reconstruct the volume. In our case, since we are only interested in the surface, once the volume is reconstructed, we can select a grey threshold determining the surface and we can save that contour as an STL file in the form of a 3D mesh.



3.3.3 Samples



Seven granite grains were chosen from a big bag of HSL ballast, trying to select a good variety of shapes and also of granite colours. All grains in the analysis are slightly bigger than the average in order to identify more features and changes in the morphology. As a reference value, the average grain mass for all the samples tested in the Micro-Deval is about 100 g / grain (i.e. samples of 10 kg composed of around 100 grains every time).


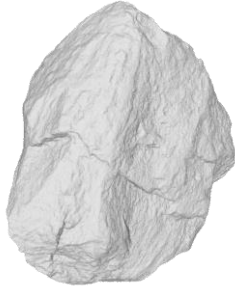
The following Table 3.2 gives a summary card for each grain at its initial state before erosion. The provided information in each card is:



- The approximate colour of the grain.
- The initial mass and volume (and so, the density).
- The three characteristic lengths and its classification in Zingg's diagram as described in section 3.2.1.
- A photo of the grain.
- A render from the tomography data (not necessarily from the same perspective).

		S1	
Colour	Dark		
Initial mass	146.13 g		
Initial volume	54162 mm ³		
Density	2698 kg / m ³		
L	86.98 mm		
I	47.10 mm		
S	42.84 mm		
Zingg classification	Rod		

		S2	
Colour	Grey		
Initial mass	142.64 g		
Initial volume	53705 mm ³		
Density	2656 kg / m ³		
L	63.80 mm		
I	53.31 mm		
S	47.61 mm		
Zingg classification	Spheroid		

		S3	
Colour	Grey		
Initial mass	126.55 g		
Initial volume	47629 mm ³		
Density	2657 kg / m ³		
L	78.86 mm		
I	46.90 mm		
S	33.38 mm		
Zingg classification	Rod		

		S4	
Colour	Dark grey		
Initial mass	155.70 g		
Initial volume	57903 mm ³		
Density	2689 kg / m ³		
L	79.92 mm		
I	69.56 mm		
S	28.49 mm		
Zingg classification	Disk		

		S5	
Colour	Light grey		
Initial mass	179.95 g		
Initial volume	69052 mm ³		
Density	2606 kg / m ³		
L	82.69 mm		
I	50.58 mm		
S	44.93 mm		
Zingg classification	Rod		





		S6	
Colour	Grey		
Initial mass	148.08 g		
Initial volume	56155 mm ³		
Density	2637 kg / m ³		
L	83.75 mm		
I	57.20 mm		
S	33.19 mm		
Zingg classification	Disk		
		S7	
Colour	Light grey		
Initial mass	103.71 g		
Initial volume	39584 mm ³		
Density	2620 kg / m ³		
L	64.63 mm		
I	48.49 mm		
S	32.34 mm		
Zingg classification	Spheroid		

Table 3.2 Summary of the seven samples.

All grains have a unique characteristic: S1 is the darkest and densest; S2 has a particularly rounded shape from the beginning; S3 is elongated and pointy; S4 is like a disk; S5 is quite porous and a bit reddish; S6 has a particular step-shaped feature on one of the faces and S7 is the smallest one by difference.

As a curiosity, the intrinsic heterogeneities of the composition of granite provide different colours and also slight differences in the densities: darkest grains are slightly denser than lighter ones.

These seven samples were mixed with 85 more grains in order to complete the 92 grain-sample conforming the required 10 kg.

In the next sections, the results of the morphology analysis will be presented into two big blocks: first the evolution of scalar parameters describing grain morphology (shape parameters and the SHS analysis) and secondly a much more detailed analysis on the evolution of the asperities and their contribution to wear using the local curvature.

3. 4 EVOLUTION OF SCALAR PARAMETERS

As we know both intuitively and thanks to our previous Micro-Deval experience, grains change shape during the wear process: surfaces become smoother, roughness is lost and angles are progressively rounded. Figure 3.5 shows the scan of the grain S6 new and after 140 minutes of Micro-Deval. The differences are evident, presenting all the changes described above. All grains

followed a similar evolution but S6 is a particular case since it also suffered some relatively big breakages losing some of the tips. Even so, the general shape of the grain was kept during the process, remaining visually recognisable even after erosion.

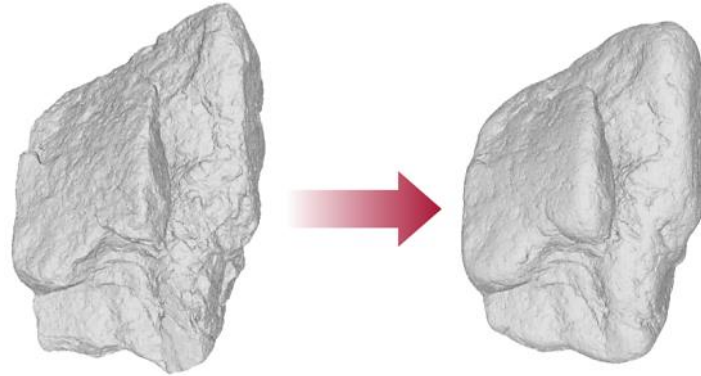


Figure 3.5 Evolution of sample S6 after a full Micro-Deval test: surface texture is almost gone, sharp edges have become much more rounded and weaker parts of the grain have broken apart.

3. 4. 1 Grain descriptors

We consider as grain descriptors the basic values describing the grains, before any interpretation of them is made, i.e. the raw data of the grain. These are basically the ones included in the summary cards of the sample: the mass and the three characteristic lengths.

Mass

The first and more obvious consequence of wear, by definition, is the loss of mass and volume of the body due to the loss of matter through erosion or breakages. As we saw in the Micro-Deval chapter, this loss of mass is not constant in time along the test, being the first half of the test more aggressive than the second. This tendency was however an average over a sample formed of around 100 grains. At the grain scale, local phenomena may happen: breakages, sharper edges, weak parts, rougher faces, particular shapes, etc. could affect the amount of wear sustained by a grain, and could also create a big variability among the sample.

Figure 3.6 shows different mechanisms suffered by sample S4 during the full Micro-Deval test that contributed to the total loss of mass of the grain, i.e. it represents the total wear produced on the grain after all the stops. The first thing we can notice is that the distribution of wear over the grain is not uniform at all. Convex edges and tips, especially the sharpest ones, are more exposed to a probable contact with other grains or with the cylinder. This makes these parts of the grain considerably more vulnerable to wear. Very sharp or isolated tips often represent, as well, weak parts that can be easily torn apart. In the figure, tips marked with a “1” represent parts that were crushed in a single cycle of erosion, while parts marked with a “2” represent edges or tips that were progressively eroded all along the test. Finally, surface texture, marked with a “3”, is also a source of wear especially during the first half of the test. After these first minutes, roughness is almost gone, leaving behind a smooth surface which will still be eroded but much more slowly.

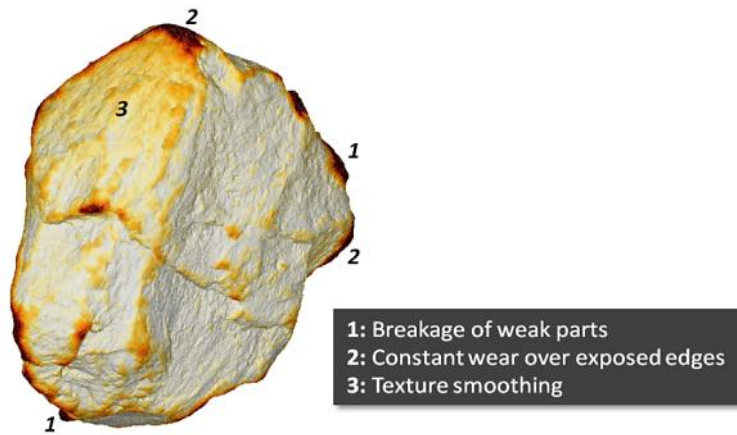


Figure 3.6 Wear mechanisms of sample S4. The image was built comparing the scan of the grain when it was new with the scan at the end of the 140 minutes of Micro-Deval. The colours are represented over the scan of the grain when it was new, the darkest colour representing 1 mm or more of wear.

Figure 3 7 shows the evolution, in percentage, of the mass of each grain along the test. The evolution of the mass of the full 10 kg sample has been added as a reference.

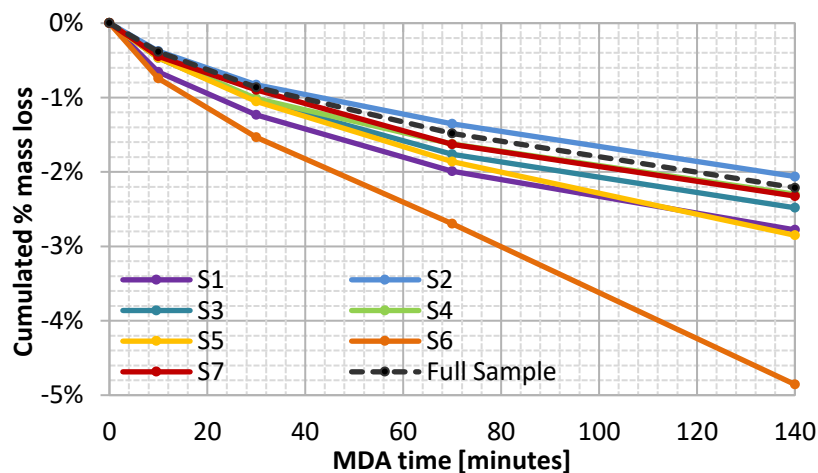


Figure 3 7 Evolution of the mass of each sample in percentage with respect to the initial mass.

The first thing we can notice is that all grains have a higher loss rate at the beginning of the test and it tends to a constant rate by the end. This is the same tendency already observed in all previous Micro-Deval tests. Except S6, which suffered some relatively big breakages all along the test, all other samples follow more or less the same tendency, losing slightly more percentage of matter than the full sample but in the same order of magnitude. This proves that the curves observed in the last chapter were not only an average result over a high variability among grains, but the grains, individually, also behave more or less in the same way.

The particular shape of each grain does not seem to affect significantly the final amount of wear. All grains lose between 2% and 3% of their mass (except S6). It is true that S2, which presents the most “rounded” shape from the beginning, is the one to lose less matter, but the difference is not actually significant. The large size of the grains is related to a higher probability of eventual weaker parts, which could explain why all of them are slightly above the average wear of the sample, but again the difference is neither significant nor concluding.

Characteristic lengths

The same way as it happens with the mass, by definition the three characteristic lengths can only shrink over time. At least, this happens if we keep the same directions over time. However, the way we have defined them allow for eventual, although unlikely, increases in the lengths. The reason is that the lengths are computed as the maximum length along the three principal directions of inertia, which may change over time especially if big breakages alter considerably the general shape. Even so, our sampled grains did not suffer major breakages and even S6 did not see its shape altered significantly. Thus their principal axis of inertia remained almost constant over the test and the three characteristic lengths were computed all the time over almost the same directions.

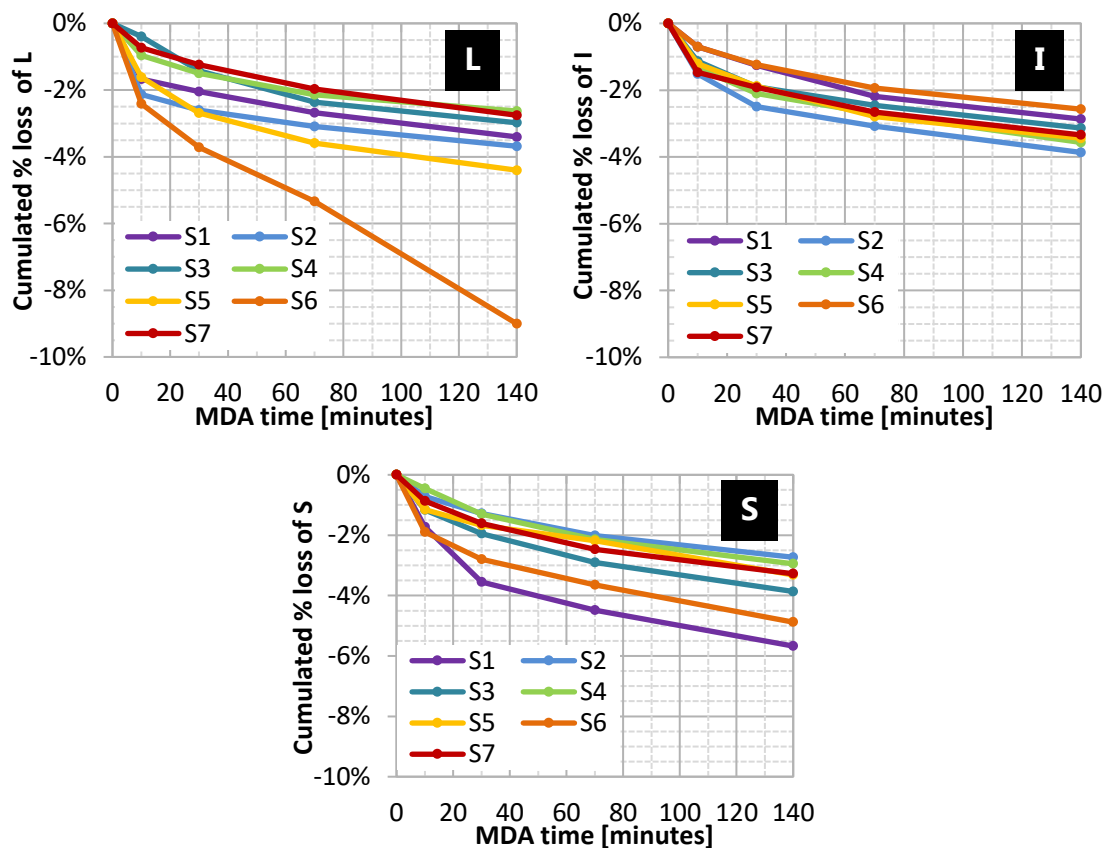


Figure 3.8 Evolution in percentage of L (upper-right), I (upper-left) and S (below) for all seven samples.

Figure 3.8 shows the evolution in percentage of all three characteristic lengths for each grain. The tendency of them is similar to that seen for the mass, presenting a higher loss rate at the beginning of the test and a total loss between 3% and 5%. It is interesting to see that the big breakages of grain S6 affect mainly the longest length *L*, which is not surprising since it is more likely to have a weak tip on one of the extremes of the longest axis.

In conclusion, all three lengths are shortened as expected, faster at the beginning of the test, but this decrease is not big since the general shape is not actually changed that much. When comparing the three lengths for each individual grain, we don't find any particular trend. Depending on where the weaker parts are, the grain will lose a bit more of *L*, *I* or *S*.

This gives a hint of what will happen with the associated shape parameters, most of them direct ratios of these lengths. We can expect only slight changes of them, most of them occurring at the beginning of the test, and for some grains they will decrease while for others they will increase, with no particular tendency.

3.4.2 Shape parameters

Intuition would say that, with enough time, wear will provoke grains tending to the shape of a sphere, as it happens for example with pebbles in the rivers. By definition of all six shape parameters presented before, the value for a sphere is always 1, so we could imagine all grains getting closer to a value of 1 for all of them.

However, the reality is that Micro-Deval test is not long enough to produce significant changes in the shape, at least for a resistant material like granite. In fact, even in the track, ballast grains are substituted much before reaching ellipsoidal grains. Therefore we cannot expect to observe clear evolutions regarding shape descriptors. In fact, what can be actually observed is much more similar to what was suspected by the end of the last section.

In order to summarize all six parameters, and taking into account the exposed above, we will focus the effort on the absolute distance of each parameter with respect to the value of 1 (sphere). The percentage increment of each parameter X is then given by the expression:

$$\Delta X = \frac{|1 - X_F| - |1 - X_0|}{|1 - X_0|} \cdot 100 = \left(\left| \frac{1 - X_F}{1 - X_0} \right| - 1 \right) \cdot 100 \quad (3.21)$$

Where X_0 and X_F are the values of the parameter X before erosion and at the end of the Micro-Deval test. This way we can normalize the evolution of all descriptors, since we would expect all of them always tending to get closer to 1. Table 3.3 shows how this distance to the shape of a sphere increases or decreases, in percentage, for each grain between the start and the end of the test. The average of all seven grains has been added as extra information.

	S1	S2	S3	S4	S5	S6	S7	Average
ER	-0.66%	0.95%	0.23%	6.47%	-1.58%	-15.23%	1.81%	-1.14%
FR	29.05%	-9.85%	1.86%	-0.44%	-1.02%	3.28%	-0.13%	3.25%
FE	4.74%	-3.86%	1.60%	0.51%	-2.46%	-7.18%	1.08%	-0.79%
SF	-8.47%	21.27%	-3.62%	-1.44%	-2.79%	49.80%	-5.39%	7.05%
SF _{Bark}	5.30%	-4.82%	1.01%	-0.10%	-1.44%	-0.94%	0.32%	-0.09%
Ψ	1.09%	-1.56%	0.61%	0.90%	-1.61%	-7.01%	0.99%	-0.94%

Table 3.3 Increase or decrease of the absolute value of the distance of each parameter to the value of 1 (sphere), between the grain new (before the test) and at the end of the full Micro-Deval test (140 min).

Looking at the table we can see that only S5 shows a tendency towards 1 for all six shape parameters. However, the approach to a sphere is very slight (less than 3% after the full test), so it could actually be just a coincidence, especially when observing the behavior of all the other samples. Grains like S1, for example, are far from the expected evolution, presenting

some parameters like FR with values almost 30% further from 1 at the end of the test than when the grain was new. In summary, changes in shape descriptors are in general relatively small, and they do not follow a particular tendency.

This is very well seen in the Zingg's diagram in Figure 3.9, where we can see the parameters FR and ER are reported in the same plot. The diagram is divided in four categories proposed by Zingg with a threshold value of $2/3$ for both parameters. A sphere or a cube would represent the upper-right corner with a value of 1 for both parameters. As it can be observed, grains are quite static during the Micro-Deval test, and only two grains (S1 and S6) show a slight evolution due to some breakages. However, not even these two grains present a change in class, and they do not tend at all to the shape of a sphere.

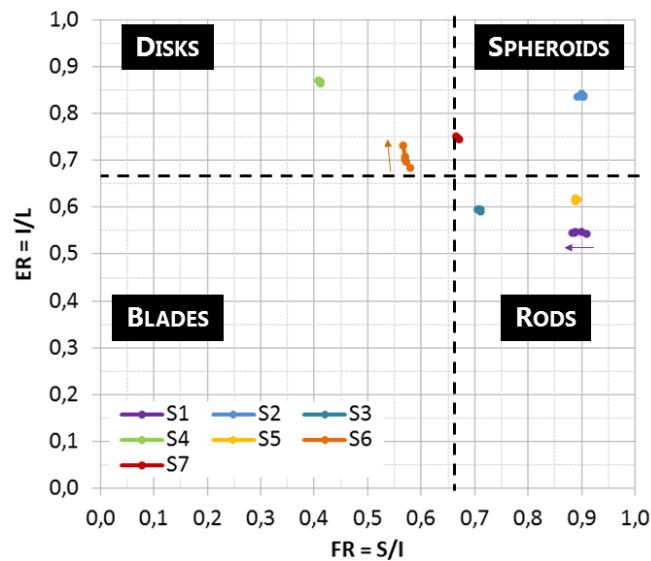


Figure 3.9 Zingg's diagram for all grains and their evolution during the Micro-Deval test.

3.4.3 SHS analysis

Before presenting the results of the parameters related to the Spherical Harmonic Series, some considerations need to be described, which were necessary in order to be able to compute the series. Due to their intrinsic definition, the development of these series quickly requires a large amount of memory in the computer, as well as computational time. The total amount of coefficients a_{nm} will directly depend on the maximum n we would like to compute, the total number of coefficients being equal to $L = (1+n_{max})^2$. The matrix Y_{nm} will then be of size $L \times N$, N being the number of voxels forming the grain surface as explained in section 3.2.2.

Therefore some restrictions had to be introduced, searching for a compromise between the computational time and the precision on the result. For this reason, we took $n_{max} = 30$ following the work of Masad on SHS [111]. This way, we are able to define shape and angularity following the thresholds set at $n=4$ and $n=25$, and there are still five coefficients remaining to give information about texture. Nevertheless, this measure, although necessary, was not enough to deal with the memory issues. Working with a mesh of 5 to 6 million elements (original scans) turned out to be impractical, so a simplification of the meshes was required. The reduction of

elements was made by decimation using an internal algorithm of the software MeshLab called Quadratic Edge Collapse Decimation, which resulted in a very acceptable simplification, preserving all the topological features.

A convergence study was performed on three of the scans of the grains when they were new. Different decimations of the original mesh were performed in order to reduce the amount of vertexes to 5 000, 10 000, 25 000, 50 000, 100 000, 250 000 and 500 000. The series were always calculated up to $n = 30$. Figure 3.10 shows the convergence in the error considering the calculation for 500 000 vertexes as the reference value.

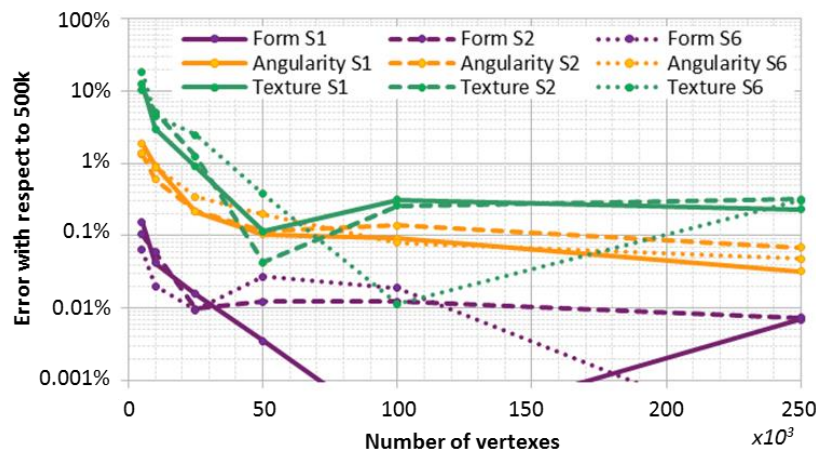


Figure 3.10 Convergence of the error, with respect to the mesh with 500 000 vertexes, for the three SHS signatures of the scans at 0 min of S1, S2 and S6. Be careful with the logarithmic scale of the Y-axis.

As we can observe, with 50 000 vertexes or more the error is stabilized below 1% for all three signatures. It indeed coincides with the visual inspection of the simplified meshes, where simpler meshes fail to represent the smaller details of the texture and the sharpness of the angles, being even possible to distinguish the individual polygons in the meshes with 5k or 10k vertexes. On the other hand, after 25 000 – 50 000 it is not possible anymore to visually distinguish any difference between meshes. After this study, the final meshes for computing SHS are formed by 250 000 vertexes, with an estimated maximum error of $\pm 0.01\%$ for the shape, $\pm 0.06\%$ for the angularity and $\pm 0.30\%$ for the texture, which is perfectly acceptable for the observed evolutions of the signatures.

The three plots of Figure 3.11 show the evolution of all three signatures for each grain (be careful that scales on the y-axis are not the same). The first thing we can observe is that all signatures follow a continuous decrease with a similar behaviour as the descriptors of the grain, with a faster decrease at the beginning of the test and slower by the end. However, the order of magnitude of this decrease is not the same at all for each signature.

Form is the one evolving more similarly to the grain descriptors, losing only between 1% and 2% along the test. Angularity loses a significant 10-15 %, showing the importance of the smoothing of edges and tips in the wear process. In addition, although it is slowed down slightly, this loss is spread all along the test for all grains. Finally, texture signature is reduced between 20 and 40%, most of it during the first half of the test (except samples S5 and S7), proving that surface roughness is generally lost quicker.

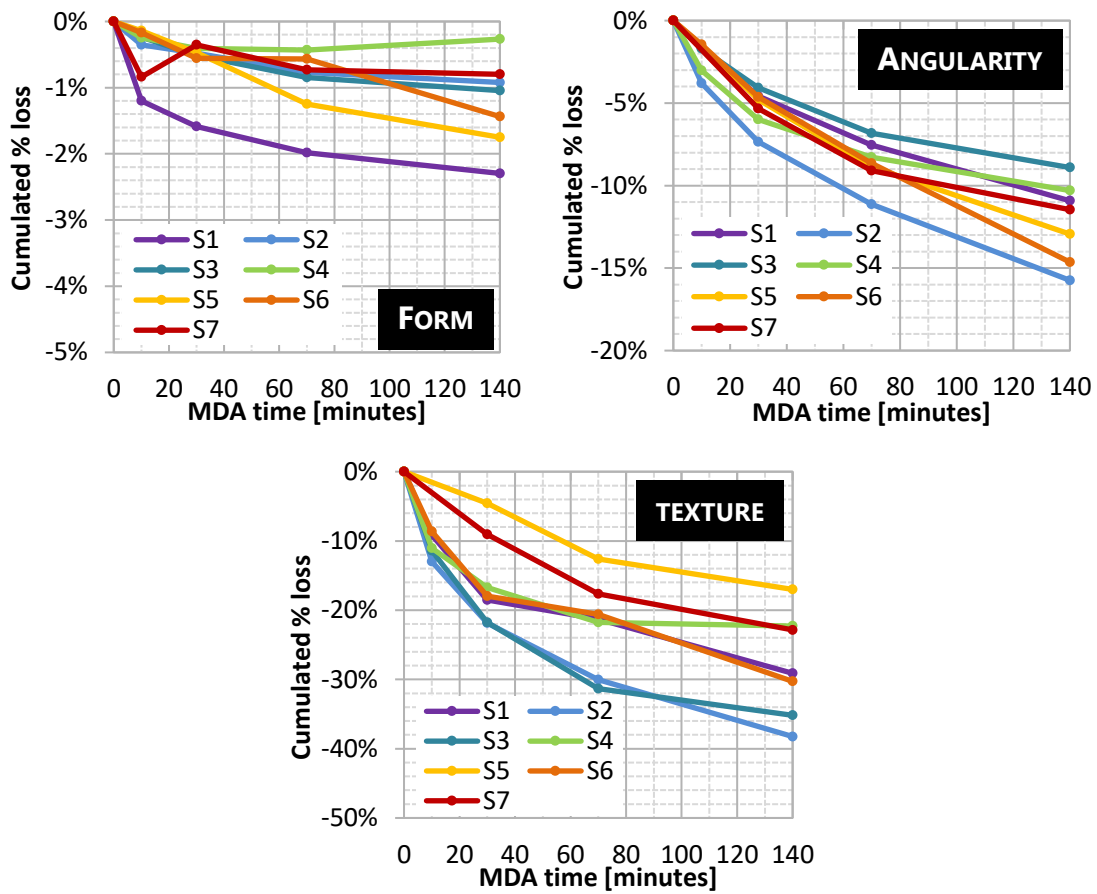


Figure 3.11 Evolution of SHS signatures in cumulated percentage with respect to the initial value.

3. 4. 4 Summary

When comparing all seven grains, the different descriptors evolve in a similar way for all of them. Thus let us do the exercise of plotting together the evolution of all the studied parameters, using the average value for all the grains (Figure 4.11). We have classified the parameters into the three different classes we have divided this study.

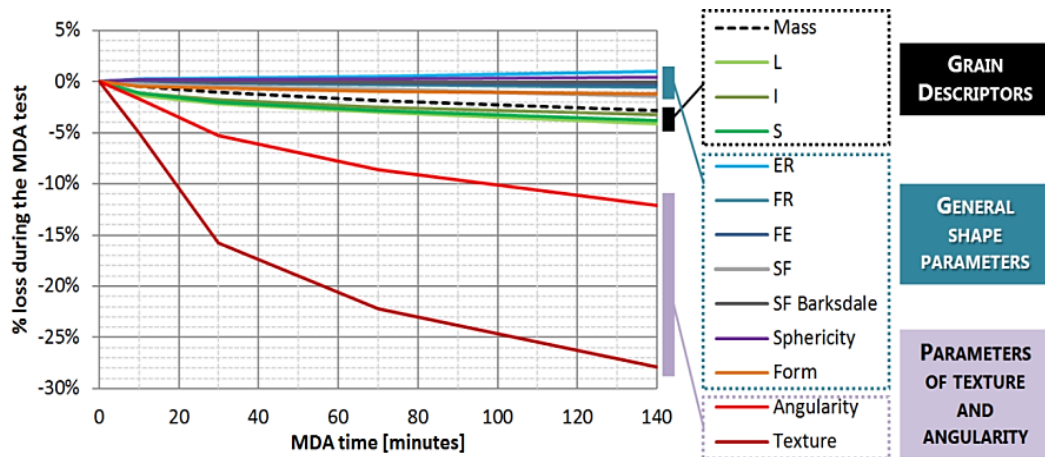


Figure 3.12 Evolution of the average cumulated loss for all the samples of all parameters.

In this section we have seen how the general shape is not changed significantly but parameters regarding angularity and texture do change considerably. This tendency can be clearly seen in the plot. Grain descriptors always decrease but at a very slow pace. General shape parameters almost do not change and, if they do, they do not show any particular tendency. Finally, angularity and texture decrease significantly compared to the other parameters.

Except for eventual major breakages, it is clear that most of wear comes from smoothing edges and vertexes and removing the surface texture. This is not a surprise though and it reaffirms the visual inspection of grain wear: convex features are the most exposed to contacts, thus having to deal with a higher number of them. In addition, tips and sharp edges are usually weak parts of the grains, with smaller cross sections unable to resist aggressive contacts. This hypothesis will be analysed in detail in the next section, where curvature and asperity radius will be locally studied and correlated with grain wear.

3.5 CURVATURE ANALYSIS

As we have seen in the previous section and, as we can observe in Figure 3.13, local curvature (or convexity) and wear seem to be strongly correlated. Convex asperities are very exposed to contacts so they tend to erode faster and deeper. On the other hand, concave parts of the grain are protected by their surroundings so, even if weak, they might not be eroded in the process.

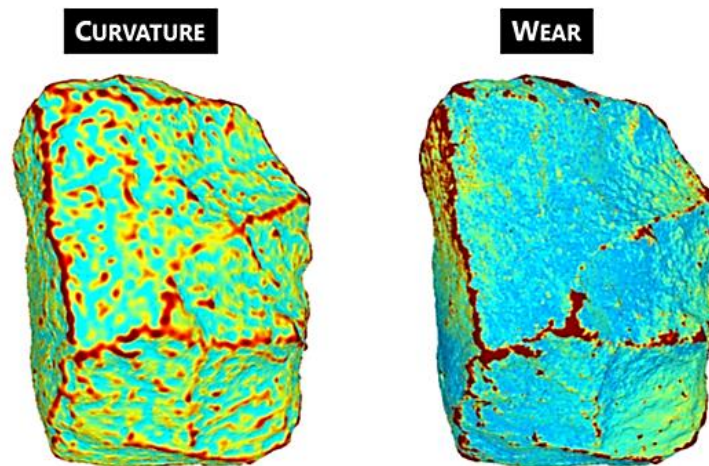


Figure 3.13 Curvature and wear of grain S7. Convexity and degradation are strongly correlated.

For this analysis, curvature will be compared with local wear. In order to compute wear, first of all, all scans of the same grain were prealigned using Python to rotate the meshes and align them with their principal directions of inertia. The centre of mass was set as the origin of coordinates. MeshLab provides an aligning tool that refines and optimizes this prealignment taking into account all five scans of each grain at once. Once the scans have been aligned, meshes have been compared in pairs in order to calculate the difference between them. This difference has been computed using Hausdorff Distance [115], also implemented in MeshLab, which provides a quality map over the surface of one of the two meshes. Thus wear in this

section will be expressed in distance between scans, and not in volume or mass. Finally, this data can be saved in a .ply file that can be treated with Python.

3.5.1 Curvature filter scale

First of all, we need to define what we mean by curvature and, consequently, how it will be computed. Curvature can be theoretically defined as the inverse of the radius, but in a discrete mesh consisting on pointy vertexes, it is required to find the best-fitting sphere for each point in order to compute curvature. This will be performed by the APSS algorithm implemented in MeshLab, as explained in section 3.2.3. This MeshLab filter includes a scale parameter, which will determine how much of the neighbour area around the point it will take into account when fitting the sphere, i.e. how locally we would like to compute curvature. It is more understandable when observing how this filter scale changes the curvature computation all around the grain (Figure 3.14).

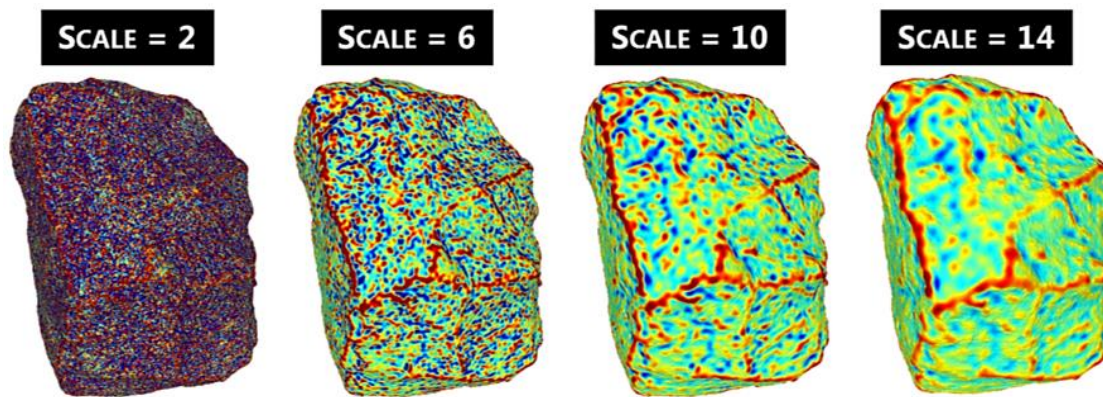


Figure 3.14 Curvature computed on grain S7 with filter scales of 2, 6, 10 and 14.

A smaller scale will be finer giving information about small details. However, ballast contacts are usually produced over a relatively large area, so the surrounding area of the asperity plays a crucial role on its exposition to wear. For instance, convex asperities inside a larger concave area are less likely to be eroded than concave asperities on a very sharp and convex edge. Thus, if we take a too detailed scale, the correlation with wear will not show up.

On the other hand, a large scale will take into account neighbour areas. Since we will be computing the average curvature of the surrounding area, that way we will be studying mainly the exposition of each point to eventual contacts. Of course, a larger scale also implies some loss of information, so a compromise is required.

Taking into account the visual inspection of the filter results and the size of ballast convex tips, a scale of 10 has been chosen. This scale allows for studying asperities with radius larger than 0.3 mm. It is important to remark that this is an arbitrary choice based only on qualitative data and an optimal answer does not exist. However, results extracted when using the previous and next scale factors (8 and 12) do not differ significantly with respect to 10. In the end, it is enough if we choose a good order of magnitude of the scale of the filter, since similar scales will lead to the same conclusions.

3.5.2 Evolution of the asperity radii

The sign convention used in this analysis states concave asperities as negative curvature or radius, so convex features will present positive curvature or radius.

Before starting to analyse the results, we need to highlight that, even if we are dealing with apparently pretty different shapes among the seven samples, the behaviour of all of them is not that different. For instance, Figure 3.15a shows the normalized histogram of the asperity radii when the grains were new (yellow) and at the end of the Micro-Deval test (purple). As we can observe, although there are slight differences, the distributions and evolution of all the grains are pretty similar.

To emphasize this observation, Figure 3.15b shows the difference, for each grain, between both corresponding histograms (at 0 and 140 minutes). As a difference between histograms, points above the line $y=0$ mean that they increase in number between the beginning and the end of the test. Again, the distributions of all grains are very similar.

All concave asperities tend to decrease in number, while convex ones depend on the asperity radius. Very convex (i.e. sharp) features tend to get smoother with wear, so they increase their radius. That means that the proportion of small radii tend to decrease or even to disappear, while proportion of higher radii increases. It is important to observe that, for all samples, the threshold between radii decreasing or increasing in number is similar (between 1.9 and 2.4 mm of asperity radius).

These very similar tendencies on all the grains allows for not differentiating between grains in the following analysis. From now on we will compute all grains as if it was only one grain. That means that we will include all asperities of all the grains as if we were talking about a single grain, combination of all the others. This will allow for using single lines for each parameter, leading to cleaner plots and more compacted information.

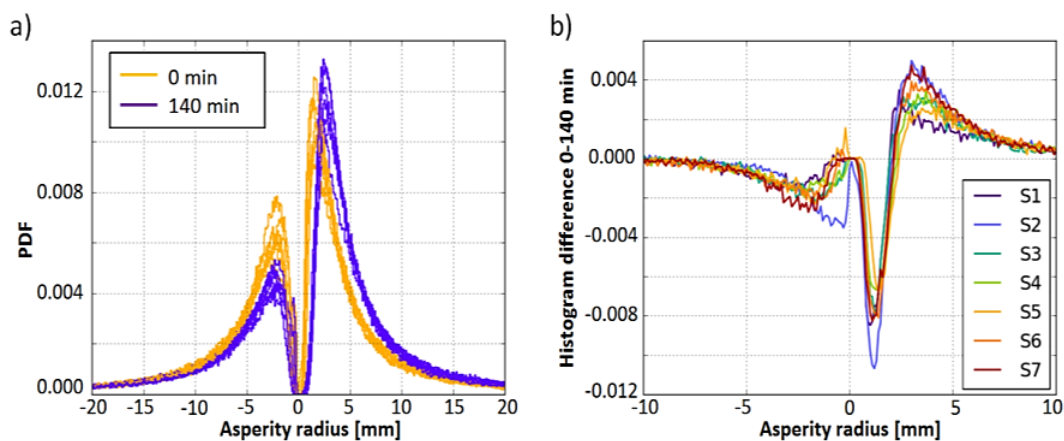


Figure 3.15 Comparison between samples. a) Histograms of the asperity radii when the grains were new in yellow (0 minutes) and at the end of the Micro-Deval test in purple (140 min). b) Difference between both histograms for each sample of the samples.

The first thing we have done is to divide the asperities into groups with respect to their radius and see how these groups evolve along the test. As we have seen in the plots above, almost all

the changes happen on the sharper asperities, i.e. those with the smaller radii, so it is important to focus especially on this group. We have established groups of 0.5 mm range, starting from 0 up to 3 mm, both for concave and convex features. We have then counted how many asperities there were inside each group for each scan. Figure 3.16 shows the evolution of the proportion of each of these classes along a Micro-Deval test.

It can be observed how concave features tend to decrease regardless of their radius. This is so because, in an overall convex shape like that of an aggregate, in order to have a concave feature, it must be necessarily surrounded (closer or further) by convex features. Therefore, when the neighbour area is eroded, concavity is automatically decreased. Very concave areas, due to their small radius, are especially sensitive to changes in the surroundings. Concave features are therefore eroded due to the overall wear of the grain.

Convex features, however, are exposed to external contacts and impacts. Very sharp tips and edges are also weak points of the grain, facilitating eventual breakages. In the chart we can observe how features with very small radius (< 1.0 mm) quickly disappear from the grains. Even asperities with higher radius like those between 1.0 and 1.5 mm are almost gone by the end of the test. The consequence is that these points are automatically transferred to higher radius class.

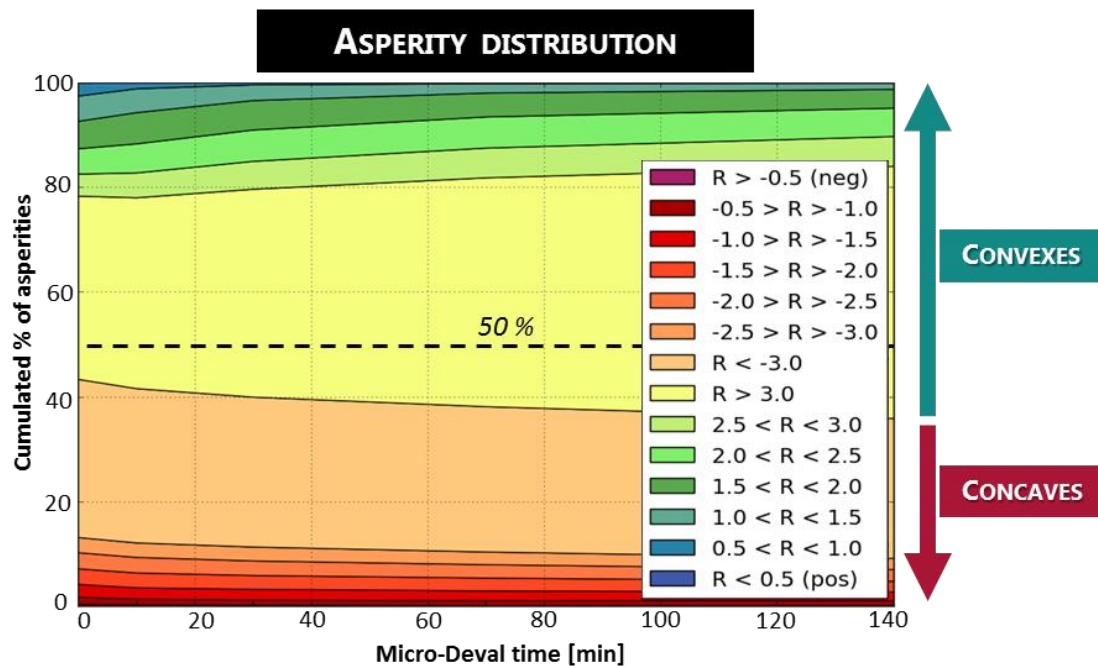


Figure 3.16 Evolution of the distribution of the asperity radii over a full Micro-Deval test.

Figure 3.17 takes the original grains as a reference, and focusing only on the convex features, it shows how many of the original asperities, in percentage, are left after a certain amount of Micro-Deval time. We insist that each curve is built comparing the scan after X minutes of test with the original scan (0 minutes). Thus, 100% means that the number of features with that radius has not changed. Of course, all asperities evolve, so 100% does not mean that the features of that class have not been affected by wear, but that the balance of incoming – outgoing features within that class is zero. Hence, lower values mean a decrease in number of

that category of asperities (0% being a total disappearance), and higher values mean an increasing number of features in that category.

From the features that initially had a radius below 1 mm, after just 10 minutes of Micro-Deval, 40% of them have disappeared, i.e. they have evolved towards larger radii. After 30 minutes, only 25% are left within this category. After 70 minutes, only 12%, and at the end of the test, only 8% are left.

Besides, after 10 minutes, all asperities with a radius below 1.4 mm have been reduced in number, i.e. fraction left below 100%. This threshold evolves towards higher values, being 1.7 mm after 30 minutes, 1.9 mm after 70 minutes and 2.1 at the end. Henceforth, by the end of the test, the number of features on the grains with a radius below 2.1 mm has been reduced, consequently increasing the number of smoother features.

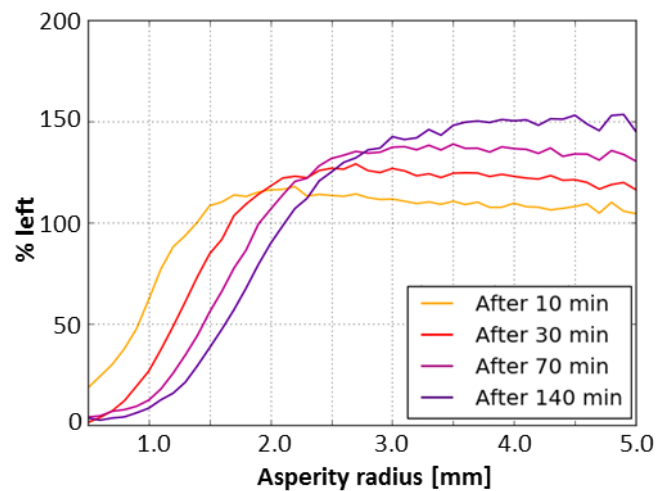


Figure 3.17 Percentage of asperities left after X amount of time in the Micro-Deval device, compared to the grain before erosion.

From these results, it is easy to extract the already mentioned conclusion: small radii tend to become larger. However, all we have seen so far is the overall distribution of asperities and, although unlikely, it could be the consequence of a random process tending to a generally more convex shape, but not a direct evolution of individual features. It is important to also compute the evolution of each independent asperity, searching for these same tendencies when linking individual points.

For linking each specific point of the surface with its corresponding point in the following scan, a K-D Tree algorithm has been used [116]. Without entering into details, this method consists on a space-positioning data structure for organizing points in a space of dimension K. For our purpose, it allows for associating each point in the original mesh with its best fitting point in a second mesh. Of course, this is an approximation but it is accurate enough to allow us to follow the evolution of the curvature for each specific zone.

Let us take, for example, the evolution of the asperities during the first 10 minutes of Micro-Deval. Figure 3.18 shows a 3-D normalized histogram where in the X-axis we have the original asperity radii (grain before erosion) and in the Y-axis we have the increment in radius that those asperities have suffered during the first 10 minutes. Thus the line $y=0$ will divide, for

convex asperities (i.e. positive radius): above, the points that have had an increment in their radius (smoothing), and below the points that have decreased their radius (sharpening). For concave asperities, since their radius is originally negative, it is the opposite: the points below $y=0$ increase their absolute radius, while the points above, either they become sharper or they get so smooth that they became convex. The diagonal line $y=x$ represent the points that have doubled their radius.

There are two main conclusions that we can extract from this plot. The first conclusion and the most obvious is that the core of the density plot, formed basically by convex features of radius from 0.5 to 1.5 mm, is entirely located over the line $y=0$, thus almost all of these features increase their radius (smoothing). This increase is not huge, they rarely double their radius, but it is consistent. And the second one is the great dispersity in the evolution, especially, of those asperities with larger radius. This is not surprising since the resulting radius of the asperity after wear depends on many factors (initial radius, local breakages, modifications on the neighbour area, exposition of the asperity, etc.). Especially in flatter areas (larger radius), a small breakage on the asperity or the neighbour area can modify significantly the computed radius and even change the concavity. In any case, most of the asperities do evolve as expected, i.e. a slight smoothing every cycle of erosion.

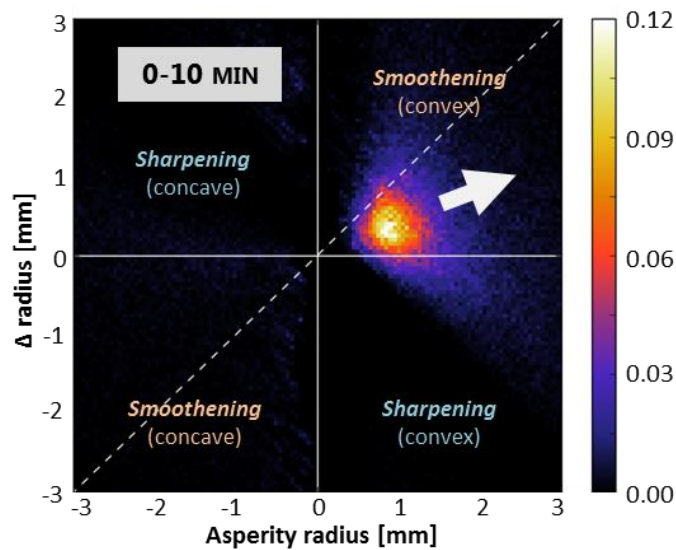


Figure 3.18 Normalized 3D histogram of the evolution of asperity radii during the first 10 minutes of Micro-Deval test.

This plot was showing the 0-10 minute cycle, but it is almost identically reproduced on the successive cycles of erosion. The only difference, represented with the arrow in the figure, is that the full dispersity cone and its core progressively shift to the right side. This is a consequence of sharper asperities (small radius) disappearing from the grain, so asperities that now become the sharpest for the next cycle become also the more exposed to wear, so they follow the same behaviour as the previously sharpest ones, and so on. The behaviour is repeated but shifted to slightly higher radius.

Of course, although there are clear tendencies, each individual point will follow a different evolution. Tendencies are easier to visualize when dividing the full sample into groups of points

and studying the statistical evolution of each population. Recovering the groups of asperities established before, we have divided asperities into the same groups as before: taking their original radius, they are classified in segments of 0.5 mm, ranging from -3 mm to 3 mm, as in Figure 3.16.

Figure 3.19a shows, as an example, the evolution of the asperities that, before any erosion, had a radius between 0.5 and 1.0 mm. It is important to insist that now we are following the same group of points all along the test and how their radius changes. The dashed red line represents the median value of the sample, the boxes delimit the percentiles 25 and 75 and the extremes the percentiles 10 and 90. As the test advances, individual evolutions diverge, leading to a higher dispersity of the sample after each cycle. But even with this dispersity, looking at the lower extremes (percentile 10%), all of them slightly increase with respect to the value before and the last one is over 1.1 mm, so we can conclude that more than 90% of this sample of grain features, that initially had a radius between 0.5 and 1.0 mm, have increased their radius (smoothened) by the end of the test.

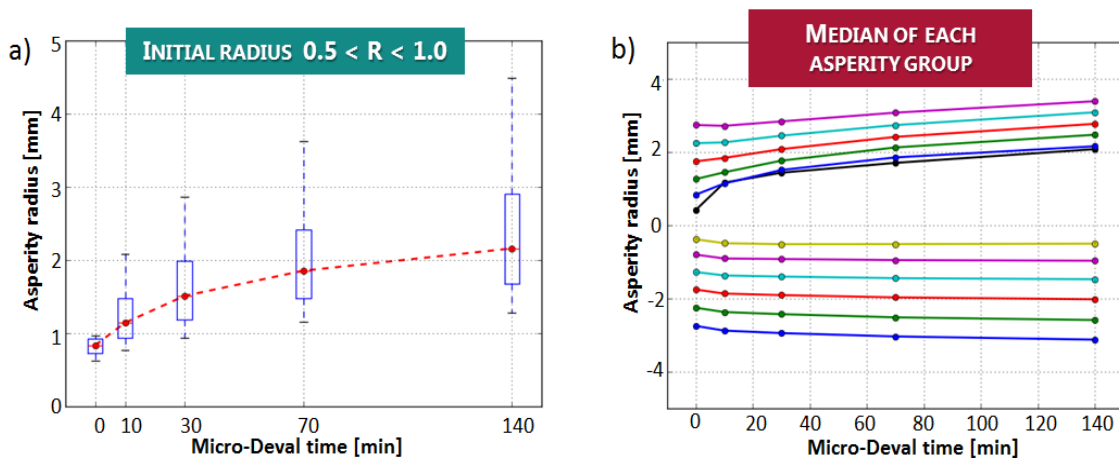


Figure 3.19 a) Evolution of the asperities that originally had radius between 0.5 and 1.0 mm. Red line is the median value, boxes represent percentiles 24 and 75 and extremes percentiles 10 and 90. b) Evolution of the median value for all groups of asperities: from -3 mm to 3 mm of initial radius in groups of 0.5 mm (i.e. 0-0.5, 0.5-1.0, 1.0-1.5, etc.).

In Figure 3.19b, the median value is plotted for all categories. We can see that, for the asperities considered (with radius below 3 mm), all of them tend to increase their radius along the test, regardless of their initial radius. Concave asperities do not show any difference between groups in the pace they change. In fact, after the first 10 minutes their evolution is very slow. Convex asperities, however, do show some differences. These differences can be seen especially at the beginning of the test: very sharp asperities quickly increase their radius at the beginning of the test, while asperities close to 3 mm of radius almost do not change during this period. In order to understand the reason, Figure 3.20 shows how the different groups of asperities are distributed on the grain surface:

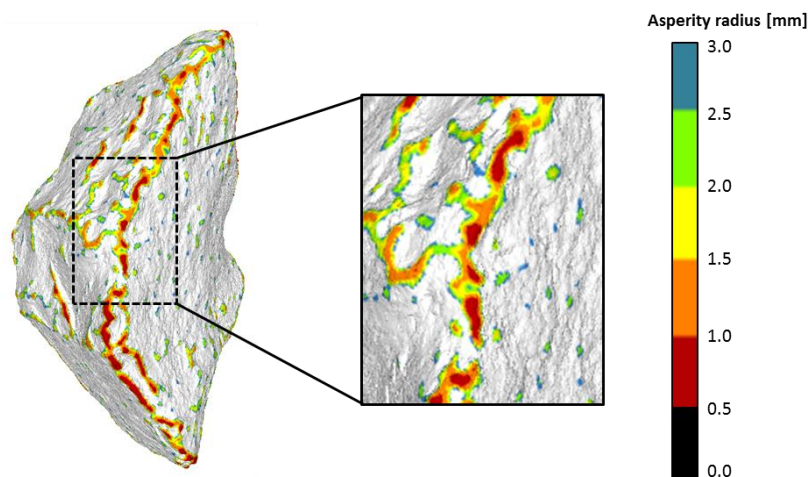


Figure 3.20 Distribution of convex asperities by radius of sample S1 before any erosion.

We can observe how the grain presents an asperity radius between 0.5 and 1.5 mm (red or orange) almost all along the edges and vertexes. On the other hand, features ranging from 2.0 to 3.0 mm of radius (green and blue) are located, either on the faces or surrounding the very convex asperities. During the first 10 minutes, these edges and vertexes wear, quickly evolving either by being removed or smoothed, while the points surrounding them are relatively “protected” by them. Once the corners have been smoothed enough, the neighbour points consequently become more exposed to contacts and erosion starts happening over larger areas. From then on, even if not so aggressive, wear continues to round more and more edges and tips, increasing their radius and progressively enlarging the exposed area, as we will see in the next section.

This phenomenon can be observed in Figure 3.21, where we can observe the evolution of the radii of these asperities along the test. At the beginning of the test, only a narrow and sharp edge presents radii below 3 mm, being most of it even below 1.5 mm. As the test evolves, the edge enlarges presenting for every cycle a wider band of points below 3 mm. The overall radius is increased as well and the asperities ranging between 1.5 and 2.5 mm of radius become more common.

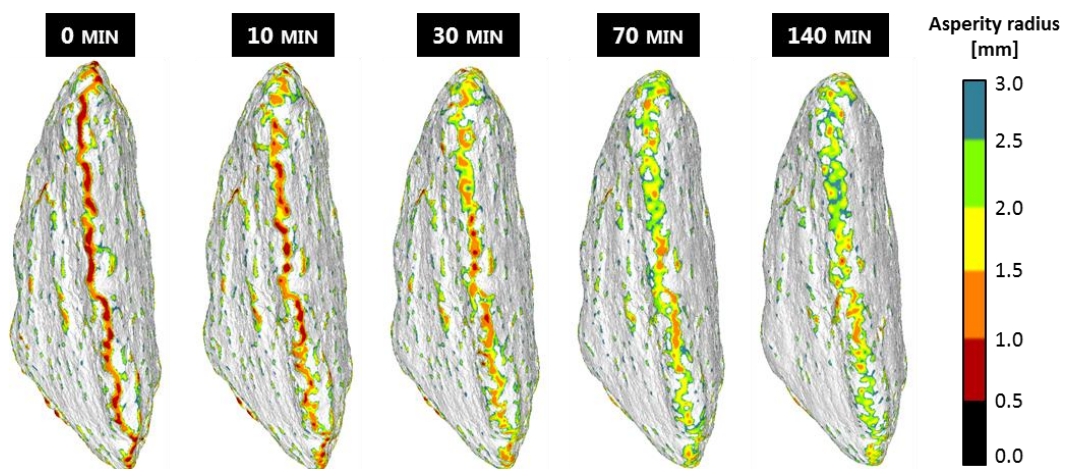


Figure 3.21 Evolution of the radii of convex asperities of sample S3 along a Micro-Deval test. These asperities are mainly located over the edges and vertexes.

3.5.3 Link between asperity radii and wear

So far we have seen how asperity radii evolve. It seems logic to think that, if there is an evolution of the radius, there is wear. However, surface could be also worn without a change in the radius, just by erasing layers of matter. So even if it is evident that edges and tips evolve, that does not necessarily mean that all the wear comes from there. Thus it is necessary to study where the erosion is produced on the grain.

Only by looking at the visual representation of wear, we can already see that edges do indeed get much more erosion than flat faces. Figure 3.22 shows the erosion of sample S3 during the full test. We can see how erosion happens mostly on the edge and vertexes while faces do not get almost any erosion. We can also observe the behaviour predicted in the previous section. At the beginning of the test, erosion is deeper and focused on the very edge of the grain, i.e. the area of influence is narrow but the maximal wear is higher. As the test goes on, the area of influence of wear gets progressively wider, but the maximal local wear decreases, even though each cycle is longer than the previous one. This behaviour is consistent with what we saw in Figure 3.21, confirming the correlation between wear and convexity of the asperities.

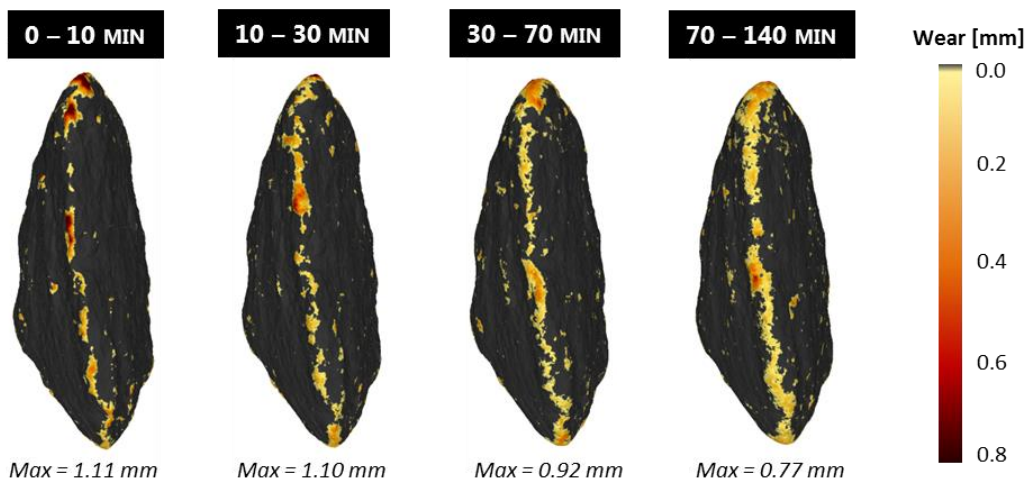


Figure 3.22 Wear of sample S3. Each image was built comparing both scans before and after each cycle of erosion, and representing wear on the scan of the grain before the cycle of erosion. The maximal value of wear of the sample is given as a reference, but it is not necessarily visible in the shown perspective.

Again, we confirm the same conclusions. During the first minutes of the attrition test, sharp edges and tips get aggressive erosion due to its high exposition to contacts and its intrinsic weakness, due to their associated small contact area and reduced cross section. Once these weak parts are removed or smoothed, asperities present a larger radius and thus a larger contact area and cross section, making them more resistant to impacts and reducing the local wear rate. This is slightly compensated by the fact that edges and tips are no longer single points or very narrow lines but wider bands, so fines are produced over a larger area.

The smoothing of roughness on the faces is a more subtle phenomenon, not so easy to identify. It is mostly produced due to the destruction of isolated sharp asperities, which will produce a reduction on the roughness measurements. However, there is also a very fine

smoothing of the overall surface that is combined with the inclusion of some fines in the micro-asperities, some getting so stuck that they cannot be removed just by cleaning the grain with water. All in all, they provoke a more even surface that can be felt just by touching the grain. Hence faces do not contribute significantly to the total production of fines, but there is indeed some wear happening on them.

Figure 3.23a shows the percentage of wear (with respect to the total wear) undergone by the different asperities according to their radius at the beginning of each wear cycle. As expected, convex asperities contribute significantly more to wear than concave. Figure 3.23b shows the normalized histogram of the asperities suffering at least 0.5 mm of wear. We can observe that aggressive wear is almost exclusive of asperities with a radius below 5 mm, at least within the Micro-Deval range of wear. There are however, some changes as the test evolves. At the beginning, wear happens in very convex asperities, below 2 mm of radius (the sharp and narrow line observed in Figure 3.21). As the test progresses, sharper asperities disappear so they can no longer contribute to wear, shifting the peak towards the next group of sharp asperities. In addition, the surrounding areas become more exposed to contacts and the area of influence of wear becomes wider, as we saw in Figure 3.21 and Figure 3.22. This results in a wider range of asperities being concerned, as we can observe in the histograms.

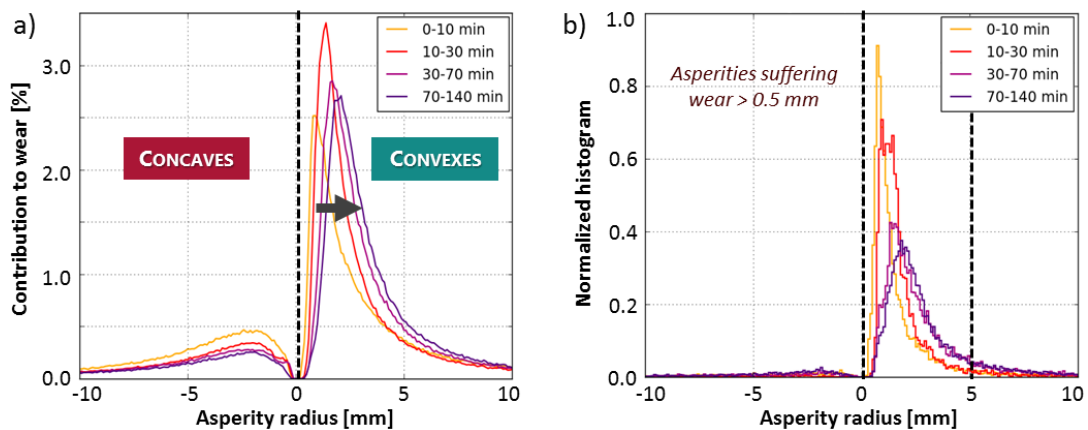


Figure 3.23 a) Percentage of wear with respect to the total wear depending on the asperity radius. b) Normalized histogram by radius of the asperities suffering more than 0.5 mm of wear.

Let us now focus on the group of asperities ranging between 0 and 3 mm of radius, which correspond to the ones taking the highest amounts of wear. Figure 3.24 shows the average amount of wear taken by these convex asperities, both in absolute value (a) and normalizing it by time (b), taking into account the different lengths of the erosion cycles (i.e. expressing it as a wear rate). It is necessary to study both plots together since the performed cycles of erosion are not equal in length, but 10, 20, 40 and 70 minutes long, respectively. It is important to remark that for asperities larger than 3 mm, mainly located on the faces, average wear is below 50 μm (which is the resolution of the tomography scans), so it means an average of less than one voxel of difference in the scans. Of course, it is not possible to be precise on those measurements but it is enough to say that generally wear on large asperities is almost zero.

The first thing we can observe is that asperities close to 0.5 mm of radius present a very high absolute wear, even higher than their own radius. This confirms that these sharp asperities are

very exposed to contacts and generally disappear very quickly. In fact, they show a similar amount of wear regardless of the Micro-Deval time. A possible explanation could be that these asperities suffer massive wear when the cycle starts, being quickly smoothed and from then on, they wear at a much slower pace. This aggressive start of the cycle is probably fast and predominant on the overall wear of the cycle, so the total amount of wear will depend mostly on those first minutes of the cycle and not so much on the total duration of the cycle. In addition, we have seen how fine particles get stuck around the grain, filling the small concave asperities and covering the grain with a thin protective layer. Thus, after some minutes, this film protects especially small features reducing their exposition to contacts. When the grains are cleaned between cycles, small asperities become again exposed to wear.

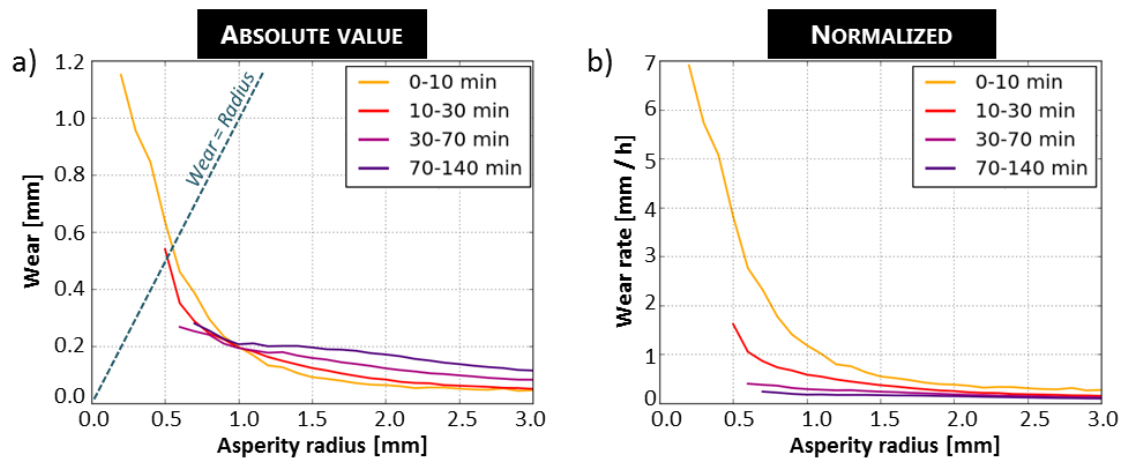


Figure 3.24 Average wear (a) or average wear rate (b) per asperity of each specific radius. Since the lengths of the wear cycles are not the same, it is necessary, not only to give the absolute value, but also to normalize it as a wear rate.

However, asperities with a radius larger than 1.5 mm behave as expected. They present larger amount of wear when the cycles are longer, but when normalizing they show all a similar wear rate. Thus, when asperities become large enough, wear becomes a more stable process, which could explain the two phases of the Micro-Deval test observed when plotting the evolution of the mass of the sample (see section 2. 4. 2).

Finally, we can also observe how the lines start each time at larger asperities. That means that smaller features have already disappeared during the previous cycles, making it even clearer that sharper asperities are the first to be eroded and always evolving towards larger radii.

3. 6 MORPHOLOGY EVOLUTION ON THE TRACK

This study has been performed using the Micro-Deval test. As we have already discussed, the conditions of this test differ from the conditions of ballast in the track, but also the likelihood of Micro-Deval system being similar to the maintenance operation of tamping. Except for those grains getting a direct impact from vibrating tines, all others move relatively free below the tamping machine, impacting other grains and suffering similar erosion to that suffered in the

Micro-Deval. Therefore we can expect asperities to evolve in a similar way as described in this chapter. However, some conclusions of this analysis can also be extrapolated to the case of the railway track.

Firstly, a full Micro-Deval test, at least with such a resistant material as granite, has proven not to be enough to change the general shape of the grains. Shape parameters do not show a clear tendency or change all along the test, with the exception of occasional major breakages. It is true that the volume and mass is indeed slightly reduced, but the general shape is not affected and changes are so fine that it is perfectly possible to identify the grain, among the full sample, at all stages of erosion only by visual recognition. In any case, a big evolution in shape due to wear would neither be representative of track conditions, since ballast grains are generally substituted before suffering such big changes. Only grains below the sleeper can suffer from large breakages, or in rare cases extreme erosion, enough to lead to an actual evolution of the general shape.

On the other hand, we have confirmed that angularity and surface texture do actually change considerably in the Micro-Deval. Surface texture, or roughness, on the faces is quickly lost, especially during the first half of the test, by eroding isolated convex tips. Due to its nature of micro-morphology, it is mainly formed by asperities below 1 mm of radius, and we have seen how these features most of the times disappear completely after the first minutes of test. In the track, grains are blocked and contacts are restricted to a localized area of the grain. This means that this wear mechanism will not initially happen all around the grain as it happens in the Micro-Deval, but where the contact is produced. In the track, contact forces can reach higher values than in the Micro-Deval test for the most demanded grains (see section 4. 2. 3). Thus we can expect the local surface texture affected by the contact to quickly disappear or to become adapted to the contact interface (self-organization [49]).

On the other hand we have angularity, a key parameter for the behaviour of the ballast layer. This parameter is mainly influenced by big features such as edges and vertexes, which due to ballast nature are generally sharp when the grains are new. We have observed how angularity is lost during the full test, getting asperities progressively smoother and more rounded. The radii of edges and vertexes progressively evolve from sharp and narrow lines towards wider and more rounded bands. This phenomenon results in a larger area being affected by contacts. These worn asperities have however a larger cross-section and are stronger than sharper ones, consequently reducing the aggressiveness of wear. In the track, vertexes and edges will generally contact a face of another grain. They will be the counter-part of the self-organization mechanism described above.

They will wear locally until a rearrangement of the grains happens and changes the contact point. For example, during a tamping operation, grains are rearranged, creating a completely new network of forces and changing the contact points. Once the vibration is finished, due to the major exposition of convex features, sharper (so weaker) asperities have more probabilities to finally become the next contact points for the next cycle. Therefore, even if in the track, contacts affect a relatively small area of the grains, after tamping these areas may change. Over the lifetime of ballast, several tamping operations are applied, so it is not surprising that the final morphology of the grains present a general wear all around the rock.

We can thus expect that, immediately after the tamping operation, an adaptation process will be required and so, the production of fines will be higher than before the maintenance. As edges become more and more rounded, if it happens that they become part of a contact again, they will be able to resist better, reducing this adaptation time.

Therefore, sharp features are the main source of fine particles, and since higher curvatures are generally found over edges and tips, these are the areas where wear is concentrated. It can be then concluded that angularity and sharpness are a source of production of fines. However and despite being a clear weakness for the grains, ballast angularity is a desired characteristic to improve the interlocking within the ballast layer and reducing the appearance of track defaults. The only way to reduce the wear is then to soften the contact forces, e.g. by spreading the external forces over the maximum amount of ballast grains, which is one of the goals of USPs.

In any case, it is clear that the morphology of edges plays a role on the amount of fines generated by a contact, and this is an aspect that needs to be taken into account when modelling ballast degradation. In the next chapter we will study in more detail the adaptation (or self-organization) mechanism due to friction and, in the last chapter, we will introduce into the model a geometric parameter φ that will serve as a first approach to take into account the reduction on the wear rate when sharpness is reduced.

In this study we have performed mainly a descriptive overview of the decrease of sharpness. Some values and estimations have been presented, but further development needs to be carried out in order to obtain an accurate understanding of the evolution rate of the angularity along time.

3.7 CONCLUSIONS

In this chapter we have observed in detail how grain morphology evolves while aggregates wear in the Micro-Deval device. First we have studied the evolution of different parameters describing shape, angularity and texture. And afterwards we have made a detailed analysis at the local scale on the evolution of the radii of asperities. All in all, it has allowed us to have a better understanding of why and how fine particles are produced while wearing.

We have observed that Micro-Deval is not able to change the overall shape of the grains, but does change considerably angularity and surface texture. In order to understand better the evolution of both morphology scales, we have performed a detailed analysis of the evolution of the asperity radius.

Convex asperities, especially sharper areas (i.e. higher curvature or smaller asperity radius), are generally the most exposed to eventual contacts and impacts with other ballast grains or with the metallic cylinder. In addition, due to their smaller cross-section, these sharp asperities show a weaker resistance to contacts. Thus they tend to disappear on the first minutes of the test, either by getting progressively rounded or by small breakages. As the asperities get rounded, they increase their eventual contact area, so they get progressively more resistant. Wear may then affect other asperities, so far protected, which may now become the ones with

more contact exposition. This results in an evolution of edges from narrow sharp weak lines to wider and stronger bands. Thus, as edges are worn, more area is affected by contacts but this area presents an overall lower wear rate.

Finally, we have assessed the importance of the different mechanisms observed in the Micro-Deval for the case of the ballasted track. Sharpness or angularity has been shown to play a key role on the wear process, so a first approach of this phenomenon will be taken into account in Chapter V when modelling ballast degradation.

Last but not least, major breakages represent another source of fine particles. As we have seen in Chapter II, breakages in the Micro-Deval are relatively rare but they happen from time to time with no particular trend. Even if any of the particles of the studied sample did not split in pieces, some breakages of small portions have been identified. These breakages create small and isolated fragments of grains that can be easily crushed by other bigger grains, being a not despicable source of fines.

Whatever the source of them, after some minutes of test, if they are not subtracted, fines get stuck to the aggregates creating a thin film that slightly protects them from wear. This film decreases the generation of new fines reducing the exposition of small and weak asperities to external contacts.

In the following chapter, we will go a step further on the analysis and start studying the actual mechanisms happening within the ballast layer inside the railway track.

IV. THE TRACK AT THE CONTACT SCALE

4. 1	Introduction.....	96
4. 2	Numerical simulation of a TGV track.....	96
4. 2. 1	Description of the system	97
4. 2. 2	Type of contacts	99
4. 2. 3	Contact forces	99
4. 2. 4	Relative displacement at the contact scale	102
4. 2. 5	Friction work	104
4. 3	Shearing experiments	107
4. 3. 1	Samples	107
4. 3. 2	Known problems and calibration tests for F_z	108
4. 3. 3	Test summary	110
4. 4	Friction coefficient	112
4. 4. 1	Geometry correction	113
4. 4. 2	Friction coefficient ballast – concrete	115
4. 4. 3	Friction coefficient ballast – ballast	116
4. 5	Morphology of the contact area	119
4. 5. 1	Evolution of the distance between samples (decrease of Z)	119
4. 5. 2	Estimation of the contact area	120
4. 5. 3	Evolution of the contact area	125
4. 5. 4	Volume loss	129
4. 6	Influence of water.....	131
4. 7	USP tests	133
4. 8	Conclusions.....	137

4. 1 INTRODUCTION

Studying wear in the Micro-Deval device is a fast and economic way to obtain an accelerated degradation, i.e. ageing, of aggregates. The resulting shape of the grains does not differ too much from that of ballast in the track at the end of their lifespan, after several cycles of service and maintenance operations. Therefore it represents a good option for assessing the resistance of materials to attrition.

However, intuitively one could suspect that the system in the track (i.e. forces, displacements, interaction between grains, networks, etc.) is not even similar to a rotating cylinder. Grains inside the ballast layer are very restricted to move, blocked by their neighbours, the sleeper or the sub-ballast layer. Free falls, like in the Micro-Deval, are not likely to happen and impacts are rare and restricted to gaps between the sleeper and ballast. We are comparing a dense packing with a loose packing dynamically loaded.

Thus it becomes necessary to study in detail how the railway track works, going from a macro-scale overview to the contact scale. In this chapter a multi-scale study is proposed using both numerical and experimental tools.

In a first phase, a simulation in discrete elements is performed to analyse the passage of a bogie over a sleeper. As we saw in section 1. 4, this kind of simulations are not new for ballast, but there is still work to do in the understanding of the layer and its contact network. As we did with the Micro-Deval case, Archard model is proposed and applied to the numerical simulation in order to assess the potential wear within the track. This procedure will permit as well to study the potential wear provided by each contact individually, making possible to identify the families of contacts that contribute the most to the total production of fines of the track. These characteristic contacts will be then reproduced experimentally.

Thus, in a second phase, a 3D shearing device called BCR3D will allow us to take the representative contact extracted from the simulations and to apply the normal contact force and the relative displacement associated, in a cyclic loading, to two individual grains. A study of the tangential forces and thus the friction coefficient at the contact scale is then performed. Finally, we will analyse the evolution of the morphology, estimating the contact area and the matter lost during the test, using a laser profilometre to scan the surfaces of both grains before and after the shearing.

4. 2 NUMERICAL SIMULATION OF A TGV TRACK

Discrete element modelling is a powerful tool to better understand the behaviour of granular media. Quantifying experimentally contact forces or relative displacements between grains is, in the best of cases, a very challenging and tricky task. DEM becomes a good alternative tool when in-situ data is not available or complete.

In this study we will simulate the passage of a series of TGV bogies over a portion of track. For the simulation we will use the same software as we used for the Micro-Deval simulation, i.e. LMGC90, and the same library of polyhedral grains.

4. 2. 1 Description of the system

In order to reduce the computational time, a reduced model of the track is considered. This reduced model consists in one block of a bi-block sleeper, i.e. half the track or one rail. The length in the longitudinal direction of the rail is 1.0 meter, limited by frictionless walls. On the transversal direction, the left border (i.e. the axe of symmetry of the track) is also limited by a frictionless wall while the right border is left open allowing for the typical slope of granular media given by the friction angle of the grains. This configuration measure slightly around 2.3 meters in the transversal direction. Finally, on the vertical direction, the floor is limited by a flat surface with the same friction coefficient as the one considered for ballast-ballast contacts and the upper-limit is of course left open, giving a total height of about 0.6 meters.

The friction coefficient considered is 0.8 for all ballast-ballast, ballast-sleeper and ballast-floor contacts. As already mentioned for the Micro-Deval simulations, this is a classic value used in the SNCF for this kind of simulations.

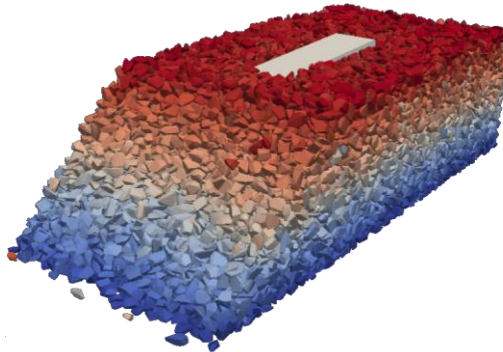


Figure 4.1 Simulation of a portion of the track. Colours have only an identification purpose.

Figure 4.1 shows a 3D perspective of the model. As for the Micro-Deval, the colours represent only the numeration of the grains. Except for some grains rolling down the slope on the free side at the beginning of the simulation, ballast layer will not lose the initial ordered structure.

Two different simulations of the track with the same configuration but different rearrangement of grains were performed. However, if it is not specified, the results shown along the chapter have been all extracted from the same simulation (Figure 4.1). This specific simulation consists in 22 756 grains plus a sleeper block, a floor and three frictionless walls. As we will see, most of the action happens directly below the sleeper and the walls are far enough not to influence the behaviour of the layer, so the fact of considering or not friction on them is irrelevant.

All grains have the freedom to move except that of the sleeper (which in terms of the simulation is considered as a ballast grain), that can only move vertically. This restriction is established to avoid possible rotations or horizontal displacements that would not be possible in the track due to the sleepers blocks being attached to the rail.

The time step considered is $2 \cdot 10^{-4}$ seconds but data is saved every 5 time steps (i.e. every 10^{-3} seconds). Data is stored in a HDF5 file that is afterwards treated using a Python code. The model is previously built by settling the different ballast layers by gravity in a closed box without the sleeper. If we desire a higher compaction for the layer, we will put the friction coefficient to zero and we will make the gravity act for a longer time. The sleeper is then included deleting the overlapping grains. Afterwards, the right border wall is erased and a first slope is created by arbitrary cutting the sample and discarding the excess grains. Finally, a relaxation phase follows allowing the ballast to “flow”, creating a stable slope.

Concerning the external load, it consists of a double peak cyclic vertical load of 23 kN of maximal force per peak extracted from the formula of Sauvage for calculating the force signal transmitted to a single sleeper during the passage of a bogie (see section 1. 1. 2). It is directly applied at the centre of mass of the sleeper block. Figure 4.2 shows the shape of this external load during the first 4 cycles and the associated settlement of the sleeper block. We can observe how the first cycles serve to fill the gaps between the sleeper and the ballast and to rearrange the grains in order to hold first the weight of the sleeper block and afterwards the external load. It is not surprising then to see such big settlements at the beginning of the simulation.

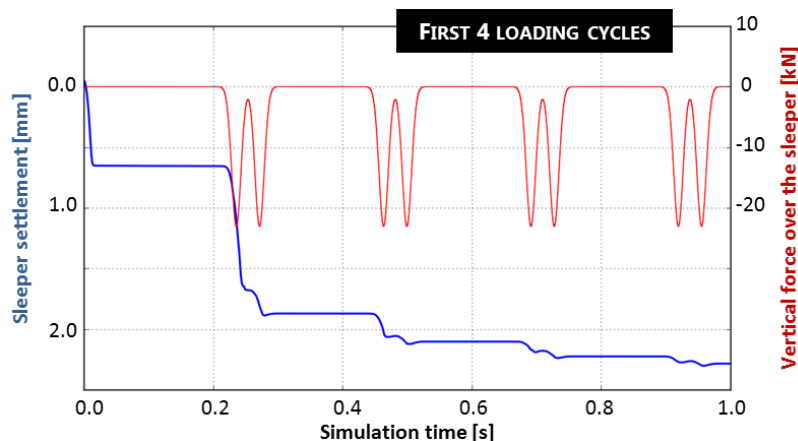


Figure 4.2 The external load is a double peak force corresponding to both bogie axes. The sleeper settlement during the first cycles is high due to the rearrangement of grains.

The total time of the simulation is 6 seconds, including a total of 13 passages of bogies. In the final version of the load we decided to wait 1 second of relaxation at the beginning before starting to load, after the first 4 cycles and after all 13 bogies. Due to memory limitations, it was not possible to save data in HDF5 during the full simulation, so we opted to only save the last two passages of bogies and the final relaxation, i.e. from 4.5 seconds to the end. Thus the final configuration is given by the following diagram (Figure 4.3):

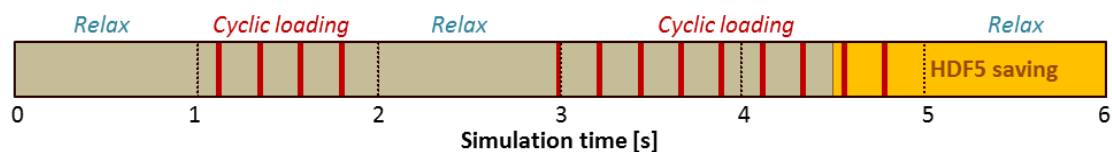


Figure 4.3 Diagram of the simulation. Red lines represent the start of a bogie loading. In yellow it is represented the data saved in HDF5 and available for study.

4. 2. 2 Type of contacts

Polyhedral grains are built on top of three geometrical primitives: vertexes (points), edges (lines) and faces (surfaces). When two grains get in touch, we can observe three different kinds of contacts that will be determined by the number of contact points used by LMGC90 to model a two-grain interaction:

- **Simple contacts** Mostly represented by vertex-face contacts, they present one and only contact point. Edge-edge contacts would also be in this category, as well as other uncommon like vertex-edge, or vertex-vertex.
- **Double contacts** They have a line in touch and are usually simplified as two contact points. The most common are edge-face contacts, but also edge-edge when perfectly aligned would be double contacts.
- **Triple contacts** They have a surface in common, only represented by face-face contacts. Of course, also if part of the face is in contact with part of the face of the other grain it would also be a triple contact. They are often simplified as three contact points.

Figure 4.4 represents the amount of each kind of contacts that we have during the simulation along the passage of two bogies.

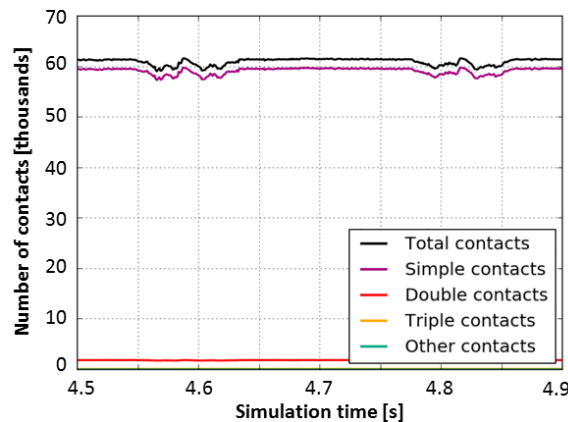


Figure 4.4 Amount of contacts of each kind during the simulation.

As we can observe, more than 95% of the contacts are simple contacts and the rest are mainly double contacts. The external load creates a slight oscillation on the total amount of contacts but the proportion of kinds is not altered.

4. 2. 3 Contact forces

The phenomenon of chains of forces in granular media is widely known [77, 2, 19]. The polyhedral shape considered for ballast grains and the relatively small thickness of the layer help even more to create a large variability within the contact network. Due to this particularity, only a small percentage of grains do actually support the external loading.

For example, in Table 4.1 we can observe how very few contacts surpass 100 N in normal force, while the maximal force registered is over 1 kN even during the relaxing phase.

<i>Normal forces [N]</i>	Mean	Percentile 99	Percentile 99.9	Max
Loading	14	145	719	13 214
Relax	5	39	113	1 347

Table 4.1 Registered forces during a bogie passage and during the relaxing phase at the end of the simulation.

These chains of forces are obviously located under the main source of load, i.e. under the sleeper. They connect the concrete block to the floor acting as pillar supports. Due to the rigidity of the grains, once these pillars are created, all the other grains are denied to take part on the main support function, unless there is a rearrangement of grains. However, these chains tend to bifurcate as they spread downwards.

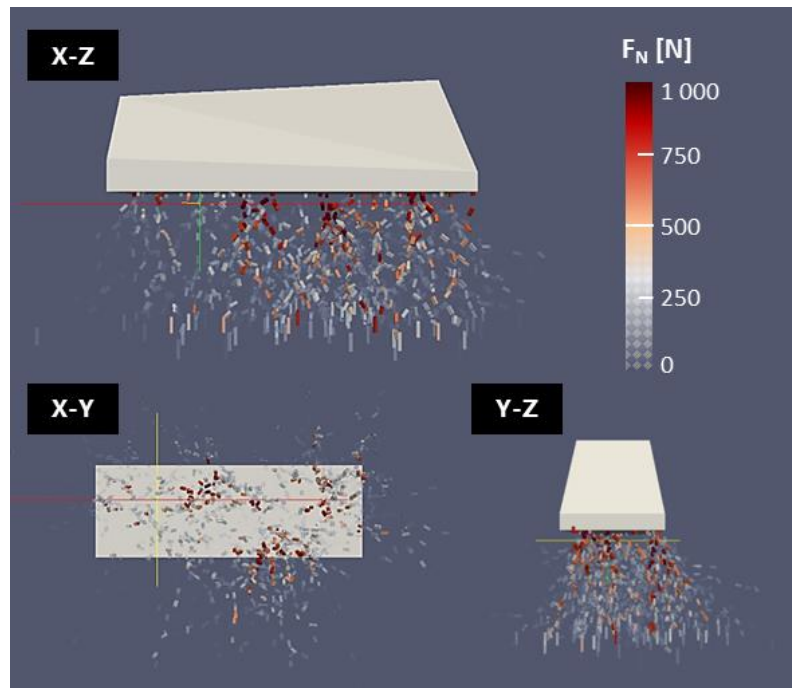


Figure 4.5 Chains of forces below the sleeper block. In the figure, contacts over 250 N are represented (colour of weaker contacts is progressively faded out).

Figure 4.5 shows the contacts that, at the exact moment of a peak of the external force, show values of over 250 N. As we can observe, all these contacts form a pyramidal network starting below the sleeper and spreading wider until they reach the soil. It is important to remark that, due to the relatively small thickness of the ballast layer, the spreading of the loading is never reaching the limiting walls of the considered portion of track.

Another consequence of this spreading phenomenon is, of course, that the higher forces will be generally located immediately below the sleeper. Forces stronger than 1 kN are rarely seen at lower levels. This is in fact in accordance with the observations in the real railway track, where grains just under the sleeper are more likely to suffer extreme wear and even crushing.

In the X-Y perspective (i.e. view from under the sleeper), we can observe how the chains are mainly originated on three different and independent clusters. The grains located in these origins present a higher risk of breakage and aggressive wear. They are taking alone the full weight of the sleeper plus the external load. This is why we can eventually observe extreme contact forces over 10 kN in the system, that would most likely crush ballast aggregates. The amount of clusters will depend on the arrangement of grains and can change from one simulation to another, but it is the main responsible for the maximal force of the system.

Figure 4.6 shows the forces at the same peak of the external load and at a moment of relax (no external loading) for two different simulations with the same configuration but different arrangement of ballast grains. The table below shows the numerical values of the forces suffered by the few grains that actually hold the layer at peak loading. As we can observe, the statistical distribution of forces is basically the same for both samples, but the maximal value differs considerably. Peak values depend more of the particular sharing of the external load among the strong chains. In this case, the sample E1 spreads better the external load over more chains of forces than the first one.

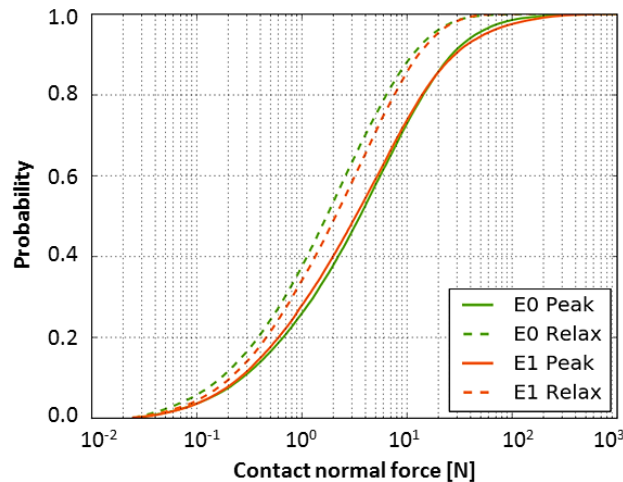


Figure 4.6 Distribution of contact forces at peak loading for two different samples of ballast grains.

Forces at peak [N]	Mean	Percentile 99	Percentile 99.9	Max
Sample E0	13	136	660	11 816
Sample E1	15	196	624	3 033

Table 4.2 Some numerical values of Figure 4.6.

In the real track, granite nor concrete are absolutely rigid so they permit some elasticity of the layer, which would allow a slightly further sharing of the load. In addition to that, the change in shape of the aggregates due to wear fosters eventual rearrangements of the network and transmission of the loads, so that these efforts tend to be either shared or toggled between different force columns.

Concerning the orientation of these efforts, it is clear that the stronger contacts are mainly oriented vertically, i.e. collinear with the external load, searching for this transmission of the efforts to the ground.

Figure 4.7 shows the orientation of the contacts along two bogie passages, on the left in terms of number of contacts following each orientation, and on the right in terms of the intensity of these contacts. All angles are represented with respect to the horizontal plane, being 0° a completely horizontal contact and 90° a vertical one.

The first thing we can notice is that during the external loading there is an increase of the number of horizontal contacts. When the grains under the sleeper are pushed downwards by the concrete block, they need to create room under the sleeper pushing the other grains. The layer being relatively thin, the easiest way to create new space is to push the grains laterally. This activates the secondary network that tries to block them favouring this creation of horizontal contacts. However, the main efforts still remain vertical. Almost all the contact forces over 100 N are vertical. It is clear that the strong chains are the main responsible of absorbing most of the energy, and the secondary network only works to stabilize them.

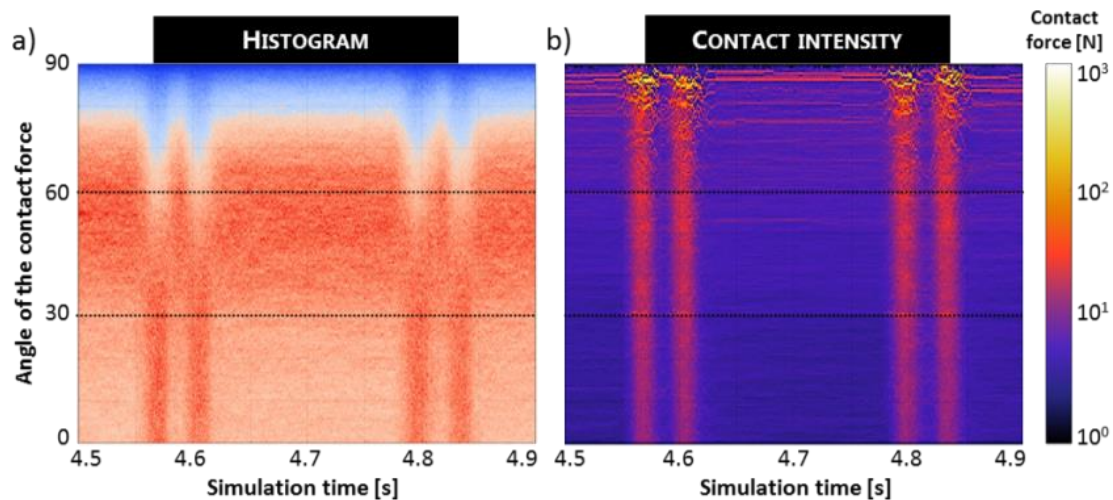


Figure 4.7 Orientation of the contacts with respect to the horizontal plane along two bogie passages. a) Qualitative histogram, red corresponding to larger number of contacts and blue to lower number of contacts. b) Intensity of the contacts.

4. 2. 4 Relative displacement at the contact scale

When two surfaces are in touch and it exists a tangential component of the contact force that can overpass the static friction force, a relative movement will be triggered. We define two main goals when studying relative displacements: assessing the order of magnitude of this relative displacement along a bogie passage, and observing which kind of trajectories are observed (i.e. relatively linear, cyclic or irregular).

Figure 4.8 shows an example of contact trajectory between two grains located just under the sleeper block, during two bogie passages. The contact between these two grains is particularly long in terms of both relative displacement and duration. The type of contact is simple, so a vertex is “drawing” a trajectory over a face. From the point of view of the vertex, the trajectory length will be null, i.e. the contact point will remain on the tip. However, this tip will draw a path on the face of the other grain which is represented by the plot on the right. The trajectory

is almost a straight line during both loadings, with a visible stop between bogie passages. Even if the loading is cyclic, the trajectory does not necessarily follow the same pattern. For instance, in this case the trajectory does not go backwards at any moment.

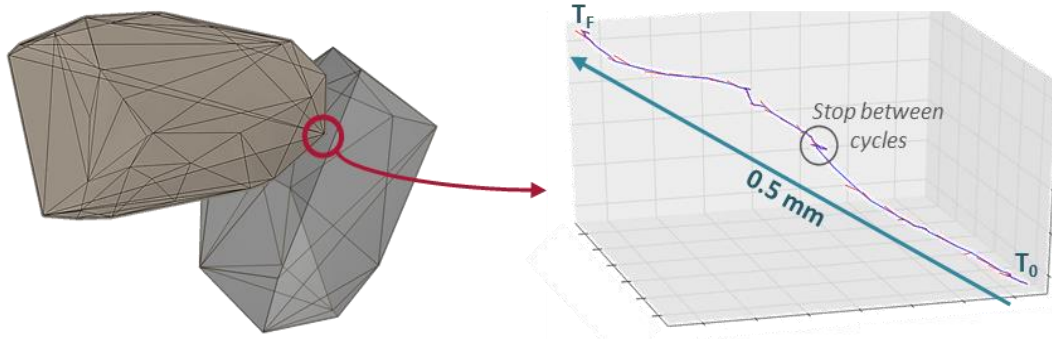


Figure 4.8 Example of contact vertex-face between two grains just under the sleeper. On the right we can observe the trajectory of the vertex over the face.

The simulation of only two bogie passages is not enough to discard a possible backwards trajectory. It should be perfectly viable and it would respond, for example, to a rearrangement of the grains. In fact, ballast layer tend to get more and more compacted over time, especially during the first cycles, so it is intuitive to think that these trajectories will have a trend towards a predominant direction. This mechanism of accumulation of permanent deformation due to cyclic loading is known as granular ratcheting [117, 17]. After these first compacting cycles, deformations are weaker and more regular and relative motion is produced in one or another direction alternatively.

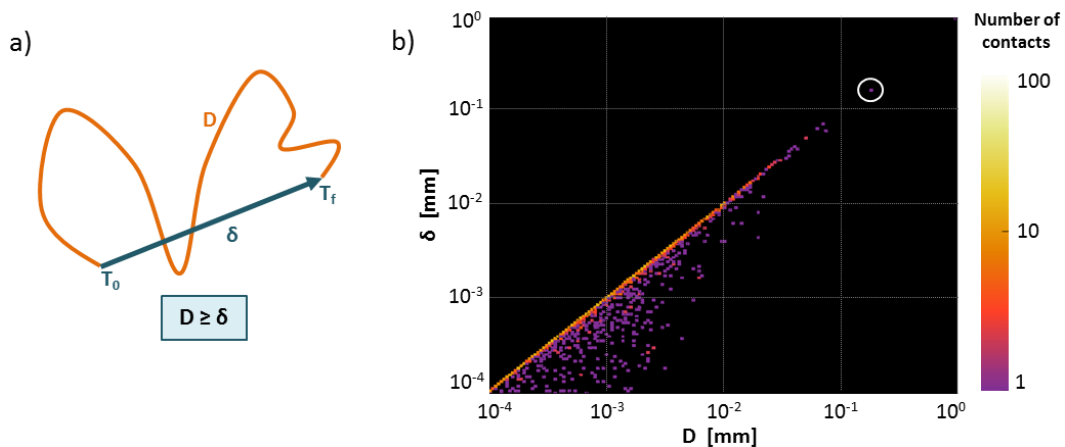


Figure 4.9 a) Definition of real displacement D and effective displacement δ . b) 3D-histogram of the real and the effective relative displacements of the contacts along one bogie passage. The white circle represents the example presented in Figure 5.7.

This one was just an example of trajectory but if we take a look to the whole sample of contacts, we observe the same tendency. Let us consider one loading cycle (i.e. one bogie passage), so that we can define the real relative displacement D as the length of the full trajectory of one contact all along the cycle, i.e. the integral of the curvilinear position, and the effective relative displacement δ as the difference between the final and the initial absolute positions (see Figure 4.9a). This way, D will be always equal or larger than δ . If both values are

similar it means a linear trajectory, while if they are very different, it means a very irregular trajectory. Figure 4.9b shows these two values for one bogie passage in a 3D-histogram, where the colour is the amount of contacts falling in each category. As we can observe, most of the contacts (note the logarithmic scale of the colours) and especially those with longer trajectories are on the surroundings of the line $D=\delta$. Contacts with a strong non-linear trajectory exist as well but they are rare cases and restricted to contacts with weak normal forces. These non-linear contacts often present as well small relative displacements, so they will not generate a significant amount of fines. Linear shearing will be then a good and representative option when later on we will reproduce experimentally the characteristic contacts between grains.

4.2.5 Friction work

Contact forces and relative displacements are the main ingredients of the equation of Archard to predict wear. As a reminder, Archard states that the volume of produced wear is proportional to the product of the contact normal force and the relative displacement between both surfaces. We have called this product the work produced by friction forces, or friction work. Therefore, and as we did with the Micro-Deval system, knowing both quantities we can easily compute the product and assess the distribution of work within the track system.

Figure 4.10 shows the distribution of the cumulated friction work during one bogie passage, on both the plane X-Z (left) and Y-Z (right) of the track. As expected, most of this work is concentrated just below the sleeper block and the surroundings. The layer immediately below the sleeper suffers the maximal forces and in that area we find as well the maximal displacements in the secondary network. We can also observe that grains close to the vertical borders of the simulation do not contribute significantly to the total work of the track, especially if we take into account the logarithmic colour scale. During the first cycles of the simulation we can eventually observe some work on the free border due to grains rolling down the slope.

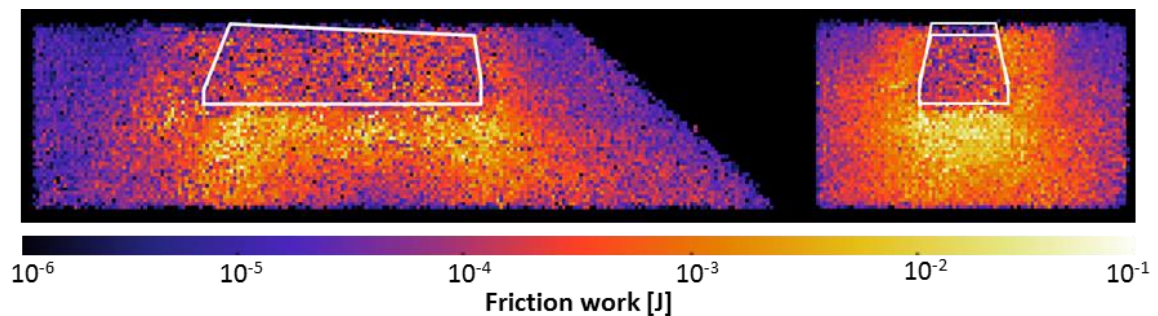


Figure 4.10 Cumulated friction work during one bogie passage.

The total friction work produced by this portion of the track is 1.0 J per bogie passage, given by steps coinciding with each loading peak (see Figure 5.2 for the evolution of the track during two bogie passages). However, as we have seen, this work is not absorbed uniformly by all grains but there is a big variance within the sample.

Figure 4.11 show the Cumulated Density Function of the work absorbed by each grain in the sample. In this chart we have added two different track simulations (the same samples used for Figure 4.6) during one bogie passage, along with the work absorbed by rotation of the drum and by grain in the Micro-Deval simulation.

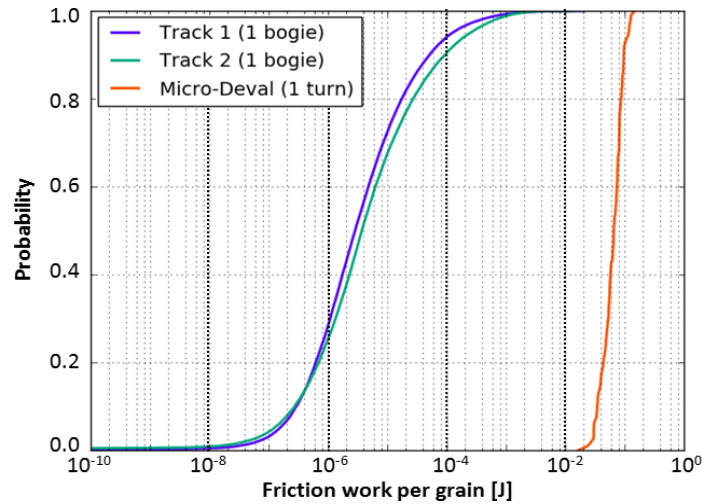


Figure 4.11 Cumulated density function of the friction work absorbed per grain during a loading cycle (bogie or cylinder turn). Two track samples are included with different ballast arrangements, along with the Micro-Deval simulation.

The first thing we can observe is that there are not significant differences between samples of the track. In order to see these differences we should zoom in the most solicited grains and we would observe a similar phenomenon that we observed studying the contact forces: the granular network of Sample 2 involves more grains on the strong chains and the secondary network, which leads to a better spread of the efforts and lower peak values. We can observe on the curves that there are more grains on the range 10^{-6} to 10^{-3} J for Sample 2. On the other hand, if we observe the top 5 values for each sample we observe the opposite trend:

	Sample 1	Sample 2
1.	0.0208 J	0.0140 J
2.	0.0197 J	0.0080 J
3.	0.0160 J	0.0075 J
4.	0.0142 J	0.0072 J
5.	0.0106 J	0.0071 J

Table 4.3 Top 5 contacts in terms of friction work for both samples.

A Micro-Deval rotation does indeed produce much more work per grain than a simple bogie passage, and even than a full train passage (i.e. one order of magnitude higher). The top grains in the track are slightly closer to the attrition test by still two orders of magnitude below. The other thing we can notice is the low variance in the Micro-Deval sample compared to the track. This is not surprising since in the cylinder all grains suffer approximately the same efforts, while in the track we combine grains that support the full loading with grains that almost do not work.

So far we have seen the friction work cumulated by each grain, including all contacts affecting

the grain. Let us now study the contacts themselves in order to put together the associated relative displacement, the maximal normal force suffered and the total work absorbed by the contact. This way, we will be able to better understand the different mechanisms that can lead to higher amounts of friction energy and thus to potential wear.

Figure 4.12a shows the cumulated relative displacement per contact during a bogie passage along with the maximal normal force suffered by that contact. The colour scale represents the amount of friction work absorbed by the contact during the full cycle. As we can see, there are contacts of all kinds, especially if we consider the whole track section: some contacts do not suffer neither relative displacements nor important contact forces and some others the opposite. The amount of work follows an increasing tendency in “diagonal bands” when the normal force increases and/or the relative displacement increases, which is not at all surprising considering the definition given by Archard. However, there seems to be an upper limit combining both forces and displacements: either contacts have larger relative displacements or larger normal forces, but both together are not possible.

Figure 4.12b shows only contacts that suffer, at least, a cumulated 0.001 J of friction work during the bogie loading. We can observe how contacts that contribute the most to the total work are indeed part of the strong network (or very close to it), since they all hold an important normal force (> 100 N). But also, they need not to be completely static, allowing a relative displacement of at least $10\ \mu\text{m}$. Again the lines in Figure 4.12b show a clear band, leading to two kinds of generation of friction work: either the contacts suffer loads higher than 1 kN with displacements below 0.1 mm, or they move more but loads stay below 1 kN.

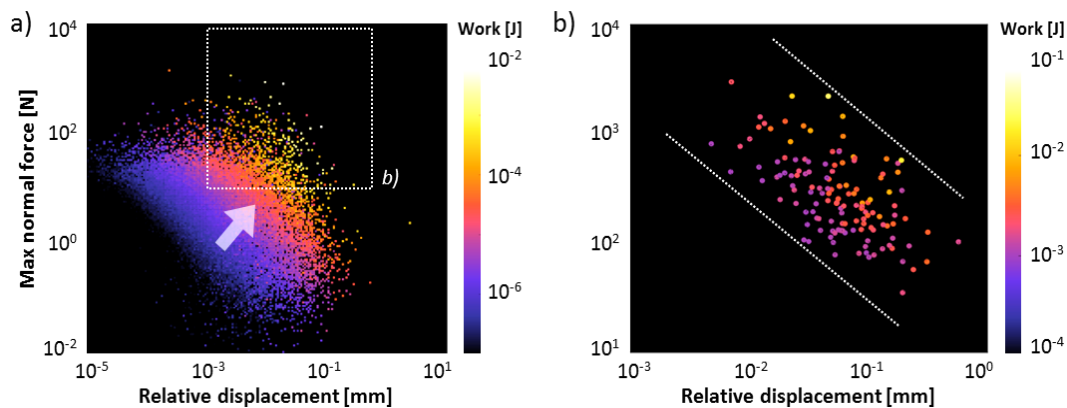


Figure 4.12 Maximal normal force and cumulated relative displacements per contact during a bogie passage for the whole track (a) and for contacts with work > 0.001 J (b).

Looking at the plot on the right, and always looking for the contacts that generate the maximum amount of friction work (yellow or white), we can define a good reference normal loading ranging between 500 N and 1 kN. These contacts represent a realistic worst-case scenario in terms of potential wear, so they are good candidates for the experimental campaign. In addition, they allow for a large range of relative displacements, unlike the contacts that show higher forces but remain completely blocked within the strong chains. As we will see in section 4.3.2, due to technical reasons of the shearing device, we will finally opt to use the upper limit of the proposed range of forces, i.e. 1 kN, as the reference value for the tests.

4.3 SHEARING EXPERIMENTS

Numerical simulations, especially discrete elements, are a convenient tool to know what is happening inside complex systems such as the granular network of the railway track, i.e. at the micro-structure scale. We have shown that they are useful to study how the network works as a whole and to assess the statistical distribution of contact forces and relative displacements, which would be hard to extract from the actual track. Nevertheless, due to intrinsic modelling assumptions, the used simulation techniques are not yet able to give any information about the deformations and breakages of the grains at the contact scale.

In order to know what happens at the contact interface, we need to come back to experimentation, using the data extracted from the simulations as guidance. Once we have extracted from simulations which kinds of contacts potentially generate more fines, we can experimentally reproduce these contacts in order to precisely qualify and quantify wear.

To do so we will be using a 3D shearing device called BCR3D (Boîte de Cisaillement direct pour joint Rocheux à 3 Dimensions) available in the Laboratory 3SR in Grenoble that will allow us to shear two individual grains with the desired conditions (Figure 4.13). The main peculiarity of this device is that all three axes can be manipulated independently, offering a lot of freedom for the application of different loading paths.

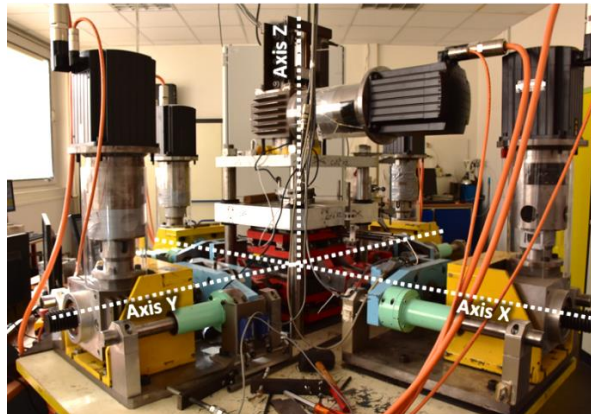


Figure 4.13 BCR3D device. The sample is located inside the red box in the centre.

The shearing tests will be performed imposing a constant normal force and the amplitude of the cyclic displacement. Samples have been scanned before and after the tests using a laser profilometre. A detailed description of both devices is given in Annex A.

4.3.1 Samples

In most of the experiments, two kinds of samples have been used: ballast tip and ballast face (see Figure 4.14). The idea was to perform shearing over what in the simulations we called “simple contacts”, i.e. vertex – face contacts. Of course, as the test evolves and the tip is eroded, the contact area will become progressively larger and we will no longer be able to consider it a single point of contact.

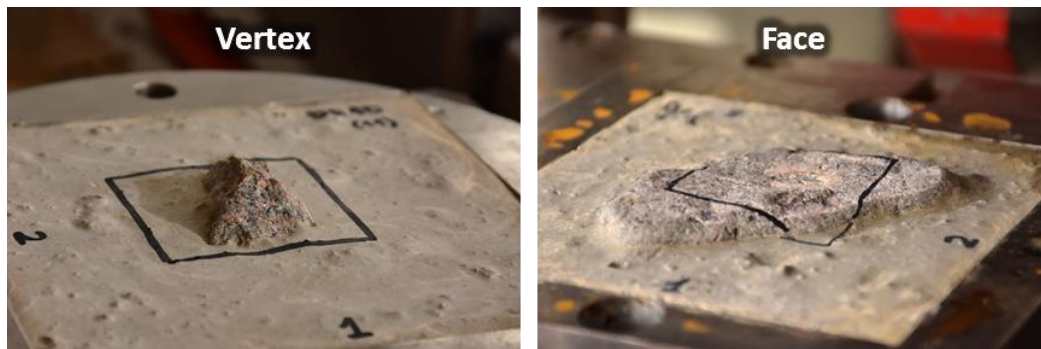


Figure 4.14 A vertex (left) and a face (right) ballast samples. The 4x4 square drawn in black over the sample corresponds to the scanned area. It is important to be sure that the contact points remain inside the scanned area along the test.

In addition, in some tests the ballast face has been substituted by a concrete surface in order to simulate the sleeper – ballast contacts, and also by two kinds of polymeric pads that are used under the sleepers to reduce vibrations and wear (USP). In all these cases, the ballast grain used to shear against was vertex oriented. A detailed explanation of the procedure can be found in Annex A, as well as the corresponding description of the used materials.

4. 3. 2 Known problems and calibration tests for F_z

Like all mechanical devices, BCR3D suffers from friction between the different elements that can affect the response of the machine to the instructions and also induce some measuring errors.

Concerning the first problem, the amount of pieces between the engine and the sample slows down the response of the machine to the instructions, especially if the surface is irregular. For our experiments, one way to solve this issue is just to decrease the frequency of the cycles so we give more time to the device to react. We also changed the type of cyclic wave from a sinusoidal one to a squared one with a speed limit. This way, the regulation forces the machine to go directly to the instruction as fast as possible (with the speed limit), and it has more time to reach it before the end of the cycle if eventual irregularities of the surface make the displacement difficult.

Concerning the measuring errors, they correspond mainly to force measurements. LVDT are located on the sample containers so they measure the actual displacements, but forces sensors are associated to the engines, so all friction is added to the measurement. In most of the applications, this error is not significant compared to the applied forces, but with ballast we are dealing with pretty low forces, so the order of magnitude of the errors becomes an issue.

We have detected that the main component producing friction is the bar connecting the upper container and the horizontal engine. This is why it is so important to keep a good lubrication of the joint. This phenomenon is more noticeable when shearing along the X-axis, instead of the Y-axis. Unfortunately, during a big part of this project, the Y-axis was not available so we had to use the X-axis.

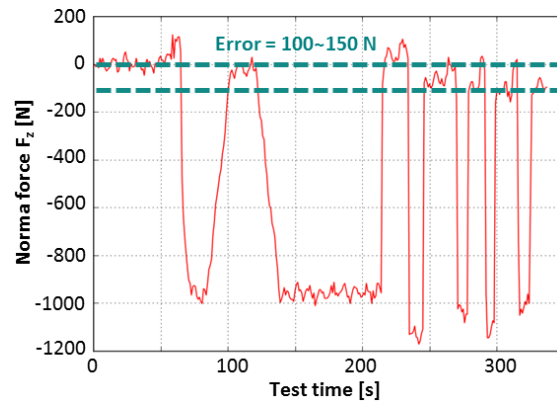


Figure 4.15 Calibration test where the machine was asked to increase the normal force up to 1 kN and return to 0 several times. By the end, a residual force of 100 – 150 N remained.

This connection mainly affects the measurement of the normal force, so a short calibration test was performed in order to assess the order of magnitude of the error. During this test, performed with two ballast samples in a vertex-face contact, BCR3D was blocked in the horizontal axes and asked to move vertically up to 1 kN of normal force and back until losing contact. The cycle was performed several times, so it was possible to measure the residual force remaining even when no contact existed and it should measure zero. Figure 4.15 shows the evolution of the normal force F_z during this calibration test. We can observe how there is an error, both at zero and at 1 kN of around 100 – 150 N.

Since this error comes from mechanical friction, it can be mitigated by taring the forces to zero before the contact after a descending movement. However, we need to take into account that these errors of measure can happen and they represent more than 10% of the actual normal force if we apply 1 kN, and even more if we wish to apply lower forces. For this reason, we decided to avoid applying lower forces and to stick to a minimum of 1 kN.

On the other side of the balance, i.e. when deciding the upper limit for the normal force, the limitation is not the BCR3D but the resistance of granite. During the first campaign of tests, performed on ballast–concrete contacts, some shearing was performed applying normal forces of 10 kN on the first sample, and 2 kN on the second. The result was basically the same: the ballast vertex was almost totally crushed, especially on the 10 kN one. Both tests were programmed to 100 cycles with 1.2 mm amplitude (i.e. a total relative displacement of 2.4 mm per full cycle), but the erosion was so aggressive that they had to be interrupted to avoid both metallic semi-boxes to get in contact with each other.

Figure 4.16 shows the vertical displacement of the Z-axis for all ballast–concrete tests, with respect to the cumulated relative displacement between the samples. We can observe how tests at 2 and 10 kN had a massive descend of the Z coordinate, dangerously reducing the gap between semi-boxes to almost 1 cm, which is approximately the initial gap. The test at 10 kN had to be stopped after barely 20 cycles, while the test at 2 kN had to be stopped after 50 cycles. We can also see how tests at 1 kN do not show such an aggressive behaviour, leading to vertical displacements below 1 mm after completing the full test. The pictures of the sample tested at 10 kN show the total crushing of the ballast vertex, as well as its corresponding deep print on the concrete surface.

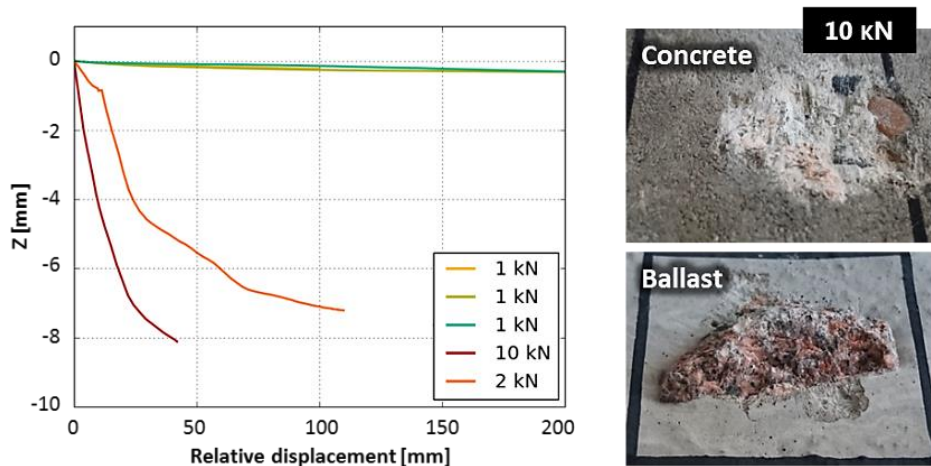


Figure 4.16 Left: Z-coordinate versus cumulated relative displacement on all five ballast-concrete tests. Right: pictures of the sample tested at 10 kN after the test.

Therefore, either due to the granite resistance or to the limitations of the device, we are restricted to 1 kN as a lower and upper limit when performing shearing on ballast using tip-face contacts. However, as we saw in section 4. 2. 5, this value is the upper-limit of the range of representative normal forces for contacts generating the highest amounts of fines, so it becomes a good balance between representability and practical constraints.

4. 3. 3 Test summary

As we have already described, three different kinds of materials have been used to create the samples: ballast (granite), concrete and USP (polymers) (see Annex A for more details about the concrete composition and the two types of USPs). Likewise, we can distinguish two kinds of ballast grains used for building the samples: some samples were created using new grains and some using grains previously eroded through a full Micro-Deval test. Finally, ballast samples can be divided into vertex and face oriented.

During the different campaigns of tests performed in the BCR3D, 26 different semi-boxes have been used, most of them more than once, combining them in different ways. The distribution of the semi-boxes, along with their identification code, is presented in the following table:

Concrete	BE (from "béton")	3
New ballast	BA (from "ballast")	13 (8 tips + 5 faces)
Worn ballast	BAU (from "ballast usé")	8 (4 tips + 4 faces)
USP	SLN & PRA , respectively	2 (1 SLN + 1 PRA)

Table 4.4 Number of semi-boxes of each kind used during the BCR3D campaign.

Even if only 26 semi-boxes were used, most of face oriented samples were worn at different contact points. On the other hand, if they were not broken or too eroded in the process, some of the tips were also reused. This way, a total of 37 tests have been performed, most of them between ballast grains, as we can observe in Table 4.5, where all tests are synthetized.

	Tip	Face	Point	F_v [kN]	Cycles	Air / water	Observations
CONCRETE	BA 1	BE 1	1	1	100		Amplitude = 0.6 mm
			2	1	100		
			3	1	100		
	BA 2	BE 2	1	10	20		Broken tip
	BA 3	BE 3	1	2	50		Broken tip
BALLAST	BA 4	BA 5	1	1	200		Broken tip
			2	1	100		Square cycle
	BA 6	BA 7	1	1	150		Instruction problems
			2	1	150	Air	
		BA 13	1	1	500	Air twice	Instruction problems
	BA 8	BA 9	1	1	150		Broken tip
			2	1	150	Air	
		BAU 8	1	1	200		
			2	1	200	Water	
			3	1	200	Start wet	
	BA 10	BA 11	1	1	150	Air	
			2	1	150		Instruction problems
			3	1-2	346	Start wet	Data lost
		BA 9	1	1	200		
	2		1	200	Water		
	3		1	200	Start wet		
	BA 12	BA 13	1	1	150	Air	
			2	1	150		
			3	1	300	Half test air	Z-captor only half test
	BAU 1	BAU 2	1	1	150		
2			1	150	Air	Instruction problems	
BAU 8		1	0.50 – 1.25	400	Air	Incremental force	
	BA 13	1	1	1059		Electrical problems	
BAU 3	BAU 4	1	1	150		Broken tip	
		2	1	150	Air		
BAU 5	BAU 6	1	1	150	Air		
		2	1	150		Broken tip	
BAU 7	BAU 8	1	1	400	Half test air	Broken tip	
USP	BA 6	SLN	1	3	15		No shearing, only vertical
			2	1	200		
	BA 6	PRA	1	2	15		No shearing, only vertical
			2	1	200		

Table 4.5 Summary of the BCR3D tests.

All tests except the first one in the table and the square cycle were performed on cyclic shearing (one axis) with a cycle amplitude of 1.2 mm (i.e. from -0.6 mm to +0.6 mm), giving a total relative displacement of 2.4 mm per cycle. The square cycle was performed over a square-shape trajectory of 0.6 mm of side, but since it did not offer any different result it will be treated as the others. The frequency of the cycles was 0.015 Hz or 0.020 Hz when the

instructions were not followed properly.

Obviously, once a ballast tip has been tested for the first time, we cannot consider it anymore as new. Faces may still be considered as new if we perform the following test over an untouched area. Thus, after the first campaign of tests, we decided to mix samples without taking into account if they were “new” or eroded. On the other hand, eroded grains, in one way or another, have probably more reproducible results, since the potential local weakness due to sharp asperities have been likely removed during the previous erosion, reducing the probabilities of breakages.

In some tests, compressed air was used to continuously remove the generated fine particles. A flux of air was located very close to the contact point, strong enough to eliminate all fines coming out of the interface. However, it is not possible to ensure the total elimination of fines since most of them are stuck within the interface or attached to the surfaces so strongly that air only is not enough to remove them. Water tests were performed spraying the sample every 20 – 25 cycles in order to keep the sample wet all along the test. On the other hand, “start wet” tests were performed wetting the interface of both ballast grains at the beginning of the test before the contact and letting the sample dry as the test progressed.

Concerning the laser scans, in most of the cases the semi-boxes were scanned before and after each combination with another semi-box, even if more than one contact point was tested. For instance, BE 1 and BA 1 were scanned before contact point 1 and after contact point 3, but not between contact points. We realised too late that this was actually an error since we were losing a lot of information for the future analysis. But in that moment, we failed in anticipating the tools we would develop later. Nevertheless, it was solved for the last tests with water, so semi-boxes from tests BA 8 – BAU 8 and BA 10 – BA 9 were scanned before and after each contact point.

Finally, we can observe some problems such as broken tips or problems for the device to follow the instructions. Broken tips show that even with 1 kN of vertical force, if the face is very rough and there are blockages, ballast weak tips can break relatively easily. In terms of the results, this kind of tests overestimate the amount of matter lost on these shearing conditions. Blockages also eventually lead to problems for the machine to follow the given instructions. This was partially solved increasing the cycle frequency and changing the wave from a sinus to a squared wave.

4.4 FRICTION COEFFICIENT

One of the interests on the shearing test was to establish a proper friction coefficient between ballast grains and between concrete and ballast at the contact scale. The values extracted from the tests serve as a reference and to check whether the values traditionally used in numerical simulations are accurate or not.

Besides, it is interesting to look at the evolution of this coefficient as grains wear, either while

conserving the fines in the interface or removing them. Finally, the influence of the presence of water at the contact was tested, representing for example the rainfall wetting the ballast layer.

Friction coefficient will be computed as the ratio between the tangential and the normal force for each point of the loading cycle, so that:

$$\mu = \frac{F_T}{F_N} \quad (4.22)$$

4. 4. 1 Geometry correction

In terms of forces, as it happens with all shearing devices, the output of the BCR3D device is the horizontal and the vertical force with respect to the machine's system of coordinates. However, ballast surface is not flat but rough and plenty of asperities. Moreover, the best-fitting plane of the face will unlikely be even, but slightly tilted. Both geometric irregularities create micro-slopes that will oppose or facilitate, depending on the sense of the cycle, the relative movement of one semi-box over the other. Due to these slopes, the horizontal and vertical forces measured by the device do not correspond to the actual tangential and normal forces exerted by the upper box over the lower one.

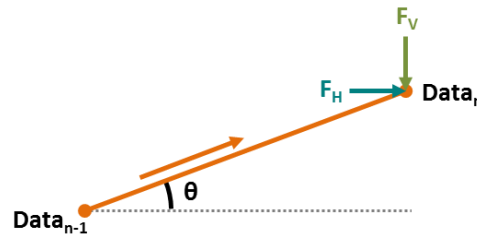


Figure 4.17 Diagram of an uphill movement between acquisition points n-1 and n. Measured values F_H and F_V do not correspond to the actual tangential and normal forces F_T and F_N , due to the inclination θ .

$$\mu_{calc} = \frac{F_H}{F_V} \quad (4.23)$$

$$\text{Upwards:} \quad \mu_{real} = \frac{\mu_{calc} - \tan(\theta)}{1 + \mu_{calc} \cdot \tan(\theta)} \quad (4.24)$$

$$\text{Downwards:} \quad \mu_{real} = \frac{\mu_{calc} + \tan(\theta)}{1 - \mu_{calc} \cdot \tan(\theta)} \quad (4.25)$$

In order to compute the real forces, a simple geometric correction is needed. For that, we will simplify the geometry of the micro-scale as an inclined plane with an angle θ between two acquisition points of the device, being the second the one where we will extract the force measures (Figure 4.17). Let us call μ_{calc} the direct ratio between the measured forces F_H and F_V (equation 5.2). The transformation to obtain the real friction coefficient μ_{real} is then given by equations 5.3 and 5.4.

Since we are taking the angle as an average of the path between point N-1 and point N and not the actual angle at point N, this method cannot be but an approximation, especially when the

surface is very irregular and plenty of asperities. It works much better when the face is almost flat but there is an overall inclination of its average plane. In any case, this approximation offers better and more symmetric results than the direct calculation of μ with the measured values.

This correction is important to properly assess friction coefficient, as this should be a property of the materials in contact, and not depending on the favourable or unfavourable topography. We should expect to obtain the same value whether we move upwards or downwards. There exist other minor agents that can affect the friction coefficient along the cycles, such as the presence of fines, water or strong blockages that are not properly dealt by this method, but the cycles should at least appear approximately symmetric.

Figure 4.18 shows the shearing cycles on a ballast – ballast sample (Point 2 of samples BA12 and BA13) with an overall inclination of the face of about 11° (a). In (b) and (c), we represent the horizontal coordinate on the X-axis, while on the Y-axis we represent μ_{calc} and μ_{real} , respectively, being positive in one direction of the cycle and negative on the other (sign of F_H). We can observe how before the correction, the values of μ_{calc} are significantly different from one way (0.6, downwards) to the other (1.3, upwards). After the correction, both directions show similar values between 0.9 and 1.0.

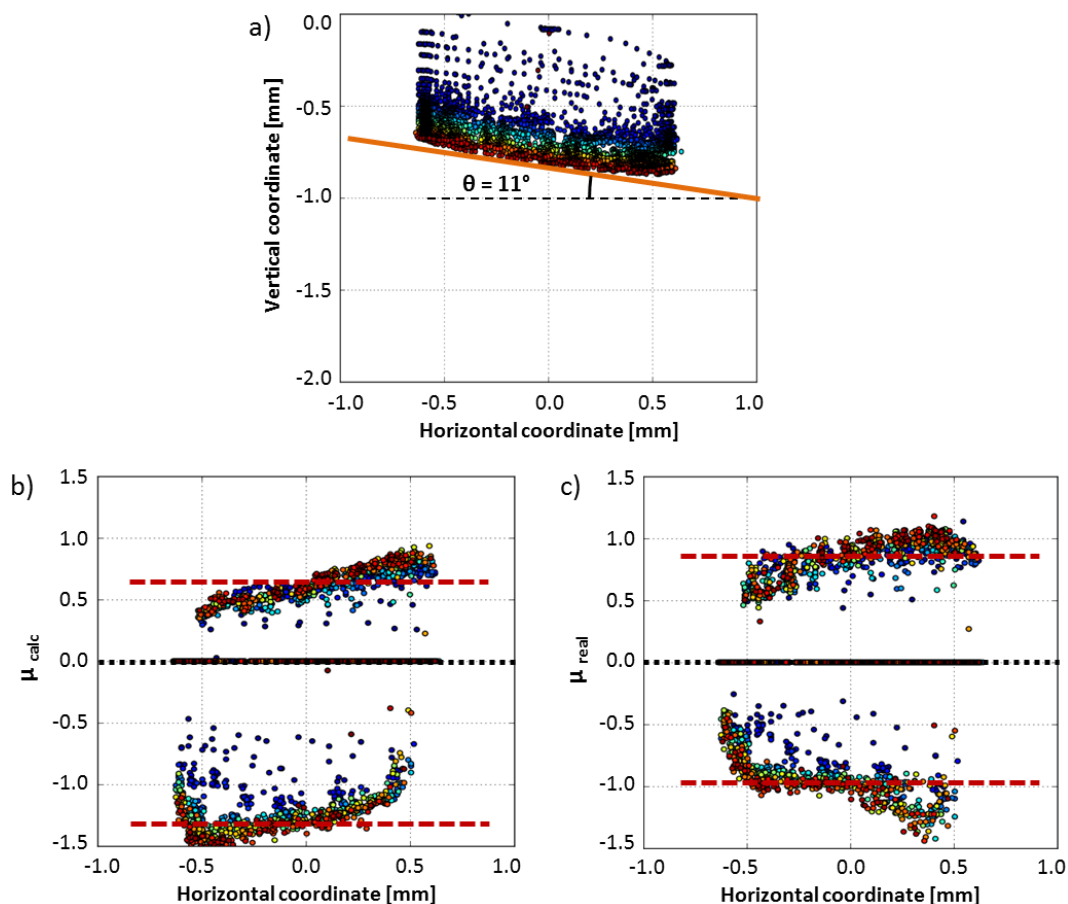


Figure 4.18 Shearing cycles on Point 2 of ballast – ballast sample BA12 – BA13. a) Inclination of the shearing segment represented by the horizontal vs. vertical direction along the test. b) μ_{calc} computed directly from the measured values F_H and F_V along with the horizontal displacement. c) μ_{real} after the correction given by equations 5.3 and 5.4 along with the horizontal displacement. For all plots, colour is added as a time reference to know the chronology of the test (from blue to red).

From now on, friction coefficient will always be computed after the correction and, in order to avoid the peaks of the corners of the cycles, it will be extracted from the half point of each direction, i.e. on the plots above at $x = 0$. Thus, for each full cycle, two values will be extracted corresponding to the mid-point of each direction. μ of the cycle will then be computed as the average of the absolute values.

4. 4. 2 Friction coefficient ballast – concrete

In two of the five tests performed between ballast and a concrete surface, the ballast vertex was totally destroyed before being able to even finish the programmed test. However, all three contact points tested at 1 kN of vertical force showed a very similar, regular and stable behaviour. Even if the first contact point was sheared over half the amplitude of the other two, that does not seem to have affected the response. All contact points were tested over 100 cycles of monotonic shearing.

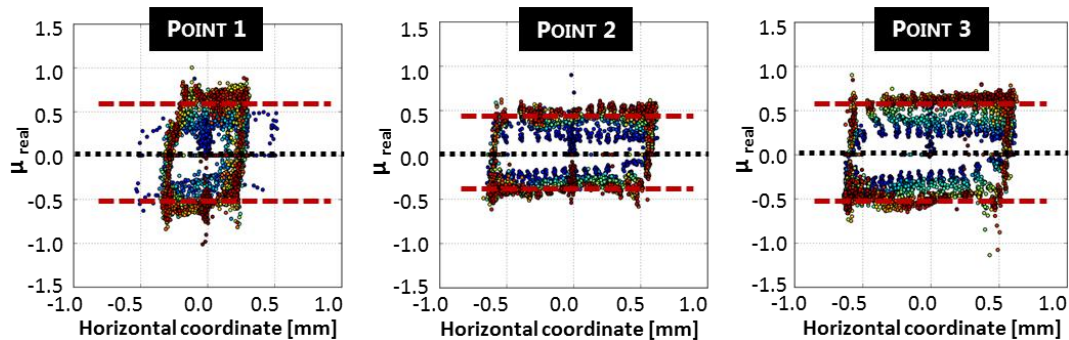


Figure 4.19 Shearing cycles of ballast – concrete test at 1 kN of normal force. Friction coefficient is represented along with the horizontal displacement. Colour is added as a time reference to know the chronology of the test (from blue to red).

Figure 4.19 shows the friction coefficient for all three tests, in the same format as we saw in Figure 4.18. The corrected coefficient μ ranges from 0.4 to 0.6 for all three tests, which is lower than expected. The lower force and a relatively flat vertex reduced significantly the wear on both surfaces, only scratching the superficial coating layer. This layer is mostly composed of cement, which could be the responsible of such a low friction coefficient. In Figure 4.20a we can observe the peculiar shape of the tip that offers a larger area of contact reducing the stress and so the depth of the scratch. We can also see that the footprint left on the concrete is really shallow (around 0.5 mm) and only affecting the cement paste.

Cycles on Figure 4.19 also show that the first cycles (in blue) happen to offer less resistance to friction than the last tests. This is confirmed on Figure 4.20b, where we can see the evolution of the friction coefficient with respect to the cumulated relative displacement for each of the three contact points, as well as for the 2 kN test up to the emergency stop. Friction coefficient seems to progressively increase during the first cycles until it reaches a plateau between 0.4 and 0.6.

The aggressive wear of the 2 kN test does not allow to see this same increasing behaviour, but it is interesting to observe that the friction coefficient remains of the same order of magnitude.

Most of the wear was produced on the ballast tip and the concrete was neither affected deep inside (a maximum of 2.5 mm where the ballast vertex was located, but an overall depth of around 1 mm).

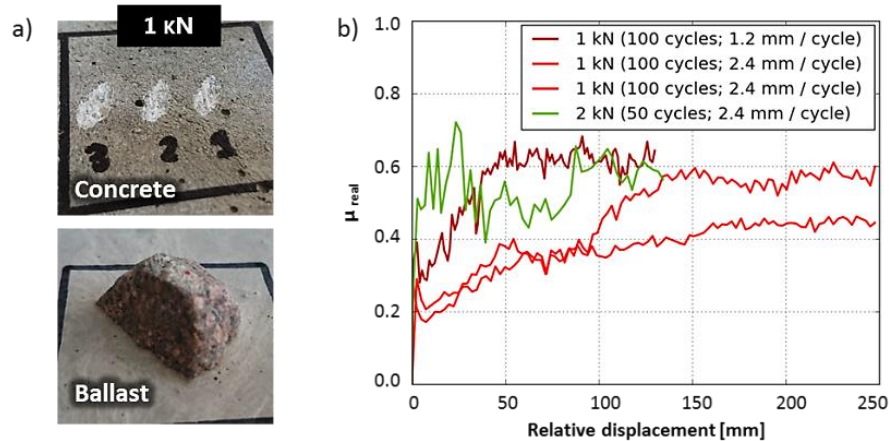


Figure 4.20 a) Picture after the tests of the ballast tip and the concrete surface used for the 1 kN shearing. b) Evolution of the friction coefficient for all three contact points along with the 2 kN test up to the emergency stop.

We can then establish an average friction coefficient between ballast and concrete of 0.5, before too much damage is produced on the concrete so the aggregate forming it is exposed.

4. 4. 3 Friction coefficient ballast – ballast

The irregular surface of ballast grains includes a large quantity of micro-asperities that can create small blockages which will interfere the smooth movement of the vertex over the face. For this reason, the friction coefficient is not easy to compute and will present a relatively large variability between samples.

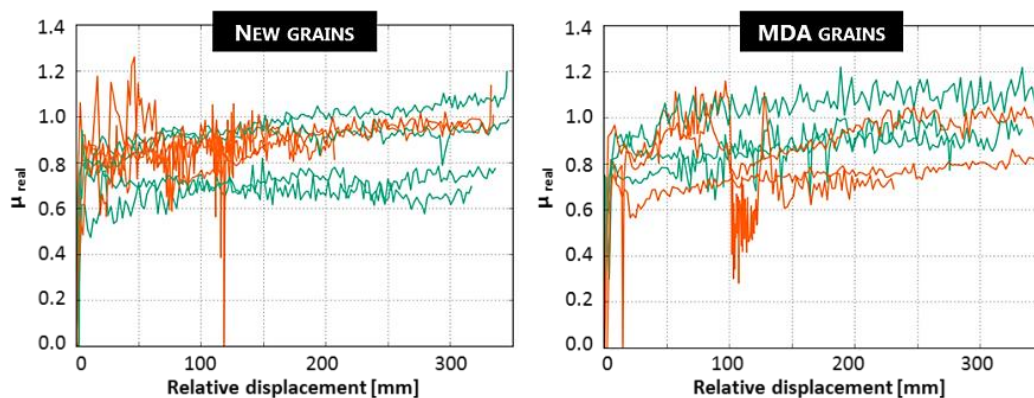


Figure 4.21 Evolution of the friction coefficient during ballast – ballast shear tests. In green, tests performed with compressed air. In orange, tests without air. Left: tests performed on new grains, never worn or only once during a previous shearing test on another contact point. Right: tests performed on grains eroded in a Micro-Deval full test.

Figure 4.21 shows the evolution of the friction coefficient with respect to the cumulated relative displacement for new grains (BA samples) and for samples previously eroded in the

Micro-Deval (BAU samples). Concerning the colours of the curves, in green we represent tests performed with compressed air blowing away fines and in orange tests without air so fines stay and accumulate around the contact. Here there are 14 tests represented corresponding to the first ballast – ballast campaign: 8 for new grains (4 air + 4 no air) and 6 for Micro-Deval grains (3 air + 3 no air).

As it can be observed, the fact that the grains have been or not previously eroded does not affect at all the friction coefficient. The presence of air eliminating the fines seems to neither have a significant relevance. It is true that 4 out of 5 of the vertex breakages were produced on tests without compressed air, but it is difficult to conclude that fines were the actual responsible for them.

We can also observe a slight incremental tendency of the friction coefficient. However, it is not so pronounced as it was on the concrete – ballast tests, and some samples achieve the plateau almost from the beginning of the shearing. The final tendency of the samples seems to have a wide range of values, from 0.7 up to 1.2. Table 4.6 shows the final tendency for the friction coefficients of all ballast – ballast tests where the data was not lost or not useful (e.g. due to a broken tip that remains in the interface producing strange results).

Tip	Face	Point	μ_{real}	F_v [kN]	Air / water
BA 4	BA 5	1	0.8	1	
BA 6	BA 7	1	0.9	1	
		2	0.7	1	Air
	BA 13	1	1.1	1	Air twice
BA 8	BA 9	1	1.0	1	
		2	1.1	1	Air
	BAU 8	1	1.1	1	
		2	0.9	1	Water
		3	1.0	1	Start wet
BA 10	BA 11	1	0.9	1	Air
		2	0.9	1	
	BA 9	1	1.0	1	
		2	0.9	1	Water
		3	1.1	1	Start wet
BA 12	BA 13	1	0.8	1	Air
		2	1.0	1	
		3	1.1	1	Half test air
BAU 1	BAU 2	1	0.8	1	
		2	0.9	1	Air
	BAU 8	1	1.0	0.50 – 1.25	Air
BAU 3	BAU 4	1	0.7	1	
		2	0.9	1	Air
BAU 5	BAU 6	1	1.2	1	Air
		2	1.0	1	

Table 4.6 Final tendency of the friction coefficient for ballast – ballast tests. The conditions of the test are added as extra information.

Although some tests show extreme values of 0.7 or 1.2, most of the tests stay within the range 0.9 to 1.1, with an average of 0.95. If we take a look at the averages in the different groups we could divide the samples (new / Micro-Deval and air / no air), it is not possible to distinguish any significant and conclusive trend: New grains = 0.95, Micro-Deval grains = 0.93, Air = 0.94, No air = 0.92.

It is interesting to take a special look at the evolution of the friction coefficient along the test performed with incremental force (Figure 4.22). This test was performed at the same contact point without losing contact at any moment. Consecutively, 100 cycles were performed at 0.50 kN, 0.75 kN, 1.00 kN and 1.25 kN of normal force, up to a total of 400 cycles. Except for the first 100 cycles at 500 N, the evolution of the friction coefficient shows continuity regardless of the normal force applied, presenting a slight incremental tendency like in the other tests at constant normal force. The increment is relatively small, going from 0.9 at 750 N just to 1.0 at the end of the test at 1.25 kN. Concerning the first cycles, the tendency (about 0.8) is not so far away from the others, but a clear step can be seen after increasing the normal force. However, as we saw in section 4.3.2, a normal force of 500 N is too small for the machine and the error in the measurement can be too high. For this reason, we should treat this part of the plot very carefully.

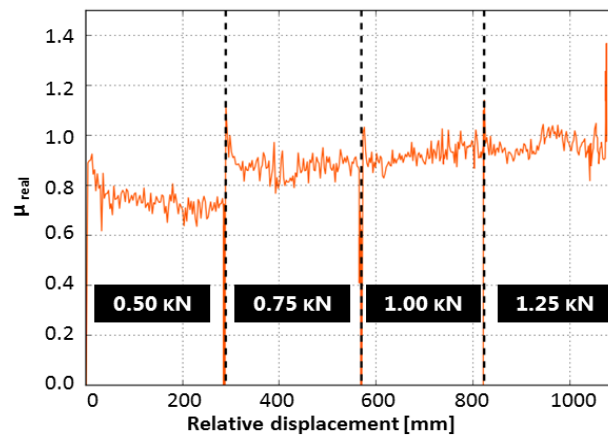


Figure 4.22 Evolution of the friction coefficient for the test with incremental normal force.

In summary, ballast – ballast friction coefficient, once corrected the influence of the local inclination, show values between 0.9 and 1.1, which is considerably higher than the value observed in ballast – concrete shearing tests. This can be considered as a micro-scale value for normal forces over 500 N. The influence of surface roughness can create blockages that will eventually increase the tangential force necessary to progress on the shearing, affecting the value of this coefficient at a macro-scale level. On the other hand, the range of normal forces applied during this campaign is small, so the influence of the normal force cannot be concluded. However, for the studied values (0.5 – 1.25 kN), the behavior of the material concerning friction coefficient does not seem to be affected by the normal force.

Particular cases such as water influence and USP tests will be studied in the corresponding section.

4. 5 MORPHOLOGY OF THE CONTACT AREA

It is obvious that while two surfaces shear one against the other, both surfaces wear inevitably. However, studying what is actually happening at the interface is not evident and it requires extracting conclusions from indirect sources such as the decrease of the Z-coordinate or from incomplete data such as the scans of the surface before and after.

The first method is a direct measure from the BCR3D device and it can inform us about the rate at which this degradation happened during the test. It has information all along the test but it lacks detail and it is not able to differentiate whether wear is coming from the vertex or from the face.

The second method requires an external device, in our case a laser profilometre that will allow us to scan the surfaces of the tested grains. It contains a lot of information, but only for the initial and the final state of the samples.

The goal of this section is to combine both inputs in order to reconstruct the test and understand the mechanisms producing wear at the contact scale.

4. 5. 1 Evolution of the distance between samples (decrease of Z)

Before starting to analyse in detail the contact morphology, there is one interesting result that comes directly from the BCR3D measurements: the decrease of the Z-coordinate, i.e. the vertical distance between the two samples. During the shearing test, due to the produced wear on ballast grains, both metallic semi-boxes become progressively closer to each other. This vertical displacement is registered by the machine all along the test and it can give us information about the rate at which the grains are eroded.

Figure 4.23a shows the evolution of this decrease on a normal test, without incidents. We can distinguish two different phases: the test starts with a very aggressive wear and after less than 50 cycles, the decrease of Z is stabilised and wear becomes much slower. If we do not take into account the numerical values of the decrease, this qualitative tendency is repeated in most of the tests, so it could be taken as a representative example of the typical behaviour. However, the specific moment where this change of phase happens is not the same for all tests. We will see in section 4. 5. 2 that it is mainly related to the specific morphology of each vertex and face in contact and how easy is the adaptation of both surfaces in order to increase the contact area.

It is intuitive to understand the reason of such differentiated phases. When we put a vertex and a face in contact, the contact area is small so it is not able to hold the normal force applied. As wear happens, the contact area increases as the vertex gets wider, reducing the stress. In fact, this situation is applicable to all kind of ballast – ballast contacts, even if both are relatively flat from the beginning. Due to the irregularities, both surfaces will always need to adapt one to the other before the contact area is large enough to sustain the normal force. The depth at which this will happen will then depend on the morphology of both surfaces.

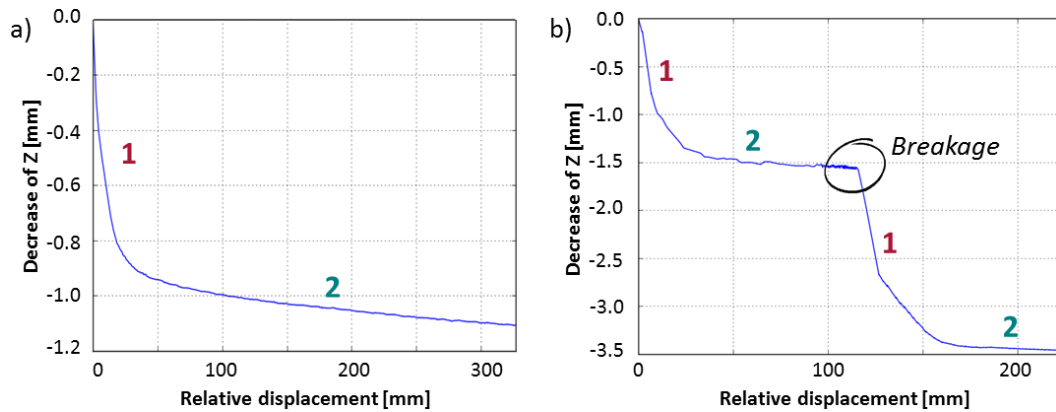


Figure 4.23 a) Decrease of Z on a “normal” test without incidents. b) Decrease of Z on a test with a vertex breakage during the shearing.

When a breakage of the vertex happens, the crack does not necessarily follow the contact plane, and often not even a parallel one. Thus it is not surprising to see that after a breakage of the tip (Figure 4.23b) the process restarts and both surfaces need to readapt again before reaching a more stable wear, i.e. the second phase.

In order to detect the threshold where the change in phase takes place, it is necessary to study in detail the morphology of the contact area in order to try to reconstruct the wear process all along the test, linking all the available information. For that, we scanned each sample with a laser profilometre (see Annex A for more details about the device) before and after being sheared in order to compare both scans.

4. 5. 2 Estimation of the contact area

After seeing the repeated behaviour of the decrease of Z, it seems clear that the contact area has indeed a big importance on the rate of wear. If we are able to estimate the evolution of the contact area, it will also show us the evolution of the rate of volume lost, and a possible threshold in terms of normal stress where the aggressive first phase changes to a softer wear.

In order to estimate the contact area, it is necessary to first reconstruct the shear test. That means to be able to place the vertex over the face in the exact location where the shear test took place. Once detected, we will be able to estimate the contact area at the beginning and at the end of the test and, studying the morphology and the rate of Z decrease, reconstruct the evolution of the contact area all along the test.

However, the laser and the BCR3D are not directly connected, so they do not share the same reference system and coordinates. Therefore this positioning is not straight forward at all. In the following section, it will be explained the positioning algorithm, as well as the hypothesis taken in order to compute the contact area.

Positioning algorithm

As we said during the description of the sample preparation, the scanned area, corresponding

to a square of 4x4 cm, was drawn with a marker over the mortar or the ballast (in the case of faces). In addition, the sample orientation while scanning was also noted down. These steps were needed in order to facilitate the alignment of the scans before and after the test. Of course, this was used only as a good first approach, but afterwards, in the data processing, an autocorrelation function was used to increase the accuracy on that alignment.

However, this method is only valid when dealing with the same sample in two different states, but it is not applicable when comparing the face and the vertex scans in order to locate the test position. For doing that, we will use the idea that we saw before: at the end of the shear test, the vertex and the face have already adapted one to each other. In other words, if we position the vertex over all possible points of the face and we compute the contact area for each of these points, the test must have happened wherever that contact area is larger. Moreover, we should not detect a single point standing out from the others, but a continuous line corresponding to the shear test segment.

Firstly, we need to remember that samples are already oriented, so they do not need to be rotated. Secondly, after the triangulation of the cloud of points, all samples are meshed using a square-grid of 0.1 mm of side. This kind of regular square-grid meshing along with the fact that rotations are not required simplifies the process reducing it to a matrix comparison. Finally, we need to take into account that boxes are not perfect and the scanning support basis is not as stable as desirable, so some slight inclination is expected. For this reason, a tolerance is fixed at 0.15 mm fixing the threshold where both surfaces will be considered in contact or not.

This way, we only need to overlap matrixes and compute the distance between both matrixes inside the overlapping area, which is a sort of 2D auto-correlation but maximizing contact area. We then count the amount of points that are below the tolerance (N) and we calculate the area as the $A = N \cdot 0.1^2$. And we repeat the process for all possible overlapping positions.

Sumarizing the steps :

1. Take the scans of the face and tip at the end of the test. Ensure that both scans follow the same orientation as they were located in the shearing machine. If necessary, rotate one of them 90 degrees to orientate them properly.
2. Flip the scan of the tip upside-down. Again, check that the tip is flipped using the correct axis or it will end up rotated 180°.
3. Put the tip over the face on the first overlapping position.
4. Compute the difference in Z for all overlaping points. Since scans can be performed at different heights and no reference has been given for the origin of Z, negative distances could happen (surfaces "crossing").
5. Substract the minimum distance to all computed distances, so that the new minimum value will be zero: surfaces in contact.
6. Count all points whose distance is below the given tolerance (in our case 0.15 mm).
7. Compute the area as Area = Number of points x Area of a mesh cell (in our case $A = N \cdot 0.1^2$).
8. Proceed to the second checking point, shifting the matrix of the tip one element, and repeat the procedure.

Let us call $F1 \times F2$ the size of the scan of the face and $T1 \times T2$ the size of the scan of the tip, the maximum number of overlapping positions to check will then be $(F1+T1-1) \times (F2+T2-1)$.

Figure 4.24 shows the result of this “correlation” algorithm for one of the tests. As we can see, most of the overlapping positions give areas below 10 mm^2 , but there is a spot that stands out from the others with areas significantly higher, close to 30 mm^2 . When zooming in, we realise that it is indeed a straight line of approximately 1.2 mm , which is exactly the total amplitude of the shearing test.

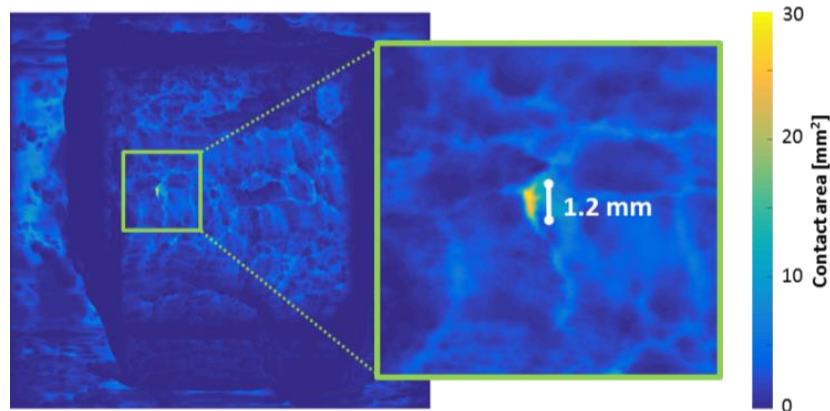


Figure 4.24 “Correlation” of the two scans (tip and face) at the end of the shear test (1st contact point of samples BA 9 and BA 10), searching for the overlapping positions so that the contact area is maximal. Thus, the colours express the contact area for each overlapping position, so that the shearing segment should appear as a straight line of the same length, corresponding to the trajectory during the test.

Once we know the test position, we can put the tip on that exact position and start the analysis. Figure 4.25 shows the three contact points for the test between samples BA 9 and BA 10 highlighting the contact area.

Of course, once we know the positioning at the end of the test, it allows for automatically knowing the position at the beginning of the test, thanks to the autocorrelation between the scans before and after. This way it is possible to compute the contact area at the initial position.

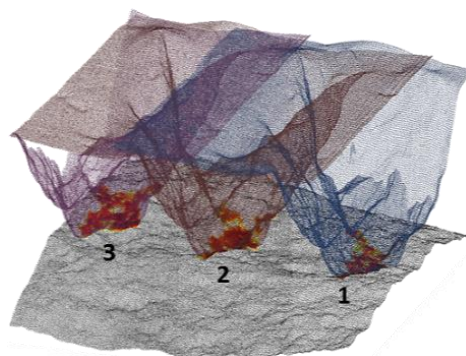


Figure 4.25 The tip (BA 10) placed over the face (BA 9) on all three shearing positions used.

This method has been extremely useful and efficient for detecting the shearing position and analysing contact areas. However, it is based on the adaptation of one surface over the other and that depends on the specific morphology of each contact area. The scans of the tip at the

end of each single shearing position are absolutely required. Concerning the scans of the face, only those before and after all contact points are needed, as far as contact points do not overlap with each other, i.e. the “scratches” are not overlapped.

Unfortunately, this code was developed after most of the tests were performed. In consequence, and due to a lack of prevision, many tests were performed over more than one contact point before rescanning, i.e. we only have the scan before all contact points and after the last one. This is not enough to take full advantage of the potential of the code. Only the last tests were performed properly, rescanning the samples after each single contact point. Thus the deeper and more detailed analysis in the following sections will be reduced to those tests, and the others will only serve as additional information.

Results

In order to better understand the behaviour in the two phases shown in the decrease of Z , it is necessary to first analyse and compare the initial and the final conditions of the test.

Figure 4.26 shows the initial and the final state for the test between BA 9 and BA 10 (first contact point). The scan images correspond to a top view with their corresponding contour lines, the upper ones corresponding to the scans of the face (BA 9) and the lower ones to the tip (BA 10). The colours represent the distance between surfaces, considering as contact everything below 0.15 mm. The profiles below are a vertical cut, corresponding to the green line on the scans, of both surfaces in contact.

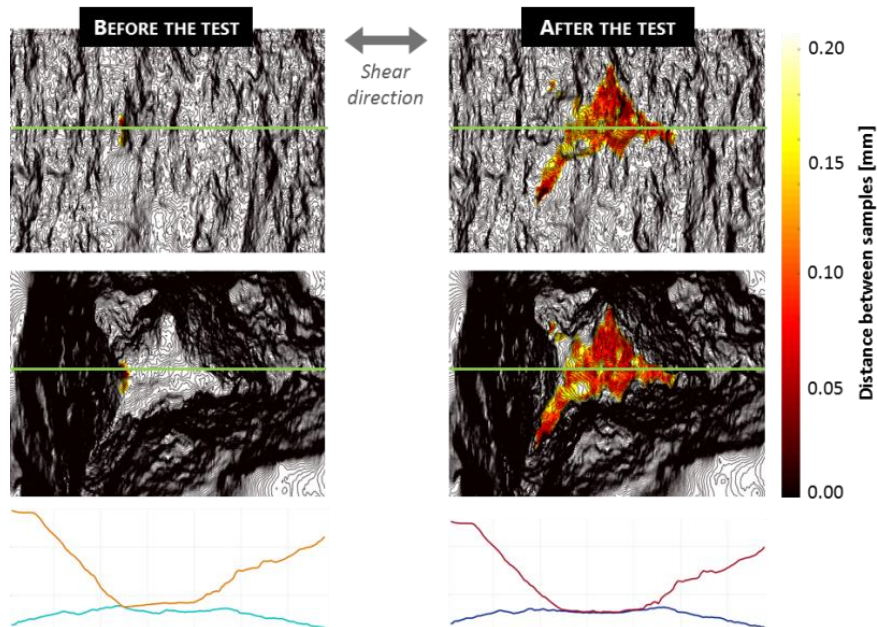


Figure 4.26 Scans of the samples BA 9 (Face) and BA 10 (Tip). The colours show the points whose distance between samples is closer than 0.15 mm. Below a cross vertical section (represented with a green line over the scans) of both surfaces in contact.

Several things can be extracted from these images. The first and most obvious is the significant increase in the contact area. At the beginning of the test, the contact area is very small, almost

a single point as it can be appreciated in the profile below. However, by the end of the test, both surfaces have eroded and adapted one to each other so that the contact area is much larger. In fact, the average contact area along the test segment evolves from barely 1 mm^2 up to 26 mm^2 . Or if we talk about normal stress, considering the applied normal force of 1 kN , it evolves from 1 GPa to a much less aggressive 38 MPa , enough to be held by granite.

Looking at the contour lines, we can observe how the surfaces in contact at the end of the test are not flat at all: they present a lot of asperities. The adaptation process is complex and factors such as previous asperities on both samples, heterogeneities of the material, small breakages, etc. can affect the final morphology of the contact.

As a consequence of these irregularities, we can expect the contact area not to be constant along the test segment. Moreover, the vertical coordinate Z will not remain constant along the segment, so even at the end of the test, the shearing will not be completely horizontal. This phenomenon was already observed in the raw data of the Z -coordinate, where some oscillations appeared in every cycle (in Figure 4.23 they were deleted by taking a single value per shearing cycle, searching for a better visualisation of the evolution of Z).

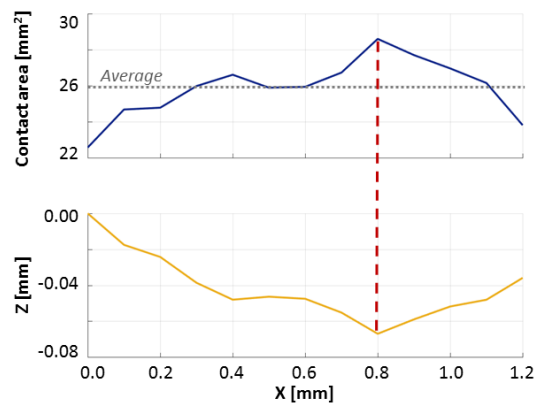


Figure 4.27 Evolution, at the end of the test, of the contact area (up) and the Z -coordinate (down) along the test segment of 1.2 mm .

Figure 4.27 shows the evolution of the contact area and the Z coordinate of the tip along the shearing segment of 1.2 mm , at the end of the test. We can observe how contact area is indeed not constant, oscillating considerably from 22 to 28 mm^2 . Looking at the evolution of the Z , it seems to be directly related to the morphology of the contact. Even if the variation of Z is small (less than 0.1 mm), maximal contact area corresponds exactly to the lowest point in the segment when a valley is formed. This valley allows for additional contact area on the slopes of the valley.

These irregularities were responsible for the different blockages and difficulties for the machine to perform the shearing. They are also the reason of the geometry correction and it is important to be aware of them to understand how shearing and wear works at the micro-scale. However, from now on and for the sake of simplicity, only the average value along the shearing test will be taken into account for the contact area.

Looking at the final values of ballast – ballast tests (Table 4.7), we can observe that for relatively short tests (100 to 200 cycles), where after the change in phase the Z did not change

significantly, the final contact area is quite consistent between 20 and 30 mm², i.e. corresponding to a pressure between 30 and 50 MPa.

Tip	Face	Point	F _v [kN]	Cycles	Contact area [mm ²]	Pressure [MPa]
BA 4	BA 5	2	1	100 (square)	33.3	30.3
BA 6	BA 7	2	1	150	20.1	49.8
BA 8	BA 9	2	1	150	27.1	36.9
	BAU 8	1	1	200	23.6	42.4
		2	1	200	20.2	49.5
		3	1	200	26.3	38.0
BA 10	BA 11	2	1	150	19.1	52.4
	BA 9	1	1	200	25.9	38.6
		2	1	200	26.2	38.2
		3	1	200	32.5	30.8
BA 12	BA 13	2	1	150	26.7	37.5
		3	1	300	30.5	32.8
BAU 1	BAU 2	2	1	150	29.9	33.4
	BAU 8	1	1	400	22.9	43.7
	BA 13	1	0.50 – 1.25	1059	50.5	24.8 (end)
BAU 3	BAU 4	2	1	150	18.8	53.2
BAU 5	BAU 6	1	1	150	20.1	49.8

Table 4.7 Final contact area for the ballast – ballast tests.

So far we have seen the initial and the final state of the samples but, in order to have the full picture of the test, it would be desirable to know how this evolution happened during the shearing. This way it would be possible to detect more accurately when and why the change in phase takes place.

4.5.3 Evolution of the contact area

Due to the limited amount of available data, the inference of the complete test becomes tricky and requires some interpolation. As we have seen, we have the initial and the final state of the samples, we can accurately position vertex and face at the shear segment and align scans before and after to compare them. We can also compute the decrease of Z by two different ways: comparing scans and from the direct data of the BCR3D. In addition, the BCR3D not only gives the total decrease of Z but its evolution along time. The idea now is to link all this information in order to assess the contact area at each moment of the test.

Methodology, hypotheses and assumptions

We will use an example in order to describe the followed methodology. It corresponds, again, to the first contact point of the test between samples BA 9 and BA 10.

First of all, let us compute the decrease of Z from the scans. To do that, we can simply align the

scans of the face before and after and place the respective scans of the tip in the corresponding initial position. We can then compare the difference in Z between both scans of the tip. For an easier visualization, Figure 4.28a shows the alignment of the 2D profiles, where we can observe a difference of 1.29 mm between the profiles of the tip. Of course, this means that, due to wear on both surfaces, the tip has descended 1.29 mm with respect to the face.

Since the lower semi-box (face) was vertically fixed, the Z coordinate recorded by the BCR3D is that of the tip, so both values should coincide or be very close. Indeed, the BCR3D had registered a total decrease of Z for this test of 1.14 mm. Detecting the exact moment of contact in the BCR3D is not always evident and some wear can occur when applying the normal force before the start of the shearing, so we can consider the difference between values as acceptable. We assume that the values extracted from the scans are more likely to be accurate.

Let us consider the 1.29 mm as the real value. We insist: that is the amount of Z the tip has descended by the end of the test, no more than that. Let us now take the initial position and initial state of both surfaces (before shearing). Leaving the face fixed, we descend the tip 1.29 mm, overlapping it inside the face (Figure 4.28b). The overlapping area corresponds to points of both surfaces that could potentially be in contact by the end of the test (red zone in Figure 4.28c). At all other points (green zone) the initial distance between face and tip is higher than 1.29 mm, so it is not possible that those points will be in contact by the end of the test.

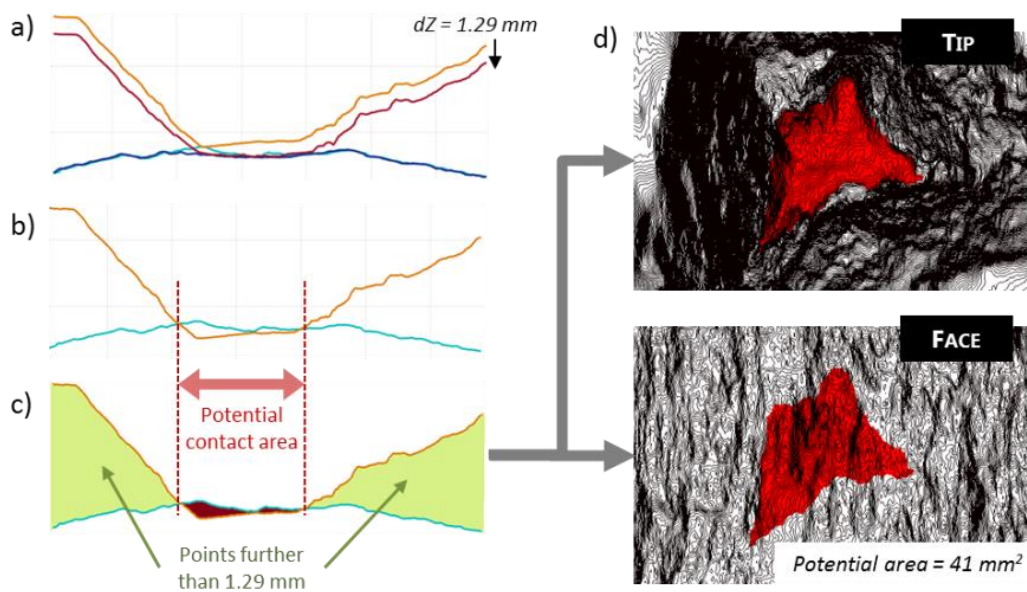


Figure 4.28 a) Alignment of the profiles of the face before and after the test, placing the respective tip in contact. We can then compute the decrease of Z. b) The tip “new” is sunk in the face “new” the decrease of Z. c) The overlapping (red) corresponds to potential points in contact at the end of the test, while the green zone corresponds to points that are too far to become in contact by the end of the test. d) The overlapping seen on the scans of the tip and the face.

Back to the 3D, Figure 4.28d shows this overlapping area on the scans of the tip and the face. The overlap covers a projected horizontal area of 41 mm^2 , which is considerably higher than the 26 mm^2 of contact area computed in the previous section for the same test (see Table 4.7). This is because this overlap only corresponds to points that could potentially, but not necessarily, become in contact. Breakages can occur during the wear process removing

fragments of both surfaces. Besides, as we have seen, the contact area is not flat at all but irregular and asperities can leave small voids where the surfaces are not in contact. Finally, shear is applied over a segment and the adaptation is performed to fit the best over the full segment, so points that are in contact at one extreme could not be in contact at the other.

In fact, when placing in contact the tip and the face before the test, we can calculate the distances between points and compute the area covered by points closer than a certain distance D . Figure 4.29 shows the area covered by points closer than a distance D at the beginning of the test. We can observe how points that are closer than the decrease of Z of 1.29 mm cover the computed area of 41 mm².

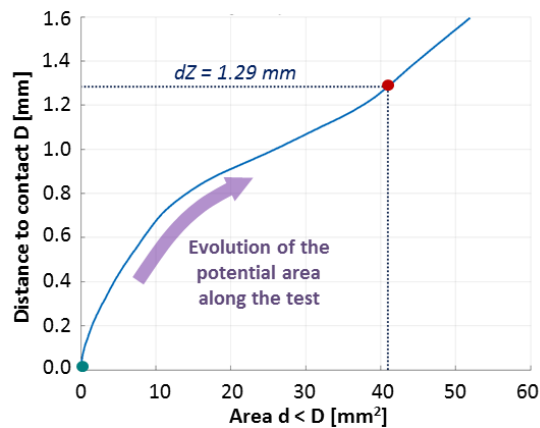


Figure 4.29 Area covered by all points where the distance between the face and the tip is less than D .

We can then extrapolate this procedure to all intermediate points between 0 mm and the final dZ of 1.29 mm. For example, when the tip has descended 0.8 mm, the potential contact area would be 14 mm².

However, as we have seen before, these values correspond to the potential areas. Since we do not have more information, we will make the assumption that the ratio between real and potential area, i.e. between 26 and 41 mm², is kept during the full test. The ratio between potential and real area can then be expressed as:

$$\lambda = \frac{A_{Rf}}{A_{Pf}} \quad (4.26)$$

Where A_{Rf} is the real contact area at the end of the test extracted from the scans following the methodology explained in section 4. 5. 2 and A_{Pf} is the potential area at the end of the test computed following the methodology above. Note that this ratio will be computed for each specific test. This way, in the intermediate point of the previous example, i.e. when the tip has descended 0.8 mm, the real contact area would be $A_{Ri} = \lambda \cdot A_{Pi} = 26/41 \cdot 14 \approx 9$ mm². This is of course an approximation, since it would require several scans along each shearing test to track a possible evolution of λ . Nevertheless, since we are only using tests where no major breakages happened, we can expect a relatively soft wear where layers are erased progressively and points get in contact in a pretty smooth way, so λ is assumed to remain relatively constant.

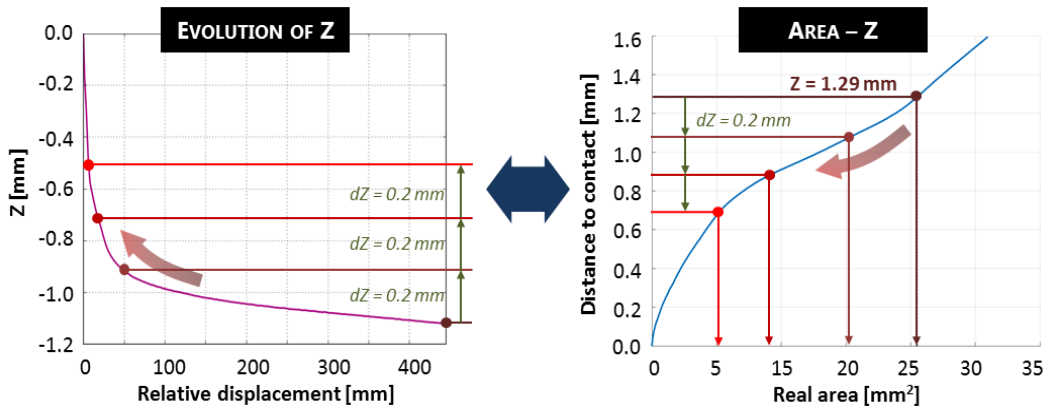


Figure 4.30 Combination of plots of evolution of Z (like Figure 5.26 but for this specific test) and area to Z (like Figure 4.29 but with real area instead of potential, i.e. once the ratio is applied), on a backwards procedure. Using together the information of both plots we can assign an area to each Z.

Once we know the real contact area corresponding to each decrease of Z during the test, we can then take the actual data of the evolution of Z registered by the BCR3D and do a backwards analysis. Starting from the end of the test and assigning to that Z the final computed area of 26 mm², we will go backwards on the Z evolution curve progressively assigning the corresponding contact area to each Z. We have chosen to proceed backwards because, as we have already said, there may be some imprecisions while detecting the starting point of the test on the Z-data from the BCR3D, so it is more accurate to start from the end where we are sure that the measurement of Z is correct. Figure 4.30 summarizes this procedure.

Results

The final idea of all this procedure is to observe how the wear rate changes depending on the contact area. The wear rate will be given by the derivative of the evolution of Z. Hence, we finally have a contact area and a wear rate for each instant of the test. Figure 4.31 shows the evolution of wear rate, in the form of the rate of decrease of Z in comparison to the horizontal relative displacement, as the contact area increases.

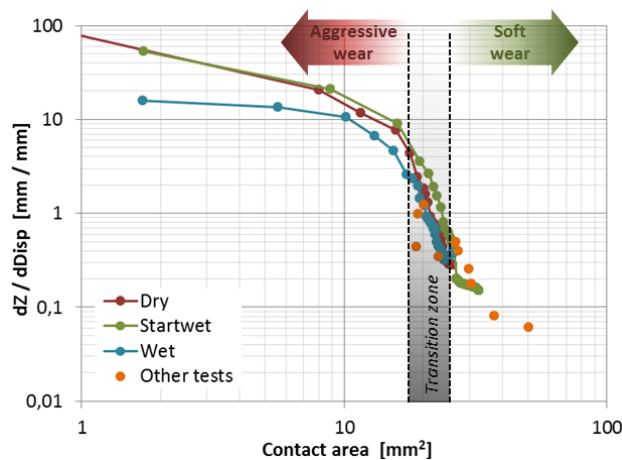


Figure 4.31 Evolution of wear rate in comparison to contact area for three different tests. In orange, we have added the final points of other tests performed in dry conditions, where the reconstruction was not possible but we know the final data point.

We can distinguish up to two phases and a transition in-between, although the last one does not have enough data to clearly show up. During the first phase, contact area is very small, below 10 mm^2 , so wear is very aggressive shown by a high decrease of Z in comparison of the shear relative displacement. Between 17 and 25 mm^2 , the wear rate drops dramatically while the contact area stays relatively constant. This phenomenon corresponds to the quick change in the slope we have already seen in the evolution of Z , so it is in fact the transition between the two phases. Finally, the second phase, corresponding to a much softer wear, is defined by a much slower wear rate that, as a direct consequence, needs many more cycles to erase layers and increase contact area. This last phase needs further research since much longer tests need to be performed in order to reach larger contact areas.

Therefore, contact area plays a crucial role on the wear process. When two surfaces get in contact for the first time in a specific area, due to the irregular nature of surface texture of ballast grains, the contact point will present a very small contact area. This will of course induce very high stresses that will lead to fast wear and even breakages at the micro-scale. As wear proceeds, both surfaces progressively adapt to each other increasing the contact area. Once a critical area is reached, where the material is able to support the normal forces while shearing, the wear rate is significantly reduced. This critical area will of course depend on the mechanical characteristics of the material. For high-performance granite and 1 kN of normal force, we can establish this transition at around $17 - 25 \text{ mm}^2$, which corresponds to a normal stress of $40 - 60 \text{ MPa}$.

We can then expect this two-phase process to happen on every new contact within the track. During the first cycles after ballast renewal or after a rearrangement (e.g. due to tamping), an adaptation process, i.e. a higher wear rate, is expected. After this first phase, a second and softer phase is reached and generation of fines is reduced. The number of cycles to reach the critical stress will change on each contact, depending on the contact force applied and the specific morphology of the contact.

4.5.4 Volume loss

The loss of volume or mass during the test is a very complex process. Even when major breakages are not produced, micro-breakages can happen and smooth wear is often an exception. In addition, due to the complex morphology of the surface, contacts usually happen over more than one contact point, even when dealing with tip – face contacts. These subtleties can be identified analysing the laser scans. For example, Figure 4.32 shows the images of the scans before and after a shear test of a tip-oriented grain. In the middle, we can observe the difference between both images given by the colours drawn over the scan before the test. Three different zones of wear have been identified: in 1 we can observe a micro-breakage that erases a relatively big chunk of the tip transforming the bottom-left leg of the tip; 2 and 3 represent two other contact points where wear was produced in a much smoother way, only eroding some layers of matter.

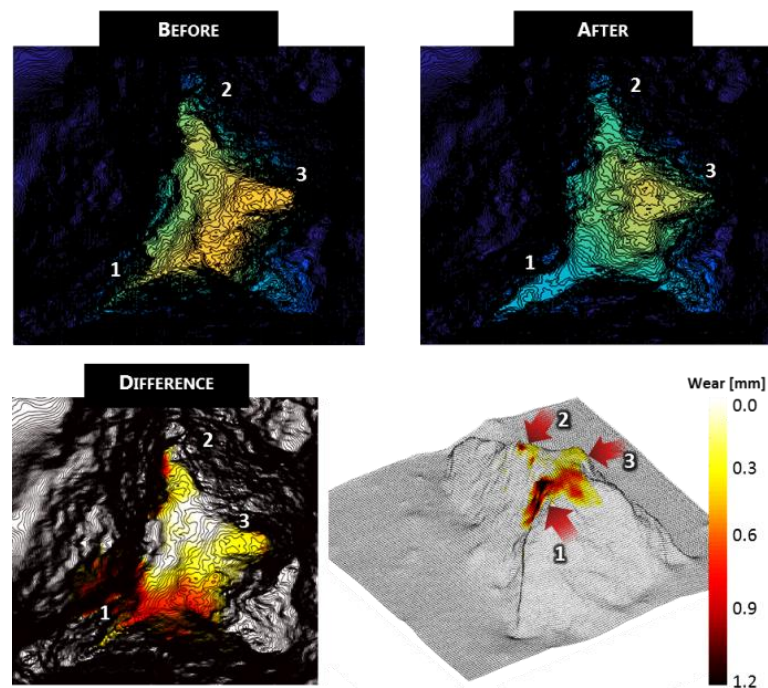


Figure 4.32 Difference between scans before and after the test. Three different zones of wear have been identified, including a micro-breakage (1) and smooth wear (2 and 3).

This irregular phenomenon happens on all tips and faces. Wear will be then produced depending on where the pressure is applied and also where the weakest parts of the grain are. Tips often present weaker parts than faces so volume lost by them is usually higher than by faces, but it is not always necessarily like this.

Surface comparison is very sensitive to small errors in the scans like slightly different inclination or the problems of the sensor when dealing with vertical faces. When this happens, computing the volume is not a simple operation of subtraction, and some filters need to be applied. This is why the specific values given in the following table need to be taken with caution, more as an order of magnitude than as an exact value.

Table 4.8 shows the volume lost in different tests by both the tip and the face (summed up). In red, we have highlighted the tests where a major breakage of the tip happened. We can observe that the order of magnitude of the volume lost is pretty similar among tests. However, this volume will vary depending on several factors. The major reason of volume loss are, obviously, major breakages that erase a big portion from one of the two surfaces, usually from the tip. But even if there are not major breakages, as we have seen during the analysis of the contact area, the volume loss will be directly depend on how close to adaptation are both surfaces, i.e. how much matter needs to be eroded to get to the critical area and this will depend on the initial state of both surfaces and on the morphology of the specific contact point.

Once reached the second phase, wear is so slow that the amount of cycles is not very relevant due to the high influence of the first phase (if longer tests were performed, the second phase would have a higher influence). Instead, the number of contact points has a larger influence since the second phase needs to be reached at each contact point. In addition, either through a

Micro-Deval test or because they have been previously used in other shearing tests, worn tip-oriented grains present a much flatter vertex, which will commonly need less matter to get adapted to relatively flat faces.

Tip	Face	Cycles	Volume loss [mm ³]
BA 4	BA 5	250 (2)	144.4
BA 6	BA 7	300 (2)	40.0
BA 8	BA 9	300 (2)	50.1
	BAU 8	200 (1)	8.6
		200 (1)	4.5
BA 10	BA 11	300 (2)	16.0
	BA 9	200 (1)	12.4
		200 (1)	7.8
BA 12	BA 13	300 (2)	18.6
		300 (1)	11.2
BAU 1	BAU 2	300 (2)	25.5
	BAU 8	400 (1)	5.4
BAU 3	BAU 4	300 (2)	40.9
BAU 5	BAU 6	300 (2)	21.6

Table 4.8 Volume loss during the different tests by the tip and the face together. In red, the tests where a major breakage happened. The number of cycles performed and the number of contact point (in brackets) are added as extra information.

This tendency was already observed in the previous chapter, where the morphology of the grains was tracked and we analysed the evolution of the asperities. Asperities that present a higher convexity like new tips erode faster and disappear during the first cycles of erosion. On the other hand, asperities with larger radius, even if they are not completely flat, erode much slower and are able to better resist normal forces. As asperities become flatter, they adapt to contacts quicker in time and in matter lost.

4.6 INFLUENCE OF WATER

During the Master Thesis of Stocco [99], we studied the influence of water not only in Micro-Deval (as exposed in section 2. 4. 2), but also in cyclic shearing in the BCR3D. Three contact points have been performed on two different couples of semi-boxes:

1. Dry conditions
2. Wet conditions spraying the sample with demineralized water every 20-25 cycles, keeping the interface wet.
3. Start wet conditions, i.e. the interface was only wet at the beginning of the test and progressively dried during the test.

Visual inspection of the sample

The first thing we notice when shearing in wet conditions is that water mixes with the generated fines, creating a paste (see Figure 4.33). However, unlike it happened in the Micro-Deval, since this is a much more static system, water does not act as a cleaning agent but this paste of water and fines gets trapped and accumulates in the interface.

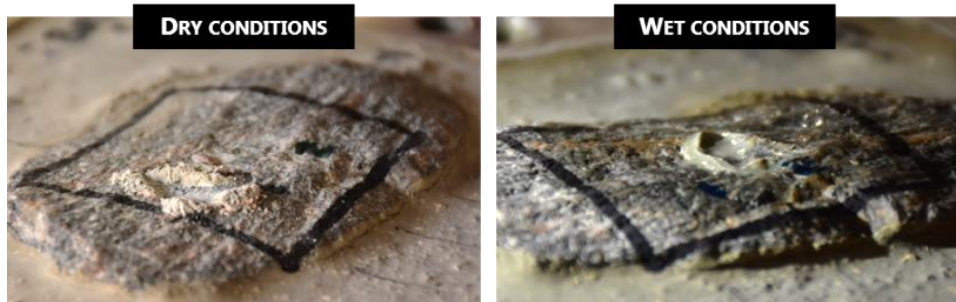


Figure 4.33 Visual inspection after a shearing test in dry conditions (left) and in wet conditions (right).

In dry conditions, most of fines are pushed away from the interface and accumulate in the surroundings of the contact area. In tests performed with compressed air, these fines are automatically removed from the sample, only leaving the fines that are stuck inside the interface. Once the test is finished and the sample is removed from the machine, the fines can be easily cleaned by just applying some air.

On the other hand, in wet conditions the paste spreads all over the interface and covers the micro-pores. It still accumulates on the surroundings of the contact area but its cohesion does not always allow for an easy air-removal. In fact, when the test finishes, if the paste is wet it can be easily cleaned with a piece of paper, but if it is dry like in the case of the “start wet” tests, it gets strongly glued to the granite surface. Compressed air only serves to erase the superficial layer, but if we want to completely clean the sample, we will need to scratch the paste with a fingernail or a soft tool (to avoid damaging the sample).

Friction coefficient

Figure 4.34 shows the evolution of the friction coefficient for each of the two samples and for each of the three contact points on each sample. We can observe that the friction coefficient for all the tests show a final tendency within the values observed in section 4. 4. 3, i.e. between 0.8 and 1.1.

When comparing the different test conditions, it seems that the presence of water has indeed a slight influence in the friction coefficient. Tests performed in wet conditions present a μ around 5-10% below dry condition tests. However, on the second sample, we observe a similar start of the test where all three contact points evolve in the same way during the first cycles.

It is not surprising that the paste formed when fines and water mix can have an influence on the interface behaviour. The limited number of experiments performed should be considered carefully when emitting conclusions, but a slight influence may indeed be real.

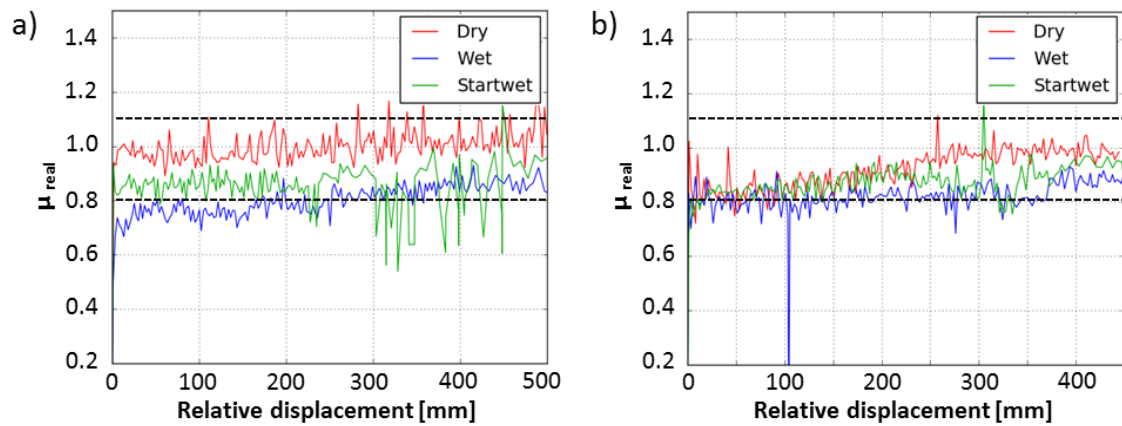


Figure 4.34 Evolution of the friction coefficient μ for wet condition tests for samples (a) BA10 – BA9 and (b) BA8 – BAU8. The order of the tests on both couple of semi-boxes was dry – wet – start wet, each performed over a different contact points.

Critical area and wear rate

On the other hand, critical area and volume loss do not seem to be affected by water. Figure 4.31 already showed that for all three types of test conditions the critical area takes the same values.

The only thing that could affect this subject is the paste changing the morphology of the interface. After each test, the surface of both grains was cleaned using air and scratching the surface with a paper and/or a fingernail. However, part of the paste, got so stuck to the granite, especially when filling small pores, that it was not possible to erase everything. The grains were then scanned with this little part of paste included, slightly changing the morphology and perhaps the computation of the contact area. In any case, the influence of the paste should be very small and we do not think it changed significantly the given values.

The wear rate does not show any clear tendency involving water, neither at the beginning of the test nor at the end. If there is any kind of influence, the pace at which samples are eroded depend so much on the morphology of the contact area that the presence of water is an insignificant factor. Moreover, since for these tests the volume loss depends mainly on the amount of matter necessary to reach the critical area, and the critical area is the same, the total amount of eroded matter will not depend on the presence of water.

4.7 USP TESTS

As explained in the preparation of the samples (section A. 1. 1), two kinds of Under-Sleeper Pads have been tested, a harder one (PRA) used to reduce ballast wear and a softer one (SLN) used to reduce mechanical vibrations. The USP have been tested against the same tip-oriented ballast grain (sample BA 6). This ballast sample had been previously used on other shear tests, but it was still in a particularly good condition. On each USP, we performed four kinds of tests:

- A vertical cyclic test (20 cycles at different forces / displacements) in order to test the rigidity of the pad and to test the maximum depth a grain could go inside the pad.
- A shear test (200 cycles) in the same conditions as the ballast – ballast tests, i.e. at 1 kN of normal force and with an amplitude of 1.2 mm (± 0.6 mm).
- A shear test (30 cycles) increasing the amplitude to 1 cm (± 5.0 mm).
- A shear test (4 cycles) increasing the amplitude to 2 cm (± 10.0 mm).

Rigidity

During the vertical tests, several sets of cycles were performed reaching normal forces high above the ones used for the shear tests. On both USP we overpass 2 kN without breaking nor wearing the ballast tip. This force can also be reached on ballast – ballast samples without breaking the tip if shearing is not applied, but wear will always be produced due to the hardness of the materials. Figure 4.35 shows the evolution of these cycles in a normal force – vertical displacement chart.

The first thing we notice is the difference in deformation of each USP. PRA allows for a deformation of 3 – 4 mm before reaching 3 kN of normal force. As an attrition reduction pad, its elastic range is long enough to permit much more deformation than concrete, but it is conceived to be used along the entire track and during long time, so it needs to be hard enough to ensure the stability of the track and to recover the initial position every single time during thousands of cycles.

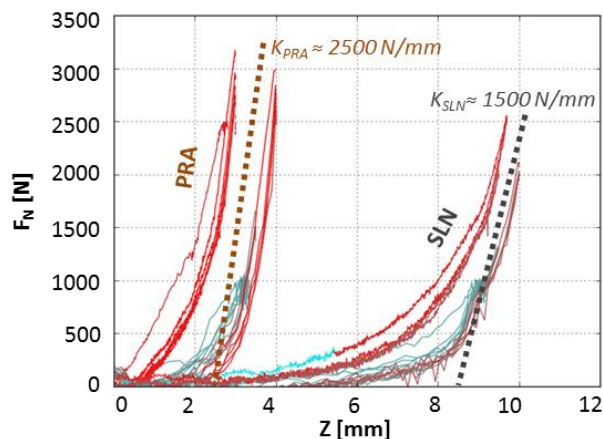


Figure 4.35 Normal force vs. vertical displacement for the vertical cycles of both USP.

On the other hand, SLN is a much softer pad used to reduce vibrations in specific locations, usually close to urban areas where trains usually travel at lower speeds. As we can see, it allows not only for deformations over 9 mm at 2 kN of normal force, but also deformations over 5 mm before the increase of normal force starts to be noticeable. That means that ballast grains will be permanently “sunk” into the pad due to only the weight of the sleeper. This elasticity is needed to effectively absorb vibrations but it will also allow larger movements of the sleeper.

As expected, not only the total deformation is higher, but also the computation of the final

average rigidity (from 1 kN to peak force) shows that SLN is softer than PRA at high normal forces.

This deformation given by both USP is important in terms of wear reduction. The elasticity allows for a better sharing of the external load. Without USP, the rigidity of the concrete limits the amount of strong chains involved in the transmission of forces to the ground. For example, and as we saw in the simulations (section 4. 2. 3), the strong chains were born by only three small clusters of grains. If some elasticity is allowed by the USP, more grains will come into contact with the pad and the external load will be spread among more force transmission chains. Of course, if more grains are involved, contact forces will be inevitably reduced and consequently wear as well.

Wear of ballast and permanent deformation of the USP

The scans of the ballast sample and the USP were performed before all tests and after the vertical test and the 200 cycles of shear test at 1.2 mm of amplitude.

Figure 4.36 shows the scans of the ballast tip before starting the USP tests and after the tests on both pads. That means a total of 400 shearing cycles (200 per USP) plus the vertical cycles. Even though, we can observe how wear was almost inexistent on the tip. In fact, looking at the picture on the right, we cannot distinguish any kind of erosion or mark on the material. This means that the direct contact between USP and ballast will barely produce fine particles. According to simulations, these contacts are usually the most aggressive ones within the track. Thus USP not only reduces wear by spreading the external load and reducing contact forces between ballast grains, but also by reducing to almost zero the generation of fines of the direct contacts sleeper – ballast. It is important to highlight that both USP are equally effective on this subject: even if being harder, PRA does not directly degrade ballast if shear amplitude is not huge.

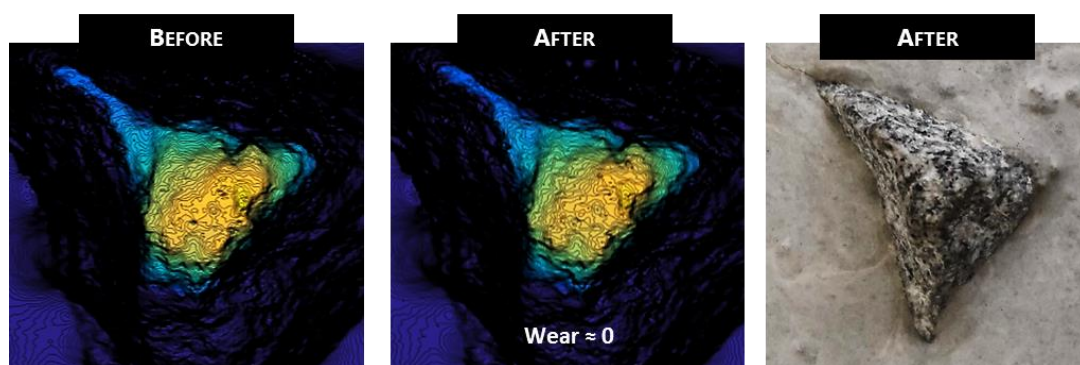


Figure 4.36 Scans before (left) and after (centre) USP tests. On the right, a picture of the ballast tip after the tests.

Concerning the scratch left on the USP, Figure 4.37 shows the scans after the tests (the scan before is mostly flat, only presenting a slight texture). Note that colour scales are not the same for each of the images, being the deformation of the SLN much more important than the deformation of the PRA, as it can be seen at the given values corresponding to the maximum depth. It is true that in both cases some permanent deformation is left after relaxation, but we

need to remember that the contact force applied during shearing (1 kN) is representative of the maximum contact forces of the track extracted from the numerical simulation.

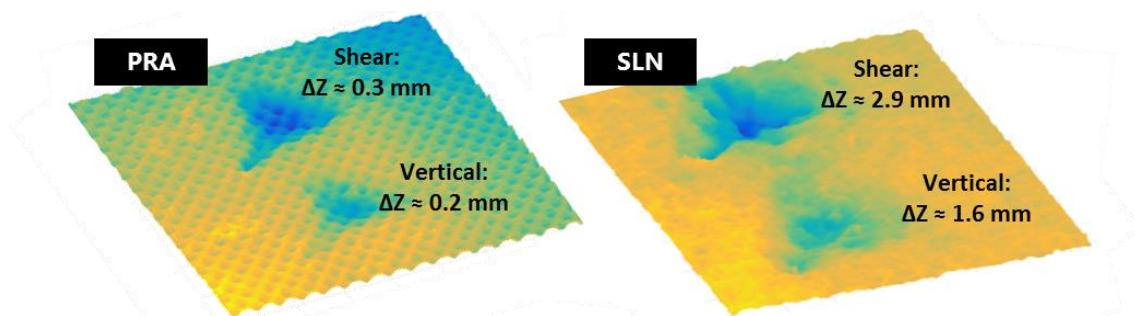


Figure 4.37 Scans after the test of the PRA and the SLN. We can distinguish the track left by each test. Be careful that colour scale is not the same on both images. The values given correspond to the maximum depth of the scratch.

After 200 cycles of shearing, the PRA has a deformation of less than half millimetre, presenting a good resistance to fatigue and thus a good durability in service in the track. On the other hand, SLN presents a considerably large deformation after shearing of almost 3 mm of depth. Moreover, the fibres forming the material are torn apart avoiding the recovering of the sample to the original condition. Therefore, grains in contact with the SLN will not only sink inside the pad but they will perforate it. After each tamping operation, since grains change positions, new holes will be created, progressively reducing the performance of the pad. This reduces the durability of the SLN compared to the PRA.

Finally, during the tests at 1 cm of amplitude, the behaviour in terms of erosion was quite similar, only that the scratch was larger. However, the test at 2 cm of amplitude was too much for the hardness of the PRA and it crushed the ballast tip, destroying in the process the polymeric material of the pad, too. However, this combination of conditions, i.e. high displacement and high contact force, never happens in the track. During the grain rearrangement after a tamping operation, we might have big displacements but contact forces in these cases are then much lower.

Friction coefficient

Friction coefficient is not an evident parameter to assess when dealing with such big deformations. The elastic recovery of the material affects the horizontal movement of the ballast grain, being hard to precise which portion is in fact due to friction.

Figure 4.38 shows the ratio between horizontal and vertical force μ (for the reasons we have said, in this case it is not accurate to talk about friction coefficient) during the cycles of amplitude equal to 1.2 mm and to 10 mm. We will not enter into details in the mechanisms involved in the horizontal movement of the ballast grain over the USP, but it is enough to understand that both types of pad need some time to recover the original position. Thus when we change the direction of shearing, the front of the movement will still be partially deformed easing the forward movement of the grain. In addition, the back will start to slowly recover, helping the grain to advance. In consequence, during the first steps, the horizontal force

applied to the grain by the pad is favourable to the movement, progressively being reduced as the front is every time more recovered (it has had more time). Eventually, this force will be zero and will go on increasing, now adding resistance to the movement. At a point, more evident in the PRA than in the SLN, the deformation in the front will be gone and the sample will need to increase the tangential force to keep moving forward (red arrows in the plots).

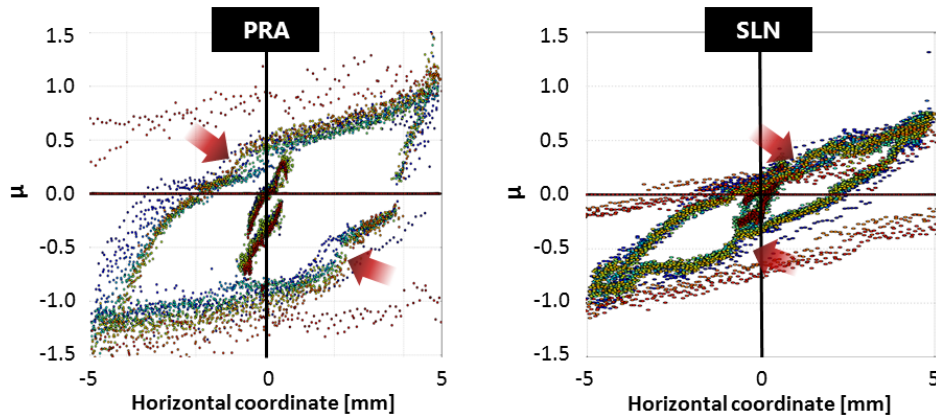


Figure 4.38 Shearing cycles on both USP. The ratio μ between horizontal and vertical forces is plotted versus the horizontal coordinate.

This phenomena provokes that, when the amplitude is small like in the tests at 1.2 mm, the apparent friction coefficient for both USP is really low, about 0.5 – 0.6 for the PRA and 0.3 – 0.4 for the SLN. However, when the amplitude is bigger, the horizontal force eventually reaches the same order of magnitude of the vertical force, giving an apparent friction coefficient over 0.9 for the PRA and around 0.7 for the SLN. Thus, we can observe that SLN also offers less resistance to movement than PRA, as expected.

4. 8 CONCLUSIONS

During this chapter we have performed a change in scale, going from the study of the ballast layer at the track scale thanks to the numerical simulations in discrete elements, to the study in detail of the contact between grains at the micro-scale.

Numerical simulations allowed us to compute the friction work extracted from Archard equation and to observe that the potential wear is concentrated on the surroundings of the sleeper, especially just below it. This is indeed in accordance with the empiric observations of the real railway track. The individual analysis of contact forces and relative displacements, showed that wear in the track is produced by two mechanisms. Some grains have some freedom of movement and they produce a lot of relative displacement with their neighbours, but these grains are not usually active within the force network. On the other hand, grains forming part of the strong chains of forces are very limited in movement but they suffer from large contact forces. From these two mechanisms, the grains with higher wear potential are usually in the second group. Thus, we established 1 kN as a representative value of the normal force to be applied while shearing on the experimental tests.

We then performed shearing tests on the BCR3D between single grains and between ballast and concrete. The shearing tests allowed us to firstly establish the friction coefficient between concrete and ballast at around 0.5 and between ballast grains between 0.8 and 1.1.

Samples were scanned before and after the test using a laser profilometre that allowed us to study the morphology of the contact and, linking it to the data of the BCR3D, allowed us to reconstruct approximately the erosion process during the test. This analysis concluded that there are two phases of wear. When two irregular surfaces get in contact, the real contact area is so small that stresses are too big to be resisted by the material. In consequence, during the first cycles, wear is very aggressive, quickly removing layers of both samples and eventually producing micro-breakages on the contact interface. Once a certain area is reached, the material is then able to resist and the wear rate is reduced drastically. This critical area depends in fact of the normal force, so it is more accurate to talk about a critical stress. For high performance granite used in HSL in France, we have narrowed down this critical stress to the range 40 – 60 MPa.

The amount of cycles needed to reach the critical stress will depend on the wear rate of the first phase given by the applied normal force and by the particular morphology of the interface. For example, worn grains usually present flatter vertexes, so it is more probable that they will adapt quicker to a relatively flat face. Thus for the tests performed in this project, where the relatively short length makes the first phase the main responsible of wear, the volume loss will mainly depend on the morphology of both surfaces and the adaptability to each other.

Concerning the experiments with water, unlike the Micro-Deval case it does not seem to have a large influence on the generation of fines. The mix of water and fines creates a paste gets strongly glued to the grain that if it dries, covering the small asperities. However, the computed critical stress is the same regardless of the conditions of the test. The main differences come from the friction coefficient, which seems to be slightly reduced.

The tests between ballast and USP have confirmed that these pads actually act as wear reducers as expected, but they do due to two different mechanisms. Direct contacts between USP and ballast barely generate fines, even when shearing at 1 kN of normal force. These contacts immediately below the sleeper were identified in the simulations as the ones presenting the highest wear potential, so it is important to at least reduce to zero this portion of fines. But also, the elastic nature of the pads allows for a better spreading of the external loading, involving more grains and creating new chains of forces. This way, the higher contact forces on the strong chains are reduced, consequently reducing wear also on the lower layers.

Last but not least, the numerical code for detecting the shearing segments over the laser scans, positioning them in accordance and then computing the contact area has been entirely developed during this thesis and will remain in the laboratory as a useful tool for future experiments in the BCR3D device.

The conclusions of this chapter, especially the two phases of wear and the concept of critical stress as a threshold between phases, will serve as a base for the degradation model of ballast that will be presented in the next chapter.

V. BALLAST WEAR MODEL

5. 1	Introduction.....	140
5. 2	Basic simplifications.....	140
5. 3	Archard in two phases.....	141
	5. 3. 1 Estimation of Archard coefficient for each phase	142
	5. 3. 2 Length of Phase 1	143
5. 4	Algorithm	146
5. 5	Results.....	148
	5. 5. 1 Wear evolution	148
	5. 5. 2 Influence of parameter φ	150
	5. 5. 3 Influence of tamping	151
5. 6	Perspectives of improvement.....	152

5.1 INTRODUCTION

After the different tests performed in the Micro-Deval and the BCR3D device, it has been possible to accurately describe the different wear mechanisms involved in such different systems.

The Micro-Deval test offers very dynamic and aggressive conditions for the grains, wear coming not only from friction but also from hard impacts after the free fall phase. This test succeeds in its primary goal of accelerating the aggregate wear, but it fails in simulating the actual conditions happening in the track. However, a clear tendency to a stable wear generation by the second half of the test was observed, which is in accordance with the Archard model. Although it has not been tested, the Micro-Deval system could fit the dynamics of the tamping operation.

On the other hand, the shearing tests performed in the BCR3D device simulate more precisely the conditions in the track, where grains producing more fines are generally those blocked due to the strong force chains: big forces and small displacements. These tests showed a two-phase behaviour, in which both grains in contact need to adapt to each other (fast degradation) before reaching a much slower degradation.

All these results provide enough knowledge and tools to progress towards the main goal of this project: building a degradation model for ballast grains which could be used to predict the amount of generated fines in the track along time.

The aim of this chapter is therefore to accurately describe a first approach proposed for this model, establishing the different hypotheses and their corresponding limitations, and giving some results and perspectives on how to improve the model in the future.

5.2 BASIC SIMPLIFICATIONS

Following the work performed so far, the proposed model combines the results extracted from the numerical simulations and the observed results from the experimental tests. That means that, in order to predict the amount of fines generated along time, we will apply over the simulation data a phenomenological model, based on Archard equation, improved by our experimental results. Thus our fundamental source of information will still be the numerical data, which is tied to some intrinsic limitations. Of course, the model leaves room for improvement if these limitations can eventually be overcome or improved.

The main simplifications have to be with the computational cost of simulating a portion of track using discrete elements. Simulations need to be relatively short, so the available loading history of each contact is not as long as desired. In the case of this study as already exposed in the corresponding chapter, only the last two passages of bogies (out of 13) are saved per simulation. Since this is the only available information we have, this data will be treated as

being repeated over and over in the following cycles.

Of course, since we are not simulating any kind of deformation or wear on the grains, they do not evolve over time in terms of shape. In the actual track, grains eventually rearrange after suffering enough wear altering the chains of forces. Again, since it is a piece of information that is not available for us, it is not possible to take it into account. Hence, the contacts will be assumed to remain unaltered along time and rearrangements will not be considered, i.e. for each specific contact appearing in the simulated bogie passage, the same loading pattern will be applied and repeated during the full ballast lifespan.

The cost of assuming those inevitable simplifications is reduced when summing up the wear produced by all the contacts. We can imagine that some grains would benefit from this possible rearrangement but some others would worsen their conditions in the network, averaging the final result. In any case, performing several simulations with the same conditions and different rearrangements of grains would give us a more reliable and averaged measurement of the wear, reducing the effect of these simplifications.

5.3 ARCHARD IN TWO PHASES

From the beginning of this project, Archard equation (equation 5.27) has been taken as the best starting point to deal with friction wear. Despite being simple in concept, this equation has proven to be reasonably accurate and widely used in tribology. Experimental tests on ballast have also proven so, since wear tends to achieve a stable and linear evolution on the grains.

$$W = k \cdot F_N \cdot Disp \quad (5.27)$$

Where W is the volume of produced wear, k is the wear coefficient coming from the simplification $k = K / H$ of the original equation (see section 1.3.3), F_N is the contact normal force, and $Disp$ is the relative displacement at the contact.

In order to build our degradation model, we will assume that Archard can be applied to ballast contacts. That means that the generated wear will be proportional to the work produced by friction work, i.e. to the product $F_N \cdot Disp$. However, this proportionality given by the wear coefficient k will not be assumed to be constant along time.

According to the BCR3D tests, it is possible to divide the wear mechanism at the contact scale through two different phases. Firstly, the contact is produced over a very small area, leading to very high stresses and quickly removing layers of matter of both grains. During this phase, if the normal force is large enough, breakages can occur producing small particles that can be easily crushed, increasing the amount of fines. This process lasts until the contact area is large enough to support the exerted normal force. From that moment, wear rate is significantly decreased, reducing the process to a fully frictional mechanism, where thin layers of matter are removed along each cycle. These two phases will be treated in the model using two different wear coefficients (k_1 and k_2), only separated by a stress threshold σ_c that will be assumed to be constant for all grains and contact conditions.

5.3.1 Estimation of Archard coefficient for each phase

In Chapter IV we performed a backwards procedure, using the laser output and the evolution of Z in the BCR3D, in order to build a link between the evolution of the shearing test and the evolution of the contact area. In that way, it was possible to obtain the rate of vertical displacement Z compared to the relative horizontal displacement ($\Delta Z_i / \Delta Disp$) and Area (A_i) for each specific instant. Using a rough approximation on the discrete data, we can estimate the wear rate, i.e. the wear volume subtracted at each instant ($\Delta W_i / \Delta Disp$), as the product between the area A_i and the corresponding rate of Z :

$$\frac{\Delta W_i}{\Delta Disp} \approx A_i \cdot \frac{\Delta Z_i}{\Delta Disp} \quad (5.28)$$

If we replace the corresponding values in the Archard equation:

$$\begin{aligned} \Delta W_i &= k_i \cdot \Delta Disp \cdot F_N \\ A_i \cdot \frac{\Delta Z_i}{\Delta Disp} &= k_i \cdot F_N \\ k_i &= \frac{A_i}{F_N} \cdot \frac{\Delta Z_i}{\Delta Disp} \end{aligned} \quad (5.29)$$

Since F_N is constant during the shearing and we know the contact area and the Z rate for each instant (Figure 4.31), we can therefore obtain k_i for each stress value using equation 5.24:

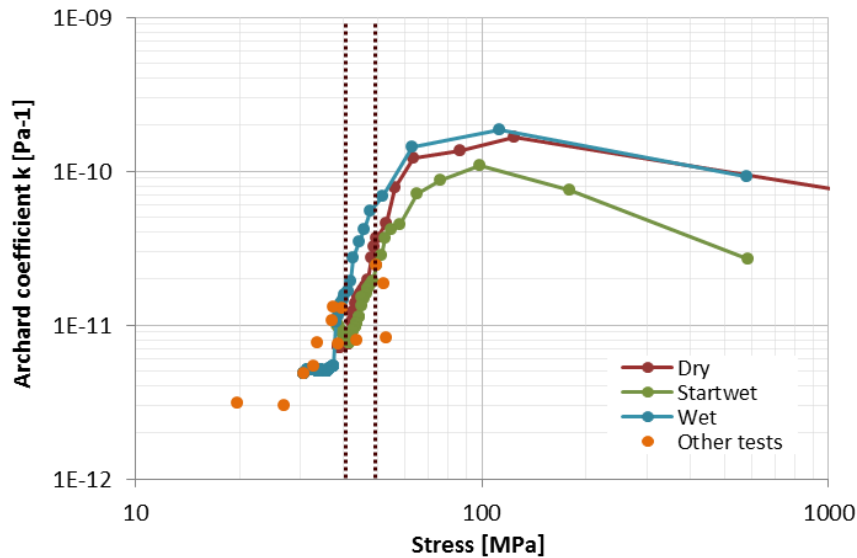


Figure 5.1 Archard coefficient compared to the stress value all along 3 different BCR3D tests. In addition and in orange, the values at the end of other tests performed in the BCR3D on which it was not possible to perform the backwards analysis.

Figure 5.1 shows the value of the wear coefficient k for each instant along three different BCR3D tests. For additional information, orange dots have been added corresponding to the

final values of other tests on which it was not possible to perform the backwards analysis. It is important to remark that, in order to properly read this plot, the actual chronological order of each shearing test is from right to left (stress becomes lower as the test progresses).

As we already saw in the BCR3D analysis, the range from 40 to 60 MPa shows an almost vertical evolution that corresponds to the transition zone between phases, where the wear aggressiveness given by k is drastically reduced within a relatively short evolution on the contact area. Thus data points higher than 60 MPa (upper-right) correspond to the first wear phase, while data points in the lower-left corner correspond to the end of the test, i.e. the second wear phase.

As expected, wear is much more aggressive at the beginning of the test, not only in Z but also in removed volume, giving values of k_1 from 1 to $2 \cdot 10^{-10} \text{ Pa}^{-1}$. Although high, this value is still one order of magnitude lower than the one obtained in the Micro-Deval ($k_{\text{MDA}} = 1.8 \cdot 10^{-9} \text{ Pa}^{-1}$ for dry tests). The reason could be the high importance of impacts during the attrition test. On the other hand, once the second phase is achieved, wear is significantly reduced, k_2 ranging from 5 to $10 \cdot 10^{-12} \text{ Pa}^{-1}$, more than one order of magnitude below. Finally, we can observe that the end of the transition zone is well delimited between 40 and 50 MPa (dashed lines in Figure 5.1).

The values of these three parameters will be left open in the model in order to be able to better calibrate them if further experiments are performed. However, for the sake of giving some numerical results, the worst scenario (most generation of fines, see Figure 5.1) will be considered, that is:

- $\sigma_c = 40 \text{ MPa}$
- $k_1 = 2 \cdot 10^{-10} \text{ Pa}^{-1}$
- $k_2 = 1 \cdot 10^{-11} \text{ Pa}^{-1}$

In summary, for each contact happening in the track, k_1 will give the wear rate, i.e. the speed at which matter is lost, depending on the friction work suffered by that contact during its Phase 1; k_2 will hence give the wear rate of the less aggressive Phase 2; and σ_c will allow us to establish how long, in terms of volume, Phase 1 will last before changing to Phase 2.

5.3.2 Length of Phase 1

During the passage of each train bogie, each contact supports a cyclic loading, generally reaching its maximum value at the peak of the external load or very close to it. Given the loading history of each contact throughout a bogie passage, it is possible to extract the maximal force supported within. Hence, for each contact, the length of its Phase 1 will be determined by the critical area A_c where the critical stress σ_c is satisfied given that maximal normal force:

$$A_c = \frac{F_N \max}{\sigma_c} \quad (5.30)$$

This hypothesis simplifies the length of Phase 1 to a single value per contact ($F_{N \max}$). This simplification does not disregard at all the rest of the cycle, it only assumes that, while not reaching the critical area given by the corresponding maximal force, all work suffered by the contact during that full cycle will be considered as Phase 1, even if within the cycle the applied normal force eventually induced a lower stress than the critical one. So it corresponds at the same time to a worst-case scenario. This assumption is however actually quite acceptable since in the vast majority of contacts this moment of peak load (along with its corresponding relative displacement) is the main and almost only responsible of the friction work of that contact. Figure 5.2 shows the evolution of the friction work on the entire track through the passage of two bogies. It can be observed how the big increases in the friction work correspond to the peaks of the external load.

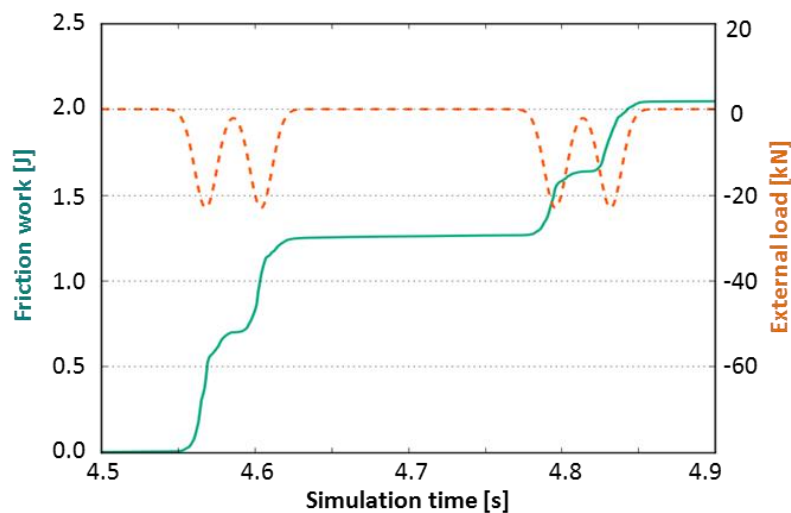


Figure 5.2 Work generated by the whole sample of the track (green) during two passages of bogie. The external loading is added in orange as a reference.

In order to achieve the critical area A_c , a certain volume of matter needs to be removed from both grains in contact. This volume will be determined by the particular morphology and adaptability of the contact. This morphology is too complex and variable over the grains to be treated individually per contact, so a simplification is needed in order to reduce this variability to a sort of “average contact geometry” within the sample.

Let us assume that all contacts are vertex-face contacts (more than 95% of contacts have been observed to fall into this category of contacts during the simulation, see section 4. 2. 2), and let us assume as well that we can simplify the shape of each grain as a polyhedral so that vertexes can be represented by pyramids with different base shapes. Along the progressive wear process, this pyramid will be cut in successive parallel planes as shown in Figure 5.4. Since the critical area A_c is taken as the base of the pyramid, the goal is to predict the volume lost depending on that area of the base of the pyramid.

The volume cut off from the initial vertex to each parallel plane represent similar pyramids, likewise similar triangles are created with parallel lines in Thales theorem. It is then easy to extrapolate the intercept theorem to its 3D version.

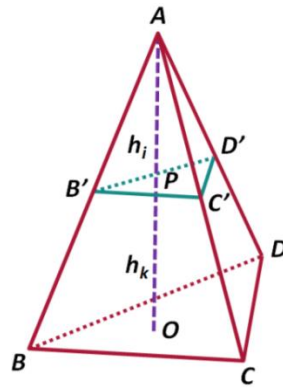


Figure 5.3 Pyramid cut by a plane parallel to the base. Thales theorem can be extrapolated to its 3D version.

At two different states of wear we will have two different parallel planes given by the height worn so far: h_i and h_k . These cutting planes create similar triangles on all the faces and also the triangles formed using the height of the pyramid are similar (e.g. ABO and $AB'P$). Therefore the ratio $h_i / h_k = \lambda$ can be applied to all respective measures in both pyramids (i.e. $B'C' / BC = AB' / AB = B'P / BO = \dots = \lambda$). The area of the polygon forming the base of the pyramid (regardless of its shape) depends always on the product of two of those measures, so that the proportionality ratio will be squared: $A_i = \lambda^2 * A_k$. In the same way, the volume of the pyramid is $Vol = A_{base} \cdot h / 3$, so the proportionality this time will be cubed: $V_i = \lambda^3 * V_k$. It is straight forward to express the volume in terms of the area of the base:

$$V_i = \varphi \cdot A_i^{3/2} \quad (5.31)$$

If we know a reference state k where we can establish the area of the base A_k and the worn volume V_k we can obtain the coefficient φ , and so calculate the volume for any parallel plane cutting the pyramid:

$$\varphi = \frac{V_k}{A_k^{3/2}} \quad (5.32)$$

That coefficient φ is in fact an indicator of the geometry of the pyramid: it will take higher values for very sharp vertexes and lower for wide open angles. Taking into account the image analysis done with the laser profilometer after the shearing tests in the BCR3D, we can get the following values for φ :

							Average
New vertexes	0.45	0.35	0.33	0.16	0.12		0.28
Used in previous BCR3D tests	0.06	0.05	0.03	0.10	0.08	0.05	0.06
Worn in Micro-Deval	0.12	0.05	0.41	0.18			0.19

Table 5.1 Estimated φ for the tips used during the BCR3D tests. φ has been calculated using the estimated worn volume and the contact area extracted from the laser analysis. Values in red represent tests where the tip was broken.

The first thing we can observe in the table is that worn grains, especially those used in previous shearing tests, have significantly lower values of φ than new vertexes. While new grains present values ranging between 0.15 and 0.40, worn grains rarely overpass 0.10. This was indeed expected since asperities in worn grains have larger radius, so at the scale of the contact the best-fit pyramid will present a wider angle (Figure 5.4a&b).

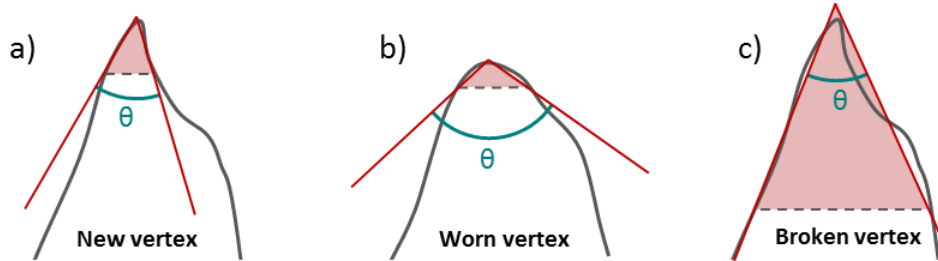


Figure 5.4 Different wear situations: new grain eroded by friction (a), already worn or rounded vertex eroded by friction (b), and a major breakage of the vertex (c). The dashed grey lines set the new surfaces of contact, the red triangles show the equivalent pyramids in terms of volume lost, and the red lines show the upper angle of the pyramids θ , closely related to the parameter φ . For friction wear, where only a few millimeters are worn, θ is larger for a worn vertex than for a new vertex. However, in a major breakage, the equivalent pyramid (and so θ) will be influenced by the general shape of the grain at that vertex.

In the case of major breakages, it may happen that φ presents higher values. This can be explained because the height of influence of the shearing is generally very small (1-2 mm in the BCR3D tests), so the “fitting pyramid” is very influenced by the local morphology of the asperity. As we wear deeper in the grain, the main shape of the grain becomes more important, sometimes closing the angle of the pyramid (Figure 5.4c).

This parameter φ will be left open in the model algorithm as an input parameter. For most of the results exposed, a value of 0.28 will be taken (the average value for the new grains). In section 5.5.2, an influence analysis of this parameter can be found.

Finally, putting together equations (5.30) and (5.31), we can obtain the total volume that will be generated during Phase 1 for each contact:

$$Vol_{Phase\ 1}[mm^3] = \varphi \cdot \left(\frac{F_{N\ max}[N]}{\sigma_c[MPa]} \right)^{\frac{3}{2}} = \varphi \cdot A_c^{3/2} \quad (5.33)$$

5.4 ALGORITHM

Summarizing the explanation above, Archard will give us the wear rate at which each contact will generate fines in each of both phases, while the length of Phase 1 will determine when that contact will change from one phase to the other one. It is important to insist that this calculation will be performed for each contact separately, so different contacts will reach Phase 2 at different moments and will move through Phases 1 and 2 at different wear rates.

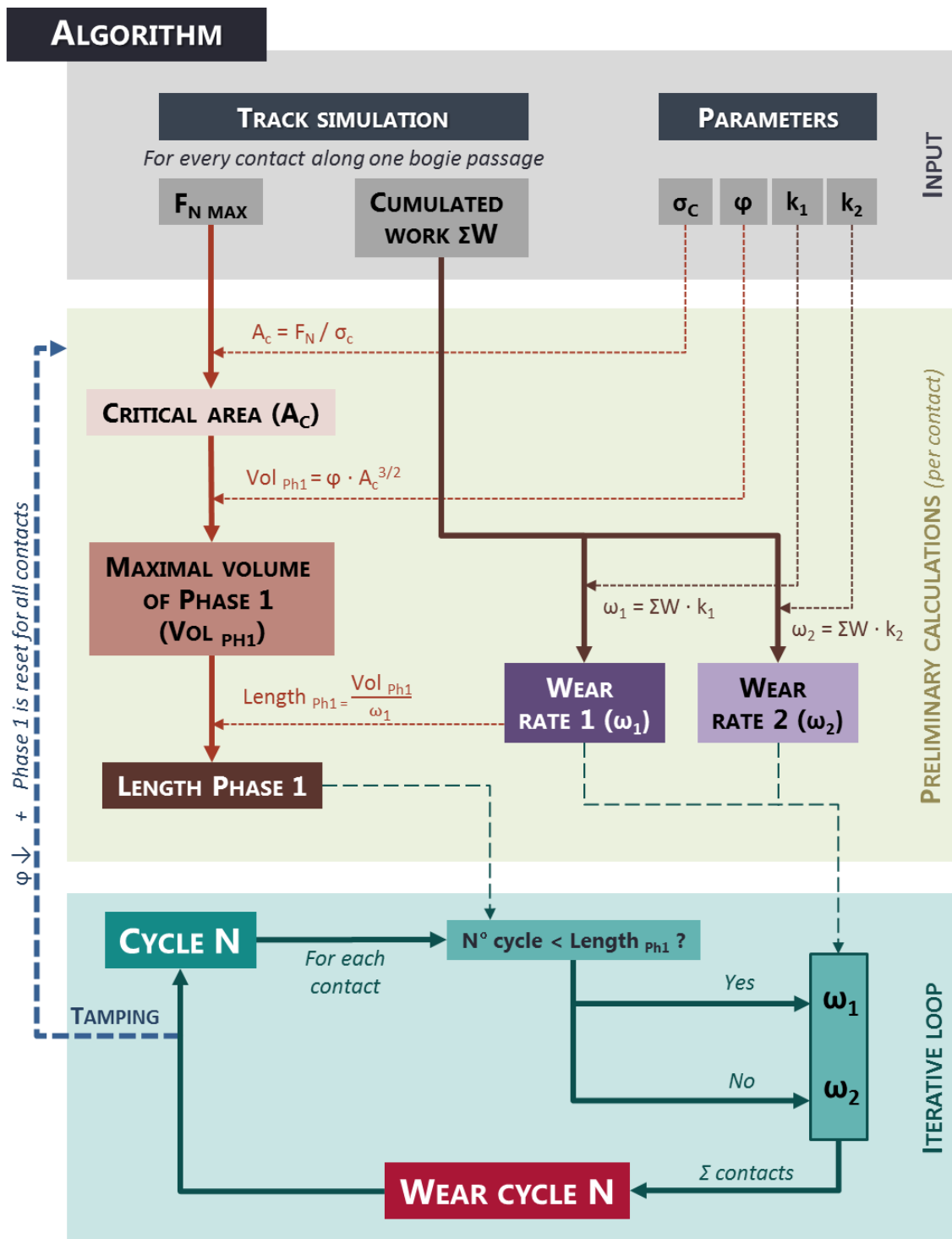


Figure 5.5 Diagram of the algorithm.

Hence we have all the ingredients to build the algorithm that will allow us to calculate the amount of fines generated by the entire sample. The input scalar parameters are the followings:

- σ_c Critical stress : stress at which the transition between phases occurs. 40 MPa is considered as the default value.

- φ Shape parameter: establishes how “open / closed” the average vertex in the sample is. The default value is set at 0.28, but it might be considered to evolve towards lower values when grains wear.
- k_1 Wear rate of Phase 1. Set at $2 \cdot 10^{-10} \text{ Pa}^{-1}$ as default value.
- k_2 Wear rate of Phase 1. Set at $1 \cdot 10^{-11} \text{ Pa}^{-1}$ as default value.

And as input data extracted from the simulations:

- $F_{N \max}$ Maximal normal force exerted at each contact along a cycle.
- ΣW Cumulated work of each contact along a cycle.

For each contact we take the maximal normal force and we calculate its critical area using the input critical stress. Then, using that value and φ , we obtain the maximal volume that will be eroded during Phase 1. Meanwhile, using the two Archard coefficients for Phases 1 and 2 and the cumulated work of each contact, we calculate the wear rate for each phase and contact (wear / cycle). Next, combining the maximal volume of Phase 1 and the wear rate of Phase 1, we can obtain the length of Phase 1 for each contact in terms of number of cycles.

With this information we can start the iterative loop of cycles. After each cycle we check for each contact whether we have reached the length of Phase 1 or not yet. If the answer is negative, we proceed calculating the wear for that contact using wear rate 1, otherwise we change to wear rate 2. Figure 5.5 shows the diagram of the algorithm.

5.5 RESULTS

5.5.1 Wear evolution

Taking the default values exposed in the sections above, the algorithm is run for a total of 10^5 trains, at an average of 13 bogies per train. This amount of trains has been chosen just for being a large enough round number, but it could indeed correspond to approximatively one year in a track with high traffic, e.g. 1 train every 4 minutes for 18 hours per day.

Figure 5.6 shows the evolution of the generated wear as the number of trains increases. The first thing that can be noticed is the evident influence of Phase 1 during the first 20 000 trains. The fact of having new grains, so sharp vertexes and edges, gives a significant first push to the generation of fines. After these first cycles, wear becomes almost linear, even if more than 40% of contacts are still in Phase 1. In fact, the reason why is because almost all of the contacts that contribute the most to the wear (those below the sleeper) have already changed phase. These contacts share that they are usually associated to a strong force, hence Phase 1 involves more volume to wear, but they also wear so aggressively due to the associated friction work that they “consume” this volume very fast, so they all have changed to Phase 2 before the end of the simulation.

By the end of the simulation, 77% of contacts are already in Phase 2. Those left in Phase 1 are grains that have such a slow wear rate that they have not yet reached the threshold volume.

Some of these contacts are not even in relative motion, so they will never generate friction work, and therefore they will not wear following Archard model. This is the reason why the asymptotic tendency is not towards 1, but around 0.8.

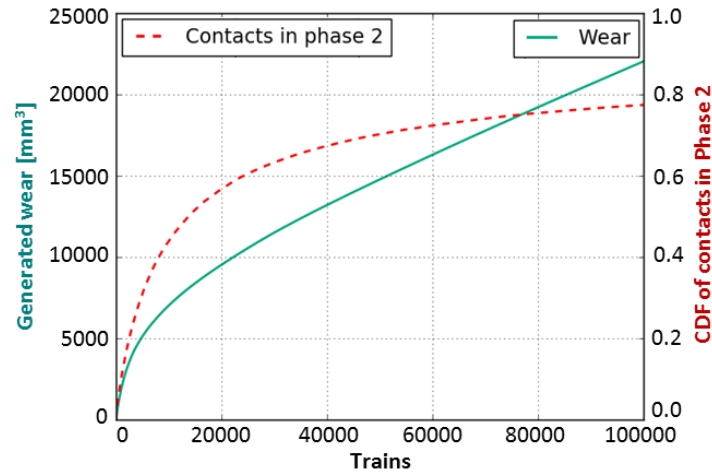


Figure 5.6 In green, evolution of the generated wear per sleeper block (half the track). In dashed red, proportion of contacts that have changed from Phase 1 to Phase 2.

After 10^5 trains, we have generated around $22\,000\text{ mm}^3$ of fines, which represents around half a ballast grain. This corresponds approximately to 14 g per million tons of train traffic. This prediction is around 10 times less than the experimental measurement performed by Perales using Vibrogir [22] (see Figure 1.15). However, he included in his computation not only fines but all particles up to 25 mm, which do increase the total mass considerably. In this project, only fine particles ($D < 1.6\text{ mm}$) were considered for computing Archard coefficient, and major breakages were discarded on the measurement of volume loss.

As we could see in the analysis of the track simulation, the variability within the track is high (Figure 5.7). The contact producing the highest amount of fines would generate 457 mm^3 , which is around half the amount of fines generated by one single grain during a full Micro-Deval test. However, during a MDA test the grain loses matter all around the grain, and here we are talking about one single contact.

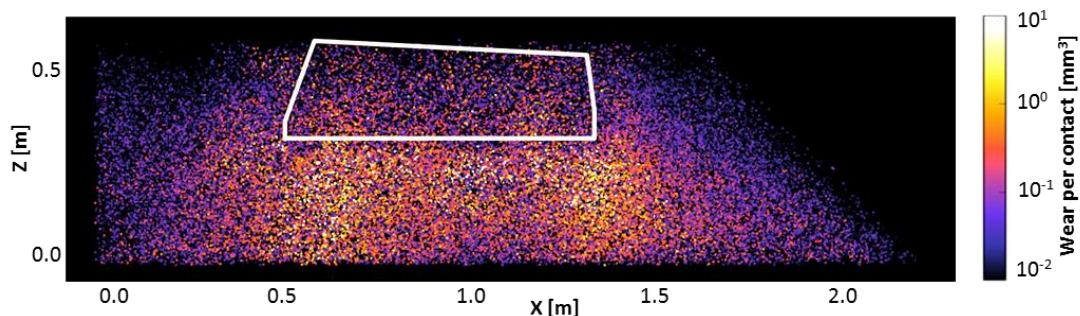


Figure 5.7 Distribution of wear within the track. Each point corresponds to a different contact. Note that the color scale is logarithmic.

As expected, wear is concentrated below the sleeper, where the friction work is higher. Even if the grains are mostly blocked in the strong chains of forces and the relative displacements are very small, these forces are high enough to compensate and create wear.

Of course, the model in its actual state is not able to take into account the precipitation of fines by gravity to lower layers over time, and neither the effect that these fines can have over the behaviour of the track. As we saw in the Micro-Deval, the presence of fines as a protective thin layer all around the grain can soften the aggressiveness of wear. It is though questionable whether the fines can reach the contact itself in systems such as the track. Grain network is so tight and grains are so blocked that surfaces remain in contact permanently, not letting the fines penetrate in the interface as easily as it can happen in a dynamic system such as the Micro-Deval.

5.5.2 Influence of parameter φ

As we have seen, parameter φ is an indicator of how much volume loss is needed to reach the critical area depending on the geometry of the vertex. Hence it will depend mostly on the morphology of the contact, especially on the average angle of the contact vertex, as we saw in Figure 5.4. By definition, it does not affect the linear Phase 2 of the wear generation, but it has a significant influence on the importance of Phase 1, so it will change the final amount of predicted fines.

Figure 5.8 shows the importance of this parameter, and in consequence the importance of Phase 1 in the wear process. The first thing that can be noticed is the important decrease (around 30%) in the final amount of fines if we change the value of φ from 0.35 to 0.10. The reason is the difference in the length of Phase 1: while for a value of 0.35 (very sharp edges) the first phase can have significant influence up to 40 000 trains, for values of worn grains such as 0.10 the first phase does not have influence but in the first 10 000 trains at most.

Due to the big assortment of grain shapes and asperities, this parameter is not at all evident to calibrate, and so far an average value extracted from a limited amount of tests has been chosen to be used. We can thus intuit that there is margin for improvement in this field. In the figure, the value of 0.28 used for the first result has been added in dashed black as a reference.

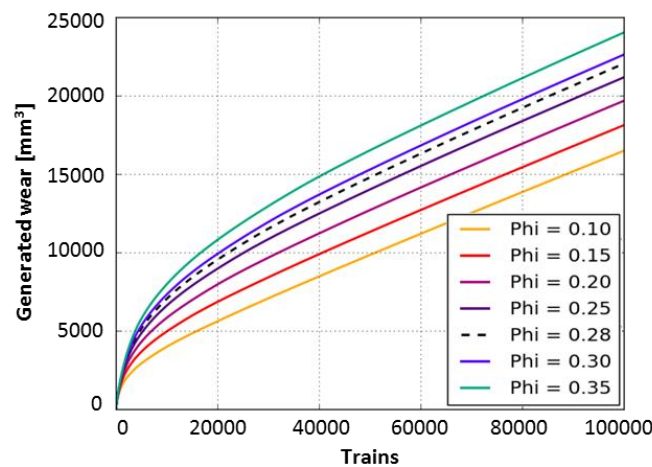


Figure 5.8 Simulation of 10^5 trains for different values of ϕ .

One of the ideas that could be implemented in future improvements of the model would be not to consider φ as fixed for every contact but to introduce a probability distribution within a

range of values. In a numerical point of view, it could even be possible to give a value for φ depending on the actual shape of each polyhedral vertex defining a contact.

In line with the difference in values of φ for different states of degradation, we can imagine a model where φ evolves after erosion. That means that, if contacts change (for example, due to tamping), the new contacts will be created over already eroded surfaces, so Phase 1 will be shorter.

5.5.3 Influence of tamping

Tamping operation is very aggressive with ballast by itself. This is a well-known effect of this maintenance operation. As exposed in the corresponding chapter, tamping could resemble the dynamics of the Micro-Deval test. Thus, in order to predict the amount of fines generated, we suggest using, as a first approach, the Archard coefficient extracted from the attrition test over the tamping simulation. However, this maintenance operation was not simulated during this project so it is not possible for us to give a value for the generated fines.

Nevertheless, tamping has a side effect that was not so obvious and that worsens even more the degradation of ballast. When tamping is performed, ballast grains, especially those under the sleeper, are vibrated and rearranged. As a consequence, grain contacts change so contact interfaces need to again adapt to each other, reinitializing Phase 1.

As an average, this new Phase 1 will be shorter than the previous one because asperities will be in average more worn. We talk about “in average” because some asperities will still be completely new since they did not take part in the first cycle, but some will repeat forming part of a contact.

Let us consider a tamping operation every 10^5 trains, and let us consider as an example that φ is linearly reduced in a rate of 0.02 points after every tamping cycle, starting from 0.28. Figure 5.9 shows what would happen in such conditions over five tamping cycles and its comparison to a hypothetical situation where no tamping was required:

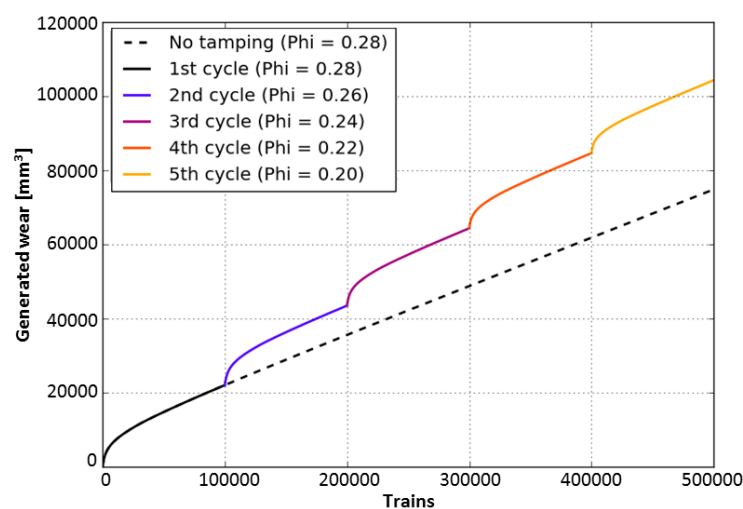


Figure 5.9 Evolution of wear over 5 tamping cycles with a linear decreasing ϕ .

It is important to insist that fines produced during the tamping operation itself are not included here. When tamping cycles are added to the model, Phase 1 becomes even more important, as after each cycle a first step to the fines production is added. In the conditions proposed, after five tamping cycles, the track would have generated around 105 000 mm³ of fines per sleeper block plus the fines generated on each tamping operation, while with no tamping we would generate around 75 000 (-28 %).

Of course, tamping is necessary in order to correct the geometrical defaults of the track and there are no alternative solutions available in the market. However, it is indeed a big source of degradation. In High-Speed Lines this problem becomes even larger since the tolerances for geometrical defaults are much more restrictive, so tamping is required with a higher frequency. Perhaps a line of investigation would be necessary in order to search for a softer method of correcting track defaults.

5.6 PERSPECTIVES OF IMPROVEMENT

The proposed model is a first approach to what it could be achieved implementing the different conclusions extracted from the experimental tests. Due to the different hypotheses and simplifications taken, it has intrinsic limitations and needs further work in order to progressively improve the precision of its predictions.

The proper calibration of the different parameters is a need where there is still room for exploration and improvement, especially concerning the shape parameter φ . It would be interesting to think how to link the results from the tomography study concerning the distribution and evolution of asperity radius with the evolution of this parameter φ . This evolution could be applied to the actual shape of the polyhedral constituting the simulation, giving a different value for each contact depending on the shape and the orientation of the normal force. Concerning the other parameters, it would be interesting to perform a higher number of BCR3D tests in order to confirm the given values. It is important to perform much longer tests and see if this wear rate for Phase 2 actually remains constant as the contact area becomes much larger. In addition, only tests at 1 kN have been considered to obtain the critical stress. In principle, using the stress value eliminates the difference between normal forces, but a confirmation that the behaviour of the material is really the same is needed.

We should not forget that all these parameters have been established only and just for high resistance granite. Low resistance materials would present higher wear rates and lower critical stress. It has not been investigated so far, but it is likely that a link between wear rates, critical stress and MDA standard coefficient does exist. This would permit an easy calibration of the model depending on the material used on each railway line, only by knowing the characteristics of the sample through standard tests. Nowadays this is already a common and required practice in the quarries, so these standard values are known for all ballast samples.

Archard model is also a limiting factor. It deals fairly well with friction wear, but it does not do so well when impacts are involved. Impacts play an important role in tamping and in the Micro-

Deval test, so a better impact model would improve the predictions for these systems. Moreover, during a first phase of the track, impacts are not very important within the ballast layer but, with time, under some sleepers a small gap is created provoking impacts with every bogie passage. This is not taken into account in this model since track conditions are not evolving with time, but if we would like to take this phenomenon into consideration, an impact model would be desirable.

Including tamping operation in the model would also be an improvement. Tamping simulation should be performed and compared to the Micro-Deval system. If it is confirmed that impact forces in both systems are similar, we could consider the proposed method of using Micro-Deval wear coefficient k to establish an estimated value of fines generated by this maintenance operation. This value could then be added at the beginning of each tamping cycle as a vertical increment.

Finally, grain crushing is neither considered in the model, but due to its complexity and computer cost it is more difficult to implement. It is important though not to forget that it has a significant role in the production of fines. Small fragments can easily be grinded by bigger grains, adding extra fines to the system. We could imagine that, with a proper calibration, this limitation could be solved by increasing the wear rate for Phase 1 (or even for both phases). However, to do so it would be imperative to obtain real data from actual tracks.

And that is indeed the most important handicap of the model: the lack of real data to confirm or dismiss the predictions. The difficulty of recovering the fines from the track makes it very unlikely to get actual data. The results given by the model are consistent with the different experimental tests, but for the moment they need to be mostly assessed in a qualitative way. Thus the very next step should be to think about how to get indirect measures from the track that could guide us towards a good calibration.

CONCLUSIONS & PERSPECTIVES

The progressive degradation of ballast due to the passage of trains and tamping lead to important consequences for the railway industry in terms of maintenance costs. Grains tend to a more rounded shape, losing their characteristic sharpness of edges and vertexes, and therefore reducing the shearing resistance of the ballast layer and its capacity of locking the sleepers at place. On the other hand, the continuous production of fine particles that accumulate in the voids stimulates the previous problem and progressively reduces the permeability of the track against rainfall and freeze-thaw cycles. In addition, the increase of speed of trains in HSL requires an additional strictness when monitoring geometry defaults in the track, requiring in consequence an increase of the frequency of tamping operations, leading to a dramatic acceleration of ballast degradation. The consequences of this phenomenon has been widely observed and analysed, but a deep research of the origins and mechanisms leading to it was required.

This thesis has presented a multi-scale approach of the problem, combining experimental and numerical tools, in order to understand the fundamental mechanisms of ballast wear at the contact scale. This knowledge has been then extrapolated to the track scale with the aim of building a predictive tool of the generation of fine particles within the railway track.

Numerical simulations by discrete elements (NSCD) allow for a proper understanding of the ballast layer taking into account its intrinsic granular nature. Thanks to these simulations, we have been able to descend from the track scale to the behaviour of the individual grains, and more particularly we assessed the distribution of contact forces and the relative motion between grains, which represent the main responsible actors of friction wear at the micro-scale.

Archard equation, implying a linear evolution of wear production, has been used as the main approach for the model. However, experiments in the Micro-Deval and the shearing tests between two single grains in the BCR3D have shown that fines production is higher during the first stages of the tests, while it becomes more stable after a certain time of degradation. The morphology study performed by wearing the grains in the Micro-Deval and scanning them using X-ray tomography has shown that sharp asperities, especially on edges and vertexes, are

more exposed to contacts and present a reduced cross-section, leading to a faster evolution towards a more rounded shape with larger asperity radii. As the grain wears, the new sharpest asperities become the most exposed and thus the ones with a higher probability of becoming in contact with other grains or the metallic drum. When asperities become large enough, they present a larger cross-section and a consequent higher resistance to wear, decreasing but stabilizing the overall production of fines. The strict selection of the aggregates for ballast layers searches for this initial sharpness, so it is a desired and intrinsic characteristic of new grains for enhancing their performance in the track. However, this strong point happens to be also its weakest point in terms of grain degradation.

The case of the track is similar, but unlike the Micro-Deval system, contacts remain the same during long periods of time before a rearrangement is produced, due to either tamping or a self-reorganisation of the ballast layer. The combination of shear tests and laser scans has shown that, in quasi-static contacts, a critical contact area or, in consequence, a critical normal stress needs to be reached before achieving a stable wear. At the beginning of the test, the contact area is so small that the normal stress becomes too high for the material to resist, producing fast and aggressive degradation. As the grains wear by friction, both the face and the vertex adapt to each other, progressively increasing the contact area and reducing the normal stress, and thus decreasing considerably the wear rate.

This behaviour is modelled by using two different phases for each individual contact. Both phases are defined using the equation of Archard but each ruled by a different wear coefficient. The threshold between phases is defined by the critical stress. In addition, a geometric parameter is introduced that allows for taking into account different degradation states of the grains, in terms of the amount of matter that is needed to reach the critical stress depending on the aperture angle of the average asperity. This model is applied to the simulation of a bogie passage, assuming that the loading path of each individual contact will remain the same during the following passages. The idea is to extrapolate the results of an affordable simulation, in terms of computational cost, to the lifespan of ballast. Each individual contact starts in Phase 1 and accumulates wear over the cycles until the theoretical amount of matter that would be required to reach the critical stress is reached, therefore changing to Phase 2. Henceforth, the proposed model does not reproduce numerically a change in state on the grains, which would be computationally very costly, but makes use of the simulations to extract the quantities involved in wear mechanisms and apply the corresponding predictive model.

The main consequence of this model with two phases resides in the importance of Phase 1. Every time a rearrangement happens and new contacts are created, Phase 1 is restarted leading to a higher production of fines during a certain time. This phenomenon affects in a direct way the maintenance using tamping. Tamping was already known to be very aggressive with ballast, especially due to the penetration of the tines. However, the after-tamping stage is also critical for wear production in the track due to the total rearrangement of the grains below the sleeper.

In any case, any strategy reducing the friction work will have a positive impact on ballast degradation. For instance, Under-Sleeper Pads not only soften the sleeper-ballast contacts, but

also they help to redistribute the loading between more chains of grains, reducing the contact force and thus decreasing the cumulated friction work per contact.

Perspectives

The model built along this thesis is coherent with the experimental observations and results obtained in the shearing between two single grains, but there is still room for improvement. A calibration of the model, either by direct quantification of the fines in the track or by further tests, is required in order to validate the results and to assess more accurately the input parameters.

It would be interesting to analyse the morphology of the grains in more details in order to perform a population balance of the asperities. This would allow for a better assessment of the rate at which the geometric parameter φ evolves.

The wear coefficients and the critical stress have been established for high-resistance granite, but for a proper modelling, they should be linked to the mechanical characteristics of the material. Henceforth, it would be an interesting future line of investigation to try to link these coefficients with the results of the standard tests, such as Micro-Deval and Los Angeles. This would allow for a quick calibration of the model depending on the type of railway line analysed.

The inclusion of crushing into the model would also be a step forward to quantify fines. These breakages generate relatively small fragments that may be grinded by larger grains, eventually producing a considerable amount of fine particles. Crushing is computationally costly to implement, but we imagine that the associated generated fines could be approximated by an increase of the wear rate on the model or by including an additional term for contacts reaching a certain normal force.

So far we have applied the model to the case of HSL traffic, but it should be applied as well to tamping. Tamping operation should be analysed in detail and compared to the Micro-Deval test in terms of dynamics of the affected area, contact forces and relative displacements between grains. We predict some similarities between both systems, which would allow for applying the model using the wear coefficient extracted in this thesis for the Micro-Deval case.

The degradation model has the final goal of becoming a predictive tool that would allow for an optimization of the different maintenance procedures. The logical next step is therefore to analyse the results and search for new solutions for ballasted tracks.

REFERENCES

- [1] J. Alias, *La voie ferrée : techniques de construction et d'entretien*, Paris: Eyrolles, 1984.
- [2] G. Saussine, "Contribution à la modélisation de granulats tridimensionnels : application au ballast," Université Montpellier II, Montpellier, 2004.
- [3] E. T. Selig and J. M. Waters, *Track geotechnology and substructure management*, London: Thomas Telford, 1994.
- [4] F. Lamas López, "Field and laboratory investigation on the dynamic behaviour of conventional railway track-bed materials in the context of traffic upgrade," Université Paris-Est, Paris, 2016.
- [5] S. Kaewunruen and A. Remennikov, "Non-destructive evaluation for dynamic integrity of railway track structure," in *International Conference on Structural Integrity and Failure*, Sydney, 2006.
- [6] Y.-J. Cui, F. Lamas López, V. N. Trinh, N. Calon, S. Costa D'Aguiar, J. C. Dupla, A. M. Tang, J. Canou and A. Robinet, "Investigation of interlayer soil behaviour by field monitoring," *Transportation Geotechnics*, vol. 1, no. 3, pp. 91-105, 2014.
- [7] UIC, "Project Under Sleeper Pads," International Union of Railways, 2009.
- [8] M. Sol Sánchez, F. Moreno Navarro and M. C. Rubio Gámez, "The use of elastic elements in railway tracks: a state of the art review," *Construction and Building Materials*, vol. 75, pp. 293-305, 2015.
- [9] K. Riessberger, "Ballast tracks for high speeds," in *Track for High-Speed Railways*, Porto, 2006.
- [10] C. Voivret, V. H. Nhu and R. Perales, "Discrete element method simulation as a key tool towards performance design of ballasted tracks," *International Journal of Railway Technology*, vol. 5, pp. 83-98, 2016.
- [11] V. N. Trinh, "Comportement hydromécanique de matériaux constitutifs de plateformes ferroviaires anciennes," Université Paris-Est, Champs-sur-Marne, 2011.
- [12] UIC 714, *Classification of lines for the purpose of track maintenance*, 4th ed., Paris: International Union of Railways, 2009.
- [13] N. Guerin, "Approche expérimentale et numérique du comportement du ballast des voies ferrées," Ecole Nationale des Ponts et Chaussées, Paris, 1996.
- [14] C. Esveld, *Modern railway track*, Duisburg: MRT-Productions, 2001.
- [15] G. Sauvage, "Railway track vertical static behaviour," INRETS - LTN, 1993.
- [16] A. Al Shaer, D. Duhamel, K. Sab, G. Forêt and L. Schmitt, "Experimental settlement and dynamic behavior of a portion of ballasted railway track under high speed trains," *Journal of Sound and Vibration*, vol. 316, no. 1-5, pp. 211-233, 2008.
- [17] J. C. Quezada, "Mécanismes de tassement du ballast et sa variabilité," Université Montpellier II, Montpellier, 2012.

- [18] C. Paderno, "Comportement du ballast sous l'actoin du bourrage et du trafic ferroviaire," Ecole Polytechnique Fédérale de Lausanne, Lausanne, 2010.
- [19] E. Azéma, "Etude numérique des matériaux granulaires à grains polyédriques : rhéologie quasi-statique, dynamique vibratoire, application au procédé de bourrage du ballast," Université Montpellier II, Montpellier, 2007.
- [20] C. Voivret, R. Perales and G. Saussine, "Ballasted track maintenance with a multi-unit tamping machine: a numerical discrete efficiency comparison," in *International Conference on Railway Technology: Research, Development and Maintenance*, Ajaccio, 2014.
- [21] R. Perales, G. Saussine, N. Milesi and Y. Descantes, "On the damaging effects of the ballast tamping operation," in *World Congress on Railway Research*, Lille, 2011.
- [22] R. Perales, *Etude de la dégradation du ballast*, SNCF (Internal document), 2010.
- [23] SNCF, *Mise en oeuvre du ballast pour voie ferrée*, La Plaine - Saint Denis: Internal document, 2010.
- [24] AFNOR, *NF EN 933-1: Essais pour déterminer les propriétés géométriques des granulats - Partie 1 : Analyse granulométrique par tamisage*, 2012.
- [25] AFNOR, *NF EN 13450: Granulats pour ballasts de voies ferrées*, 2003.
- [26] SNCF, *Ballasts neufs pour voies ferrées*, La Plaine - Saint Denis: Internal document, 2010.
- [27] SNCF, *Etude de vieillissement du ballast*, Internal document, 2010.
- [28] AFNOR, *NF EN 933-3: Essais pour déterminer les propriétés géométriques des granulats - Partie 3 : détermination de la forme des granulats*, 2012.
- [29] AFNOR, *NF EN 1097-1: Essais pour déterminer les caractéristiques mécaniques et physiques des granulats - Partie 1 : détermination de la résistance à l'usure (micro-Deval)*, 2011.
- [30] AFNOR, *NF EN 1097-2: Essais pour déterminer les caractéristiques mécaniques et physiques des granulats - Partie 2 : méthodes pour la détermination de la résistance à la fragmentation*, 2011.
- [31] H. Bach, "Evaluation of attrition tests for railway ballast," Institut für Eisenbahnwesen und Verkehrswirtschaft, Graz, 2013.
- [32] E. Azéma, F. Radjaï and G. Saussine, "Quasistatic rheology, force transmission and fabric properties of a packing of irregular polyhedral particles," *Mechanics of Materials*, vol. 41, no. 6, pp. 729-741, 2009.
- [33] C. Lecocq, "La dégradation du ballast," Conservatoire National des Arts et Métiers, Paris, 1985.
- [34] G. R. McDowell, W. L. Lee, A. C. Collop and N. Thom, "Comparison of ballast index tests for railway trackbeds," *Geotechnical Engineering*, vol. 157, no. 3, pp. 151-161, 2004.
- [35] B. Indraratna, N. T. Ngo, C. Rujikiatkamjorn and J. Vinod, "Behavior of fresh and fouled railway ballast subjected to direct shear testing: discrete element simulation," *International Journal of Geomechanics*, vol. 14, no. 1, pp. 34-44, 2014.

- [36] W. L. Lim, "Mechanics of railway ballast behaviour," University of Nottingham, Nottingham, 2004.
- [37] M. Blanc, *Determining the properties of ballast using a simulation test with Vibrogir*, UIC, 1993.
- [38] P. L. Menezes, M. Nosonovsky, S. V. Kailas and M. R. Lovell, "Friction and Wear," in *Tribology for Scientists and Engineers*, New York, Springer, 2013, pp. 43-88.
- [39] G. Amontons, "De la résistance causée dans les machines," *Mémoires de l'Académie Royale*, pp. 257-282, 1699.
- [40] C.-A. Coulomb, *Théorie des machines simples*, Paris: Bachelier, 1821.
- [41] J. A. Greenwood and J. B. P. Williamson, "Contact of nominally flat surfaces," *Proceedings of the Royal Society of London. Series A, Mathematical and Physical Sciences*, vol. 295, no. 1442, pp. 300-319, 1966.
- [42] G. G. Adams and M. Nosonovsky, "Contact modeling - forces," *Tribology International*, vol. 33, pp. 431-442, 2000.
- [43] M. Nosonovsky, "Modelling size, load and velocity effect on friction at micro/nanoscale," *International Journal of Surface Science and Engineering*, vol. 1, pp. 22-37, 2007.
- [44] M. M. Koura, "The effect of surface texture on friction mechanisms," *Wear*, vol. 63, no. 1, pp. 1-12, 1980.
- [45] N. P. Suh, *Tribophysics*, Englewood Cliffs: Prentice Hall, 1986.
- [46] E. Rabinowicz, *Friction and wear of materials*, New York: John Wiley & Sons, 1995.
- [47] P. L. Menezes, "Studies on friction in steel-aluminium alloy tribo-system: Role of surface texture of the softer material," in *Society of Tribologists and Lubrication Engineers (STLE) 2011 - Annual meeting and exhibition*, Atlanta, 2011.
- [48] S. Stupkiewicz and Z. Mróz, "Modelling of friction and dilatancy effects at brittle interfaces for monotonic and cyclic loading," *Journal of Theoretical and Applied Mechanics*, vol. 3, no. 39, pp. 707-739, 2001.
- [49] G. S. Fox-Rabinovich and G. E. Totten, *Self-organization during friction*, Boca Raton: CRC Press, 2006.
- [50] M. Godet, "The third-body approach: a mechanical view of wear," *Wear*, vol. 100, no. 1-3, pp. 437-452, 1984.
- [51] Y. Berthier, L. Vincent and M. Godet, "Velocity accommodation in fretting," *Wear*, vol. 125, no. 1-2, pp. 25-38, 1988.
- [52] A. Zmitrowicz, "Wear patterns and laws of wear - A review," *Journal of Theoretical and Applied Mechanics*, vol. 44, no. 2, pp. 219-253, 2006.
- [53] C. Hatchett, "Experiments and observations on the various alloys, on the specific gravity, and on the comparative wear of gold," *Philosophical Transactions of the Royal Society*, vol. 1, pp. 43-194, 1803.
- [54] G. Rennie, "Experiments on the friction and abrasion of the surface of solids," *Philosophical Transactions of the Royal Society*, vol. 34, no. 1, pp. 143-170, 1829.

- [55] N. G. Yilmaz, "Abrasivity assessment of granitic building stones in relation to diamond tool wear rate using mineralogy-based rock hardness indexes," *Rock Mechanics and Rock Engineering*, vol. 44, no. 6, pp. 725-733, 2011.
- [56] J. F. Archard, "Contact and rubbing of flat surfaces," *Journal of Applied Physics*, vol. 24, pp. 981-988, 1953.
- [57] R. Holm, *Electrical contacts*, Stockholm: Hugo Gebers, 1946.
- [58] K. Kato and K. Adachi, "Wear mechanisms," in *Modern tribology handbook*, Boca Raton, CRC Press LLC, 2001.
- [59] S. Bahadur, "Wear research and development," *Journal of Lubrication Technology - Transactions of the ASME*, vol. 100, no. 4, pp. 449-454, 1978.
- [60] H. C. Meng and K. C. Ludema, "Wear models and predictive equations: their form and content," *Wear*, Vols. 181-183, no. 2, pp. 443-457, 1995.
- [61] A. Ravikiran, "Wear quantification," *Journal of Tribology - Transactions of the ASME*, vol. 122, no. 3, pp. 650-656, 2000.
- [62] K. Kato, "Classification of wear mechanisms/models," *Proceedings of the Institution of Mechanical Engineers, Part J: Journal of Engineering Tribology*, vol. 216, no. 6, pp. 349-355, 2002.
- [63] N. Yoshioka, "Fracture energy and the variation of gouge and surface roughness during frictional sliding of rocks," *Journal of Physics of the Earth*, vol. 34, no. 4, pp. 335-355, 1986.
- [64] R. L. Biegel, W. Wang, C. H. Scholz, G. N. Boitnott and N. Yoshioka, "Micromechanics of rock friction 1. Effects of the roughness on initial friction and slip hardening in westerly granite," *Journal of Geophysical Research*, vol. 97, no. B6, pp. 8951-8964, 1992.
- [65] W. Wang and C. H. Scholz, "Wear processes during frictional sliding of rock: A theoretical and experimental study," *Journal of Geophysical Research*, vol. 99, no. B4, pp. 6789-6799, 1994.
- [66] T. Hirose, K. Mizoguchi and T. Shimamoto, "Wear processes in rocks at slow to high slip rates," *Journal of Structural Geology*, vol. 38, pp. 102-116, 2012.
- [67] C. H. Rycroft, A. Dehbi, T. Lind and G. Salih, "Granular flow in pebble-bed nuclear reactors: Scaling, dust generation, and stress," *Nuclear Engineering and Design*, vol. 265, pp. 69-84, 2013.
- [68] J. Rojek, E. Oñate, H. Kargl, C. Labra, J. Akerman, U. Restner, E. Lammer and F. Zarate, "Prediction of wear of roadheader picks using numerical simulations," *Geomechanik und Tunnelbau*, vol. 1, pp. 47-54, 2008.
- [69] E. Arlaud, "Modèles dynamiques réduits de milieux périodiques par morceaux : application aux voies ferroviaires," Ecole Nationale Supérieure d'Arts et Métiers, Paris, 2016.
- [70] L. Hall, "Simulations and analyses of train-induced ground vibrations in finite element models," *Soil Dynamics and Earthquake Engineering*, vol. 23, no. 5, pp. 403-413, 2003.

- [71] R. Paolucci, A. Maffei, L. Scandella, M. Stupazzini and M. Vanini, "Numerical prediction of low-frequency ground vibrations induced by high-speed trains at Ledsgaard," *Soil Dynamics and Earthquake Engineering*, vol. 23, no. 6, pp. 425-433, 2003.
- [72] T. M. P. Hoang, G. Saussine, D. Dureisseix and P. Alart, "Domain decomposition with discrete element simulations using shared-memory parallel computing for railways applications," *European Journal of Computational Mechanics*, vol. 21, no. 3-6, pp. 242-253, 2013.
- [73] P. A. Cundall and O. D. L. Strack, "A discrete numerical model for granular assemblies," *Géotechnique*, vol. 29, no. 1, pp. 47-65, 1979.
- [74] M. Jean, "The non smooth contact dynamics method," *Computer Methods in Applied Mechanics and Engineering*, vol. 177, no. 3-4, pp. 235-257, 1999.
- [75] M. Jean and J. J. Moreau, "Unilaterality and dry friction in the dynamics of rigid body collections," in *Proceedings of Contact Mechanics International Symposium*, Lausanne, 1992.
- [76] J. J. Moreau, "Unilateral contact and dry friction in finite freedom dynamics," in *Nonsmooth Mechanics and Applications*, Vienna, Springer, 1988, pp. 1-82.
- [77] B. Cambou and M. Jean, *Micromécanique des matériaux granulaires*, Hermes Science, 2001.
- [78] F. Radjai and F. Dubois, *Discrete-element modeling of granular materials*, John Wiley & Sons, 2011.
- [79] C. Cholet, G. Saussine, P.-E. Gautier, F. Dubois, C. Bohatier, G. Combe and K. Sab, "Application of discrete element methods to the modelling of ballasted track," in *World Congress on Railway Research*, Edinburgh, 2003.
- [80] J.-F. Ferrellec, R. Perales, V.-H. Nhu, M. Wone and G. Saussine, "Analysis of compaction of railway ballast by different maintenance methods using DEM," in *EPJ Web of Conferences - Powders & Grains*, Montpellier, 2017.
- [81] T. M. P. Hoang, G. Saussine, D. Dureisseix and P. Alart, "Behaviour of a portion of railway track under maintenance operation," in *World Congress on railway Research*, Lille, 2011.
- [82] G. Saussine and O. Néel, "High speed regulation in extreme conditions," in *Proceedings of the 2nd International Conference on Railway Technology: Research, Development and Maintenance*, Ajaccio, 2014.
- [83] F. Dubois, M. Jean, M. Renouf, R. Mozul, A. Martin and M. Bagnéris, "LMGC90," in *10e Colloque National en Calcul des Structures*, Giens, 2011.
- [84] M. Lu and G. R. McDowell, "The importance of modelling ballast particle shape in the discrete element method," *Granular Matter*, vol. 9, pp. 69-80, 2007.
- [85] J. Irazábal González, "Numerical analysis of railway ballast behaviour using the Discrete Element Method," *Universitat Politècnica de Catalunya*, Barcelona, 2017.
- [86] M. Lu, "Discrete element modelling of railway ballast," *University of Nottingham*, Nottingham, 2008.

- [87] J.-F. Ferrellec and G. R. McDowell, "A simple method to create complex particle shapes for DEM," *Geomechanics and Geoengineering*, vol. 3, no. 3, pp. 211-216, 2008.
- [88] L. Wang, J.-Y. Park and Y. Fu, "Representation of real particles for DEM simulation using X-ray tomography," *Construction and Building Materials*, vol. 21, no. 2, pp. 338-346, 2007.
- [89] N. Ouhbi, C. Voivret, G. Perrin and J. N. Roux, "3D particle shape modelling and optimization through Proper Orthogonal Decomposition: application to railway ballast," *Granular Matter*, vol. 19, no. 86, 2017.
- [90] N. Ouhbi, "Une description morphologique précise des grains pour l'étude numérique des propriétés mécaniques du ballast ferroviaire," Université Paris-Est, Paris, 2017.
- [91] C. Ergenzinger, R. Seifried and P. Eberhard, "A discrete element model predicting the strength of ballast stones," *Computers & Structures*, Vols. 108-109, pp. 3-13, 2012.
- [92] O. Harireche and G. R. McDowell, "Discrete element modelling of cyclic loading of crushable aggregates," *Granular Matter*, vol. 5, pp. 147-151, 2003.
- [93] S. Lobo-Guerrero and L. E. Vallejo, "Discrete element method analysis of railtrack ballast degradation during cyclic loading," *Granular Matter*, vol. 8, pp. 195-204, 2006.
- [94] J. Eliáš, "Simulation of railway ballast using crushable polyhedral particles," *Powder Technology*, vol. 264, pp. 458-465, 2014.
- [95] G. Mollon, "A numerical framework for discrete modelling of friction and wear using Voronoi polyhedrons," *Tribology International*, vol. 90, pp. 343-355, 2015.
- [96] G. R. McDowell and H. Li, "Discrete element modelling of scaled railway ballast under triaxial conditions," *Granular Matter*, vol. 18, no. 66, 2016.
- [97] I. Deiros, "Experimental study of the roughness of ballast," Université Joseph Fourier, Grenoble, 2014.
- [98] D. Tunkin, "Experimental characterization of ballast grain shape by means of X-Ray Tomography," Université Joseph Fourier, Grenoble, 2014.
- [99] F. Stocco, "Experimental characterization of railway ballast degradation under wet conditions," Université Grenoble Alpes, Grenoble, 2017.
- [100] E. Z. Lajtai, R. H. Schmidtke and L. P. Bielus, "The effect of water on the time-dependent deformation and fracture of a granite," *Sciences & Geomechanics Abstracts*, vol. 24, no. 4, pp. 247-255, 1987.
- [101] L. N. Y. Wong, V. Maruvanchery and G. Liu, "Water effects on rock strength and stiffness degradation," *Acta Geotechnica*, vol. 11, no. 4, pp. 713-737, 2016.
- [102] ASTM, *E384-11: Standard test method for Knoop and Vickers hardness of materials*, West Conshohocken: ASTM International, 2011.
- [103] J. K. Mitchell and K. Soga, *Fundamentals of soil behavior*, New Jersey: John Wiley & Sons, 2005.
- [104] W. C. Krumbein, "Measurement and geological significance of shape and roundness of sedimentary particles," *Journal of Sedimentary Research*, vol. 11, no. 2, pp. 64-72, 1941.

- [105] R. D. Barksdale, M. A. Kemp, W. J. Sheffield and J. L. Hubbard, "Measurement of aggregate shape, surface area, and roughness," *Transportation Research Record*, no. 1301, pp. 107-116, 1991.
- [106] T. Zingg, "Beitrag zur Schotteranalyse," Eidgenössische Technische Hochschule Zürich, Zürich, 1935.
- [107] L. B. Wang, J. D. Frost and J. S. Lai, "Three-dimensional digital representation of granular material microstructure from X-ray tomography imaging," *Journal of Computing in Civil Engineering*, vol. 18, no. 1, pp. 28-35, 2004.
- [108] H. Kim, C. Haas, A. Rauch and C. Browne, "Wavelet-based three-dimensional descriptors of aggregate particles," *Transportation Research Record: Journal of the Transportation Research Board*, vol. 1787, pp. 109-116, 2002.
- [109] E. J. Garboczi, "Three-dimensional mathematical analysis of particle shape using X-ray tomography and spherical harmonics," *Cement and Concrete Research*, vol. 32, no. 10, pp. 1621-1638, 2002.
- [110] M. E. Kutay, H. I. Ozturk, A. R. Abbas and C. Hu, "Comparison of 2D and 3D image-based aggregate morphological indices," *International Journal of Pavement Engineering*, vol. 12, pp. 421-431, 2011.
- [111] E. Masad, S. Saadeh, T. Al-Rousan, E. Garboczi and D. Little, "Computations of particle surface characteristics using optical and X-ray CT images," *Computational Materials Science*, vol. 34, no. 4, pp. 406-424, 2005.
- [112] G. Guennebaud and M. Gross, "Algebraic Point Set Surfaces," *ACM Transactions on Graphics*, vol. 26, no. 3, pp. 23-29, 2007.
- [113] E. C. G. Andò, "Experimental investigation of micro-structural changes in deforming granular media using x-ray tomography," Université de Grenoble, Grenoble, 2013.
- [114] J. Hsieh, *Computed tomography: principles, design, artifacts and recent advances*, 2nd ed., SPIE and John Wiley & Sons, 2009.
- [115] D. P. Huttenlocher, G. A. Klanderman and W. A. Rucklidge, "Comparing images using the Hausdorff distance," *IEEE Transactions on Pattern Analysis and Machine Intelligence*, vol. 15, no. 9, pp. 850-863, 1993.
- [116] J. L. Bentley, "Multidimensional binary search trees used for associative searching," *Communications of the ACM*, vol. 18, no. 9, pp. 509-517, 1975.
- [117] F. Alonso-Marroquín and H. J. Herrmann, "Ratcheting of granular materials," *Physical Review Letters*, vol. 92, no. 5, 2004.
- [118] G. Armand, "Contribution à la caractérisation en laboratoire et à la modélisation constitutive du comportement mécanique des joints rocheux," Université Joseph Fourier, Grenoble, 2000.
- [119] J. Hans and M. Boulon, "A new device for investigating the hydro-mechanical properties of rock joints," *International Journal for Numerical and Analytical Methods in Geomechanics*, vol. 27, no. 6, pp. 513-548, 2003.

- [120] Getzner, "Sylodyn®," [Online]. Available: <https://www.getzner.com/en/products/sylodyn>. [Accessed January 2018].
- [121] Getzner, "Getzner wins order worth 5 million euros from French railways," [Online]. Available: <https://www.getzner.com/en/press/getzner-wins-order-worth-5-million-euros-from-french-railways>. [Accessed January 2018].

Annex A. DEVICES AND SAMPLES

A. 1. BCR3D device.....	168
A. 1. 1. Sample description and preparation	168
A. 1. 2. Positioning the sample in the machine	172
A. 2. Laser profilometre	174

A. 1. BCR3D DEVICE

The acronym BCR3D comes from the French name “Boîte de Cisaillement direct pour joint Rocheux à 3 Dimensions” which translates as “Direct Shearing Box for rock joints at 3 dimensions”. This machine has been entirely developed for the Laboratory 3SR in Grenoble in 2000 [118, 119] and its initial purpose was to study the hydromechanical behaviour of rock joints subjected to direct shearing.

The main peculiarity of this device is that all three axes can be manipulated independently, thanks to five different engines, offering a lot of freedom for the application of different kinds of loads and unique advantages.

BCR3D consists of three loading axis, one for the vertical efforts (Z) and two other orthogonal ones at the horizontal plane (X and Y), who are the responsible of the shearing itself (see Figure 4.13). The sample is located at the centre inside two metallic boxes, usually called semi-boxes, allowing for samples that can be fitted inside a 10x10 cm square, 6 cm deep. Each horizontal axis is moved thanks to two different engines, with its corresponding speed reducer, that permit the independent movement of the upper and the lower semi-boxes of the sample. A fifth engine is in charge of moving and controlling the vertical axis.

Thanks to this particular setup, it is possible to shear samples on whatever the horizontal direction and even following the desired trajectory. Another advantage is that, since both parts of the sample can be moved independently, it is possible to perform a symmetric shearing so that the vertical force is always kept centred along the test.

In terms of captors, each of the five engines is associated to a force captor and to a displacement captor. The device uses LVDT's (“Linear Variable Differential Transformer”), offering a 6 cm range, to keep control of the positioning. For the forces, 5 Traction – Compression force cells (type F522TC), with a capacity of ± 100 kN, are used.

There are several modes of control, given by the electronics of the machine. For instance, in terms of displacement it is possible to run the experiment imposing the displacement and/or the speed. On the other hand, it is possible to control either the force or the stress, or even other combinations like rigidity. However, for this project the device is used in its simplest mode, imposing a constant normal force and amplitude of the cycle. Due to the irregular nature of ballast, it is not necessary to keep the vertical force centred so, in order to reduce the mechanical friction, only one of the semi-boxes will move while the other will try to remain still, correcting the movements induced by the shearing. More details about the conditions of the tests are given in the corresponding section 4. 3. 3.

A. 1. 1. Sample description and preparation

Ballast samples need to be prepared using the proper metallic semi-boxes that fit the dimensions of the sample compartment. These boxes consist of a detachable metallic frame,

made up of four screwed pieces. This is so to be able to uncouple the sample from the box once the experiments are finished. The space left by the frame, 10x10x6 cm in size, is enough for fitting one ballast grain on each semi-box (Figure A.1).

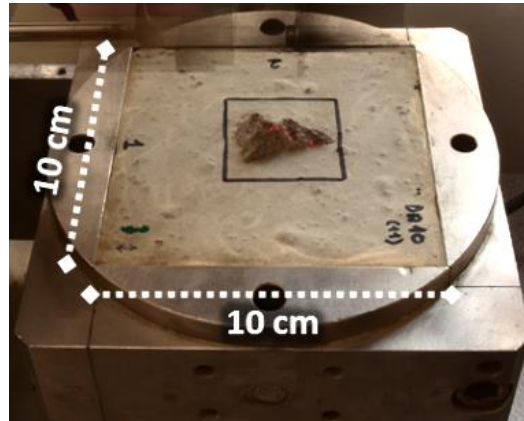


Figure A.1 Vertex – Ballast sample inside the metallic frame.

Depending on which kind of sample we want to prepare, the procedure will be different. However, whatever the type of sample, it is important to previously clean carefully the metallic frame from previous tests and to join all four pieces using the screws strong enough to resist the efforts and to seal the walls against leaks during the hardening phase of the mortar / concrete.

Ballast samples

The process that will be explained below can only be used as a guide for preparing ballast samples or samples that follow the same specific characteristics. The main advantage of using ballast grains for shearing is that the surface is rough all around it, so choosing a specific contact point is not that important, nor it is the inclination of the sample even if we will try to orientate the face more or less horizontally. Thus a prealignment of the boxes is not necessary and it facilitates a lot the preparation of the samples. In any case, in order to ease the positioning afterwards inside the machine and to perform the laser scans, it is recommended to approximately centre-locate the ballast aggregates within the box.

Ballast grains are fixed to the metallic box using rapid-set mortar, which gives the sample resistance enough to hold the grain during the applied shear. Before, in order to orientate the grains in either vertex or face setup, playdoh is used as a basis support. This playdoh is not removed and the mortar is poured around it.

Ballast samples are chosen so that they offer the required characteristics. Grains for “face samples” need to offer, obviously, at least one pretty flat (although rough) face. On the other hand, for “tip samples” we will generally use elongated grains that usually offer at least one pointy end, but ensuring that it is not too weak, so it can resist shearing. In both cases it is important to consider that the grain needs to be fixed by mortar, so the “sunken” part of the grain needs to be large enough to get properly glued.

Once we have the metallic frame clean, assembled and ready for preparation and we have chosen the ballast grains, the steps are then the following:

1. Place the frame over an impermeable and flat surface, e.g. a piece of wooden shuttering. It is important that the full “hole” left by the frame for the actual sample is covered. The frame has not a base itself, so this step is needed to be able to pour the mortar in the frame.
2. Spread grease over the walls of the frame in order to facilitate the future disassembling of the sample from the frame.
3. Create a thin pillar of playdoh, but capable enough to hold a ballast grain. Locate it in the centre of the sample area.
4. Place and orientate the ballast grain on the top of the playdoh pillar. The playdoh can be moved and reshaped to optimize the setup. The idea is to minimize the playdoh material but ensuring the right positioning of the grain and that the ensemble playdoh – grain does not move during the pouring.
 - a. If preparing a vertex sample, try to centre the tip making it stand 1.5 – 2.0 cm above the upper plane of the metallic frame. In order to avoid issues with the laser scans, it is better to avoid too vertical walls and negative inclinations.
 - b. If preparing a face grain, make sure it stands at least 0.5 cm above the frame. Try also to keep the horizontality of the face as much as possible.
5. Prepare the mortar in a separate container following the instructions of the manufacturer.
6. Carefully pour the mortar inside the sample area, all around the grain. Take care that the grain does not change its position during the process. Fill up to the upper plane of the frame, trying to keep an even surface at the top. Use a stick or a spoon to spread homogeneously the paste.
7. Let the sample dry following the recommendations of the manufacturer. If time is not a constraint, it is better to let it dry for 3-4 weeks.

After the drying, the sample is ready for use and we can then proceed to scan it with the laser profilometre before the shearing tests. In order to keep track of the scanning area and to always rescan within the same area and orientation, we can draw the scanned square with a marker. Usually the scanned area is much smaller than the full sample. In our case, we considered that a scan of a 4x4 cm square was enough to cover the shearing area. Since there is a lot of space left of mortar surface, another recommendation is to keep track of the tests performed over each specific sample, not only noting down the tests on a paper or informatics document, but also on the sample itself with a marker.

Concrete samples

Due to the limited space for the sample, concrete needs to be a bit particular. Aggregates used to prepare it need to be small enough to both fit inside the sample area and be able to spread and mix so that we obtain a homogeneous enough material. For this reason, the maximal aggregate size is 1.1 cm. Table A.1 shows the mixing ratios used:

Component	Quantity (kg / m ³)
Cement CEM I 52.5R	280
Sand 0/4mm	650
Sand 0/2mm	150
Aggregate 11.2/22.4mm	780
Aggregate 4/11mm	330
Plasticizer – OPT 203	2.8
Water	157 (w/c = 0.56)

Table A.1 Mixing proportions of the concrete used for the ballast – concrete shearing tests.

Concerning its mechanical properties, this concrete offers compression strength of 43.4 MPa and a tensile strength of 3.75 MPa.

Concrete samples are prepared upside-down to ensure a flat shearing surface and the irregular bottom surface is evened using sealing cement. The steps are the followings:

1. Prepare the desired concrete.
2. Place the metallic frame upside-down on a flat and impermeable surface. Again, a piece of wooden shuttering is a good idea.
3. Pour the concrete on the sample area filling it almost completely. It is important that concrete does not spill over the frame. In fact, it is better to leave a 1-2 mm margin.
4. Vibrate the concrete in order to eliminate air bubbles and to homogenize the material.
5. Ensure that no material is over the frame top plane and, if necessary, remove the extra material.
6. Let the sample dry, if possible, up to at least 28 days.
7. Once the sample is dry enough (it is not necessary to wait the 28 days for this step), prepare the sealing cement and fill the margin with it. Use a ruler or a long straight tool to ensure a perfectly flat surface. Remember that this is the bottom part of the box, so it is important to properly execute this step to ensure there will be no gap below the sample.

Again, drawing the scanned area with a marker will help us to rescan always on the same area facilitating the posterior data analysis.

Under-sleeper Pads (USP)

One of the solutions to reduce the amount of ballast wear, already implemented in some railway tracks, are under-sleeper pads or USP. These pads serve not only to reduce wear but also to reduce vibrations, especially in urban areas. As its name indicates, these pads are placed under the concrete sleepers and constitute an additional elastic layer between the block and ballast. They are made of different polymeric materials depending on its function and its thickness ranges from 0.5 to 1.0 cm or even slightly more. In this project, two different USP provided by the company Getzner to SNCF have been tested (Figure A.2):

- Vibration reduction (SLN ©Sylodyn). A highly elastic closed-cell elastomer that offers an important reduction of vibrations and noises [120].

- Attrition reduction (PRAG v3). Also known as PRA (Patin Réducteur d'Attrition), and developed from 2006 to 2010 by Getzner especially for SNCF, this USP improves the distribution of the external loads to the ballast layer, effectively reducing the amount of wear suffered by ballast. Also elastic but much stiffer than SLN, PRA is able to also offer a long durability at the expense of not being a proper solution for vibration reduction [121].

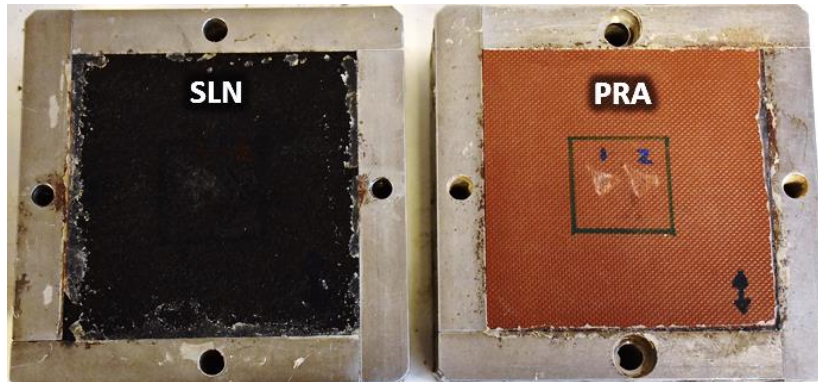


Figure A.2 The two kinds of USP used: vibration reduction or SLN (left) and attrition reduction or PRA (right).

The idea of these tests is to study the interaction between the USP and the ballast grains, especially in terms of degradation of the aggregates. Even if these pads are fixed to the sleepers using the concrete itself, as a matter of simplicity it was easier to use mortar to fix them to the boxes. The result is actually the same since we are just testing the interaction pad-ballast.

1. Cut the pad either with scissors or with a saw to the dimensions of the sample area (10x10 cm).
2. Glue the USP at the top of the metallic frame using silicon with the flat surface on top. It is important to carefully seal all the holes to avoid leaks.
3. Put the frame upside-down and pour the mortar in the sample area. Again, it is important that the mortar does not spill over the frame and, if necessary, remove the extra material.
4. Let the sample dry.
5. Correct the bottom part of the box with sealing cement, if necessary, to ensure a flat surface.

A. 1. 2. Positioning the sample in the machine

Although it is not a complicated machine, BCR3D has some peculiarities that need to be taken into account when performing tests on it. In addition, it is the first time that the device has been used to perform tests of such a kind, i.e. shearing directly two single grains. We have seen how the preparation of the samples already required some tricks and imagination like the use of playdoh to place the grain in the proper position and orientation. Due to these peculiarities, the positioning of the sample inside the machine requires also some additional steps that will

be explained in this section. Thus, the same way the previous section was a guideline on how to prepare the samples, this one intends to be a user guide on the positioning of these specific samples, based on our experience, that could be useful for future experiments of the same kind. Nevertheless, other general aspects like the procedure of turning on the machine and the regulation or how to perform an experiment will not be detailed here, there is already a manual of the device where everything is explained.

The idea to place both boxes in the machine is to first fix the lower box, which does not give any problem. Then put the upper box over the lower and slowly descend the machine until it fits the sample and we can fix the box. Traditionally, due to the nature of rock joints and concrete interfaces, samples for BCR3D were prepared so that both semi-boxes could stack one over the other. In some cases, that required a precise alignment of both boxes that was performed thanks to screws joining both samples. In some other cases the sample was already built “gluing” both boxes, e.g. when studying concrete – rock interfaces. However, in the case of ballast, due to the irregularity of the surfaces, both semi-boxes cannot stack together. Fortunately, alignment is not a must so we solved this issue using two additional metallic pieces of equal size that allow for a temporary stack of both semi-boxes (Figure A.3). These pieces are extracted once the upper box is well fixed to the machine, but this procedure requires extra steps and caution during the positioning.

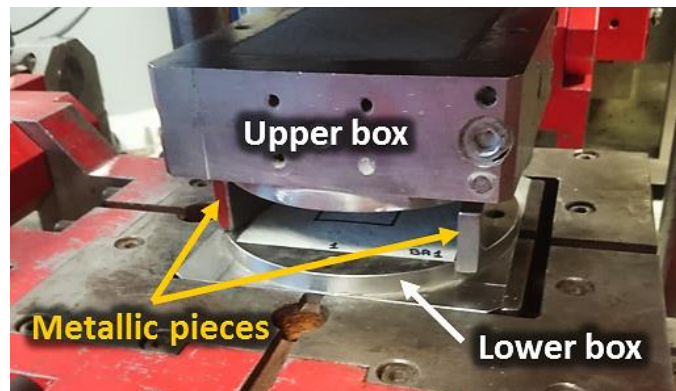


Figure A.3 Position of both boxes before fixing the upper box, stacked thanks to both equal-sized metallic pieces.

Let us assume that the machine is clean and empty from the last test. The upper compartment is up and uncoupled from the horizontal engine, and the Z LVDT is removed (all of that is necessary in order to extract the previous boxes). The steps to follow are the following:

1. Decide the horizontal axis on which the test will be performed. Decide as well if there is a desired direction of shearing for each sample. It is useful to draw an arrow to indicate this preference.
2. Place the lower box in the lower sample container taking care of the shearing direction of the box decided on step 1.
3. In order to facilitate the extraction of the semi-box after the experiment, the sample container is bigger than the semi-box itself and the screws are not long enough to cover that gap. For this reason, a metallic piece is added to fill part of the gap before screwing up (in Figure A.3, this piece can be seen on the right of the lower box).

4. Fix the lower semi-box tight with the screws.
5. Put the additional metallic pieces and the upper semi-box upside-down on them, like in Figure A.3. Again, be careful with the orientation of the box, if a shearing direction is preferable.
6. Descend the upper container of the machine up to almost touching the upper box.
7. With the help of a mirror, adjust the position of the upper box so that it fits the upper container. Check that all four sides have enough room.
8. Slowly descend the upper container monitoring the normal forces. If everything is ok, it should descend smoothly without any increment of the normal force. However, if an increment appears, that means that the semi-box is touching one of the sides, so stop the movement and go up again to correct the position of the semi-box.
9. Descend up to cover the full upper semi-box. The last part, do it slowly until the normal force starts to increase, which means that the container and the box are in contact. It is also possible to use an approach algorithm implemented in the software.
10. Fix the upper box with the screws. Like with the lower semi-box, one of the axes leaves too much gap, so a metallic piece is required before screwing tight.
11. Go up a couple of millimetres with the machine in order to remove the metallic pieces.
12. Descend up to almost contact between the samples.
13. Connect the horizontal engine with the upper container using the metallic bar and a hammer. Try to use a bar that is lubricated enough to reduce the friction. This connection is the main responsible of normal force measuring errors.
14. Connect the Z LVDT, ensuring the full test will be in its working range. Be careful, this step is easily forgettable.
15. Recommendation: tare to zero all measuring values at this point. In order to reduce measuring errors, it is important to tare the normal force when coming from a descending movement of the upper container.

After the experiment, we will follow the opposite procedure to extract the sample. Again, it is important to remember to remove the Z LVDT and to uncouple the horizontal engine from the upper container.

A. 2. LASER PROFILOMETRE

When dealing with relatively flat surfaces, a laser displacement sensor, or laser profilometre, is a good scan method. It is fast, easy to use and we can repeat scans as many times as desired. Due to the amount of samples tested, this last point was essential for this project.

The device consists in several independent parts that were assembled together in order to get an instrument capable of providing data in the form of coordinates in all three axes.

The main part is the laser displacement sensor itself, which uses the direct reflection on the measured surface of the light from a red laser beam in order to determine the distance to the surface, measuring the time-of-flight of the light. Since the beam comes from a zenithal

position, vertical or very steep features can lead to some measurement inaccuracies. Of course, features below negative slopes are completely hidden to the laser. It is not colour sensitive so it is possible to directly scan samples with heterogeneous surface colour like the case of granite. High-reflective materials like granite quartz crystals could eventually create some false measurements, but they occur rarely and if they happen they are easily detected and erased.

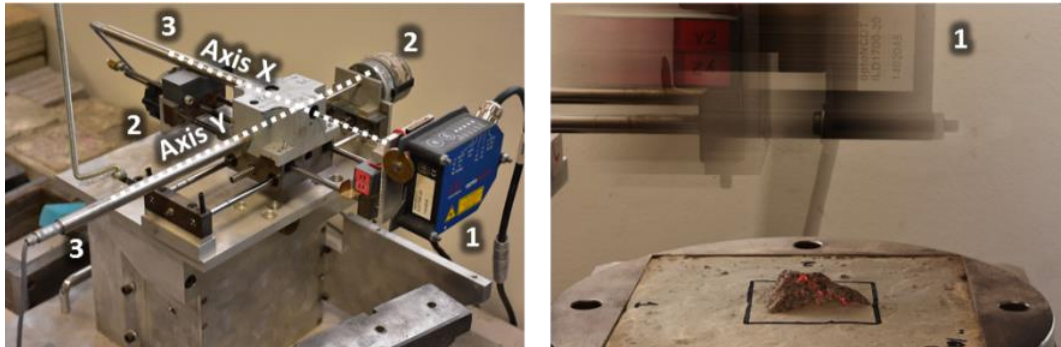


Figure A.4 Laser profilometre. Left: full structure of the device, the sample to scan would be placed under the sensor (1). Right: sample being scanned.

Figure A.4 shows the device and how it works. The sensor (1) is attached to two horizontal axis moved by two little engines (2) through screws, which at the same time are attached to LVDT sensors (3) that give the horizontal coordinates. The sensor will do a passage back and forward along the X-axis and then it will move a small step on the Y-axis to perform another passage. This way, the full scan is built on parallel lines oriented in the X-direction. In the end we will obtain a cloud of points that will allow for a posterior reconstruction, in our case with Matlab.

The supporting structure was made in the laboratory and it fails to take full advantage of the sensor capacity. Again, the mechanical parts become the weak point of the device. Two problems have been identified associated to the horizontal axes. First of all, on the X-axis, the support is only fixed on one side, so a bending moment appears and creates a difference of more than 1 mm between extremes. Besides, this bending moment does not follow a regular shape along the Y-axis, so it cannot be fixed using a simple correction function. The second error corresponds to the screw moving the laser sensor along the Y-axis, it creates a wavy behaviour with the same wave length as the pitch of the screw and a vertical amplitude in some areas (again, it is not homogeneously distributed) of even more than 0.1 mm. Figure A.5 shows the scan of a calibrated flat surface. We can clearly distinguish both described errors: the major change in colour corresponds to the bending and the horizontal lines to the screw wave.

In order to solve both problems, since the error is consistent in position, we took the scan of the flat surface as a reference subtracting it from each posterior scan. As an additional measure, it can be observed that the wave behaviour is less pronounced on the top half of the scan, i.e. between 40 and 80 mm in the Y-axis, than on the bottom half. Since the required area for the shearing test was never bigger than 40x40 mm, we decided to always scan within the range 40-80 mm in the Y-direction. Finally, slight difference was detected when the laser was going forward compared to going backwards, so in the analysis we decided to only take into account data taken either forwards or backwards, but never together.

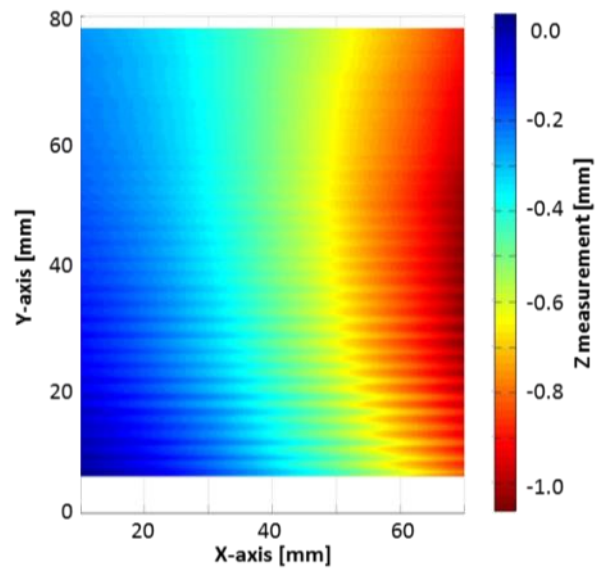


Figure A.5 Scan of a flat surface. The difference in colour corresponds to the bending and the horizontal lines to the wave behaviour due to the screw.

Thanks to all these steps, we estimate the accuracy of the laser on at least ± 0.02 mm in the vertical direction. Concerning the horizontal resolution, it was considered enough to have a scan line every 0.10 mm.

